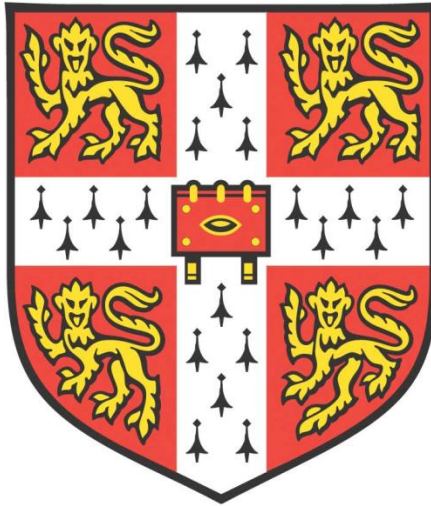


# *XRAY GENERATION BY FIELD EMISSION*



**Richard Parmee**  
**Pembroke College**

**Electrical Engineering Division**  
**Department of Engineering**  
**University of Cambridge**

**This dissertation is submitted for the degree of Doctor of Philosophy**

**April 2018**



## DECLARATION

This dissertation is submitted to the University of Cambridge for the degree of Doctor of Philosophy. The work described was carried out between October 2010 and March 2018 at the Department of Engineering, University of Cambridge. This dissertation is my own work, although some work was done in collaboration with others as specified in the Acknowledgements. It has not been previously submitted, in part or whole, to any university or institution for any degree, diploma, or other qualification.

In accordance with the Department of Engineering guidelines, this thesis does not exceed 65,000 words, and it contains less than 150 figures.

Signed: \_\_\_\_\_

Date: \_\_\_\_\_

Richard Parmee MA  
Cambridge



## ABSTRACT

Since the discovery of X-rays over a century ago the techniques applied to the engineering of X-ray sources have remained relatively unchanged. From the inception of thermionic electron sources, which, due to simplicity of fabrication, remain central to almost all X-ray applications at this time, there have been few fundamental technological advances. The emergence of new materials and manufacturing techniques has created an opportunity to replace the traditional thermionic devices with those that incorporate Field Emission electron sources.

One of the most important attributes of Field Emission X-ray sources is their controllability, and in particular the fast response time, which opens the door to applying techniques which have formerly been the preserve of optical systems. The work in this thesis attempts to bridge the gap between the fabrication and optimisation of the vacuum electronic devices and image processing aspects of a new approach to high speed radiographic imaging, particularly with a view to addressing practical real-world problems.

Off the back of a specific targeted application, the project has involved the design of a viable field emission X-ray source, together with the development of an understanding of the failure modes in such devices, both by analysis and by simulation. This thesis reviews the capabilities and the requirements of X-ray sources, the methods by which nano-materials may be applied to the design of those devices and the improvements and attributes that can be foreseen. I study the image processing methods that can exploit these attributes, and investigate the performance of X-ray sources based upon electron emitters using carbon nanotubes. Modelling of the field emission and electron trajectories of the cathode assemblies has led me to the design of equipment to evaluate and optimise the parameters of an X-ray tube, which I have used to understand the performance that is achievable. Finally, I draw conclusions from this work and outline the next steps to provide the basis for a commercial solution.

## Xray Generation by Field Emission

## ACKNOWLEDGEMENTS

I would like to express my sincere thanks to all involved, directly and indirectly, with my work over the last seven years. Both those inside the department who shared their expertise and those outside who helped make this time so enjoyable, without your friendship this thesis would not have been possible. I am most grateful for the help and guidance from my supervisor, Professor Bill Milne. His patience and support was invaluable. Special thanks go to Dr. Matthew Cole and Dr. David Hasko, whose energy, advice and knowledge in guiding me through the academic and practical aspects of my work were outstanding and this work would not have been possible without them. I am grateful for the help of and Professor Ravi Silva, who provided CNT samples, and Dr. Xuesong Yuan, who, as a visiting scholar to our group, assisted with electron trajectory modelling. I would like to thank all the members of the Electronic Devices and Materials Group, and more generally the wider group of academics in the Electrical Division, Engineering Department, past and present. Their support has made my period of work a pleasure and they were always available to answer my questions, listen to my ideas and encourage me. Special thanks are reserved for all my friends at Pembroke College and throughout the University over the last 7 years. Their interest in my activities has been much appreciated, and they have been a wonderful source of encouragement and entertainment and I value all our memories. I must also mention the Disability Resource Centre, for their assistance, and my clinical teams in Addenbrookes Hospital, who have variously, over the last years, cured me of cancer, fixed my broken leg and regularly helped to keep me upright and walking.

Last but not least I would like to thank my long term shield and defender, Barbara. Her support and assistance for the last 37 years have helped me to achieve all that I have. This thesis would not have been possible without her friendship and it is dedicated to her.

## Xray Generation by Field Emission

## PUBLICATIONS

### Journal Articles

M. T. Cole, M. Doherty, **R. Parmee**, P. Dawson, & W. I. Milne, “Ultra-broadband polarisers based on metastable free-standing aligned carbon nanotube membranes”, *Adv. Opt. Mater.*, 2, 10, 929-937, 2014

**Parmee R**, Collins C, Milne W and Cole M “X-ray generation using carbon nanotubes” *Nano Convergence* 2, 1, 2015

Ding S, Cole M, Li C, Zhou Y, Collins C M, Kang M H, **Parmee R J**, Lei W, Zhang X, Dai Q, Milne B and Wang b “Towards Graphane Field Emitters” *RSC Advances* 5 (127) 105111-105118 2015

C. M. Collins, **R. J. Parmee**, W. I. Milne, & M. T. Cole “High Performance Field Emitters” *Adv. Sci.*, 2, 3, 2016

M. T. Cole, **R. J. Parmee**, & W. I. Milne “Nanomaterial-based X-ray Sources” *Nanotech.*, 27, 8, 2016

M. T. Cole, **R. J. Parmee**, A. Kumar, C. M. Collins, M. H. Kang, J. Xiao, C. Cepek, X. Yuan, & W. I. Milne “Conjugated Polyelectrolyte Nano Field Emission Adlayers” *Nanoscale Horiz.* 1, (4), 304-312 2016

M. T. Cole, S. Coskun, **R. J. Parmee**, P. Hiralal, C. Cepek, A. W. Robertson, C. Li, Q. Dai, J. H. Warner, W. I. Milne, & H. Unalan “Suppressed Hysteretic Field Emission from Polymer Encapsulated Silver Nanowires” *IEEE Nano. Exp.*, 99, 2016

X. Yuan, Y. Zhang, M. T. Cole, Y. Yan, X. Li, **R. Parmee**, J. Wu, N. Xu, W. I. Milne & S. Deng “A Truncated-Cone Carbon Nanotube Cold-Cathode Electron Gun” *Carbon* 2017

Nagaraja Rao, Brian Ament, **Richard Parmee**, Jonathan Cameron, Martin Mayo “Rapid, non-destructive inspection and classification of inhalation blisters using low-energy x-ray imaging”, J.Pharm.Innovation, 1-13. May 2018

#### Book Chapters

M. T. Cole, C. Collins, **R. Parmee**, & W. I. Milne, “NanoCarbon Electron Emitters: Advances & Applications”, Chemical Functionalisation of Carbon Nanomaterials: Chemistry & Applications - Structure & Synthesis , (Taylor & Francis), 2014

# CONTENTS

<b>1</b>	<b>RESEARCH PROBLEM STATEMENT .....</b>	<b>21</b>
1.1	BACKGROUND.....	22
1.2	SPECIFIC APPLICATION FIELD .....	22
1.3	PRIOR WORK .....	23
1.4	SCOPE OF THE PROJECT .....	23
1.5	COMMERCIAL BACKGROUND .....	25
1.6	CONTENTS OF THIS THESIS .....	25
1.7	REFERENCES .....	26
<b>2</b>	<b>BACKGROUND .....</b>	<b>27</b>
2.1	HISTORICAL PERSPECTIVE .....	27
2.2	IMPORTANCE OF X-RAY TECHNOLOGY .....	30
2.3	APPLICATIONS IN MANUFACTURING .....	31
2.4	CONSTRUCTION OF THE XRAY SOURCE .....	32
2.5	FIELD EMISSION SOURCES AND THE PRINCIPLES OF FIELD EMISSION .....	36
2.6	CARBON NANOTUBES IN A FIELD EMISSION DEVICE.....	38
2.7	CONCLUSIONS .....	38
2.8	REFERENCES .....	38
<b>3</b>	<b>INTRODUCTION TO NANO ENGINEERED ELECTRON SOURCES.....</b>	<b>43</b>
3.1	ELECTRON EMISSION .....	43
3.2	FIELD EMISSION APPLICATION OF CNTs .....	47
3.3	CATHODE FABRICATION .....	49
3.3.1	<i>Drop, Spray and Cast</i> .....	52
3.3.2	<i>Electrophoresis</i> .....	52
3.3.3	<i>Vacuum filtration &amp; screen printing</i> .....	53
3.3.4	<i>Chemical vapour deposition</i> .....	56
3.4	CONCLUSIONS .....	58
3.5	REFERENCES .....	58
<b>4</b>	<b>FUNCTIONAL ENHANCEMENTS .....</b>	<b>65</b>
4.1	BEAM PROFILING.....	65
4.2	HIGH BEAM CURRENT.....	67
4.3	ENHANCED TEMPORAL STABILITY.....	69
4.4	MICRO-FOCAL SOURCES.....	72

4.5	PULSED SOURCES .....	73
4.6	STATIC TOMOGRAPHY & TOMOSYNTHESIS .....	77
4.7	MULTI-PIXEL SOURCES .....	79
4.8	COMPACT & MINIATURE SEALED TUBES .....	81
4.9	USE OF ADLAYERS .....	84
4.10	CONCLUSIONS .....	85
4.11	REFERENCES .....	85
<b>5</b>	<b>ENCODED APERTURE.....</b>	<b>91</b>
5.1	INTRODUCTION .....	91
5.2	OBJECTIVES .....	92
5.3	METHODOLOGY .....	92
5.4	APPARATUS .....	92
5.5	THE PROGRAM .....	93
5.5.1	<i>Motor interface features</i> .....	94
5.5.2	<i>Detector interface features</i> .....	95
5.5.3	<i>Sequences section</i> .....	96
5.5.4	<i>Dexela 1512CL-Detector</i> .....	96
5.5.5	<i>Control of X-ray Generator</i> .....	96
5.5.6	<i>Stepper motor</i> .....	96
5.6	METHOD AND DESCRIPTION.....	97
5.6.1	<i>Moving to position</i> .....	97
5.6.2	<i>Covertng to a 16 bit picture</i> .....	97
5.6.3	<i>Unscrambling</i> .....	97
5.7	FLAT FIELD CORRECTION .....	98
5.8	DECONVOLUTION.....	99
5.8.1	<i>Deblurring an image via deconvolution.</i> .....	100
5.8.2	<i>Code selection</i> .....	101
5.8.3	<i>Singular Value Decomposition:</i> .....	102
5.9	RESULTS .....	102
5.10	DISCUSSION ON TOMOGRAPHY .....	104
5.11	CONCLUSIONS .....	105
5.12	REFERENCES .....	106
<b>6</b>	<b>EVALUATION OF SEALED INSERTS.....</b>	<b>107</b>
6.1	INTRODUCTION .....	107

6.2	CONSTRUCTION OF CATHODE ASSEMBLY .....	108
6.3	GENERATOR DESIGN .....	110
6.4	SAFETY CONSIDERATIONS .....	113
6.5	RESULTS .....	113
6.6	FAILURE MODES .....	117
6.7	ANNEALING AND SEASONING OF THE CATHODE IN PASTE PRINTED DEVICES..	119
6.8	CONCLUSIONS .....	122
6.9	REFERENCES .....	124
<b>7</b>	<b>DEMOUNTABLE ASSEMBLY .....</b>	<b>125</b>
7.1	BACKGROUND.....	125
7.2	DESIGN OF MOTORISED CATHODE ASSEMBLIES .....	125
7.3	CATHODE CONCEPT DESIGN - MOTORISATION .....	126
7.4	DETAILED 3D MODEL AND DESIGN.....	127
7.5	CATHODE CONCEPT DESIGN – CHIP CARRIER .....	128
7.6	CATHODE CONCEPT DESIGN – ELECTRICAL .....	128
7.7	CATHODE CONCEPT DESIGN – GATE.....	129
7.8	3D PRINTED PROTOTYPE .....	129
7.9	CATHODE-ANODE ASSEMBLY MOTORISATION .....	130
7.10	VACUUM SYSTEM.....	131
7.11	VACUUM TESTING .....	133
7.12	INTERCHANGE OF PARTS .....	133
7.13	RESEARCH VACUUM CHAMBER ASSEMBLY .....	135
7.14	CONTROL ELECTRONICS .....	137
7.15	SPECIAL XGEN CONTROL FUNCTIONS .....	138
7.15.1	<i>Motor control functions .....</i>	<i>138</i>
7.15.2	<i>Alternative drive via high level commands.....</i>	<i>140</i>
7.15.3	<i>Calibration of motors.....</i>	<i>141</i>
7.15.4	<i>Cathode Gap Calibration .....</i>	<i>141</i>
7.15.5	<i>Anode Position Calibration .....</i>	<i>143</i>
7.15.6	<i>Pressure gauge monitoring and Pump interlock .....</i>	<i>143</i>
7.16	MODIFICATIONS TO THE CHAMBER.....	145
7.16.1	<i>Beryllium window. ....</i>	<i>145</i>
7.16.2	<i>Thermal dissipation. ....</i>	<i>145</i>
7.17	PRACTICAL CONSTRUCTION .....	146

7.18	OPTIONS FOR CREATING PULSE X-RAY SOURCE .....	148
7.19	CONCLUSIONS .....	149
7.20	REFERENCES .....	150
<b>8</b>	<b>FIELD EMISSION MODELLING .....</b>	<b>151</b>
8.1	INTRODUCTION .....	151
8.2	COMSOL MODELLING .....	152
8.3	MODELLING OF INDIVIDUAL SOURCE .....	154
8.4	MODELLING OF ARRAY OF EMITTERS .....	155
8.5	MODELLING IRREGULAR ARRAYS .....	158
8.6	SIMULATION OF TRIODE CONFIGURATION .....	158
8.7	MODELLING EMITTERS WITH CONTROL ELECTRODES .....	159
8.8	MODELLING EXTENDED GEOMETRICAL STRUCTURES .....	160
8.9	MODELLING OF MACRO CATHODE ASSEMBLY (CST) .....	162
8.10	CONCLUSION.....	169
8.11	REFERENCES .....	169
<b>9</b>	<b>FIELD EMISSION ELECTRON SOURCE .....</b>	<b>171</b>
9.1	CATHODE ASSEMBLY.....	171
9.2	FABRICATION METHODS .....	172
9.3	CNT GROWTH .....	172
9.4	DESIGN OF THE EMITTER .....	172
9.6	PARALLEL PLATE MEASUREMENTS .....	176
9.7	RESULTS FROM PARALLEL PLATE RIG.....	177
9.8	SAMPLES FROM SURREY .....	179
9.10	SURREY “AFTER DENSIFICATION” PLOTS .....	183
9.13	RESULTS FROM A PATTERNED ARRAY .....	187
9.14	FURTHER SURREY SAMPLES .....	189
9.16	TWO TERMINAL TESTING OF THE CATHODE/GRID SECTION.....	191
9.17	THREE TERMINAL TESTING.....	192
9.18	CONCLUSIONS .....	194
9.19	REFERENCES .....	194
<b>10</b>	<b>DETECTOR AND SCINTILLATOR CHARACTERISTICS.....</b>	<b>197</b>
10.1	INTRODUCTION .....	197
10.2	TEMPORAL PERFORMANCE OF X-RAY DETECTORS .....	198
10.3	REQUIREMENT FOR ENCODED APERTURE IMPLEMENTATION .....	199

10.4	SCINTILLATOR RESPONSE TIME .....	200
10.5	MANUFACTURERS DATA .....	201
10.6	DEVELOPMENT OF SCINTILLATOR TESTING RIG .....	202
10.7	METHODOLOGY .....	203
10.8	CONCLUSIONS .....	206
10.9	IMPACT OF NON-IDEAL SCINTILLATOR RESPONSE .....	206
10.10	REFERENCES .....	207
<b>11</b>	<b>CONCLUSIONS .....</b>	<b>209</b>
11.1	SUMMARY OF WORK COMPLETED .....	209
11.2	FURTHER WORK .....	211
<b>12</b>	<b>APPENDICES .....</b>	<b>213</b>

## LIST OF TABLES

TABLE 1: SUMMARY OF ELECTRON TRAJECTORY SIMULATION.....	165
TABLE 2 : SUMMARY OF CLARE EMITTER PERFORMANCE .....	178
TABLE 3: SUMMARY OF SURREY”AS GROWN” EMITTER PERFORMANCE.....	182
TABLE 4 : SUMMARY OF SURREY “DENSIFIED” EMITTER PERFORMANCE .....	183
TABLE 5 : SUMMARY OF ALL EMITTER PERFORMANCE .....	184
TABLE 6 : CSI SCINTILLATOR WITH FIBRE-OPTIC PLATE .....	206

## LIST OF FIGURES

FIGURE 1: THE HAND OF FRAU ROENTGEN .....	28
FIGURE 2 : X-RAY APPLICATIONS. ....	31
FIGURE 3: SPECTRUM OF X-RAY SOURCE. ....	33
FIGURE 4 : PENUMBRA EFFECT OCCURS WITH FINITE-SIZED FOCAL SPOT.....	34
FIGURE 5 : SCHEMATIC OF GLASS INSERT .....	34
FIGURE 6: EFFECT OF TARGET ANGLE ON FOCAL SPOT SIZE.....	35
FIGURE 7 : SCHEMATIC OF ROTATING ANODE MICROFOCAL X-RAY TUBE .....	35
FIGURE 8 : COMMERCIAL BERYLLIUM WINDOW X-RAY TUBE. ....	36
FIGURE 9 : SEM OF SPINDT EMITTER.[46].....	37
FIGURE 10: THERMIONIC AND FIELD X-RAY EMISSION TECHNOLOGIES. ....	44
FIGURE 11: COMMON CARBON NANOTUBE THIN FILM DEPOSITION TECHNIQUES. ....	52
FIGURE 12: SHAPED CNT CATHODES.....	67
FIGURE 13: PULSED SOURCES. ....	74
FIGURE 14: CNT-BASED TOMOSYNTHESIS SYSTEMS. ....	79
FIGURE 15: MULTI PIXEL SOURCES. ....	80
FIGURE 16: MINIATURE CNT-BASED FE X-RAY SOURCES.....	83
FIGURE 17: USE OF ADLAYERS TO REDUCE WORK FUNCTION .....	84
FIGURE 18: LAYOUT OF EQUIPMENT USED .....	93
FIGURE 19: SCREENSHOT OF THE MOTOR INTERFACE PROGRAM .....	94
FIGURE 20: MOVEMENT OF THE OBJECT THROUGH THE X-RAY BEAM .....	95
FIGURE 21: DIAGRAM OF SCRAMBLING IN COLUMNS.....	97
FIGURE 22: NO FLAT FIELD CORRECTION .....	99
FIGURE 23: FLAT FIELD CORRECTION .....	99
FIGURE 24: OVERVIEW OF THE ALGORITHM .....	99
FIGURE 25: LINEAR LEAST SQUARES PROBLEM IN IMAGE DEBLURRING.....	101
FIGURE 26: PSF USED IN TESTS (LENGTH 52) - FROM [1].....	101
FIGURE 27: (A) BLURRED IMAGE. (B) RESULTS OF THE DECONVOLUTION.....	103
FIGURE 28: DETAILED IMAGES SHOWING ARTEFACTS .....	103
FIGURE 29: BLURRED AND FINAL PROCESSED IMAGES .....	105
FIGURE 30: THERMIONIC AND FIELD X-RAY EMISSION TECHNOLOGIES. ....	108
FIGURE 31: SCHEMATIC OF THE CONSTRUCTION OF CNT FIELD EMISSION X-RAY TUBE. ..	109
FIGURE 32: COMPONENTS OF SEALED XRAY TUBE .....	110

FIGURE 33: ASSEMBLED TANK, WITH LEADED GLASS PLATE FOR VIEWING. ....	110
FIGURE 34: BLOCK DIAGRAM OF GENERATOR AND CONTROL ELECTRONICS. ....	112
FIGURE 35: SIMPLIFIED HIGH VOLTAGE MULTIPLIER SCHEMATIC. ....	112
FIGURE 36: IMAGE TAKEN WITH X-RAY GENERATOR USING SEALED CNT INSERT. ....	113
FIGURE 37: GATE CHARACTERISTICS AT VARIOUS SETTINGS OF ANODE VOLTAGE, $V_A$ . ....	114
FIGURE 38: $I_G$ AND $I_A$ AS A FUNCTION OF $V_G$ FOR $V_A = 44kV$ . ....	115
FIGURE 39: $I_G$ AND $I_A$ AS A FUNCTION OF $V_G$ FOR $V_A = 20kV$ . ....	115
FIGURE 40: $I_G$ AS A FUNCTION OF $V_G$ FOR ALL VALUES $V_A$ . ....	116
FIGURE 41: $I_A$ AS A FUNCTION OF $V_G$ FOR ALL VALUES $V_A$ . ....	116
FIGURE 42: SEM OF GATE OF FAILED SEALED INSERT. ....	118
FIGURE 43: FAILURE MODE OF SEALED INSERT. ....	118
FIGURE 44: SEM OF PASTE PRINTED CNT EMITTER. ....	119
FIGURE 45: PLOT OF ATTEMPTED RE-SEASONING OF TUBE. ....	121
FIGURE 46: PLOT OF ATTEMPTED RE-SEASONING. ....	121
FIGURE 47: PLOT OF ATTEMPTED RE-SEASONING 48 HOURS. ....	122
FIGURE 48: DETAIL OF THE CATHODE ASSEMBLY SHOWING JACKING SCREW. ....	127
FIGURE 49: RENDERED DRAWING OF CATHODE ASSEMBLY. ....	128
FIGURE 50: STEPPER MOTOR USED TO OPERATE JACK. ....	129
FIGURE 51: 3-D PRINTED CATHODE ASSEMBLY COMPONENTS. ....	130
FIGURE 52 : VACUUM CHAMBER LAYOUT. ....	131
FIGURE 53 : SCHEMATIC OF THE VACUUM CIRCUIT. ....	132
FIGURE 54 : CALIBRATION OF PRESSURE GAUGES. ....	132
FIGURE 55 : CONSTRUCTION OF CNT FIELD EMISSION X-RAY TUBE. ....	133
FIGURE 56 : VACUUM CHAMBER OPENED TO VIEW EMITTER CHIP. ....	134
FIGURE 57 : OPEN CHAMBER SHOWING CONNECTIONS AND KF40 FITTING. ....	134
FIGURE 58 : VACUUM CHAMBER TEST RIG. ....	135
FIGURE 59 : DETAIL OF VACUUM TEST RIG. ....	136
FIGURE 60 : CONTROL CIRCUITRY FOR TEST RIG. ....	137
FIGURE 61 : SDK INTERFACE FOR THE XGEN CONTROL MODULE. ....	138
FIGURE 62 : CONTROL CIRCUITRY FOR DRIVING STEPPER MOTORS. ....	140
FIGURE 63 : CALIBRATION OF MOVEMENT OF STEPPER MOTORS. ....	141
FIGURE 64 : CALIBRATION CHART FOR THE CATHODE STEPPER MOTOR. ....	142
FIGURE 65 : CALIBRATION CHART FOR THE ASSEMBLY STEPPER MOTOR. ....	143
FIGURE 66 : PRESSURE GAUGE MONITORING IN NORMAL RUNNING CONDITION. ....	144

FIGURE 67 : PRESSURE GAUGE MONITORING WITH ROUGHING PUMP INACTIVE. ....	144
FIGURE 68 : DRAWING OF PHASE 2 VACUUM CHAMBER WITH X-RAY PORT.....	146
FIGURE 69 : RECOVERED BERYLLIUM WINDOW TO CREATE X-RAY PORT. ....	147
FIGURE 70 : HVFEED-THROUGH WITH RECOVERED ANODE (INTERNAL TO CHAMBER) .....	148
FIGURE 71: SCHEMATIC OF A BASIC TRIODE ASSEMBLY .....	152
FIGURE 72 : (A) SEM IMAGE OF A TCPA. (B) AND (C) SIMULATED E-FIELD .....	153
FIGURE 73 : VARIOUS SHAPES OF THE CARBON NANOTUBE) TIP. ....	155
FIGURE 74 : SPATIAL DISTRIBUTION OF CNT ELECTRIC POTENTIAL. ....	156
FIGURE 75 : SPATIAL DISTRIBUTION OF 2D CNT ELECTRIC POTENTIAL.[11].....	157
FIGURE 76 : SPATIAL DISTRIBUTION OF CNT ELECTRIC POTENTIAL. ....	157
FIGURE 77 : VARIOUS FORMS OF CNT ELECTRIC POTENTIAL. ....	158
FIGURE 78 : SIMPLE SIMULATION OF A TRIODE CONFIGURATION.....	159
FIGURE 79 : EFFECT OF CONTROL ELECTRODES.....	160
FIGURE 80 : INVERSE PILLAR VARIANTS.....	161
FIGURE 81 : SURFACE ELECTRIC FIELD OF A 2D HEXAGONAL ARRAY.....	162
FIGURE 82 : EMITTER DESIGN ON 10MM SI CHIP.....	173
FIGURE 83 : SEM OF ARRAY OF CNT PILLARS, ON SILICON SUBSTRATE .....	173
FIGURE 84 : SEM OF CNT PILLARS, DIFFERENT GROWTH PERIODS .....	174
FIGURE 85 : SEM OF ARRAY OF DENSIFIED TEPEES.....	175
FIGURE 86 : SCANNING ANODE FIELD EMISSION MICROSCOPE.....	176
FIGURE 87 : LOW TEMPERATURE CPA GROWTH. ....	179
FIGURE 88 : DENSE FORESTS “AS GROWN” .....	180
FIGURE 89 : DENSE FORESTS POST DENSIFICATION.....	180
FIGURE 90 : UNPATTERNED SAMPLES .....	185
FIGURE 91 : UNPATTERNED SAMPLE IV PLOT.....	186
FIGURE 92 : UNPATTERNED SAMPLE FN TYPE PLOT .....	187
FIGURE 93 : SEM OF PATTERNED SAMPLE .....	188
FIGURE 94 : PATTERNED SAMPLE - IV PLOTS- 3 SWEEPS .....	188
FIGURE 95 : TEM GRID WITH MESH DIMENSION OF 100 MICRONS .....	189
FIGURE 96 : SCHEMATIC OF THE FINAL TRIODE ASSEMBLY .....	190
FIGURE 97 : STAGES OF TRIODE ASSEMBLY .....	191
FIGURE 98 : TRIODE ASSEMBLY – IV AND FN TYPE PLOTS.....	192
FIGURE 99 : ANODE RESPONSE FOR SWEEPED CATHODE AND STEPPED GATE VOLTAGE.....	192
FIGURE 100 : GATE RESPONSE FOR SWEEPED CATHODE AND STEPPED GATE VOLTAGE.....	193

FIGURE 101: TRIODE GAIN PLOT – $I_A$ VS $I_G$ .....	193
FIGURE 102 : CONSTRUCTION OF A X-RAY AREA SENSOR. ....	198
FIGURE 103 : DEMONSTRATION OF THE EFFECT OF MOTION BLUR IN X-RAY IMAGES. ....	200
FIGURE 104 : TEMPORAL RESPONSE OF SCINTILLATOR.....	201
FIGURE 105 : TEMPORAL RESPONSE OF SCINTILLATOR [3]. ....	202
FIGURE 1066 : ROTATING SHUTTER TO TEST SCINTILLATOR TEMPORAL RESPONSE. ....	203
FIGURE 1077 : SCINTILLATOR TEST - DETECTOR OUTPUT (BARE SILICON).....	203
FIGURE 108 : CSI SCINTILLATOR WITH FIBRE-OPTIC PLATE .....	204
FIGURE 109 : CSI SCINTILLATOR LEADING EDGE WITH FIBRE-OPTIC PLATE .....	204
FIGURE 110 : CSI SCINTILLATOR TRAILING EDGE WITH FIBRE-OPTIC PLATE.....	204
FIGURE 111 : GADOX WITH FIBRE-OPTIC PLATE – POROUS SIDE.....	205
FIGURE 112 : GADOX WITH FIBRE-OPTIC PLATE – LEADING EDGE – POROUS SIDE.....	205
FIGURE 113 : GADOX WITH FIBRE-OPTIC PLATE – TRAILING EDGE – POROUS SIDE .....	205

## LIST OF ABBREVIATIONS AND ACRONYMS

<b>Term</b>	<b>Meaning</b>
FE	Field emission
TE	Thermionic emission
PE	Photoelectric emission
$\beta$	Field enhancement factor
$\phi$	Electron work function
FN	Fowler-Nordheim
$I_a$	Anode current (A)
$I_g$	Gate current (A)
J	current density (A/cm <sup>2</sup> )
$V_a$	Anode voltage (kV)
$V_g$	Gate voltage (kV)
CNF	Carbon nanofibres
CNT	Carbon nanotubes
SWCNT	Single-walled carbon nanotubes
MWCNT	Multi-walled carbon nanotubes
CVD	Chemical vapour deposition
RPS	Radiation Protection Supervisor
GM	Geiger Muller (radiation meter)
PEEK	Polyether ether ketone – machinable plastic
XGEN	Xray generator control circuit
SEM	Scanning electron microscope
TEM	Transmission electron microscope (grids)
SAFEM	Scanning anode field emission microscope
PSF	Point spread function
SVD	Singular value decomposition
QR	Type of orthogonal/triangular matrix decomposition
LDA	Linear diode array

## LIST OF APPENDICES

APPENDIX 1 – FIELD EMISSION CHARACTERISTICS .....	214
APPENDIX 2 – LITERATURE SUMMARY .....	225
APPENDIX 3 – DATA CAPTURE PROGRAM .....	231
APPENDIX 4 – XGEN SOFTWARE .....	239
APPENDIX 5 – FIRMWARE FOR CNT GENERATOR.....	245
APPENDIX 6 – SOFTWARE FOR ENCODED APERTURE.....	253
APPENDIX 7 – MOTOR CALIBRATION .....	271

# 1 RESEARCH PROBLEM STATEMENT

Engineering is about problem solving. The search for solutions is driven by the existence of a need. The desire to “build a better mouse-trap” is accelerated by the motivation to make a device that is better – more efficient, reliable, humane – or even cheaper. In these respects, there is an inevitable linkage to commercial aspects, so that the most successful engineering developments result from the pull by market requirements.

There is currently an explosion of research, in many areas, but particularly in the field of novel nano materials and the associated techniques required to fabricate them. Indeed, during this period of study, the author has participated and assisted in a number of aspects of this work. This has given rise to a considerable amount of attention to rather arcane areas that are often far removed from practical applications. In other words, no longer strictly aligned with engineering.

The vast amount of new material arising from this research is fertile ground for the creation of new ideas. The scope for the invention and development of innovative concepts has never been greater. It is the conversion of those concepts into machines and systems that represents the biggest challenge, but also the greatest opportunity at this time.

The author has been working in the field of engineering for many years, in particular in real-time radiography, image processing and electro-mechanical handling. Indeed he has been responsible for many of the innovations in the sector in which he has worked. The

motivation for this work has been to identify and develop ideas, resulting from a detailed awareness of the state of the research environment coupled with creative thinking, to develop solutions that have tangible and practical applications in real world situations.

## 1.1 Background

The work described in this thesis is directed towards the application of nano materials and associated techniques, to the improvement of means of generating and detecting Xrays, as well as the capturing and processing of the associated image data. In particular, the study looks into methods that can be applied to the high speed inspection of manufactured products. Implicit in this, is the need to understand and address the failure modes that have been seen in prior work.

This work bridges the area of materials and field emission, as a means of obtaining a controllable source, and that of image processing to manage the deconvolution methods required to extract and render the additional information that can become available.

The author's observations have been that much of the published material has demonstrated relatively fragile solutions. These need to be evolved to stand up to the rigour necessary in an industrial or commercial environment.

## 1.2 Specific application field

Many manufactured products are now inspected using Xray techniques, to confirm assembly, product integrity and absence of foreign bodies [5, 12]. Traditionally this has been accomplished using Linear Diode Arrays (LDA) and Constant Potential (CP) X-ray sources. The objects are normally transported on a continuously moving conveyor where the lateral resolution is almost exclusively determined by the scanning rate. However, there is a limit to the resolution of the image, determined by the Xray photon flux, detector diode area and integration time available to achieve an acceptable signal-to-noise level.

Increasing the resolution by reducing the diode size can be accomplished by the use of area sensors, but with a corresponding increase in integration time. This gives rise to motion blurring of the image when the products are transported on continuously moving conveyerised processes. This may be addressed by using indexing feed mechanisms, but those limit the throughput of objects and are usually regarded as inconvenient or unreliable in a production environment.

A further method of addressing the problem of image blur is the use of pulsed X-rays (analogous to stroboscopic lighting in optical systems [4]). However, pulsed X-ray sources, based on thermionic tubes, are difficult to design, require very high instantaneous power levels and are therefore relatively unreliable.

It is the objective of this work to produce a concept that will provide the benefits of high resolution area sensors, with the speed associated with linear diode arrays, by means of the use of highly controllable pulse X-ray sources and image processing as an alternative to using complex and unreliable thermionic pulse sources.

### 1.3 Prior work

Motion de-blurring using encoded apertures in optical systems has been the subject of research since the 1970's[9]. Latterly these were developed by Mitsubishi as the "Flutter Shutter" application [6]. These systems used either liquid crystal shutters or binary light integration inherent in the optical sensor, to achieve the required image signal modulation. [1, 7].

### 1.4 Scope of the project

The previous examples of encoded aperture have employed a gated (or shuttered) detector, to implement the time-based encoding strategy. In this work we are studying the potential to use fast pulse switching in the X-ray source as a means to provide the encoding.

Traditional X-ray sources incorporate thermionic cathodes, which do not readily lend themselves to rapid switching, due to the thermal inertia of the filament. However, the recent availability of field emission sources has the potential to permit fast pulsing of the X-ray beam. In particular the power output, longevity and controllability of such sources appear to have begun to improve, as a result of recent developments.

Strategies for developing new X-ray sources are based on criteria driven by the needs of current applications. Despite the apparent maturity of the technology, many critical challenges remain, including; rapid beam pulsing, dose reduction, improved image contrast, and enhancement of the spatial and temporal resolution. In this work I provide a review of the use and potential of carbon nanotubes (CNTs) as a platform for the emerging novel field emission X-ray sources. I look at the current state-of-the-art in CNT emitter fabrication including the electron source and the gate electrode micro-fabrication.

A series of functional enhancements have been made recently, including reduced turn-on electric fields and improved stability via the incorporation of adlayers [3], more isotropic X-ray beam distribution symmetry achieved through cathode shaping [10], micro focal sources, pulsed emission [2], multi-pixel sources [11], and miniaturisation [8].

In this thesis I describe the work carried out on the use of a nanocarbon X-ray triode structure to produce a pulsed, and time-encoded source. Unlike existing field emission sources based on metallic Spindt emitters, nanocarbon conductors have been shown to have extremely high current carrying capabilities, some 1000 times greater than Copper, extremely non-linear bias responses, almost instantaneous time responses, as well as high aspect morphologies that lend themselves to efficient, low-voltage turn-on. This may be used to image moving objects directly onto a large area CMOS sensor. The resulting image data would be subject to deconvolution to restore image sharpness, using image processing techniques analogous to those employed in the Encoded Aperture system [6]. This differs from prior work in that,

for the first time, I am proposing to apply this to X-ray imaging, and the source of radiation is fluttered, rather than the acquisition of the image by the detector.

To evaluate the advantages over existing methods, it should be noted that :

In a traditional LDA system with a conveyor running at 60m/min, a resolution of 1 mm would require a diode size of 0.5 mm. To get sufficient signal level would require a continuous X-ray source of at least 500 W.

In a specific example, a conventional pulsed X-ray source used with an area sensor, would require a pulse of duration of approximately 1 ms, thereby dissipating an instantaneous power of typically 7000 W. The use of a fluttered source with a typical image acquisition over 25 mm of movement (giving an average integration time of 25 ms) would require a mean power level of 8% of the equivalent pulsed source. However, as the source is controllable, this would require an X-ray output for only the period of motion, as opposed to a continuous output. Thus, for a throughput rate of 600 products per minute, the generator would be operating for only 15% of the time. The mean power usage of the generator would be less than 100 W. At this level, the generator would operate at a much lower temperature which would give rise to a much higher reliability. Additionally, the resulting system would be regarded as much safer, as radiation emissions are occurring only when there is an object in the beam.

## 1.5 Commercial background

This objective relates to the market of foreign body inspection, particularly in rigid containers, so-called “glass-in-glass” systems. These systems are designed to detect a shard of broken glass in a product packaged in a glass jar. Clearly in this circumstance, glass is a primary source of contamination, which may be introduced at various points in the manufacturing and filling process.

Some 30 years ago, Parr Technologies in USA developed a pulse X-ray system using Image Intensifier tubes. Despite the high cost and poor reliability, these were deployed for a number of years, but with the advent of more reliable systems based on Linear Diode Arrays, these systems ceased to be produced. LDA systems have been used by several key producers in this area Dylog (IT), InspX (USA), Safeline (UK), Rayonics (IT). In 2012, Heuft (DE) started to produce systems once again based on pulse X-ray, at a unit price of US\$400k. The Heuft machines achieve better performance by virtue of the area sensor, but at the expense of very poor system reliability and high cost, pointing to a clear requirement for an improved implementation.

## 1.6 Contents of this thesis

In this thesis I will, in chapter 2, firstly describe the historical background to the field of X-ray generation and imaging. In chapter 3, there will be a review of the type of field emission electron sources that can be fabricated, and the methods of producing these. Chapter 4 will discuss the functional enhancements that can be achieved, and their benefits in real-world implementations of the technology.

The practical studies in this thesis will firstly involve a proof of concept of “Encoded Aperture” described in chapter 5, which identifies the motivation behind the development of fast switching electron sources. Chapter 6 details the initial work undertaken on sealed inserts, and the limitations encountered, followed by the development of a “Demountable” field emission rig to provide a test bench for the optimization of the physical parameters of an X-ray source, described in chapter 7, including steps which could then be incorporated into a chamber capable of generating and emitting X-rays. Chapter 8 describes the modeling of field emission sources, with practical work on the construction of a triode source, including the measurements and optimization of the parameter set, discussed in chapter 9. The specific problem of detection speed is

addressed by a study of detector and scintillator response times in chapter 10. Finally, in chapter 11, I draw conclusions from this work and outline the next steps to provide a potentially commercial solution.

## 1.7 References

- 1 AGRAWAL AMIT K, R. R. 2008. *Increasing Object Resolutions from a Motion-Blurred Image*. USA patent application US7639289 (B2).
- 2 CALDERÓN-COLÓN, X., GENG, H., GAO, B., AN, L., CAO, G. & ZHOU, O. 2009. A carbon nanotube field emission cathode with high current density and long-term stability. *Nanotechnology*, 20, 325707.
- 3 COLE, M. T., PARMEE, R. J., KUMAR, A., COLLINS, C. M., KANG, M. H., XIAO, J., CEPEK, C., YUAN, X. & MILNE, W. I. 2016. Conjugated polyelectrolyte nano field emission adlayers. *Nanoscale Horizons*, 1, 304-312.
- 4 HEUFT BERNHARD, P. W. 2002. X-ray apparatus for generating short x-ray pulses, and inspecting device operating by means of such an x-ray apparatus. US7079623 (B2).
- 5 PARMEE, R. 1990. X-rays give in-depth inspection. *Sensor Review*, 10, 84-86.
- 6 RASKAR, R., AGRAWAL, A. & TUMBLIN, J. 2006. Coded exposure photography: motion deblurring using fluttered shutter. *ACM Trans. Graph.*, 25, 795-804.
- 7 RASKAR RAMESH, T. J., AGRAWAL AMIT. 2007. Method for reducing blur in an image of a scene and method for deblurring an image of a scene. US7580620 (B2).
- 8 REYES-MENA, A., JENSEN, C., BARD, E., TURNER, D. C., ERDMANN, K., QIU, Q., GAO, B., LU, J. & ZHOU, O. 2005. Miniature X-ray tubes utilizing carbon-nanotube-based cold cathodes. *Advances in X-ray Analysis*, 48, 204-209.
- 9 RICHARDSON, W. H. 1972. Bayesian-Based Iterative Method of Image Restoration. *Journal of the Optical Society of America*, 62, 55-59.
- 10 RYU, J., KANG, J. & PARK, K. 2012. Carbon Nanotube Electron Emitter for X-ray Imaging. *Materials*, 5, 2353-2359.
- 11 WANG, S., CALDERON, X., PENG, R., SCHREIBER, E. C., ZHOU, O. & CHANG, S. 2011. A carbon nanotube field emission multipixel x-ray array source for microradiotherapy application. *Applied Physics Letters*, 98, 213701-213701-3.
- 12 ZWIGGELAAR, R., BULL, C. R., MOONEY, M. J. & CZARNES, S. 1997. The Detection of "Soft" Materials by Selective Energy Xray Transmission Imaging and Computer Tomography. *Journal of Agricultural Engineering Research*, 66, 203-212.

# 2 BACKGROUND

## 2.1 Historical Perspective

Since the discovery of X-rays in 1895, [1], the field of Xray analysis and diagnostics has been one of the most widely researched areas in science. In the first quarter of the last century, almost half of the Nobel prizes were awarded, for contributions connected with this field.

Wilhelm Conrad Roentgen was one of many physicists and engineers who contributed to the early experimentation with this new phenomenon. The excitement of this period is captured in several publications written to celebrate the centenary of the discovery by Dick Mould [2], [3]. Indeed, J.J. Thomson wrote “The discovery by Prof. Roentgen of the rays which bear his name, has aroused an interest perhaps unparalleled in the history of physical sciences” [4]. The initial work was as a result of Roentgen’s research into the generation of cathode rays using Crookes tubes, which resulted to the discovery of fluorescence in materials covered by optically opaque card. This lead to further experimentation, wherein the X-rays were found to pass through structures, such as walls and metallic plates. It was noted that these rays would be transmitted through differing materials with varying levels of transparency – **Figure 1** shows the seminal representation of this was the photograph of the “Hand of Frau Roentgen” [5]. Roentgen received the Nobel Prize for this work in 1901.



***Figure 1: The hand of Frau Roentgen***

The first X-ray image was produced on sensitised paper and published on 28<sup>th</sup> December, 1895.

Whilst the initial discoveries in this field created a great interest and thirst for information, it was a only relatively short period before the applications of this “new light” became evident. J.J. Thomson had already established the ionising nature of these rays [4]. It was recognised that X-rays had different characteristics, initially termed qualitatively as “hard”, “medium” and “soft” X-rays [6], a classification which related to the relative absorption by soft tissue and bone. This indicates that the technique was already being applied to human radiography, with early examples being the identification of bullets in wounded soldiers, and of bone fractures. These discoveries resulted in the development of a range of instruments, variously densitometers, chiroscopes, osteoscopes, [7] which involved a means of detection – initially based upon chemical colour change, such as radiochromators, and lead to quantification of the Xray characteristics [7]. Within a short time this lead to recognition and analysis of the diagnostic capabilities and therapeutic benefits of this new technology. [8]

Whilst the primary techniques for medical radiography relied on the absorption of these rays, there were already other methods being developed. W.H. Bragg discovered the diffraction of Xrays by crystals in 1912, and together with his son, W.L. Bragg (who had previously worked under J.J. Thomson) [9], the father and son team won the Nobel Prize

in 1915 for the contribution to Crystal structure analysis by Xray diffraction. In this application, a narrow Xray beam is directed towards a sample, resulting in a coherent small angle scatter, which can provide information about the periodicity and orientation of the underlying crystal structure. Most notably, this led ultimately to evidence of the structure of DNA [10]. Together with the work of M.von Laue [11], this was responsible for the field of Crystallography. The associated area of Xray Spectroscopy has also accounted for the discovery of the relationship between the elements, and validation of the periodic table.

During the 1920's Compton discovered additional Xray scattering effects known as inelastic scatter or back-scatter [12] [13], for which he received the Nobel Prize in 1927. This is an interaction between the Xray photons and bound electrons, which gave rise to a new group of Xray applications, to measure the physical density, including flaws such as bubbles, [14], [15]

Xray fluorescence (XRF) is a technique whereby a secondary emission is stimulated by incident high energy Xrays, resulting in ionisation of the target atoms. This ionisation is created when one or several electrons are ejected from each atom with the result that the outer electrons fall into the vacated orbit, thereby releasing an Xray photon of a lower energy – creating “fluorescence”. The method was first described by Glocker and Schreiber [16], and is particularly used for elemental analysis. This has applications in many areas such as archaeology, art conservation and geology.

The primary area of application of Xrays remained in medical diagnosis. However the complex nature of the human body had limited its use to the imaging of relatively dense features. Computed (Axial) Tomography (CT or CAT scanning) was developed to address the issues associated with the limitations of contrast resolution in soft tissue, experienced in conventional transmission radiography. CT involves taking multiple 2 dimensional scans to reconstruct a 3 dimensional image, thereby revealing additional and high contrast data. It was invented and developed during the 1960's by Godfrey Hounsfield [17], and required rotating Xray sources and multiple detectors to acquire this image data.

Tomosynthesis uses the same principles as CT, but employs a limited angle image set of discrete exposures. This enables a series of reconstructions at different depths, to be accomplished at higher speeds with lower doses of radiation. This is commonly used in mammography, also known as DBT or Digital Breast Tomosynthesis. In addition to

diagnosis, Xrays are employed in a therapeutic role, particularly for electrotherapy and radiotherapy.

## 2.2 Importance of X-ray technology

Despite the growing range of X-ray techniques, the primary area of application of X-rays has been in medical diagnosis. In addition to this, X-ray sources have proven important in a wide range of inspection technologies; from medical and analytical, to security and industrial quality control. As illustrated in **Figure 2**, X-ray sources have a wide range of applications, including materials analysis (X-ray fluorescence, X-ray diffraction), medical and dental diagnosis and treatment (transmission radiography, computed tomography, tomosynthesis, radiotherapy and brachytherapy), electronics inspection, food security, non-destructive testing, thickness and defect monitoring, pharmaceutical quality control, and international border security. Indeed, X-ray sources are ubiquitous and have impacted on almost every area of science and industry. The X-ray field is diverse and has a market value anticipated to reach \$10B/year by 2018. Though a significant market, few technological changes have occurred in the underpinning technology over the past century.

The ever more demanding needs of the medical, security and manufacturing communities have stimulated the search for newer, functionally advanced sources with capabilities such as high-speed, pulsed operation and real-time 2D and 3D imaging for in situ applications. This is particularly relevant in the pharmaceutical, food security, and heavy industries (**Figure 2**). Indeed, there is considerable global interest in the realisation of low energy, real-time x-ray imaging techniques for advanced computed tomography and tomosynthesis. Replacement of costly and bulky multiple sources and gantries are a central financial driver alongside reduced scanning times and dose levels. It is only now that key developments in nanomaterial based x-ray sources are taking place, and which are highlighting the technological barriers and outstanding theoretical and manufacturing problems hindering the widespread adoption of these functionally unique systems.

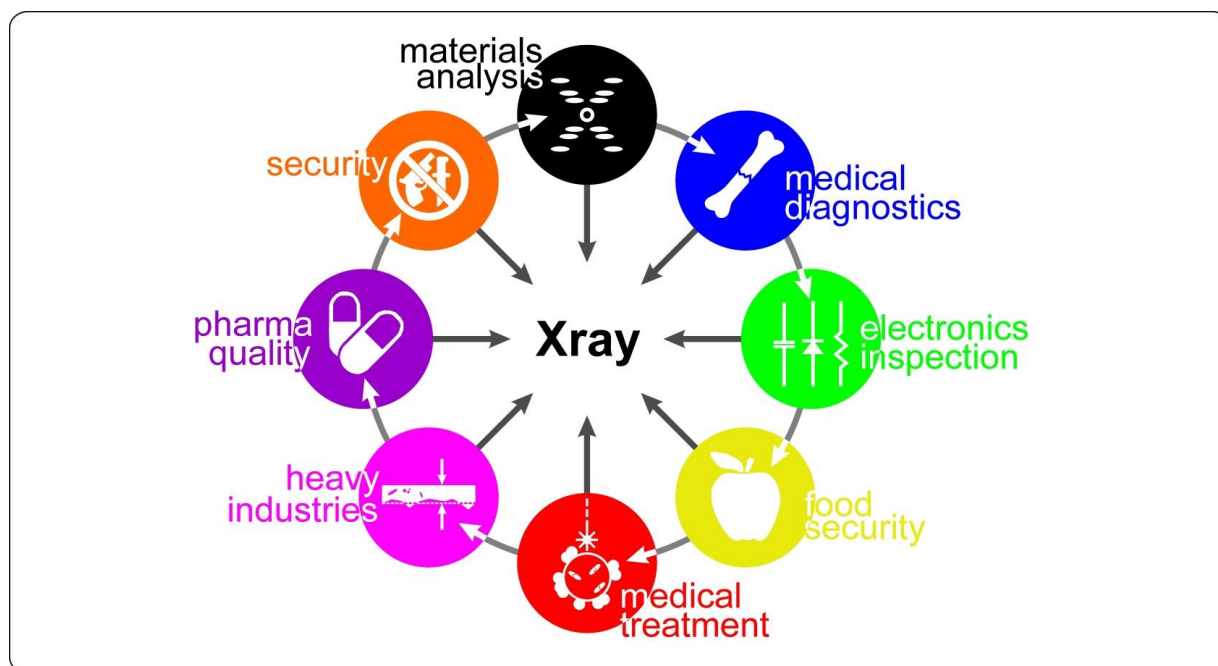


**Figure 2 : X-ray applications.**

X-ray sources find application in a wide range of applications including medical diagnostics, electronics inspection, food security and border control. Conventional X-ray sources are ubiquitous and the integration of carbon nanomaterials has the potential to complement the market dominance of traditional thermionic technologies.

## 2.3 Applications in Manufacturing

In the last 20 years, X-ray inspection has become a fundamental aspect of manufacturing industry. In particular, the food and pharmaceutical sectors have embraced this technology[18]. Hitherto, it was standard practice to place metal detectors on such production lines. However metal detectors are not especially suitable for detecting metal in such circumstances, faced with variable temperatures, matrices with polar molecules such as products containing fat, and latterly packaging incorporating foil or metallised film.

In contrast, basic X-ray transmission radiography can provide a means of detection of metallic foreign bodies at a greater sensitivity than conventional metal detectors, and further, based upon its sensitivity to  $Z_{\text{eff}}$  – the effective atomic number of the material to be detected [19], is able to efficiently detect glass (Si, Na), bone (Ca), mineral stones (various atomic constituents) and certain plastics such as PVC (Cl). Such systems are designed to provide 100% automated inspection while operating at production lines speeds of many hundreds or even thousands of objects per minute.

Whilst this has now become an accepted, main stream technology, there are still many challenges remaining. For example, a continuous requirement for improved resolution, which requires smaller detector elements, is at odds with the capabilities of the standard X-ray equipment, where the source flux of the Xray generator, when related to the detector pixel size and scanning rate is the limiting factor. This is particularly the case in areas such as detection of pin bones in fish fillets. With many retailers now wishing to offer “guaranteed bone-free” products, when combined with an increasingly litigious environment, there are real requirements for new methods and engineering solutions. This has provided the motivation for this work, particularly to investigate methods which can provide higher speeds and lower emissions.

## 2.4 Construction of the Xray source

Central to such equipment, and indeed any X-ray application is the generation of the radiation. An Xray tube requires a source of electrons, emitted from the cathode, and directed towards an anode, to which a high voltage is applied. The anode voltage determines the energy of the electron at the point it interacts with the anode target material, and hence the energy of the emitted photon. Standard X-ray sources will have an anode voltage which can be between 5kV and 500kV, although in the forgoing applications is more likely to be in the range 50kV to 160kV.

The cathode in the Crookes Tube used by Roentgen comprised a flat metallic plate. In order to improve efficiency of the emission of these “cathode rays” or electrons, the design of the Xray tube subsequently incorporated an electron source based upon Thermionic Emission (TE) from a heated filament [20], known initially as the Coolidge tube. Since the emission was a function of the temperature of the filament, this provided an easily manufactured and controllable source of electrons. The fundamental principles of TE Xray tubes have remained virtually unchanged to this day.

A series of variants of these traditional Xray tubes has evolved, which optimise the characteristics for different applications.

**Anode target material.** Typically only 1% of the power applied to an Xray tube is converted to useful radiation – the remainder is dissipated as heat. The anode of an Xray tube would normally be constructed of copper, to provide a cheap and efficient way to conduct away this heat. Within this, is cast an embedded target material. **Figure 3** shows

the spectral output of an Xray tube comprises of two components, being the continuous “Bremsstrahlung” spectrum [21], and a series of emission peaks, characteristic of the target material. This target material is commonly Tungsten, Copper, Molybdenum, and is selected for the emission peak determined by the energy levels at which the tube is designed to operate. [22]

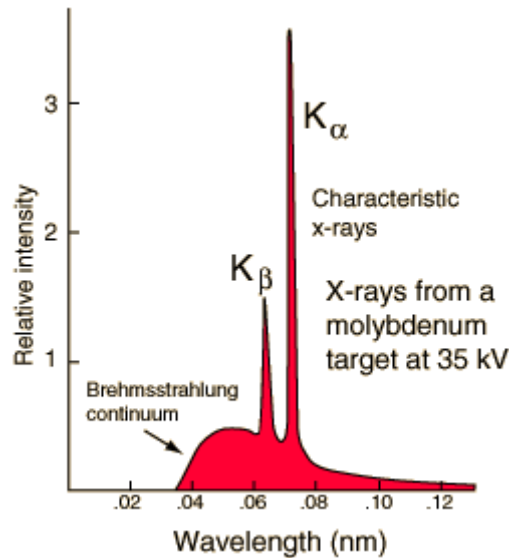


*Figure 3: Spectrum of X-ray source.*

The spectrum comprises two characteristic peaks ( $K\alpha$  and  $K\beta$ ) determined by the target element, and the continuous “Bremsstrahlung” emissions.

**Focal spot size.** The beam of electrons directed towards the anode will determine the size of the focal spot. The size of the focal spot of the Xray tube will impact the resolution of the resultant Xray image. A large focal spot will create a penumbra effect where the spot subtends a significant angle at the subject, seen in **Figure 4**. Standard Xray tubes have a focal spot size of typically around 1mm diameter. These are useful where the subject is close to the imaging device, or where high resolution is not required. For greater resolution, the tube type is defined as “mini-focus” with a spot size down to 50 microns, or “micro-focus” with a spot size of typically 5 microns. [23]

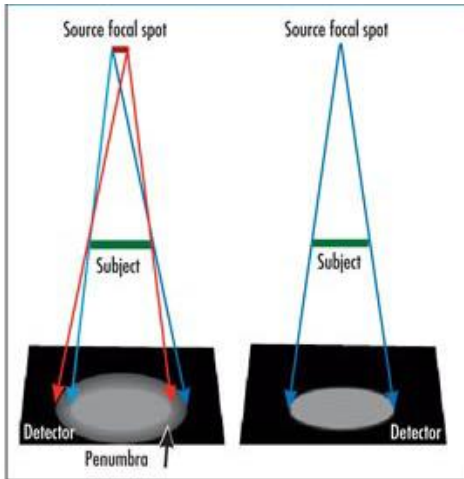


*Figure 4 : Penumbra effect occurs with finite-sized focal spot*

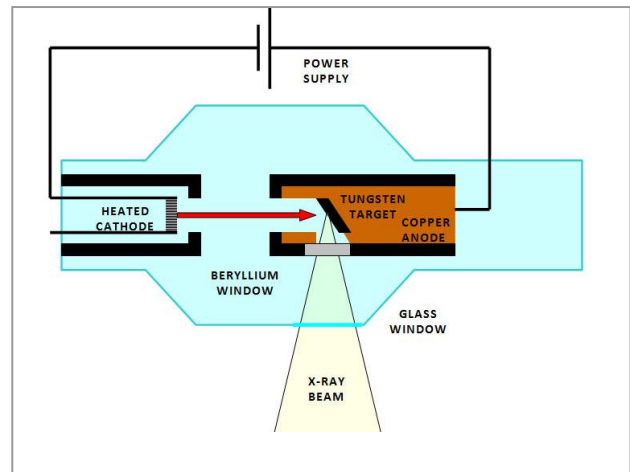


*Figure 5 : Schematic of glass insert*

A conventional Xray tube will use a “cup” around the heated filament cathode assembly (**Figure 5**), which to a first order, will focus the electrons onto the centre of the anode, by means of the electrostatic effect. Careful design will minimise the size of the focal spot. [24,25]. Additionally, further electrostatic rings or focussing coils may also be employed to redirect the flow of electrons emanating from the cathode.

The size of the focal spot is determined, initially, by the target angle of the anode and the area of the electron beam impinging on the target, as in **Figure 6**. The current density that flows through this area will clearly be determined by the beam current and its diameter, so that smaller focal spots give rise to substantially higher current density.

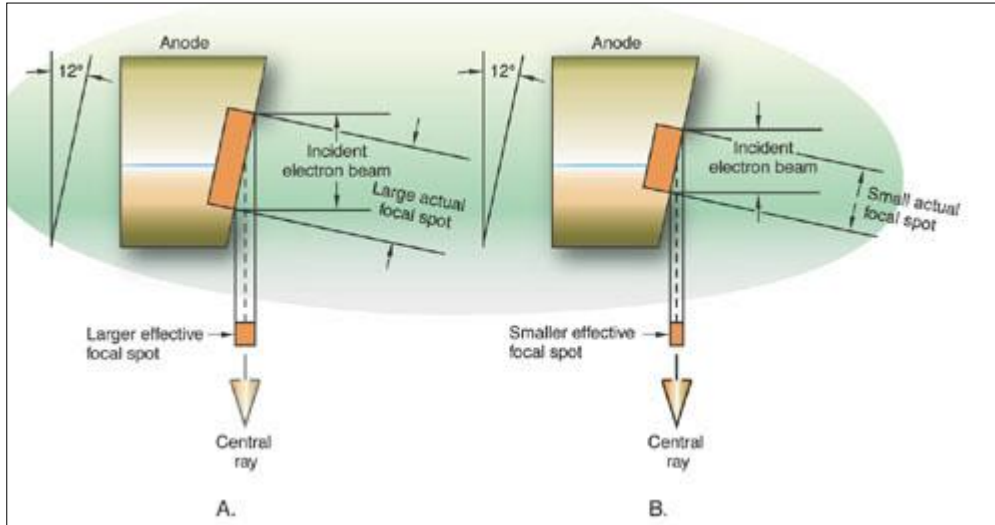


**Figure 6: Effect of target angle on focal spot size**

The focal spot size may readily be determined by measuring the Point Spread Function using standard methods, such as pin-hole imaging. [26]. The flow of a continuous current through a small area will give rise to pitting or burning of the anode over a long period of time. In one solution, shown in **Figure 7**, this has been addressed by the use of a rotating anode, in which the anode assembly is continuously turned to mitigate the effects of erosion by the electron beam [27].

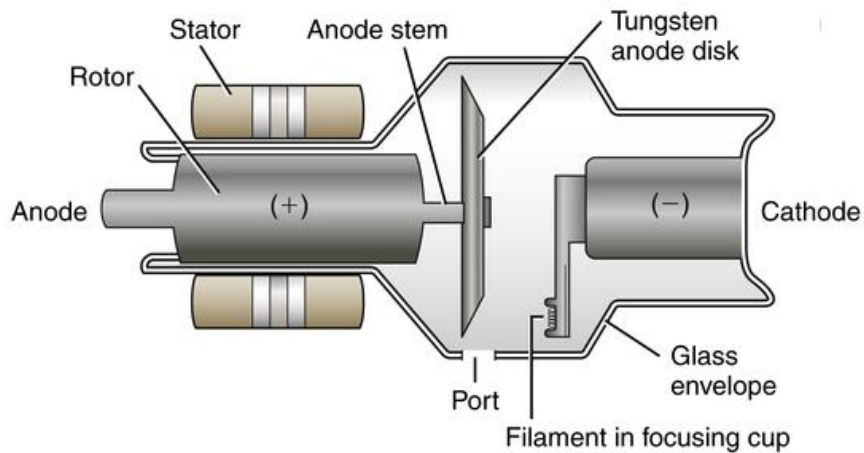


**Figure 7 : Schematic of rotating anode microfocus X-ray tube**

**Window material.** From the earliest days, X-ray tubes were constructed in an evacuated glass envelope. This has the advantage of being relatively inexpensive, easy to work and capable of sustaining a high vacuum. However, when working at low energies – for

example in Xray Diffraction or Xray Fluorescence, the glass can act as an opaque barrier to the Xray photons – this is a function of the atomic weight of the aperture material and its thickness. Therefore the selection of the ideal window material is based on the lowest atomic number that will sustain the conditions – the usual choice is Beryllium (atomic number = 4). This may be incorporated by mounting a window with a Beryllium foil, typically 0.25 to 0.5mm in thickness, as in **Figure 8**. [28] [29]



**Figure 8 : Commercial Beryllium window X-ray tube.**

**Demountable Xray tubes.** While the majority of Xray tubes use a fixed, sealed glass or ceramic envelope, there are situations where there can be considerable benefit in having the ability to open a tube, replace parts and then re-evacuate it. This gave rise to the “demountable Xray tube” [30]. In particular, this offers the advantage that both the anode assembly may be replaced – either for one of different target characteristic, or to replace a unit which had been degraded as a result of continuous high beam current – and the cathode assembly may be exchanged following failure or deterioration due to prolonged vapourisation. In particular, demountable tubes have been used extensively in Non-Destructive Testing (NDT) applications where there is a requirement for high beam current micro-focus tubes. [31]

## 2.5 Field Emission Sources and the Principles of Field Emission

Thermionic tubes, by their nature, are generally unable to respond rapidly, which means that it is often complex to image objects that are not stationary.

Field emission offered an alternative to thermionic emission, initially through Spindt emitters, using Molybdenum structures, and subsequently through carbon nanotubes.

[32] A Spindt emitter is conical in form, having a tip radius < 1 micron. An extraction

electrode, located within a few microns from the tip creates the electric field which draws electrons from the tip (**Figure 9**). The field of Vacuum Electronics is now well established, based on the fabrication of these devices.

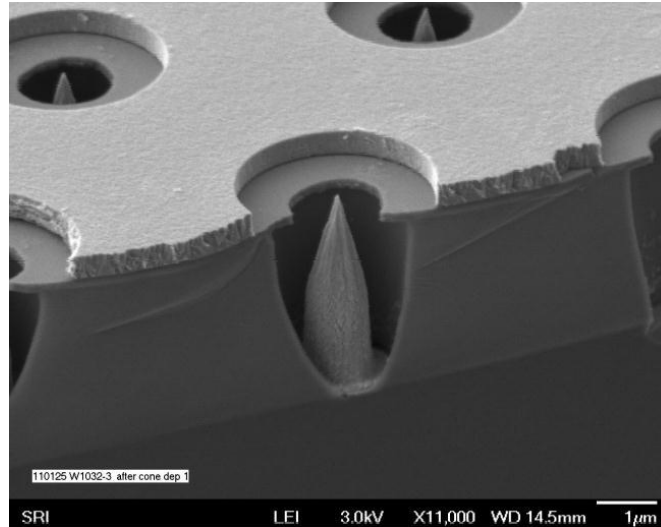


**Figure 9 : SEM of Spindt emitter.[46]**

Since the early part of the last decade, there have been a number of examples of FE based Xray tubes, although the problems associated with output and lifetime have limited these to research work. In particular, there have been demonstrations of pulsed generators, which have been used to sequentially switch sources –this has been applied to Tomosynthesis, for experimental medical diagnostics work, as described in Chapter 4.

A field emission device will emit electrons under the influence of a high electric field at its tip. The emission is predicted by the Fowler Nordheim theory [33] which defines the field-emission in terms of a tunnelling current through a potential barrier between the surface of a metal and vacuum.

$$I = aV^2 \exp(-b\phi^{3/2}/\beta V), \quad \text{Equation 1}$$

where  $I$ ,  $V$ ,  $\phi$ ,  $\beta$  are the emission current, applied voltage, work function, and field enhancement factor, respectively.

A detailed analysis of the theoretical background can be found in [34]. Various refinements to this model have been applied [35] to take account of extreme curvature and high temperatures. The high electric field that is needed to create field emission is affected by the curvature of the tip – this field enhancement depends upon a number of geometrical factors such as the precise form of the emitting tip. [36]

## 2.6 Carbon Nanotubes in a Field Emission Device

The discovery of Carbon Nanotubes is generally credited to Iijima in the early 1990's [37], although it is clear that there had been significant activity in this area for a considerable time [38]. The publication of this work, however, led to a heightened interest which gave rise to the study of field emission in CNTs resulting in publications in 1995 [39], [40]. By the early years of the following decade a range of applications had been identified, utilising these field emission properties, including high resolution electron beam microscopes [41], flat panel displays, electron beam lithography and X-ray cathode emitters [42]. An early review paper [43], provides an overview of the state of the art at that time.

Whilst individual CNT field emitters are shown to produce the highest electric fields, the proximity of adjacent emitters will effectively shield the field enhancement. In a field emission device, where our interest is in the available current density, the optimum arrangement will not necessarily be that with the highest density of emitters. [44] [45]. In addition, the emission pattern of the field emitter is not uniform.

In this document, there are described examples of a range of emitter patterns, as well as assembly processes. Each has an range of benefits as well as limitations or disadvantages, and it is the purpose of this work to identify and understand these, as a means of moving towards an optimum solution. In the next chapter there will be a detailed review of the many techniques currently available.

## 2.7 Conclusions

The field of X-ray generation is remarkably broad. The fundamental technique of Thermionic Emission that has been applied to widescale deployment, is largely unchanged in more than a century. However, in the last 20 years, Field Emission is starting to be recognized as a viable alternative.

## 2.8 References

1. Roentgen, On a New Kind of Rays. *Nature* **53**, 274-276, (1896).
2. RF Mould A century of X-rays and radioactivity in medicine: with emphasis on photographic records of the early years; (CRC Press, 1993).

3. RF Mould, The early history of X-ray diagnosis with emphasis on the contributions of physics 1895-1915. *Physics in Medicine and Biology* **40**, 1741, (1995).
4. JJ Thomson, The Röntgen rays. *Nature* **53**, 581-583, (1896).
5. S Pamboukian, "Looking Radiant": Science, Photography and the X-ray Craze of 1896. *Victorian Review* **27**, 56-74, (2001).
6. R Kienbock, Über die Einwirkung des Rontgen-Lichtes auf die Haut. *Wiener Kiin. Wschr.* **13**, 1153, (1900).
7. L Benoist, Experimental definition of various types of X-rays by the radiochromator. *C. R. Acad. Sci. Puns* **135**, 225, (1902).
8. C Beck, Röntgen-Ray Diagnosis and Therapy. *Archives of The Roentgen Ray* **9**, 110-110, (1904).
9. WL Bragg The diffraction of short electromagnetic waves by a crystal. In *Proceedings of the Cambridge Philosophical Society*, 1913; pp 4.
10. RE Franklin, RG Gosling, Molecular configuration in sodium thymonucleate. *Nature* **171**, 740-741, (1953).
11. M von Laue, Concerning the detection of X-ray interferences. Nobel lecture, (1915).
12. AH Compton, A quantum theory of the scattering of X-rays by light elements. *Physical Review* **21**, 483, (1923).
13. AH Compton, On the mechanism of x-ray scattering. *Proceedings of the National Academy of Sciences of the United States of America* **11**, 303, (1925).
14. CR Bull, R Zwigelaar, RD Speller, Review of inspection techniques based on the elastic and inelastic scattering of X-rays and their potential in the food and agricultural industry. *Journal of Food Engineering* **33**, 167-179, (1997).
15. L Guang, Z Shang-qi, H Zhong, C Shuang-kou, Applications of Compton scattering. *J Chongqing Univ.-Eng. Ed.* **5**, (2006).
16. R Glocker, H Schreiber, Quantitative Röntgen spectrum analysis by means of cold cathode excitation. *Ann. Phys.* **85**, 1089-1102, (1928).
17. GN Hounsfield, Computed Medical Imaging. *Journal of Computer Assisted Tomography* **4**, 665-674, (1980).
18. R Parmee, X-rays give in-depth inspection. *Sensor Review* **10**, 84-86, (1990).
19. H Kallmann, H Mark, Über die Dispersion und Streuung von Röntgenstrahlen. *Annalen der Physik* **387**, 585-604, (1927).
20. WD Coolidge, A Powerful Röntgen Ray Tube with a Pure Electron Discharge. *Physical Review* **2**, 409-430, (1913).
21. G Hettinger, N Starfelt, Bremsstrahlung spectra from roentgen tubes. *Acta Radiologica [Old Series]* **50**, 381-394, (1958).

22. HG Moseley, XCIII. The high-frequency spectra of the elements. The London, Edinburgh, and Dublin Philosophical Magazine and Journal of Science **26**, 1024-1034, (1913).
23. J Madsen, Focal spot size measurements for microfocus X-ray sets. NDT international **22**, 292-296, (1989).
24. W Ehrenberg, WE Spear, An Electrostatic Focusing System and its Application to a Fine Focus X-Ray Tube. Proceedings of the Physical Society. Section B **64**, 67, (1951).
25. BM Moores, P Brubacher, Focal spot studies and electron focusing in a demountable X-ray tube. Physics in Medicine and Biology **19**, 605, (1974).
26. ASfTaM Philadelphia, Standard Test Method for Measurement of Focal Spots of Industrial X-Ray Tubes by Pinhole Imaging. Annual book of ASTM standards **ASTM-E-1165-12**, (2010).
27. S Yoshihiro Cooling system for a rotating anode of an x-ray tube. Google Patents, 1970.
28. RR Machlett, An Improved X-Ray Tube for Diffraction Analysis. Journal of Applied Physics **13**, 398-401, (1942).
29. T Rogers, High-intensity radiation from beryllium-window X-ray tubes. Radiology **48**, 594, (1947).
30. TB Rymer, PG Hambling, Demountable X-ray tube for crystallography. Journal of Scientific Instruments **29**, 192, (1952).
31. Yxlon *High-resolution Y.FXE microfocus X-ray tubes* [Online]. 2014; <http://www.yxlon.com/Products/X-ray-tubes-and-generators/Microfocus-X-ray-tubes> (2014).
32. I Brodie, C Spindt, Advances in Electronics and Electron Physics edited by PW Hawkes, vol. 83. (1992).
33. RH Fowler, L Nordheim, Electron Emission in Intense Electric Fields. Proceedings of the Royal Society of London. Series A, Containing Papers of a Mathematical and Physical Character **119**, 173-181, (1928).
34. P Hawkes, E Kasper, Principles of Electron Optics Vol. 2: Applied Geometrical Optics Academic. San Diego, 953-970, (1996).
35. CJ Edgcombe, U Valdrè, Field emission and electron microscopy. Microscopy and Microanalysis **6**, 380-387, (2000).
36. J-M Bonard, T Stöckli, O Noury, A Châtelain, Field emission from cylindrical carbon nanotube cathodes: possibilities for luminescent tubes. Applied Physics Letters **78**, 2775-2777, (2001).
37. S Iijima, Helical microtubules of graphitic carbon. Nature **354**, 56-58, (1991).
38. A Oberlin, M Endo, T Koyama, Filamentous growth of carbon through benzene decomposition. Journal of Crystal Growth **32**, 335-349, (1976).
39. LA Chernozatonskii, YV Gulyaev, ZJ Kosakovskaja, NI Sinitsyn, GV Torgashov, YF Zakharchenko, EA Fedorov, VP Val'chuk, Electron field emission from nanofilament carbon films. Chemical Physics Letters **233**, 63-68, (1995).

40. A Rinzler, J Hafner, P Nikolaev, L Lou, S Kim, D Tomanek, P Nordlander, D Colbert, R Smalley, Unraveling nanotubes: field emission from an atomic wire. *SCIENCE-NEW YORK THEN WASHINGTON-*, 1550-1550, (1995).
41. N de Jonge, Y Lamy, K Schoots, TH Oosterkamp, High brightness electron beam from a multi-walled carbon nanotube. *Nature* **420**, 393-395, (2002).
42. H Sugie, M Tanemura, V Filip, K Iwata, K Takahashi, F Okuyama, Carbon nanotubes as electron source in an x-ray tube. *Applied Physics Letters* **78**, 2578-2580, (2001).
43. Nd Jonge, J-M Bonard, Carbon Nanotube Electron Sources and Applications. *Philosophical Transactions: Mathematical, Physical and Engineering Sciences* **362**, 2239-2266, (2004).
44. O Gröning, O Küttel, C Emmenegger, P Gröning, L Schlapbach, Field emission properties of carbon nanotubes. *Journal of Vacuum Science & Technology B* **18**, 665-678, (2000).
45. L Nilsson, O Groening, C Emmenegger, O Kuettel, E Schaller, L Schlapbach, H Kind, J Bonard, K Kern, Scanning field emission from patterned carbon nanotube films. *Applied Physics Letters* **76**, 2071-2073, (2000).
46. C Spindt A brief history Vacuum Nanoelectronics, the IVNC, and the present status of the Spindt cathode. In *Vacuum Nanoelectronics Conference (IVNC), 2012 25th International, 2012*; pp 1-2.



# 3 INTRODUCTION TO NANO ENGINEERED ELECTRON SOURCES

## 3.1 Electron emission

Fundamental to almost all commercial X-ray tubes is a source of electrons. Emitted from the cathode, these electrons are directed in a high vacuum towards an anode to which a positive voltage is applied. Emission of electrons will occur from a metal surface when subjected to a high electric field. **Figure 10(a)** and **10(b)** show commercially available thermionic X-ray sources and their mode of operation, respectively. **Figure 10(c)** shows the approximate band diagram at the metal-vacuum interface. To stimulate appreciable electron emission the electrons must either be excited from the Fermi level over the potential barrier, or tunnel through it. This gives rise to three principle forms of electron emission; photoemission (PE), thermionic emission (TE), and field emission (FE).

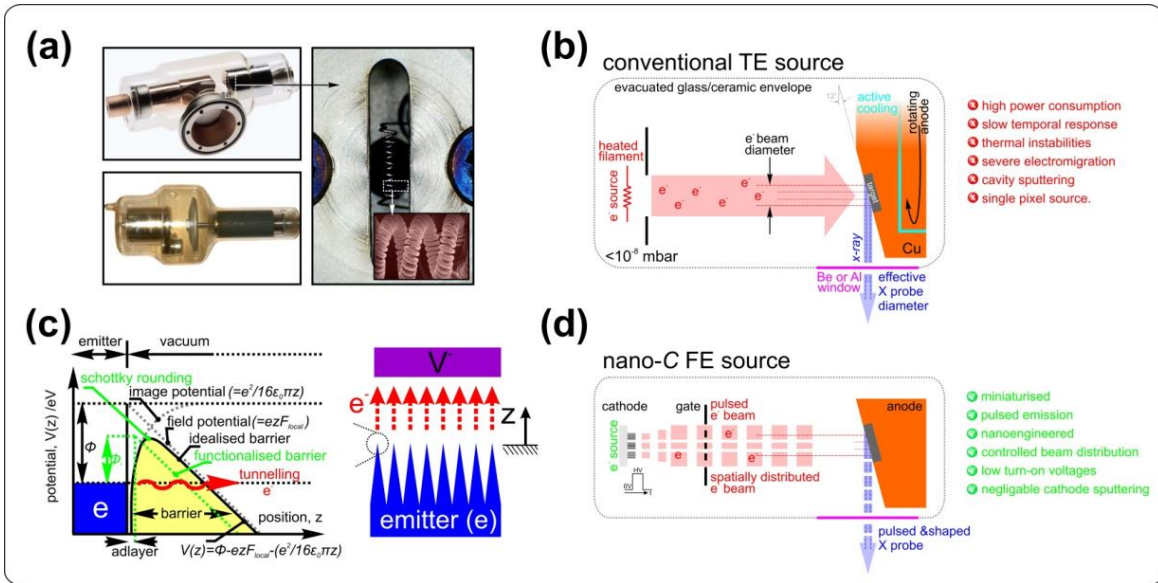


**Figure 10: Thermionic and Field X-ray emission technologies.**

(a) Images of micro-coil and rotating anode thermionic emission (TE) electron sources. (b) Schematic depiction of the operation principles of a thermionic emission (TE) electron emitter based X-ray source. Note the active anode cooling. (c) Band diagram illustrating the routes to thermionic, photo, and field emission as means to stimulate an electron beam by overcoming the surface potential barrier. (d) Schematic depiction of the operation of a field emission (FE) X-ray source. Adapted from [1].

PE occurs where the metal is irradiated with an optical source; where the wavelength is selected such that it defines an energy greater than the work function ( $\phi$ ) of the emitter and which typically lies in the ultra violet part of the spectrum. Electrons are excited and pass over the potential barrier. PE electron sources have a low efficiency as much of the incident optical radiation is absorbed in the bulk material of the emitter with only a small proportion of the photon population contributing to the direct emission. Although they have the potential to achieve extremely fast response rates, and correspondingly high bandwidths, PE has gained very little traction in most electron emission applications as only very low emission currents are possible.

In contrast, TE can stimulate the appreciable current densities that are required to be capable of stimulating X-ray emission. **Figure 10(a)** shows examples of static and rotating anode TE X-ray sources. The core components of these systems are illustrated in **Figure 10(b)** which also outlines the principle mode of operation. Here, sealed in an inexpensive and easily fabricated evacuated glass or ceramic envelope, the electrons are liberated from a metallic filament, such as Tungsten, Joule heated to in excess of 1000°C

[2]. Since the emission is directly dependent on the filament temperature [3] – as increasing the emitter temperature allows for much of the electron population to pass over the surface barrier – such tubes enable analog control over the magnitude of the emission current. In TE sources this beam current is controlled by monitoring the anode current and adjusting the filament current and hence its inferred temperature using a closed-loop control system. The intrinsic finite thermal inertia of the heated coil, when coupled to the lagging response of such feedback control systems, results in a slow response time, often several hundreds of milliseconds. In addition, care must be taken to limit the drive parameters of the filament to prevent excessive power dissipation, with subsequent risk of damage or destruction of the filament. A key design functional parameter is the focal spot size, which is related, in part, to the dimensions of the electron emission area. In the case of TE sources the physical size of the filament, typically of the order of 2 mm in outer diameter and 10 mm in length, requires the adoption of techniques to provide first order focussing. Some TE X-ray tubes are fitted with two filaments, allowing a choice of focal spot sizes, though this is at the expense of maximum available beam current and hence photon output. In order to achieve further reduction in the focal spot size, electrostatic and magnetic focussing techniques are often employed. Despite these complexities, TE has the benefit of being the accepted technology and of a very considerable period evolution, which has resulted in extremely high reliability. Field emission (FE) offers a number of significant benefits. **Figure 10(d)** illustrates a typical FE source. FE sources are often physically compact compared to their thermionic counterparts. The emission process occurs at room temperature and as such does not necessitate a direct heating element. FE is a tunnelling process and provides, as a result, near-instantaneous emission. Pulsed emission with a rise time of less than 50  $\mu\text{s}$  has been reported [4]. As illustrated above, electrons are emitted under the influence of a high electric field, typically of the order of a few  $\text{V}/\mu\text{m}$ . These electrons subsequently tunnel through the narrowed potential barrier. Traditionally the emission has been broadly described by the Fowler-Nordheim theory [5], although this is now generally considered to be an incomplete representation in the case of electron emission from most nanomaterials. Nonetheless, an approximation of the field emission current,  $I$ , can be defined by;

$$I = \left( \frac{A\beta^2 V^2}{\phi} \right) \exp \left( \frac{-B\phi^{3/2}}{\beta V} \right)$$

*Equation 2*

where  $V$  is the applied voltage across the vacuum cavity,  $\phi$  is the emitter work function,  $\beta$  is the field enhancement factor, and  $A$  and  $B$  are related to physical constants [30]. An extended analysis of the background theoretical emission mechanisms can be found in [6]. Various refinements to this model have been applied [7] to take account of the potentially elevated temperatures during emission and the extreme curvature at the CNTs apex when the CNTs are used as the field emission source. Indeed, the high electric field that is required for field emission is closely associated with the curvature and aspect ratio of the emitting material – this field enhancement factor,  $\beta$ , depends upon a number of geometrical factors such as the precise form and orientation of the emitter; in general sharp whisker-like tips emit at significantly lower potentials compared to the same material that has adopted a planar morphology [8]. This geometry-based argument is the leading rationale for the use of high aspect nanowires in field emission applications. Contrary to conventional beliefs, studies are emerging which appear to indicate that the emitter morphology has a more profound impact on reducing the turn-on and threshold electric fields compared with the effects of the emitter's work function. However, it remains challenging to attain such perturbed, high aspect ratio emitters.

Following early FE work by Dyke [9, 10], in 1968 Spindt published details of a new method of fabricating FE arrays based on Mo conical structures. These structures were 1.5  $\mu\text{m}$  high with a tip radius of 50 nm [11, 12]. During the following years, the use of Spindt emitters was widely adopted and they have since become common place in many electron emission systems. They can be found in systems from field emission displays [13-15] to high speed radio frequency devices [16-18], such as travelling wave tubes [19-21]. Current densities of up to 20 A/cm<sup>2</sup> have been achieved [22]. Nevertheless, the issue of developing suitably high current densities with low turn-on voltages remained a challenge, principally due to demanding requirements on the emitting material. At the time, low attainable aspect ratios that Spindt emitters offered, though better than their planar counterparts, limited emitter performance. A new material capable of forming extremely high aspect ratios was required. Self-assembly via chemical vapour deposition and the emergence of nanowires and nanotubes allowed for such high aspect ratios to be achieved. The geometry of these new emitters allowed for a corresponding amplification in the field enhancement factor and consequently a reduction in turn-on voltage, typically by an order of magnitude.

In order to understand the impact of both aspect ratio ( $\beta$ ) and work function ( $\phi$ ) on the emission performance of different materials, a detailed paper review was conducted.

**Appendix 1, figure (a)** summarises the various functional advantages of field emission (FE) sources over traditional TE and Schottky sources. The dashed orange circle depicts the characteristics of an ideal electron source. **Appendix 1, figure (b)** depicts the mean turn-on and threshold electric fields,  $E_{on}$  and  $E_{th}$  respectively, and maximum current density ( $J_{max}$ ) from FE sources fabricated from various materials. **Appendix 1, figure (b)** is structured in order of increasing dimensionality (1D, 2D to 3D/bulk) where each of these dimensional classes is further organised in terms of increasing emitter work function ( $\phi$ ). The mean ( $\pm 1\sigma$ ) work functions are shown. Each data point was acquired over multiple studies, nominally three or more, with the figure taking into account material only. The absence of  $\phi$  errors in some of the data indicates that only one such FE study has been conducted, typically due to the recent emergence of this given material. To extract comparable data all current densities in the considered literature were normalised relative to their maximum current densities, where this normalised value,  $J' = J/J_{max}$ , where  $0 \leq J' \leq 1$ .  $E_{on}$  and  $E_{thr}$  were defined as the electric field required to emit  $0.1J'$  and  $0.3J'$ , respectively. For clear assessment purposes of how the material type relates to efficient FE various emitter morphologies were considered. Note that there is no clear increase in  $J_{max}$  or decrease in  $E_{on}$  or  $E_{thr}$  with decreasing  $\phi$ , as one would expect for a consistent view with earlier band arguments. Indeed, emitter geometry clearly smears out much, if not all the functional benefits associated with the novel electronic properties of any given material. Nonetheless, the graphitic carbons are evidently largely beneficial in their electron emission performance. Combined with the wide range of allotropes observed to date - including the zero-dimensional fullerenes, the one-dimensional nanotubes and nanofibres, the two-dimensional graphene, and three-dimensional graphite - carbon has a morphological character perfectly matched to its impressive electronic properties.

### 3.2 Field emission application of CNTs

The discovery of carbon nanotubes (CNTs) occurred in the early 1990s [23], although there had been activity in this area for a considerable time [24]. This work, however; lead to a heightened interest which gave rise to some of the first studies on FE using CNTs in 1995 [25, 26]. As stated previously, by the early 2000's a range of applications were emerging, including high resolution electron beam microscopes [27-30], flat panel displays [14, 15, 31-33], RF devices [18, 21], electron beam lithography [34-36] and X-

ray cathode emitters [37-40], as described in an early review [35]. A detailed historical perspective on the development of CNT-based FE sources is provided in [41]. In this chapter, I provide a condensed review of the progress, as it pertains to X-ray sources, since then, which is shown in **Appendix 2**.

CNTs have some of the highest attainable aspect ratios, high thermal conductivity, low chemical reactivity in non-oxidising atmospheres, highly parallelised *en masse* fabrication, low sputtering cross-section, low secondary electron coefficient, an insensitivity to direct ion-bombardment, and are becoming progressively inexpensive with the release of new, larger growth reactors. However, field emitters require ultrahigh vacuum ( $<10^{-8}$  mbar) to provide stable operation. This limits their practical application as the material platform on which the emitters are fabricated largely dictates the tip robustness towards poor or compromised vacuum conditions which result in aggressive local ionization. In the case of the metallic Spindts, poor vacuum conditions causes tip degradation. As a result, much of the published work has been accomplished using demountable systems, which incorporate vacuum pumps to maintain the performance, although there are some notable exceptions [42, 43]. A useful summary on this was published in 2010 [44].

It is the group of applications associated with carbon nanotube-based X-ray FE emitters [37] that is the subject of this work, as the properties of the electron emitting CNTs offer many functional and performance advantages over conventional TE X-ray sources [45, 46]. In the next chapter, there will be a description of various beneficial enhancements, including shaped cathodes, micro-focal sources, pulsed sources, multi-pixel sources, and miniaturised emitters, etc. as well as considering other techniques directed towards improved performance by significantly reducing the work function of the emitters, such as the use of adlayers.

As will be described in the experimental section, severe problems with CNT electron source fabrication, reliability, time stability, spatial uniformity, and reproducibility have been encountered. It is clear that this has prevented the wide spread adoption, particularly in high beam current applications. Nevertheless, CNT-based X-ray sources were proposed following the emergence of CNTs and in 2001 Sugie *et al.* [37] were some of the first to describe the use of CNTs as a FE-based X-ray source. Here they grew

vertically aligned forests of CNTs on Co coated W wire, with the electron beam controlled by a counter electrode mounted 0.5 mm from the emitter. This setup produced a beam current of just 1.5  $\mu\text{A}$ , but was sufficient to image onto an X-ray sensitive film a range of samples including integrated circuits. The lifetime of the cathode assembly was little more than one hour and the images exhibited severe noise artefacts. Nevertheless, this work did convincingly demonstrate the potential of CNTs in X-ray applications whilst simultaneously highlighting critical functional issues such as fluctuations in emitted beam current that needed to be addressed. Another early example of a functioning X-ray tube was produced by Haga *et al.* [39]. Catalytically synthesised CNTs and carbon nanofibres (CNFs) grown on a Pd wire were used as the FE source, although there was no counter electrode, or gate used to extract the electron beam. This device operated for several hours at 30 kV with a beam current of 50  $\mu\text{A}$ . Clear images were acquired, though requiring a long and technologically unacceptable integration time of the order of minutes. The same group produced a triode-configuration (incorporating a gate electrode) which increased the beam current to about 1 mA [40]. Many more examples have now been published on the use of similar triode configurations [38, 47-50]. These include designs with additional focusing electrodes for a micro focal imaging system operating at 18 kV, developed utilising 3D beam simulation tools [47].

### 3.3 Cathode fabrication

All X-ray tubes require the generation of a beam of electrons. This electron beam is directed towards the anode, which subsequently liberates X-rays when impacted. It is the cathode assembly that provides the source of electrons and it is the cathode design and materials which dramatically influence the resultant performance. The commercial field of vacuum electronics is now well established and was initially principally based on Spindt-like emitters, a comprehensive review on which is provided by Temple *et al.* [51]. The incorporation of CNTs within the cathode is the focus of this study. It is the objective to enhance the electron emission, and hence, X-ray emission performance.

The first FE emitters using one-dimensional carbon allotropes were based on CNFs deposited on metallic tips [35, 37, 39, 52]. These sought to enhance the native emission characteristics of the conventional tips by depositing CNFs, generally by CVD.

Subsequent developments, however; centered on the use of planar substrates in attempts

to realise more reproducible devices applicable to a wider range of electron emission applications. CNTs may be deposited on the cathode assembly using several different processes [53]. **Figure 11** summarises these.

CNT thin films are readily patterned using a variety of techniques. There are numerous aspects which are yet to be well developed in the literature. Nevertheless, the attainable pattern resolution is closely related to the orientation of the constituent CNTs within the thin film and the patterning technique employed. Aligned CNTs give higher resolution than misaligned CNTs. Wet processed thin films – such as drop, cast, vacuum filtrate, spray, and screen printed – are fundamentally wet chemistry deposition techniques that can be patterned by either stencilling or shadow masking to protect zones from being coated with the CNT inks during the deposition process. These shadow approaches provide a modest maximum resolution of around 100  $\mu\text{m}$  as the inks often bleed beneath the masking layer, resulting in diffuse and uncontrolled edges. Without the application of external driving forces, such as are present in electrophoresis, such patterns result in CNTs that are always misaligned with one another. Dip pen nanolithography and micro-ink jet printing can also be used to drop deposit CNT inks at controlled locations, with a common maximum resolution of 1  $\mu\text{m}$ . Nevertheless, again the CNTs are disordered and misaligned. In these additive approaches there remain significant challenges in preventing the nozzle from clogging during the deposition or the nanolithography tip becoming deformed. As a result inkjet printing and dip-pen nanolithography necessitate the use of very short CNTs, which significantly compromises their usefulness in FE applications. Micro-contact printing is another additive approach to cathode patterning. Here a polymeric stamp is inked with a CNT solution and then placed in contact with a substrate which has an engineered hydrophilic surface to ensure the CNTs adhere. Interfacial engineering marks the broadband application of this technique and often necessitates the use of self-assembled monolayers which act as effective adhesion promoters. Such approaches have proven useful in patterning carbon nanomaterials [54], though their spatial resolution is again limited to a few micrometers at present. In addition to the additive patterning approaches discussed, there are various subtractive means available. Most common is by way of conventional lithographically patterning the deposited CNT thin film, depositing a hard mask, and oxygen plasma etching the exposed CNTs. This approach gives high resolution, typically  $\leq 0.4 \mu\text{m}$ . Nevertheless, common to all wet chemistry approaches to CNT deposition remains the fact that the CNTs are disordered and unaligned with respect to one another.

Chemical vapour deposition (CVD) processes dramatically increase the maximum potential resolution to around  $< 0.1 \mu\text{m}$  by direct patterning of the physical vapour deposited catalyst and growth of vertically aligned CNTs. Indeed, inclusion of plasma during heating and exposure to the gaseous hydrocarbon and atomic hydrogen sources can be used to assist in the catalytic activity and alignment of the CNTs. CVD is well suited to patterning well-aligned CNT geometries, however it is restrained to the use of high temperature ( $>300^\circ\text{C}$ ) compatible substrates, such as glass, quartz, and silicon. Techniques are now being developed where the heating of the substrate is being mitigated by heating of the incident gases.

Another important consideration when considering the various merits of the available deposition techniques is the effective roughness and area uniformity that can be achieved. These deposition techniques will produce films of varying thickness uniformity. CVD exceeds the degree of uniformity of all other techniques, followed, in rank order, by casting, vacuum filtration, screen printing, and finally spray and drop casting; the latter of which typically gives coffee-stained like thin films that have a significant spatial variation in CNT density. Indeed, CVD, as demonstrated by the group of Milne, have yielded variations in surface roughness of  $< 3\%$  [55]. Nevertheless, most CNT-based FE X-ray sources are based on wet chemistry processed thin films. What follows here summarises the fabrication details of some of the more common CNT thin film fabrication techniques, with particular emphasis on those that have been used in CNT-based FE X-ray sources.

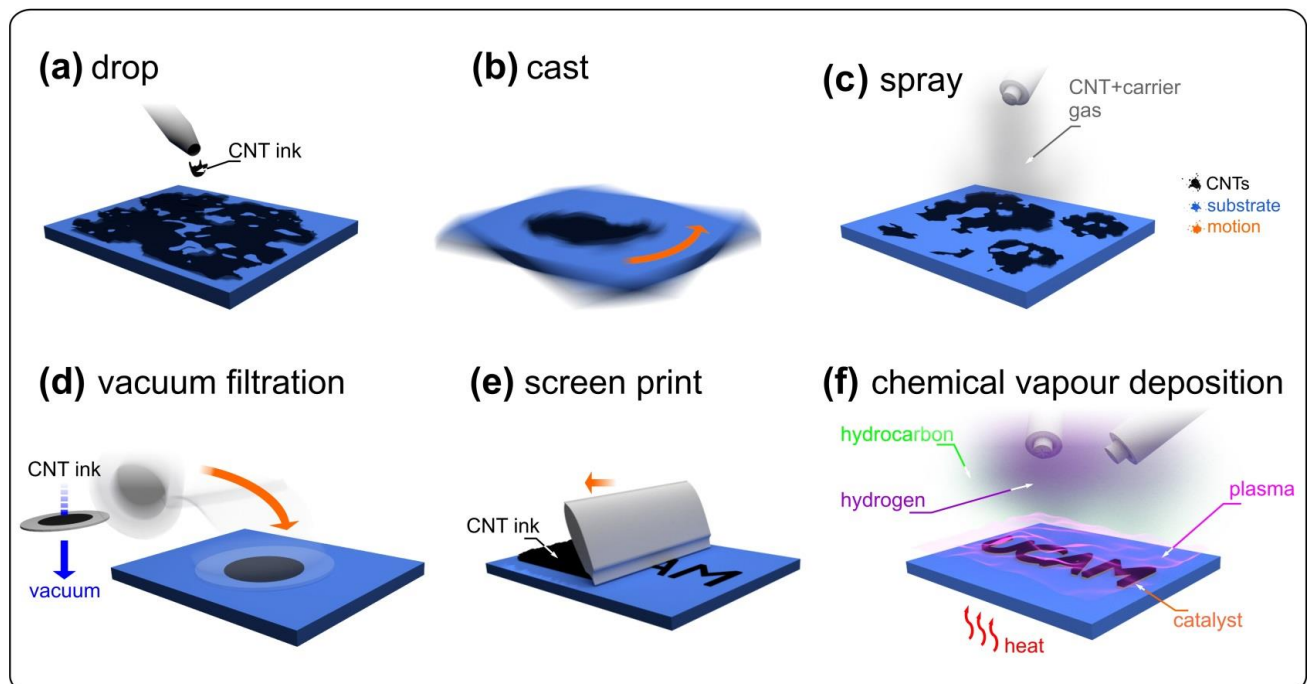


**Figure 11: Common carbon nanotube thin film deposition techniques.**

(a) drop, (b) cast, (c) spray, (d) vacuum filtration, (e) screen printing, and (f) chemical vapour deposition. Adapted from [1].

### 3.3.1 Drop, Spray and Cast

Drop (**Figure 11(a)**), cast (**Figure 11(b)**), and spray (**Figure 11(c)**) approaches have proven, to be thus far, the fabrication methods of choice by many. This is likely a direct consequence of the low cost and the straightforward processes on which they are based, rather than any direct functional enhancements that the fabrication techniques allow for. Drop, cast and spray techniques all require CNT inks. In each case, respectively, these are deposited either by direct dropping of the ink, spin coating or casting of the ink at high rotational speed, or spray coating of the ink using a pressurised carrier gas. All these approaches initially require wet processing of the as-grown CNTs and it is this which, common to all, limits their usefulness and the consequent performance of the resulting X-ray source. The required high power sonication and vacuum unstable surfactants needed to form the stabilised, homogenous inks results in compromised temporal stability, deleterious hysteresis, and generally degraded emission.

### 3.3.2 Electrophoresis

Electrophoresis is a derivative of inking deposition. Electrophoresis involves the motion, placement, and potentially modest alignment of drop or spray deposited CNTs. Electrophoresis exploits the CNTs native anisotropic charge distribution and its interaction with an applied electric field [49, 56, 57]. Elsewhere it has been widely used as a means of depositing phosphor materials. It has also been applied to the deposition and alignment of bundles of SWCNTs on various substrates, such as stainless steel or doped Si [56-58]. Composite CNT films deposited by electrophoresis have been fabricated with controlled surface density with good field emission performance, current density and long-term stability under high operating voltages, which has been applied to an electron source for high-resolution X-ray imaging [49]. Wang et al. [58] deposited MWCNTs on Cr/Cu electrodes supported on an oxidised Si support with a glass interlayer adhesion promoter. The emitters were annealed at 480°C for 30 min following deposition to mobilise the glass interlayer and reduce the effective interfacial resistance. As with other solution-based fabrication techniques, in order to reduce the emitters turn-on bias they were taped to activate them; a threshold field of 3.5 V/μm was measured (for

an emission current density of  $10 \mu\text{A}/\text{cm}^2$ ). Though a simple and low-cost means of defining the pixel size, electrophoretically defined emission zones only allow for relatively large cathode diameters, of the order of 2 mm, which reduces the systems functionality. Calderón-Colón *et al.* [49] employed photolithography and liquid phase electrophoretic deposition to pattern disordered and unaligned MWCNTs in an homogenous solution with  $\text{MgCl}_2$  and glass frits. Here film thickness was broadly controlled by the deposition time and the magnitude of the applied voltage, though accurate sample-to-sample reproducibility and control over the thickness, to  $< 10 \text{ nm}$  surface roughness, is challenging. Such techniques are comparatively low in uniformity and reproducibility, a direct consequence of the simple macro scale processing. Moreover, the common binder matrices are far from pure, making clarity of the underlying emission mechanisms somewhat challenging, though nonetheless functional. Indeed, as with all other inking deposition techniques, the emitters do require mechanical activation for the cathodes to be of any practical use, though electrophoretic patterning is rapid and simple to implement.

### 3.3.3 Vacuum filtration & screen printing

Many of the FE X-ray sources demonstrated have employed screen printed or vacuum filtrated CNT thin films [45, 58-60] (**Figure 11(d)**). Here CNT solutions are deposited at the macro-scale and form highly disordered, nominally planar, spaghetti-like networks with but a few individual CNTs standing upright, at many unregistered angles relative to one another, as illustrated in **Figure 12(a)** (see next chapter). In the case of vacuum filtration the CNT ink is poured onto a porous mixed (nitro) cellulose ester membrane, which has a partial vacuum applied on its opposite side. Such porous membranes have controlled apertures, typically around  $0.2 \mu\text{m}$  in diameter. The reduced pressure stimulates the solvent within the CNT ink to pass through the membrane, whilst the membrane stops the CNTs from passing. Once the ink reservoir is depleted the thin film is rinsed with de-ionised water to remove much of the deleterious surfactants, leaving a thin CNT film on the membrane. Note, however; that much of the surfactant still remains even after extensive rinsing using deionised water. The CNT thin film can then be transferred to an arbitrary acetone-resistant substrate by applying modest pressure ( $40 \text{ g}/\text{cm}^2$ ) and heat (ca.  $70^\circ\text{C}$ ) for an extended period of time (often of the order of 3 h). The membrane is then dissolved, by exposure to acetone or methanol, and the CNT thin film

remains. The CNT film thickness, and hence sheet resistance and optical transparency, is controlled by adjusting the amount of CNT ink filtered through the membrane. CNT thin film fabrication by vacuum filtration has been employed for more than a decade. It offers a rapid, low cost way to fabricate CNT thin films. Little to no infrastructure is required and the films can be processed rapidly, over large areas. Nonetheless, as in the case of drop, cast and spray, such *chemi douche* processing requires stabilised inks. CNTs experience high inter-tube van der Waals forces; they tend to agglomerate. Though this interaction has been exploited elsewhere to fabricate new novel aligned nanostructured membranes [61], such agglomeration is problematic in producing homogenous CNT inks and solutions. As such various, often sodium-based, surfactants such as sodium dodecylbenzene sulphate, sodium dodecyl sulphate, and Triton X are required to produce homogenous solutions with the CNTs well-dispersed throughout the solution. Further aggressive acid treatments and extended durations under high power ultrasonication significantly degrade the length, crystallinity and subsequent electronic character of the CNTs which necessarily limits the electron emission performance. These inks are then transferred to metallic disks using conventional screen printing methods or vacuum coated mixed cellulose ester membranes that are subsequently dissolved in acetone following transfer [62]. The morphology of these films is highly disordered. They typically lack high aspect ratio protrusions, resulting in poor field emission performance. FEs fabricated in this way have a number of intrinsic problems; chiefly that mechanical taping is required to activate the surfaces and enhance their field emission characteristics. Taping, using adhesive coated tape, increases the surface roughness of the CNT thin-films. It is a macro-scale process with very little reproducibility. Moreover; the necessary surfactants are usually vacuum unstable giving rise to emission profiles that drift with time [59, 63-65]. CNT inks can often have significant out-gassing [66] when even modestly heated, thereby compromising the vacuum envelope. The resultant reduction in field emission performance and reduced current density has, as a result, prevented CNT-based pastes and ink from gaining commercial traction, although cathodes fabricated in this way are appealing as the reduced reproducibility is offset by the ease of fabrication. Such films are also somewhat dynamic and often have weak adhesion to the substrate. Their morphology shifts with time during the application of a high electric field due to the intrinsic torque induction within the CNTs due to the tip or root positioning of the growth catalyst particle.

To obviate issues of weak interfacial adhesion between the substrate and electron emitting MWCNTs, Kim et al. [43, 67], using screen printing, as illustrated in **Figure 11(e)**, employed ball-milled pastes combined with inorganic fillers including Ag and Ni alloyed nano-particles and oxides in an ethyl cellulose powder and terpeneol solvent. No surfactants were used. The pastes were deposited on indium tin oxide coated glass substrates followed by 300°C post-bake to remove residual solvents. The derived slurry showed strong adhesion to the substrate, good uniformity and reproducibility with a current density of up to 350 mA/cm<sup>2</sup>. Nevertheless, ball-milling degrades the graphitic quality of the MWCNTs, which adversely impacts the long-term time stability relative to high quality crystalline material, although these devices did show excellent high-temperature operation (up to 800°C), robustness towards harsh vacuum environments, impressive spatial uniformity, a low turn on voltage of 1 V/μm, and enhanced temporal stability relative to conventional CNT pastes, although the anode current is still degraded by around 30% under DC operation over a 100 hr period. Another fabrication problem associated with screen printing is the limitation on the pattern resolution. The sonicated CNTs within the inks are typically of the order of 5 μm in length. These can clog the screen printing mesh resulting in a low porosity and inability to print. Formation of stabilised, homogenous inks is central to drop, cast, spray, vacuum filtration and screen printing. The formation of these inks, as highlighted above, requires deleterious ultra-sonication and aggressive acid treatments, both of which degrade the length and electronic character of the CNTs. Though the necessary wet chemistry approaches provide a facile, rapid and inexpensive route to fabricate the emitter, the constituent CNTs are coated with vacuum unstable surfactants that can only be removed following high temperature post-deposition treatments which, if not fully removed, would otherwise cause significant out-gassing during operation [49]. Maintaining slurry and ink consistency over time and between batches is difficult, reducing device-to-device reproducibility and hence are unsuitable for devices to be used in an industrial engineering environment. It is also challenging to pattern emitters fabricated in this way though screen printing (the migration of CNT inks through patterned apertures within a regular mesh), as demonstrated by Kim *et al.* previously, has proven one useful approach. Though screen printing is indeed large-area compatible, it is rather low resolution and thus limits the degree of control over the detailed design of the electron source. Oxygen plasma etching coupled to conventional lithographic techniques is another viable option though significant surface roughness of the CNT thin film can again compromise the

maximum resolution. Moreover, plasma etching techniques are only applicable to non-organic substrates.

While there have been reports that electrophoresis can produce a degree of alignment [68, 69] this is relative only to the very randomly orientated screen printing and ink-based processes. Misalignment prevents any fabricated devices from realising the full field enhancement factor of the composite CNTs; in order to achieve this, alternative fabrication methods capable of aligning the CNTs *en masse*, must be considered, with chemical vapour deposition being the most promising method to date.

### 3.3.4 Chemical vapour deposition

Chemical vapour deposition (**Figure 11(f)**) provides a more controllable means of growing CNTs. The CNTs self-assemble from atomic units in a highly parallelised process, which when coupled with high resolution lithographic techniques for the application of catalysts, allows for near nano-scale engineering of the CNTs and CNFs. CVD techniques mediate the growth of chemically untreated disordered or aligned CNT thin films depending on the substrate, catalyst and growth precursors employed. In a typical implementation, Silicon is coated with a physical vapour deposited metal catalyst which can be patterned *via* lithographic or masking techniques by either additive or subtractive process, such as magnetron sputtering, or plasma etching, respectively. The substrate is then heated to temperatures often in excess of 500°C, and the growth of the CNTs on these sites is initiated by supplying a hydrocarbon feedstock gas, such as CH<sub>4</sub> or C<sub>2</sub>H<sub>2</sub>, combined with an *α*-C etching gas species, typically H<sub>2</sub> or NH<sub>3</sub> both of which readily pyrolyse to give a constant supply of carbon and atomic hydrogen. In situ plasma can also be employed to enhance the catalysis and align the CNTs during growth. Cole *et al.* have compiled a concise overview of the CVD of nanocarbons [70].

Using thermal-CVD synthesised MWCNTs directly deposited on shadow-masked Mo discs (as well as Si, fused quartz, mica, copper, and highly ordered pyrolytic graphite), with a bilayer Al/Fe (0.5/10 nm) catalyst, Sarrazin *et al.* [71] have routinely measured current densities in excess of 1 A/cm<sup>2</sup>. Here the MWCNTs were several microns in length and randomly orientated, with most running adjacent to the substrate; CVD techniques allow for CNT alignment, though random orientation is still possible. Very little control over the type, orientation and area packing density of the CNTs was evidenced with a largely qualitative analysis presented. Nevertheless, a turn-on bias of approximately 2 V/μm was observed. Rather surprisingly, the robustness of the cathodes

toward arcing was clearly shown resulting in an increase in the voltage for a given current following repeated arcing events. They suggest that either the emitting sites are not completely destroyed or that they are efficiently replaced by other nanotubes within the film. Indeed, disordered films are structurally dynamic when under the influence of a high electric field, which can augment their emission characteristics. Though film reorganisation benefits the long term stability, in that degraded CNTs are in essence replaced, the short term temporal stability is likely to be not advantageous in applications for X-ray devices with closed loop beam current control. More than 100 cathodes were tested and a poor reproducibility was indeed noted, a probable consequence of the disorder and uncontrolled microscale morphology of the emitter.

As is the case for the screen printed and vacuum filtration methods, one potential problem is the degree of adhesion between the CNT and the substrate when exposed to high electric fields. Detailed control of the underlying catalyst has shown that such emitter removal concerns can be solved. Li and Cole *et al.* showed very low variation in anode current of  $< \pm 0.7\%$  for emission over  $> 200$  hrs using an ITO/Ni (10/1 nm) bilayer catalyst which effectively enhanced the degree of adhesion [72].

Using rapid thermal CVD, Kim *et al.* [73] deposited CNTs directly on stainless steel sheets coated with TiN/Ni. The emitters showed a maximum current of 2 mA (data on the emitter area was unavailable) at an anode potential of 5 kV. The CNTs were 30  $\mu\text{m}$  long, with Raman analysis suggesting a very defective material, whilst scanning electron microscopy showed vertically aligned forests with a high packing density. Though the emission showed good performance the geometry was not optimised; the dense forest results in significant shielding of the CNTs from the applied electric field – the material appears as bulk - such that the full field enhancement factor of the CNTs was realised in this instance. Whilst individual one dimensional nanowire and nanotube emitters have been empirically evidenced to produce the highest local electric fields, the proximity of other emitters will effectively shield the field enhancement [35, 74]. In a field emission device, where our interest is in the total available current density, the optimum arrangement will not be that with the highest density of emitters [75, 76]. In addition, the emission pattern of the field emitter is not uniform CVD growth can result in individual CNTs, or structures such as CNT pillar arrays and toroids [49, 56, 77-80]. In addition, patterns of control electrodes may be grown, in such a way as to focus or concentrate the field from the tip.

The use of CVD to nanoengineer X-ray sources has remained in its infancy due to a number of challenges in explicating the underlying materials growth. Nevertheless, following recent advances in the understanding of nanocarbon catalysis [81-83], the use of CVD-grown CNTs and CNFs in FE X-ray sources appears to be accelerating and is emerging as an exciting candidate for viable commercialisation.

### 3.4 Conclusions

There is a range of assembly techniques for the growth and assembly of CNT field emitters. The problems associated with many of these are the limit of performance as field emission devices, and the reproducibility of results. Of all the methods reviewed, CVD (chemical vapour deposition) is the most compelling in terms of a well-controllable production process.

### 3.5 References

1. RJ Parmee, CM Collins, WI Milne, MT Cole, X-ray generation using carbon nanotubes. *Nano Convergence* **2**, 1, (2015).
2. WD Coolidge, A Powerful Röntgen Ray Tube with a Pure Electron Discharge. *Physical Review* **2**, 409-430, (1913).
3. EL Murphy, RH Good, Thermionic emission, field emission, and the transition region. *Physical Review* **102**, 1464-1473, (1956).
4. W Lei, C Li, MT Cole, K Qu, S Ding, Y Zhang, JH Warner, X Zhang, B Wang, WI Milne, A Graphene-Based Large Area Surface-Conduction Electron Emission Display. *Carbon* **56**, 8, (2013).
5. RH Fowler, L Nordheim, Electron Emission in Intense Electric Fields. *Proceedings of the Royal Society of London. Series A, Containing Papers of a Mathematical and Physical Character* **119**, 173-181, (1928).
6. P Hawkes, E Kasper, *Principles of Electron Optics Vol. 2: Applied Geometrical Optics Academic. San Diego*, 953-970, (1996).
7. CJ Edgcombe, U Valdrè, Field emission and electron microscopy. *Microscopy and Microanalysis* **6**, 380-387, (2000).
8. J-M Bonard, T Stöckli, O Noury, A Châtelain, Field emission from cylindrical carbon nanotube cathodes: possibilities for luminescent tubes. *Applied Physics Letters* **78**, 2775-2777, (2001).
9. WP Dyke, J Trolan, Field emission: large current densities, space charge, and the vacuum arc. *Physical Review* **89**, 799, (1953).
10. W Dyke, W Dolan, Field emission. *Advances in electronics and electron physics* **8**, 89-185, (1956).

11. CA Spindt, A Thin-Film Field-Emission Cathode. *Journal of Applied Physics* **39**, 3504-3505, (1968).
12. I Brodie, C Spindt, *Advances in Electronics and Electron Physics* edited by PW Hawkes, vol. 83. (1992).
13. CA Spindt, I Brodie, L Humphrey, ER Westerberg, Physical properties of thin-film field emission cathodes with molybdenum cones. *Journal of Applied Physics* **47**, 5248-5263, (1976).
14. CA Spindt, CE Holland, I Brodie, JB Mooney, ER Westerberg, Field-emitter arrays to vacuum fluorescent display. *Electron Devices, IEEE Transactions on* **36**, 225-228, (1989).
15. L Yukui, Z Changchun, L Xinghui, Field emission display with carbon nanotubes cathode: prepared by a screen-printing process. *Diamond and Related Materials* **11**, 1845-1847, (2002).
16. DR Whaley, BM Gannon, CR Smith, CM Armstrong, CA Spindt, Application of field emitter arrays to microwave power amplifiers. *Plasma Science, IEEE Transactions on* **28**, 727-747, (2000).
17. H Makishima, S Miyano, H Imura, J Matsuoka, H Takemura, A Okamoto, Design and performance of traveling-wave tubes using field emitter array cathodes. *Applied Surface Science* **146**, 230-233, (1999).
18. WI Milne, KBK Teo, E Minoux, O Groening, L Gangloff, L Hudanski, J-P Schnell, D Dieumegard, F Peauger, IYY Bu, MS Bell, P Legagneux, G Hasko, GAJ Amaratunga, Aligned carbon nanotubes/fibers for applications in vacuum microwave amplifiers. *Journal of Vacuum Science and Technology B* **24**, 345-348, (2006).
19. KL Jensen, Field emitter arrays for plasma and microwave source applications. *Physics of Plasmas (1994-present)* **6**, 2241-2253, (1999).
20. H Makishima, S Miyano, H Imura, J Matsuoka, H Takemura, A Okamoto, Design and performance of traveling-wave tubes using field emitter array cathodes. *Applied Surface Science* **146**, 230-233, (1999).
21. KBK Teo, E Minoux, L Hudanski, F Peauger, JP Schnell, L Gangloff, P Legagneux, D Dieumegard, GAJ Amaratunga, WI Milne, Microwave devices - Carbon nanotubes as cold cathodes. *Nature* **437**, 968-968, (2005).
22. EF Barasch, HP Demroff, TS Elliott, TB Kasprowicz, B Lee, T Mazumdar, PM McIntyre, Y Pang, DD Smith, H-J Trost Gated Field-Emitter Cathodes for High-Power Microwave Applications. In *Proceedings of the 1992 Linear Accelerator Conference; Ottawa, Ontario, Canada, 1992*.
23. S Iijima, Helical microtubules of graphitic carbon. *Nature* **354**, 56-58, (1991).
24. A Oberlin, M Endo, T Koyama, Filamentous growth of carbon through benzene decomposition. *Journal of Crystal Growth* **32**, 335-349, (1976).
25. LA Chernozatonskii, YV Gulyaev, ZJ Kosakovskaja, NI Sinityn, GV Torgashov, YF Zakharchenko, EA Fedorov, VP Val'chuk, Electron field emission from nanofilament carbon films. *Chemical Physics Letters* **233**, 63-68, (1995).
26. A Rinzler, J Hafner, P Nikolaev, L Lou, S Kim, D Tomanek, P Nordlander, D Colbert, R Smalley, Unraveling nanotubes: field emission from an atomic wire. *Science*, 1550-1550, (1995).
27. N de Jonge, Y Lamy, K Schoots, TH Oosterkamp, High brightness electron beam from a multi-walled carbon nanotube. *Nature* **420**, 393-395, (2002).

28. S Akita,H Nishijima,Y Nakayama,F Tokumasu,K Takeyasu, Carbon nanotube tips for a scanning probe microscope: their fabrication and properties. *Journal of Physics D* **32**, 1044, (1999).
29. M Mann,K Teo,W Milne,T Tessner, Direct growth of multi-walled carbon nanotubes on sharp tips for electron microscopy. *NANO* **1**, 35-39, (2006).
30. H Nishijima,S Kamo,S Akita,Y Nakayama,KI Hohmura,SH Yoshimura,K Takeyasu, Carbon-nanotube tips for scanning probe microscopy: Preparation by a controlled process and observation of deoxyribonucleic acid. *Applied Physics Letters* **74**, 4061-4063, (1999).
31. W Milne,K Teo, Growth and characterization of carbon nanotubes for field-emission-display applications. *Journal of the Society for Information Display* **12**, 289-292, (2004).
32. W Choi,D Chung,J Kang,H Kim,Y Jin,I Han,Y Lee,J Jung,N Lee,G Park, Fully sealed, high-brightness carbon-nanotube field-emission display. *Applied Physics Letters* **75**, 3129-3131, (1999).
33. N Lee,D Chung,I Han,J Kang,Y Choi,H Kim,S Park,Y Jin,W Yi,M Yun, Application of carbon nanotubes to field emission displays. *Diamond and related materials* **10**, 265-270, (2001).
34. KBK Teo,M Chhowalla,GAJ Amaratunga,WI Milne,P Legagneux,G Pirio,L Gangloff,D Pribat,V Semet,VT Binh,WH Bruenger,J Eichholz,H Hanssen,D Friedrich,SB Lee,DG Hasko,H Ahmed, Fabrication and electrical characteristics of carbon nanotube-based microcathodes for use in a parallel electron-beam lithography system. *Journal of Vacuum Science & Technology B* **21**, 693-697, (2003).
35. Nd Jonge,J-M Bonard, Carbon Nanotube Electron Sources and Applications. *Philosophical Transactions: Mathematical, Physical and Engineering Sciences* **362**, 2239-2266, (2004).
36. SM Vieira,KB Teo,WI Milne,O Gröning,L Gangloff,E Minoux,P Legagneux, Investigation of field emission properties of carbon nanotube arrays defined using nanoimprint lithography. *Applied Physics Letters* **89**, 022111, (2006).
37. H Sugie,M Tanemura,V Filip,K Iwata,K Takahashi,F Okuyama, Carbon nanotubes as electron source in an x-ray tube. *Applied Physics Letters* **78**, 2578-2580, (2001).
38. GZ Yue,Q Qiu,B Gao,Y Cheng,J Zhang,H Shimoda,S Chang,JP Lu,O Zhou, Generation of continuous and pulsed diagnostic imaging x-ray radiation using a carbon-nanotube-based field-emission cathode. *Applied Physics Letters* **81**, 355-357, (2002).
39. A Haga,S Senda,Y Sakai,Y Mizuta,S Kita,F Okuyama, A miniature x-ray tube. *Applied Physics Letters* **84**, 2208-2210, (2004).
40. S Senda,M Tanemura,Y Sakai,Y Ichikawa,S Kita,T Otsuka,A Haga,F Okuyama, New field-emission x-ray radiography system. *Review of Scientific Instruments* **75**, 1366-1368, (2004).
41. F Charbonnier, Developing and using the field emitter as a high intensity electron source. *Applied Surface Science* **94**, 26-43, (1996).
42. Y Iwai,T Koike,Y Hayama,A Jyouzuka,T Nakamura,Y Onizuka,M Miyoshi,H Mimura, Field emission characteristics of inflated graphite at high temperature and its applications. *Technical Digest of IVNC*, 274-275, (2012).

43. J-W Kim, J-W Jeong, J-T Kang, S Choi, J Choi, S Ahn, Y-h Song A digital compact x-ray tube with carbon nanotube field emitters for advanced imaging systems. In *SPIE Medical Imaging*; International Society for Optics and Photonics, 2013; pp 861-866.
44. Y Saito Carbon Nanotube and Related Field Emitters: Fundamentals and Applications. Wiley-VCH Verlag; Weinheim, 2010.
45. Y Cheng, O Zhou, Electron field emission from carbon nanotubes. *Comptes Rendus Physique* **4**, 1021-1033, (2003).
46. I Oxford *Cold Cathode vs Thermionic X-ray Tubes* [Online]. 2000; [http://wigner.elte.hu/koltai/science/pub/Which\\_Source\\_Cold\\_cathode\\_or\\_Thermionic.pdf](http://wigner.elte.hu/koltai/science/pub/Which_Source_Cold_cathode_or_Thermionic.pdf).
47. H Y Choi, W S Chang, H S Kim, Y H Park, J U Kim, Acquisition of X-ray images by using a CNT cold emitter. *Physics Letters A* **357**, 36-41, (2006).
48. J Zhang, Y Cheng, Y Z Lee, B Gao, Q Qiu, W L Lin, D Lalush, J P Lu, O Zhou, A nanotube-based field emission x-ray source for microcomputed tomography. *Review of Scientific Instruments* **76**, 094301-094304, (2005).
49. X Calderón-Colón, H Geng, B Gao, L An, G Cao, O Zhou, A carbon nanotube field emission cathode with high current density and long-term stability. *Nanotech.* **20**, 325707, (2009).
50. G Pirio, P Legagneux, D Pribat, K Teo, M Chhowalla, G Amaratunga, W Milne, Fabrication and electrical characteristics of carbon nanotube field emission microcathodes with an integrated gate electrode. *Nanotechnology* **13**, 1, (2002).
51. D Temple, Recent progress in field emitter array development for high performance applications. *Materials Science and Engineering: R: Reports* **24**, 185-239, (1999).
52. S H Heo, A Ihsan, S O Cho, Transmission-type microfocuss x-ray tube using carbon nanotube field emitters. *Applied Physics Letters* **90**, 183109-183103, (2007).
53. WIM Qing Zhang *Advances in Nanodevices and Nanofabrication*; (Pan Stanford Publishing, 2012).
54. M T Cole, T Hallam, W I Milne, G S Duesberg, Field Emission Characteristics of Contact Printed Graphene Fins. *Small*, (2013).
55. K B K Teo, S B Lee, M Chhowalla, V Semet, V T Binh, O Groening, M Castignolles, A Loiseau, G Pirio, P Legagneux, D Pribat, D G Hasko, H Ahmed, G A J Amaratunga, W I Milne, Plasma enhanced chemical vapour deposition carbon nanotubes/nanofibres - how uniform do they grow? *Nanotechnology* **14**, 204-211, (2003).
56. B Gao, G Z Yue, Q Qiu, Y Cheng, H Shimoda, L Fleming, O Zhou, Fabrication and electron field emission properties of carbon nanotube films by electrophoretic deposition. *Advanced materials* **13**, 1770-1773, (2001).
57. A R Boccaccini, J Cho, J A Roether, B J Thomas, E Jane Minay, M S Shaffer, Electrophoretic deposition of carbon nanotubes. *Carbon* **44**, 3149-3160, (2006).
58. S Wang, X Calderon, R Peng, E C Schreiber, O Zhou, S Chang, A carbon nanotube field emission multipixel X-ray array source for microradiotherapy application. *Applied Physics Letters* **98**, 213701-213703, (2011).

59. J Li, W Lei, X Zhang, X Zhou, Q Wang, Y Zhang, B Wang, Field emission characteristic of screen-printed carbon nanotube cathode. *Applied Surface Science* **220**, 96-104, (2003).
60. F Sprenger, X Calderon, E Gidcumb, J Lu, X Qian, D Spronk, A Tucker, G Yang, O Zhou Stationary digital breast tomosynthesis with distributed field emission x-ray tube. 2011; pp 79615I-79615I-79616.
61. MT Cole, M Doherty, R Parmee, P Dawson, WI Milne, Ultra-broadband Polarisers Based on Metastable Free-Standing Aligned Carbon Nanotube Membranes. *Advanced Optical Materials*, (2014).
62. M Qian, T Feng, K Wang, H Ding, Y Chen, Q Li, Z Sun, Field emission of carbon nanotube films fabricated by vacuum filtration. *Physica E* **43**, 462-465, (2010).
63. Y Cho, H Song, G Choi, D Kim, A simple method to fabricate high-performance carbon nanotube field emitters. *J Electroceram* **17**, 945-949, (2006).
64. YS Shi, C-C Zhu, W Qikun, L Xin, Large area screen-printing cathode of CNT for FED. *Diamond and Related Materials* **12**, 1449-1452, (2003).
65. J-Y Pan, C-y Chen, Y-L Gao, C-C Zhu, Improved field emission characteristics of screen-printed CNT-FED cathode by interfusing Fe/Ni nano-grains. *Displays* **30**, 114-118, (2009).
66. H-Y Shin, W-S Chung, KH Kim, Y-R Cho, B-C Shin, Effects of bonding materials in screen-printing paste on the field-emission properties of carbon nanotube cathodes. *Journal of Vacuum Science and Technology B* **23**, 2369-2372, (2005).
67. J-W Kim, J-W Jeong, J-T Kang, S Choi, S Ahn, Y-H Song, Highly reliable field electron emitters produced from reproducible damage-free carbon nanotube composite pastes with optimal inorganic fillers. *Nanotechnology* **25**, 065201, (2014).
68. K Yamamoto, S Akita, Y Nakayama, Orientation and purification of carbon nanotubes using ac electrophoresis. *Journal of Physics D* **31**, 34-36, (1998).
69. Kunitoshi Yamamoto, Seiji Akita, Yoshikazu Nakayama, Orientation of Carbon Nanotubes Using Electrophoresis. *Japanese Journal of Applied Physics* **35**, L917, (1996).
70. MT Cole, C Collins, R Parmee, C Li, WI Milne NanoCarbon Electron Emitters: Advances & Applications. In *Chemical Functionalisation of Carbon Nanomaterials: Chemistry & Applications - Structure & Synthesis* Taylor & Francis, 2015.
71. P Sarrazin, D Blake, L Delzeit, M Meyyappan, B Boyer, S Snyder, B Espinosa, Carbon-nanotube field emission x-ray tube for space exploration XRD/XRF instrument. *Advances in X-ray Analysis* **47**, 8, (2004).
72. MT Cole, C Li, Y Zhang, SG Shivareddy, JS Barnard, W Lei, B Wang, D Pribat, GAJ Amaratunga, WI Milne, Hot Electron Field Emission *via* Individually Transistor-Ballasted Carbon Nanotube Arrays. *ACS Nano* **6**, 3236-3242, (2012).
73. HS Kim, D Quang, JH Kim, HJ Lee, DM Yoon, SS Shin, JW Ha, KJ Lee, YG Hwang, CH Lee, Field-Emission Electron Source using Carbon Nanotubes for X-ray Tubes. *Journal of Korean Physical Society* **52**, 3, (2008).
74. MT Cole, KBK Teo, O Groening, L Gangloff, P Legagneux, WI Milne, Deterministic Cold Cathode Electron Emission from Carbon Nanofibre Arrays. *Scientific Reports* **4**, (2014).

75. O Gröning, O Küttel, C Emmenegger, P Gröning, L Schlapbach, Field emission properties of carbon nanotubes. *Journal of Vacuum Science and Technology B* **18**, 665-678, (2000).
76. L Nilsson, O Groening, C Emmenegger, O Kuettel, E Schaller, L Schlapbach, H Kind, J Bonard, K Kern, Scanning field emission from patterned carbon nanotube films. *Applied Physics Letters* **76**, 2071-2073, (2000).
77. S Fujii, S-i Honda, H Machida, H Kawai, K Ishida, M Katayama, H Furuta, T Hirao, K Oura, Efficient field emission from an individual aligned carbon nanotube bundle enhanced by edge effect. *Applied Physics Letters* **90**, -, (2007).
78. JL Killian, NB Zuckerman, DL Niemann, BP Ribaya, M Rahman, R Espinosa, M Meyyappan, CV Nguyen, Field emission properties of carbon nanotube pillar arrays. *Journal of Applied Physics* **103**, -, (2008).
79. P Rai, DR Mohapatra, KS Hazra, DS Misra, SP Tiwari, Nanotip formation on a carbon nanotube pillar array for field emission application. *Applied Physics Letters* **93**, 131921-131921-131923, (2008).
80. JL Silan, DL Niemann, BP Ribaya, M Rahman, M Meyyappan, CV Nguyen, Carbon nanotube pillar arrays for achieving high emission current densities. *Applied Physics Letters* **95**, -, (2009).
81. K Celebi, MT Cole, KBK Teo, HG Park, Observations of Early Stage Graphene Growth on Copper. *Electrochemical and Solid-State Letters* **15**, K1-K4, (2012).
82. K Celebi, MT Cole, JW Choi, F Wyczisk, P Legagneux, N Rupesinghe, J Robertson, KBK Teo, HG Park, Evolutionary Kinetics of Graphene Formation on Copper. *Nano Letters* **13**, 967-974, (2013).
83. H Kim, C Mattevi, MR Calvo, JC Oberg, L Artiglia, S Agnoli, CF Hirjibehedin, M Chhowalla, E Saiz, Activation Energy Paths for Graphene Nucleation and Growth on Cu. *ACS Nano* **6**, 3614-3623, (2012).



# 4 FUNCTIONAL ENHANCEMENTS

In reviewing the published literature relating to X-ray sources using field emission electron sources, it is clear that the technique offers a series of potentially valuable functional enhancements. These features are examined in this chapter.

## 4.1 Beam profiling

A number of publications have reported growth of CNTs, by CVD or similar derivatives, directly onto conical or other shaped tips, on common Spindt-like materials [1], such as silicon [2-4] or bulk metals [5]. As such, these systems do not exploit the full geometric potential of the CNTs; they simply amplify, often only marginally, the existing field enhancement factor of the tip structures and almost always result in an induced asymmetry in the electron beam profile that is challenging to accommodate with conventional electrostatic focussing devices. Indeed, even conventional X-ray TE cathode assemblies will, in general, produce an anisotropic focal spot, as a result of the electron beam dimensions, imperfect focusing, and the impact of the target angle. One potential route to realising symmetrical X-ray sources with defined beam profiles is to shape the cathode such that the emergent electron beam defines, at least in part, the spatial distribution of the resultant X-ray beam. This requires patterning of individual CNTs or CNT forests into well-defined geometries. Several groups have considered the use of

cathode shaping as a mean to achieve beam profiling. Most have used elliptical cathode geometries to define a circular distribution of the emergent X-ray beam [6]. Two examples are as shown in **Figure 12(a, b)**. Shaping has also been shown to enhance the FE performance by exploiting the natively high field enhancement factor at the shaped emitter's edges. In particular, the group of Milne have shown field emission properties of individual CNFs and patterned forests [7-9]. No systematic studies on the effect of shaped cathode eccentricity, or other controlled geometrical parameter, on the symmetry or profiling of the emergent X-ray beam appear to have been considered to date. Indeed, the electrophoretically deposited and photolithographically patterned elliptical cathodes of Calderón-Colón *et al.* [6] showed impressive emission characteristics though no detailed assessment of the emergent beam shape was reported, making it difficult to assess the success of such beam shaping techniques (**Figure 12a**).

Using Si-supported CNT arrays, Ryu *et al.* demonstrated the potential of CVD in X-ray source applications [3]. A resist-assisted patterning process was used to produce a cathode assembly consisting of a gate and focusing electrode. This assembly was approximately 0.5 mm x 2.0 mm and gave an isotropic focal spot [3]. Ryu *et al.* also described a further shaping technique for post processing the as-grown vertically aligned CNTs. Here they used hydrofluoric acid to produce an array of conical pillars (**Figure 12b**), rather reminiscent of earlier Spindt emitters. Hydrofluoric acid, though cheap and readily available, is rather hazardous to handle and poses a significant health risk. This somewhat limits the commercial viability of the compaction technique presented. Nevertheless, they demonstrated anode currents of up to 90 mA at 7.8 V/ $\mu\text{m}$ , with a turn-on electric field of approximately 3 V/ $\mu\text{m}$ . To increase the geometric uniformity of the emitters the team used an electrical aging treatment, similar to annealing, which degrades the taller tubes and bundles that would dominate the emission. For a high performing emitter this aging, also termed seasoning, is not desirable and CNTs of very uniform height and diameter are preferred, as evidenced by Teo *et al.* [10], to obviate the need for such post-growth treatments. Nevertheless, part of the Ryu *et al.* ageing process [3] was to remove the Ni catalyst particles at the CNTs apex, which they argued reduced the emission current. Detailed analysis and theoretical studies of the emission implications of the metallic nanoparticle in the emitter tip are lacking in the literature.

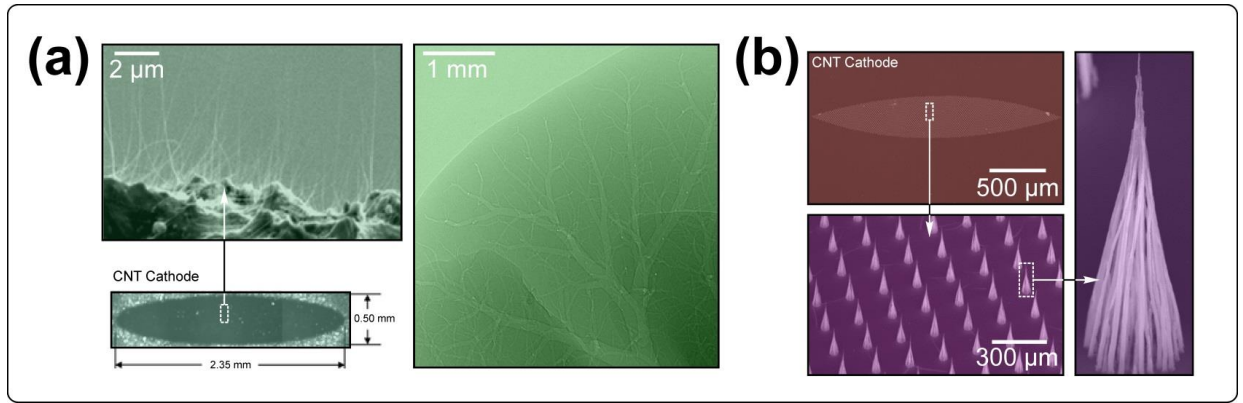


**Figure 12: Shaped CNT cathodes.**

Control over the electron beam distribution, and subsequent symmetry of the X-ray beam, can be achieved by shaping the electron emitting areas on the cathode by conventional lithographic techniques. **(a)** A screen printed elliptical shaped electron emitter and subsequent X-ray image of a leaf [6] (Scale bars: 2  $\mu\text{m}$ , 1 mm). Copyright Institute of Physics. **(b)** Scanning electron micrographs of an elliptical electron source, formed from tepee-like CNTs, demonstrated by Ryu *et al.* (Scale bar: 500  $\mu\text{m}$ , 300  $\mu\text{m}$ ) Adapted from [3], Copyright 2012, Multidisciplinary Digital Publishing Institute.

## 4.2 High beam current

High beam current, and therefore current density, is desirable. This gives rise to higher photon flux, and hence shorter detector integration times, in addition to improved signal-to-noise ratios. Combined with the use of gate control to pulse the X-ray source, high beam currents can be very advantageous to system designers. Recently, micro-fabricated Spindt-like emitters have been used for applications such as static tomography [11]. Here each cathode was formed from approximately 50,000 tips covering an area of about 1  $\text{mm}^2$ . These emitters had a measured current capacity greater than that reported for CNTs, although CNTs will almost certainly exceed this once the technology matures. For current CNT-based sources the emission current density is several orders of magnitude less than that of equivalent area Spindt emitters. Nevertheless, for CNT-based emitters, current densities of up to 1  $\text{A}/\text{cm}^2$  have been reported [12], with studies elsewhere suggesting that individual CNTs are capable of conducting current densities corresponding to  $5 \times 10^6$   $\text{A}/\text{cm}^2$  [13], which is significantly larger than any attained by Spindt-like emitters fabricated to date.

Using electrophoretically deposited SWCNTs [14], high electron beam currents have been achieved using a triode configuration by Yue *et al.* [15]. Here, the gate assembly was mounted approximately 100  $\mu\text{m}$  adjacent to the CNT electron emitter resulting in a device geometry capable of sustaining a beam current of several milliamps, although this would likely prove challenging to manufacture in a practical X-ray source. In addition, they demonstrated peak pulse currents of up to 28 mA (emitted area not stipulated), without vacuum breakdown, at an anode potential of 14 kV. Using CVD grown CNT arrays, Ryu *et al.* [3] reported emission currents of up to 90 mA (emitted area not stipulated) in a diode configuration, although in a gate-controlled triode arrangement, the beam currents were substantially reduced.

Some improvement towards increasing the current density has also been achieved by controlling the emitter morphology. Toroidal CNT arrays, which have a central void [16], are one such example. By subsequent surface treatments, it is also possible to enhance the native FE characteristics of such arrays by means of the formation of nano tips, tepees and micro cones, as outlined previously [3, 17]. The use of emitter forming post-treatments has also been widely investigated. One leading example is the use of conical CNTs [78] which enhanced the beam current and stabilised the emitter geometry. Another alternative towards higher beam currents is to augment the electronic character of the CNTs, via the dry or wet deposition of various adlayers. Such adlayers adjust the interfacial characteristics at the critical emitter-vacuum interface. This often leads to a decrease in the turn-on voltage and increase the emission current density at a given anode bias. As was highlighted above, FE is highly surface sensitive; as an example, at  $10^7$  A/cm<sup>2</sup> for a vacuum arc, a 1% change in the surface work function, can increase the current density by more than 10% [18]. This can be due to intentional adlayer sputtering or indirect sputtering from reactive gas species in the vacuum cavity. Little work has been reported on the use of adlayers to enhance the emission performance of CNT-based FE X-ray sources. Nevertheless, significant advantages may be achieved by carefully designing the emitter-vacuum interface to provide high emission currents, limit adverse effects of vacuum leakage, prevent unintentional work function shifts, as well as creating systems that are robust towards local ionisation and plasma etching, all of which are critical to ensure long term temporal stability.

### 4.3 Enhanced temporal stability

The failure mechanisms of Spindt and CNT based emitters, which are similar in many respects, have been widely studied [19], most notably by Bonard *et al.* [20]. Thermal migration, field sharpening and subsequent avalanche breakdown are perhaps the most common failure mechanism in such whisker-like emission geometries [21]. Although recent work on CNT-based emitters has claimed impressive lifetimes of several thousand hours, with only a 10% emission degradation [22], it remains an on-going challenge to design and fabricate high temporally stable emitters. As noted previously, the electron emission is sensitive to the bulk emitting material and the emitters' surface chemistry. CNTs have a high sublimation temperature and high maximum current densities, making them resilient towards arcing events. Pristine CNTs are also largely inert, although when defects are added to the graphitic lattice, often through plasma processing, they are readily damaged and the dangling bonds that are formed, bolster the CNTs emission performance, usually at the expense of the long term stability. The enhanced emission is due to the augmented surface characteristics. This effect is often noted as a shift to higher turn-on biases during hysteresis studies. Indeed, many plasma and some dopants, such as oxygen when the emitter outgases, can be particularly damaging to the CNTs. Local Ohmic ( $I^2R$ ) heating can also increase the rate of emitter degradation, as too can vacuum breakdown. It has been shown that the axial resistance of CNFs increases with increasing temperature. Interestingly this intrinsic property helps protect the CNFs from degradation during local heating and helps prevent thermal run-away increases in emission current [21]. Vacuum breakdown results in the emission of very high current densities which causes a plausible local oxygen micro-plasma being developed – this etches the CNTs, particularly at their apex. This shaping, and associated plasma etching, stimulates the formation of defects in the graphitic lattice, which preferentially emit electrons, thereby enhancing the emission, however; this results in a temporarily unstable emission profile. The CNTs can be sharpened with time, which tends to increase the emission current, or can alternatively be entirely ablated, which reduces the emission current due to the reduced number of electron emitters available.

There have been various methodologies proposed which attempt to reduce temporal instabilities. Thermal annealing or electrostatic seasoning, to remove residual surfactants and non-uniform emitter profiles, are perhaps the most common, and certainly the most

simple and readily implemented [6]. During thermal annealing the cathode assemblies are heated to temperatures in excess of 300°C under high vacuum conditions. This out-gases the emitter, removing weakly surface bound chemisorbed species which increases the work function uniformity across the surface of the emitter. Such out-gassing techniques are also useful in emitter recovery following an arcing event. Arcing events stimulate high current flow which heats and subsequently out-gases the emitter. This out-gassing can lead to further transient arcs which, if allowed to continue, will degrade the emitter. If the emitter is initially well out-gassed any local arcs will only marginally increase the cavity pressure and the emitter will stabilise more rapidly, as described in Section 6.6. Annealing is also employed to enhance the pressure of the vacuum cavity, making local plasma formation increasingly unlikely. In the case of electrostatic seasoning, the extraction electric field is slowly ramped up to around 80% of the nominal emission voltage. The emitters are then left emitting for tens to hundreds of hours to increase the surface smoothness of the emitter and hence, stabilise the emission current. Such approaches are critical in achieving intrinsic emitter stability, and though feedback techniques have been employed to artificially control the stability, engineering intrinsic stability remains central to the formation of a long-term stable emitter. In feedback based systems, in the same way as conventional TE generator designs, the anode current is monitored and the extraction voltage adjusted accordingly to maintain a known, safe, emission current. Though a viable and widely adopted approach to ensuring emitter stability, the slow response times of the feedback loop cannot entirely remove transient effects, such as arcing events, and only careful design of the electron source can achieve this.

Though CVD is certainly coming to the fore as the most reproducible fabrication technique with the finest degree of control over the emitter design, it, like other techniques, is faced with issues of tip-to-tip uniformity. Poor uniformity in effective surface roughness is known to de-stabilise the temporal stability. Indeed, wet chemistry ink approaches to emitter fabrication result in much greater surface roughness, and this exacerbates and further compromises their temporal stability. Small height variations between tips can instigate preferential emission from a small proportion of the longer CNTs, which consequently burn-out. It has been shown elsewhere that individual CNTs can in practice pass a current of several microamps [23]. Currents in excess of this threshold cause the CNT to sublime, which manifests as a temporal instability in the

anode current, and subsequent X-ray emission. In the case of CVD-synthesised CNT emitters one solution – originally described for application with Spindt emitters [24] and initially proposed for general electron emission applications by [25] – consisted of integrating a ballast resistor micro-fabricated in series with the electron emitter. Here resistive deposited layers are fabricated in series with the electron emitters. The series resistance ballasts the emission, functioning as a current limiting resistance, thereby preventing emitter sublimation and subsequently enhances temporal stability. Yet to be applied immediately to the design of an X-ray source, the group of Milne in Cambridge have developed a novel field effect transistor (FET) ballasted field emission source, where each individual CNF electron source is equipped with its own dedicated FET ballast layer which is capable of limiting, and electronically controlling, the emission current to prevent emitter sublimation and significant temporal instabilities [26]. However, this will inevitably limit the response time of the source. Other thin film deposition techniques have also been considered [27, 28] though these too have yet to gain any significant interest.

Individual CNTs are fragile. Their propensity toward tip or root growth results in an axial asymmetry in their magnetic susceptibility which manifests as rotational torque induction when exposed to high electric fields - an effect which is typically exploited during electrophoretic alignment. However, during FE this can result in the removal and transfer of the CNTs from the cathode to the gate assembly, or the anode. This severely impacts the lifetime and stability of any field emission device into which they are incorporated. Several approaches have been taken to improve the robustness of the emitting elements by increasing the degree of adhesion between the CNTs and the supporting substrate. Bundles of vertically aligned CNTs, or CPAs (CNT Pillar Arrays) - typically with a height of around 10  $\mu\text{m}$  or less, and a diameter of 30  $\mu\text{m}$ , have been shown to be one such robust assembly, that is not readily damaged or easily removed. However, FE preferentially occurs at the periphery of the patterned CNT forest or array [29, 30] suggesting that if some CNTs are in fact removed the emission stability may simply be recovered by new CNTs contributing to the emission current of those removed; emitter areal design can in part accommodate and engineer out temporal instabilities. Nevertheless, there is a continuing effort to engineer the CNT-support interface to enhance the degree of adhesion and hence enhance the temporal stability. In the case of ink approaches various solution additives have been exploited, such as glass frits [6],

though the exact implications of such approaches with regards to the turn-on field and maximum current density remain unclear.

Elsewhere there has been significant work on the use of surface treatments to stabilise the temporal stability of the electron emission [3, 31]. As discussed previously, such low work function adlayers do indeed increase the emission current density, though they also, depending on the adlayer material and means of deposition, hermetically seal the CNTs – which act as a high aspect support structure – thereby increasing the emitters stability [27].

#### 4.4 Micro-focal sources

FE sources have the potential for extremely high spatial modulation. By controlling, the electron emitter location at the nanoscale, coarse control over the position of the electron beam, and subsequent X-ray beam are possible. A range of focussing techniques has also been developed to reduce the electron beam focal spot size. Standard X-ray tubes have a focal spot size of typically around 1 mm diameter. For greater spatial resolution, “mini-focus” X-ray tubes have been developed, with a spot size down to 50  $\mu\text{m}$ , as well as “micro-focus” X-ray tubes with a spot size of  $\sim 5 \mu\text{m}$  [32]. Almost exclusively, X-ray sources with effective focal spot sizes of  $< 10 \mu\text{m}$ , which are commercially available, employ electrostatic or magnetic focussing and require high beam current pulsing techniques, to prevent limitation in their imaging resolution by motion-induced blurring [33]. The size of the electron beam at its source and latterly as it impacts the target material, contributes, in part, to the size of the X-ray focal spot, which itself impacts on the resolution of the resultant X-ray image. A large electron beam focal spot will create a penumbra effect where the X-ray spot subtends a significant angle at the subject; this blurs the resultant image. Conventional X-ray tubes will use a lensing cup around the heated filament assembly. This, to a first order, electrostatically focuses the electrons onto the centre of the anode. Careful design of the cathode and supporting electrostatic lenses will minimise the size of the focal spot [34, 35]. Additionally, further electrostatic rings or focussing coils may also be employed to redirect the flow of electrons emanating from the cathode, to further reduce the spot size, where the focal spot size is determined by measuring the Point Spread Function using standard methods [36].

In just such a way, a transmission CNT X-ray tube with a solenoid focussing unit was constructed by Heo *et al.* to produce a 5  $\mu\text{m}$  focal spot [37]. Liu *et al.* developed a single electrostatic focusing lens to produce a source with a nominal focal spot size of 65  $\mu\text{m}$ , which was further reduced to 35  $\mu\text{m}$  by limiting the dimension of the cathode assembly [38], a concept yet to be fully exploited. A similar mini-focus tube, used for small animal CT work, was also described. This used two focussing electrodes to produce a focal spot size of about 100  $\mu\text{m}$ , using a mesh gate electrode to maximise the electron emission from the cathode [39]. FE tubes with cathodes constructed from CNFs have also incorporated conventional three stage electrostatic Einzel lenses. Such systems have achieved focal spot sizes down to 40  $\mu\text{m}$  [5].

## 4.5 Pulsed sources

A pulse Xray source may be created by :

- Gating or shuttering a CP (constant potential) source such as a thermionic or field emission Xray tube.
- Using a resonant pulse power supply (capable of producing pulses ca. 50ns at 300kVp).
- Using a laser-produced plasma source with electron injection, for sub-nanosecond pulses.
- Synchrotron sources.

In this study, the interest in this work is in the application of gated CP sources. In this case the source is a field emission tube controlled by a gate electrode.

FE sources have the potential for a high level of temporal control. Compared to other one-dimensional nanomaterials, CNTs allow for near ballistic conduction making them ideally suited for such high-speed applications. Pulse X-ray sources are practically beneficial when imaging moving objects. The principle of operation is analogous to stroboscopic lighting in optical imaging. Conventional TE X-ray sources are generally not capable of rapid control; they cannot be pulsed much more rapidly than a few tens of milliseconds, without sophisticated gating mechanisms. The means of controlling the beam current in a TE source is by adjusting the filament current and hence temperature, which introduces

time delays due to the finite cooling and heating time of the filament. Pulse sources are therefore generally implemented by switching the anode voltage, or by means of mechanically controlled shutters, the latter only allowing for relatively coarse control over the pulse shape, or period, and mark-to-space ratio, and will inevitably create a trapezoidal pulse. In the case of existing FE and TE sources, the short duration of the pulse must be compensated by increased power levels, resulting in significant engineering design constraints with regards to the resilience of the emitting material; conventional electron emitting materials degrade rapidly when used in such high power applications.

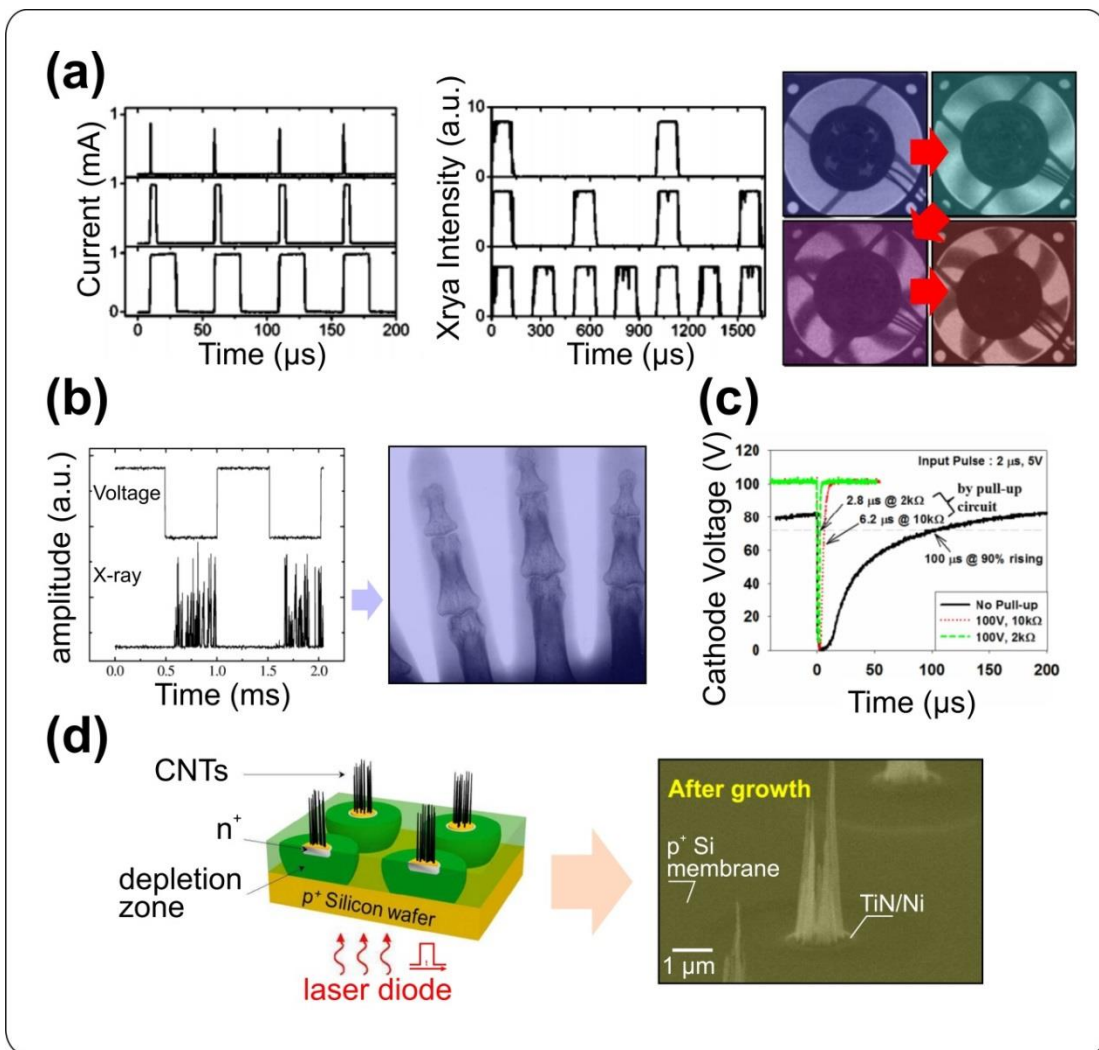


**Figure 13: Pulsed Sources.**

(a) Anode current and X-ray intensity temporal response plots showing an X-ray beam turn-on time of  $< 50 \mu\text{s}$ , and X-ray images of a rotating computer cooling fan acquired at a constant fan angular velocity with decreasing X-ray emission pulse width. Note the

increased sharpness of the fan blades with increasingly rapid beam pulsing [40]. Copyright 2005, Joint Committee on Powder Diffraction Standards. (b) Bias voltage and X-ray emission temporal response plots with an acquired X-ray image of a users hand [15, 41]. Copyright 2003, Elsevier and American Institute of Physics. (c) The time dependence of the cathode voltage with integrated pull-up resistance showing a rise time of  $< 3 \mu\text{s}$  [42]. Copyright 2013, SPIE. (d) Schematic depiction of a red-source photo-gated CNF-based electron source. Each vertically aligned CNF bundle sits on top of a pin+ photodiode coated with a TiN diffusion barrier coated and a Ni catalyst, as illustrated in the scanning electron micrograph taken after the CNT growth (Scale bar:  $1 \mu\text{m}$ ). Adapted from [43]. Copyright 2014, Thales Electron Devices.

In FE X-ray sources often the means of controlling the beam current is via the gate voltage. Depending on the exact emitter geometry, this voltage can be considerably lower than the anode voltage and so at a much lower power level; it can be switched virtually instantaneously. Gate electrodes can certainly be incorporated into more traditional TE sources also, though much more control over the on/off current ratio and pulsing performance can be achieved when using FE sources as the gate and anode can be controlled simultaneously, with both responding equally rapidly. The result is that a FE X-ray source may readily be pulsed with a high on/off current ratio. This lowers the total thermal dissipation, reduces the total amount of emitted radiation – allowing for safer operating conditions in medical diagnostics, and eliminates the need for bulky mechanical components.

Most devices fabricated to date operate in either DC or low frequency (tens of Hz) mode [3, 4, 6, 28, 37, 42, 44-58] with only a very limited set of electronically controlled devices operating at frequencies in excess of a few hundred Hz to a few kHz [15, 40, 59, 60]. The highest electronic pulse rate achieved to date is of the order of  $10^7$  Hz, as reported by Cheng *et al.* [61]. Nevertheless, the pulse rate achieved by Thales [43] in their optically gated devices exceeds all other devices by some significant margin. **Figure 13(a)** shows the anode current and X-ray intensity temporal response by Reyes-Mena *et al.* [40]. Here the X-ray beam 0-90% turn-on time is  $< 50 \mu\text{s}$  and the system is used to image a rotating cooling fan. Images were acquired at a constant fan angular velocity with decreasing X-ray emission pulse width. As the X-ray pulse width decreases the fan blade sharpness increases evidencing the usefulness of beam pulsing in acquiring high resolution images in moving systems. The pulsing of the gate voltage has also been shown to give turn on

times of the order of 100  $\mu\text{s}$  [15, 40]. At an early stage, Yue *et al.* [15], as shown in **Figure 13(b)**, demonstrated peak beam currents of up to 28 mA, at anode potentials of 14 kV, without degradation of the field emitters. An interesting artefact of their rapid pulsing was the chaotic and rather noisy X-ray emission, which showed an approximate periodicity of 100  $\mu\text{s}$ . The noise here must certainly be reduced if a practical device is to be realised.

The limiting factor in many pulsed systems is often the capacitance of the gate assembly. Kim *et al.* [42] showed that pulsing performance could be improved and demonstrated  $< 3 \mu\text{s}$  pulse periods, as indicated by the cathode voltage, via the use of a simple high voltage MOSFET pull-up circuit to switch the cathode, proposing that their pulsed source may find application in angiography. However it is worth noting that such a measure does not correlate with the X-ray photon flux [40]. Liu *et al.* [33], by pulsing the gate bias using a pulse generator with a constant anode bias of 40 kV, showed a stable 0.3 mA temporal response over 15 h with an approximate pulse rise time of  $< 5 \text{ ms}$ . Certainly electronic control over the pulsing performance has some use. Though the bandwidth is dramatically reduced, by at least an order of magnitude, the on/off ratio can be increased and the emitter fabrication simplified. Nevertheless, this is necessarily at the expense of other technological challenges, chiefly the associated RC constant of the vacuum cavity. This RC constant induces intrinsic time delays that are not experienced in the optically stimulated case. As illustrated in **Figure 13(c)**, Kim *et al.* [42] employed 10 k $\Omega$  pull-up resistances to negate RC lag issues. The pulsing performance of arrayed sources has also been considered. Wang *et al.* [4] showed a millisecond temporal response in a matrix source designed for micro radiotherapy. This had an array of 5 x 10 pixels achieving an emission current of 3 mA per pixel.

In order to obviate issues associated with the devices RC time constants, as depicted in **Figure 13(d)**, Thales Electron Devices have demonstrated even higher pulse rates by exploiting integrated photodiodes and direct optical excitation. Vertically aligned CNFs were grown on p-i-n<sup>+</sup> photodiodes on a back etched Si membrane. CNFs were grown on n<sup>+</sup> doped areas defined by ion implantation in a 5  $\mu\text{m}$  thick intrinsic layer, whilst the p<sup>+</sup> doped silicon wafer was subsequently thinned to obtain the 7  $\mu\text{m}$  thick membrane [43]. These arrayed emitters were then irradiated, over the entire emitter area, with red laser

light allowing them to attain high bandwidth and on-off ratio of around 10, and a maximum on current of around  $100 \mu\text{A}/\text{cm}^2$ .

The availability of rapidly pulsed sources opens up the potential for high-speed, real-time inspection technologies, capable of coupling high throughput, on-line manufacturing with real-time inspection. Indeed, with controlled high pulse rates the potential to perform medical diagnostics without strict patient restraints is considered, allowing inspection of dynamic organs without image blurring due to the intrinsic motion of quasi-periodic respiration and heart beats, for example. One possible approach considered is to lock the gate electrode pulsing to the patients' cardiac or respiration rate. Such motion-induced artefacts can thus be reduced as the X-ray exposure is synchronised with a patients physiological rhythm, or indeed the motion of an object [33].

## 4.6 Static tomography & tomosynthesis

X-ray based Computed Tomography (CT) imaging is fundamental to medical diagnostics. However, at present such imaging devices are affected by long scan times. Enabled by advances in computer and detection technologies, integration time issues are exacerbated when considered in relation to the concept of real-time 3D X-ray imaging. Multi-pixel sources offer one viable solution. Multi-pixel sources present a unique opportunity in next-generation inspection techniques, especially when considering the physically small cathode of CNT FE sources, and the potential for nano-engineering and rapid switching. Pulsed multi-pixel sources give rise to a potential solution to a series of previously challenging applications typically relating to real-time medical diagnostics [62].

Tomography relies on the acquisition of large numbers of images, whilst viewing a subject at a range of angles. These systems, at present, incorporate X-ray sources and detectors on a rotating gantry, which allows the system to capture an array of independent images, as a result of the physically rotating components, patients, or samples on an expensive and bulky mechanical system. The emerging alternative is to have multiple, distributed X-ray sources which are sequentially switched. Here, the subject remains stationary with the added benefit of more rapid data acquisition and potentially higher image quality. Indeed, such systems are largely immune to image blurring, which persists in conventional moving-source systems.

A range of different approaches to the application of tomography or tomosynthesis have been presented. The University of North Carolina, Chapel Hill, illustrated in **Figure 14(a)**, have demonstrated high-resolution stationary tomosynthesis using 31 individually addressed CNT X-ray sources distributed within a single large vacuum enclosure [62]. Each source had a 0.6 mm focal spot size, was operated at 28 kV at an anode current of 38 mA. Though an excellent demonstrator of the potential of CNT-based multi-pixel sources, the system is extremely large and fails to fully exploit the potential of emerging CVD techniques to pattern multiple sources on a single chip as a means to facilitate miniaturisation. Nevertheless, the system is at present one of the most advanced of the CNT-based FE X-ray sources yet reported. It is based on physically separate CNT ink deposited thin films with inter-emitter pitches of the order of a few tens of centimetres. The system has also demonstrated real-time 3D image reconstruction. **Figure 14(b)** shows another stationary computed tomography system by North Carolina. This system consists of 4 cathode banks, with a total of 52 separate cathode assemblies. Though rather large and limited to stationary or slow moving objects, this prototype system is the first in a new wave of CNT-based real-time 3D tomosynthesis scanners.

High spatial resolution requires a small X-ray spot size. However, practical systems also require a wide field of view in order to be able to inspect suitably large areas. Thus, to realise high resolution large area scans the X-ray source must be constructed from multiple cathodes, each with focussing electrodes. One way to maximise the field of view is to carefully engineer the vacuum chamber to maximise the total angular field of view. A 5 source system has been constructed by Zhang *et al.* [63]. Their system provided sequentially acquired images over a finite angular range, each fitted with an electrostatic focusing electrode to control the size and scanning of the focal spot, which has a width of less than 300  $\mu\text{m}$ . Operating at 40 kV, they showed that the electronic switching time was largely negligible with high emission reproducibility, both in FE curves and beam diameter, between the individual electron sources. Yang *et al.* demonstrated a multiple source digital breast tomosynthesis unit using an array of 25 cathodes, each individually programmed using analogue controls. Their sources employed CNT-based inks, each with a dedicated gate and an electrostatic focusing ring to control the focal spot size to approximately 200  $\mu\text{m}$  [64]. In this system an impressive total angular field of view of up to 48° was realised, and the performance compared favourably with commercially

available moving-source systems. A similar system, termed a multi-beam FE X-ray source, described a similar geometry [59]. A simple linear multiple source using an array of 31 CNT FE cathodes has also been constructed, for the purposes to digital breast tomosynthesis, which was shown to be capable of a total scan angle of  $30^\circ$  [48]. In a further extension, a digital chest tomosynthesis scanner was demonstrated [65]. This system used 75 CNT FE sources, operating at up to 80 kV with a  $20^\circ$  beam angle.

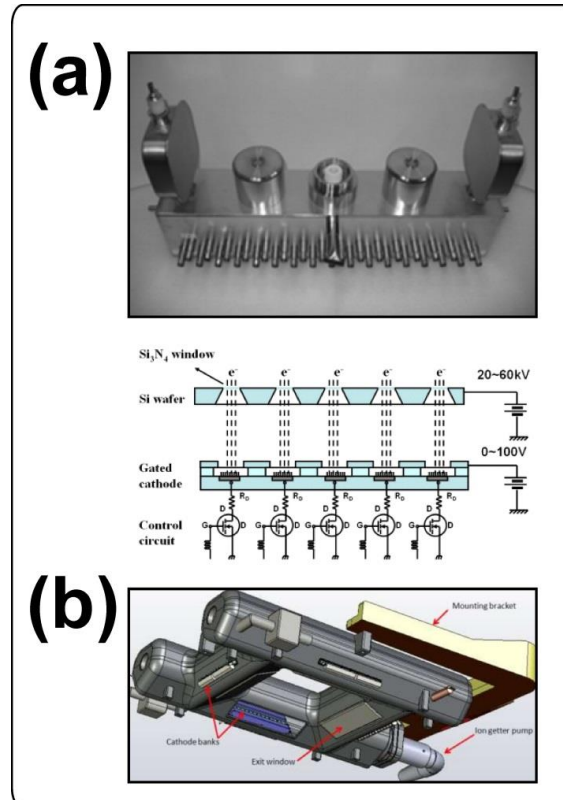


**Figure 14: CNT-based tomosynthesis systems.**

(a) A distributed CNT tomosynthesis unit consisting of 31 individually addressable X-ray sources enclosed in a single vacuum chamber, and below a schematic the corresponding drive circuitry. Adapted from [62]. Copyright 2012, American Association of Physicists in Medicine. (b) An actively pumped multi-pixel X-ray source consisting of 52 individually controlled sources. Courtesy of the University of North Carolina at Chapel Hill [66].

## 4.7 Multi-pixel sources

In the majority of the multi-pixel systems discussed above, the electron sources have largely been constructed using individual cathodes fabricated in linear arrays. A two

dimensional geometry based on a series of linear arrays in a square or hexagonal format of physically separate detectors and sources, has been evaluated using simulation. Such a system is highly manufacturable [67], however; the inspection technique relies on close alignment of the generators and detectors which will be challenging. Guzilov *et al* [68] have proposed circular arrays of FE emitters to emulate the classical rotary gantries used for CT, although their practical implementation has been limited to staggered linear arrays. Two dimensional arrays have a number of advantages over their linear counterparts, chief amongst which is the potential for ad hoc beam shaping of the emergent X-rays. Micro-integration of two dimensional source arrays allows for higher spatial resolution and the required ad hoc beam shaping. Such micro-integrated two dimensional FE source arrays have been realised, though only few such devices have been investigated. **Figure 15(a)** depicts a 5 x 10 electron beam array fabricated by Wang *et al.* [4], as mentioned above. Deposited using screen printing techniques (**Figure 15(b)**), the 50 individually addressable electron beams allow for arbitrarily defined, and ad-hoc selectable electron and hence X-ray beam shapes, for application in radiotherapy. An example of an ad hoc beam shaped, electronically defined, X-ray intensity distribution is illustrated in the bottom image of **Figure 15(c)**. A dose rate of 1.24 Gy/min at the centre of the irradiated object was obtained at an emission current of 3.0 mA [4]. High energy sources for tomosynthesis based on such multi-pixel sources, with high anode potentials of up to 160 kV, have also been demonstrated by Sprenger *et al.* [69]. This was achieved using a square array of 4 x 13 electron sources for applications including image guided radiotherapy.

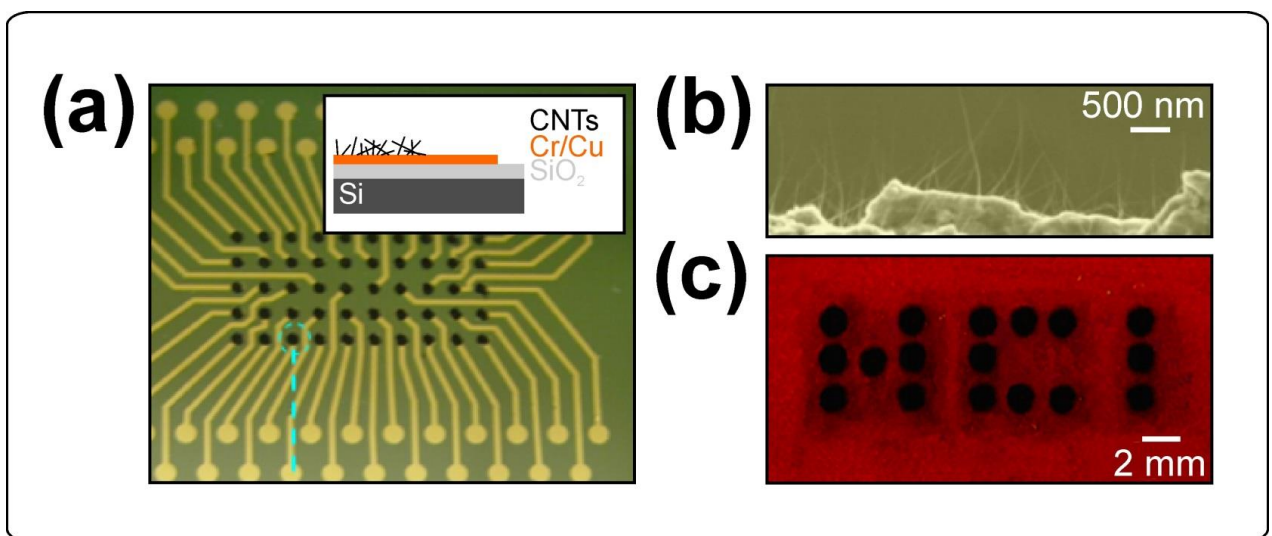


**Figure 15: Multi Pixel Sources.**

(a) Electrophoretically deposited multiple X-ray source chip and the corresponding (b) scanning electron micrograph of deposited CNTs, and (c) the resulting electronically reconfigurable X-ray distribution. Adapted from [4]. Copyright 2011, American Institute of Physics.

## 4.8 Compact & miniature sealed tubes

X-ray generators are often bulky devices, as a result of the dissipation and consequently the cooling requirements. Certain user requirements necessitate a greater of miniaturisation, with various industries defining requirements for physically small X-ray sources. Miniaturised sources find use in hand-held non-destructive testing, X-ray spectroscopy, electrically controlled brachytherapy and *in situ* radiation therapy. Miniature TE sources have been available for many years, but can prove challenging to design and engineer [70], Amptek launched a series of X-ray sources [71]. Sealed FE sources, on the other hand, lend themselves to these applications, and in particular are well suited for portable X-ray applications. Though difficult to manufacture, miniaturised sources are emerging on the market place. As in the case of pulsed and multi-pixel sources, much progress has been made towards a miniaturised CNT-based FE X-ray source though, to the best of the author's knowledge, no such devices have, as yet, made it to market.

One of the smallest tubes fabricated, at the time of this thesis, as far as the author is aware, is that of the Electronics and Telecommunications Research Institute, Korea (**Figure 16(a)**). This cylindrical diode source, which is smaller than the average human finger, has an impressive outer diameter of only 6 mm and a length of 31 mm, and is based on CNTs deposited by a paste printing technique [52, 72]. Developed for miniaturised X-ray diffractometry, the X-ray source of Sarrazin *et al.* [49], **Figure 16(b)**, can support current densities of up to  $1 \text{ A/cm}^2$ , whilst Heo *et al.* [51], who demonstrated a 10 mm diameter and 50 mm long miniature source, as illustrated in **Figure 16(c)**, derived around  $0.12 \text{ A/cm}^2$ . The sealed device can be operated up to 70 kV. The cathode was formed from sintered SWCNTs mixed with Ag nanoparticles to form a paste which was deposited on a flattened, 0.8 mm diameter, W wire. Here a conically machined Be window was magnetron sputtered with  $1.5 \mu\text{m}$  W thin film forming a transmission type target. The vacuum brazed alumina tube with Kovar electrodes and non-evaporable getter

weighs just 14.5 g. The anode voltage to produce a field required to extract  $10 \text{ mA/cm}^2$  was 29 kV, with a maximum current density of  $0.12 \text{ A/cm}^2$ , giving a nominal stability of  $\pm 2\%$  at 50 kV, with a similar variation in the X-ray dose. Radially, the X-ray dose rate was  $108 \text{ Gy/min}$  and was broadly isotropic (20% variation) with a typical focal spot size of the order of 3-4 mm. Serious heating prevented the source from being operated for significant lengths of time at the maximum anode bias. Kim *et al.* [42], as shown in **Figure 16(d)**, have developed a similar brazed compact sealed source, measuring just 3.5 cm in diameter and 7.5 cm in length. This pentode device - consisting of a cathode, gate, two focusing electrodes, and an anode - had a focal spot of the order of  $300 \mu\text{m}$  in diameter when operated with an anode current of 50 mA. The CNT cathode was just  $0.15 \text{ cm}^2$  and was formed from a screen-printed and ball-milled complex CNT paste combined with inorganic fillers, oxides, metallic nano particles and a photo-initiator monomer with organic components including acrylates. The CNT films were relatively uniform between samples, in macroscopic terms, although rather perturbed and irreproducible microscopically. No active pumping system was integrated, though a non-evaporable getter was fabricated in an attempt to maintain the vacuum environment. The tube pressure was only of the order of  $10^{-6} \text{ mbar}$  upon sealing. The cavity pressure during emission was not noted. Pulse mode operation (10% duty cycle) was opted for - at 30 kV and 10 mA, to reduce thermally stimulated outgassing. Nevertheless, the tube still operated at approximately  $200^\circ\text{C}$  which almost certainly compromised the vacuum, even for a previously well-outgassed cathode assembly. **Figure 16(e)** shows the Oxford Instruments X-ray Technology Inc. miniature MWCNT FE X-ray tube with a 2 mm diameter cathode and integrated gate. The device develops a somewhat asymmetrical and diffuse focal spot with a major axis length of the order of  $700 \mu\text{m}$  [49]. This device is no longer produced as the manufacturer was unable to achieve an acceptable reliability and lifetime specification.

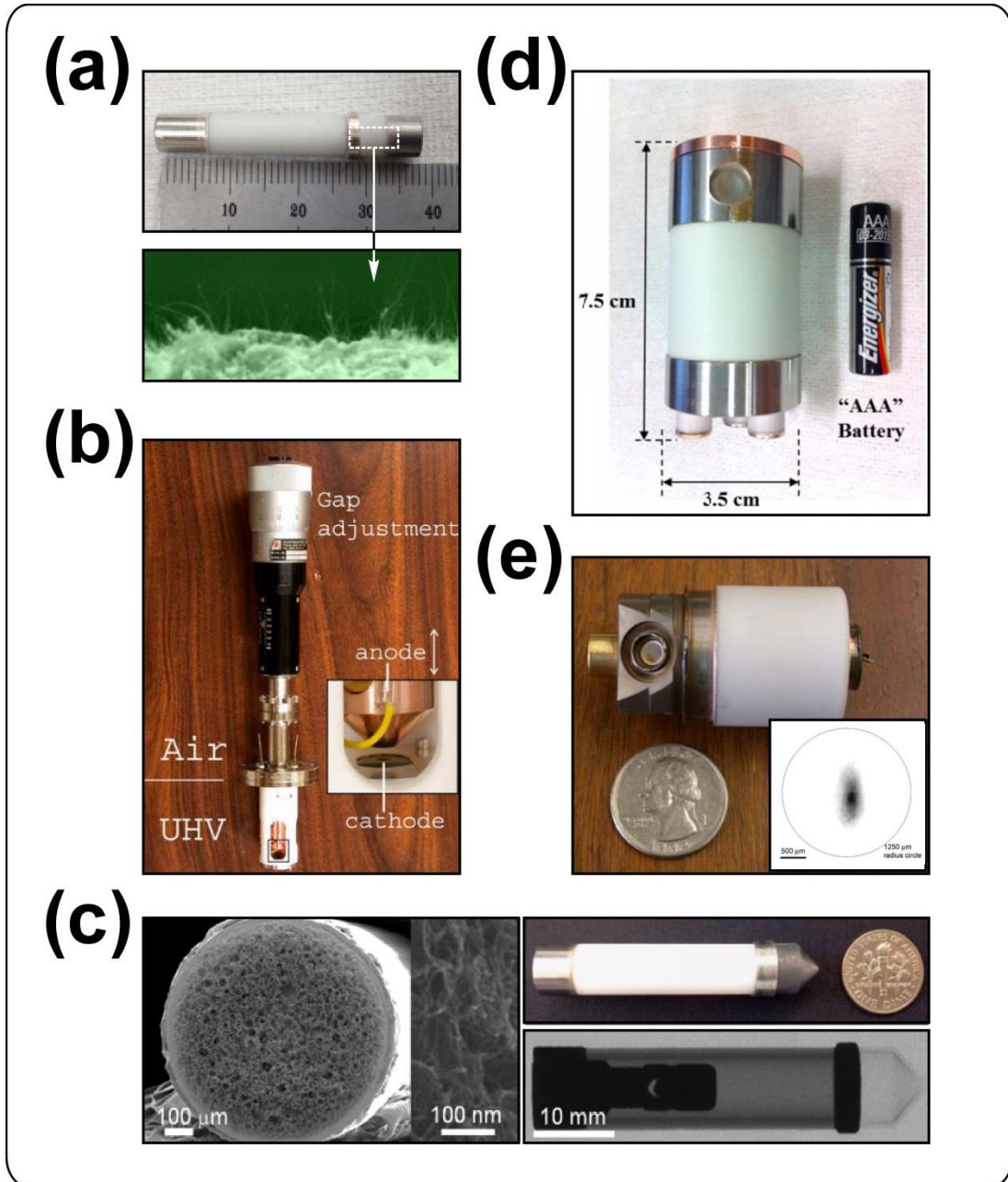


**Figure 16: Miniature CNT-based FE X-ray sources.**

(a) A disordered miniature CNT, brazed triode X-ray source fabricated by ball milling, and firing of a CNT paste on the apex of a 0.6 mm Kovar rod, and operated at 12 kV [72]. Copyright 2013, Electronics and Telecommunications Research Institute. [52]. Copyright 2013, American Institute of Physics (b) A miniature X-ray source fabricated by thermal CVD capable of supporting current densities of up to 1 A/cm<sup>2</sup> [49]. Copyright 2004, Joint Committee on Powder Diffraction Standards. (c) A sintered SWCNT paste transmission-type miniature CNT cathode X-ray source, weighting 14.5g, and operating up to 70 kV with uniform spatial dose distribution [51]. Copyright 2012, Springer. (d) A 7.5 cm long sealed CNT-based X-ray source operating at 30 kV. [42]. Copyright 2013, Society of Photo-Optical Instrumentation Engineers. (e) An

Oxford Instruments X-ray Technology Inc. miniature field emission X-ray tube with gated MWCNT 2 mm diameter cathode. Adapted from [73]. Copyright 2004, Joint Committee on Powder Diffraction Standards.

## 4.9 Use of adlayers

One of the most interesting strategies to further optimise the performance of the emitters, is the coating of materials, or adlayers, on the nano-scaffolds. Although the largely empirical data from the paper review provided in **Appendix 2** indicates that the aspect ratio is the more significant factor in field emission, the use of adlayers to get a reduced work function will clearly assist in promoting emission at lower electric fields.

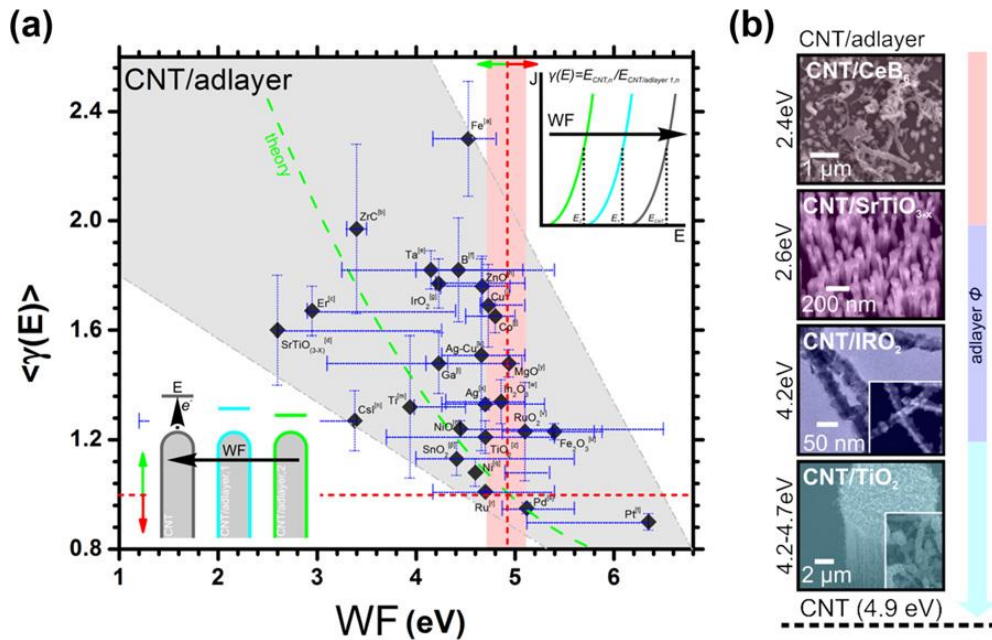


**Figure 17: Use of adlayers to reduce work function**

(a) Enhancement of carbon nano-based electron sources as a function of adlayer work function (WF). (b) Scanning electron micrographs of various adlayers on carbon nanotube scaffolds. Adapted from [74].

**Figure 17** summarises some of the more common adlayers considered to date. Such approaches benefit from the morphological advantages of the nanomaterial, whilst also exploiting the electronic characteristics of the otherwise planar adlayer. The composite material functions better than either of the individual components. Indeed, the exploitation of the novel properties of various nanomaterials allow for new device geometries capable of enhanced function, such as the use of graphene as a highly

transparent gate electrode [75]. This general approach of combining nanomaterials has also led to the development of hermetically sealed emitters with structured adlayers that have been shown to both reduce the turn-on field and also to enhance emission stability [76, 77]. Though certainly for the functional improvement of these devices, such multi-nanomaterial systems further compounds issues relating to challenging manufacturing.

## 4.10 Conclusions

X-ray generators incorporating field emission electron sources, offer a wide range of functional benefits to the system designer. In particular, the high level of controllability and control over the geometry of the devices open the door to many exciting possibilities.

## 4.11 References

1. C-K Park, J-P Kim, S-J Yun, S-H Lee, J-S Park, Field emission properties of carbon nanotubes grown on a conical tungsten tip for the application of a microfocus x-ray tube. *Thin Solid Films* **516**, 304-309, (2007).
2. K Teo, M Chhowalla, G Amaratunga, W Milne, G Pirio, P Legagneux, F Wyczisk, D Pribat, D Hasko, Field emission from dense, sparse, and patterned arrays of carbon nanofibers. *Applied Physics Letters* **80**, 2011-2013, (2002).
3. J Ryu, J Kang, K Park, Carbon Nanotube Electron Emitter for X-ray Imaging. *Materials* **5**, 2353-2359, (2012).
4. S Wang, X Calderon, R Peng, EC Schreiber, O Zhou, S Chang, A carbon nanotube field emission multipixel X-ray array source for microradiotherapy application. *Applied Physics Letters* **98**, 213701-213703, (2011).
5. W Sugimoto, S Sugita, Y Sakai, H Goto, Y Watanabe, Y Ohga, S Kita, T Ohara, A fine-focusing x-ray source using carbon-nanofiber field emitter. *Journal of Applied Physics* **108**, 044507-044506, (2010).
6. X Calderón-Colón, H Geng, B Gao, L An, G Cao, O Zhou, A carbon nanotube field emission cathode with high current density and long-term stability. *Nanotech.* **20**, 325707, (2009).
7. MT Cole, KBK Teo, O Groening, L Gangloff, P Legagneux, WI Milne, Deterministic Cold Cathode Electron Emission from Carbon Nanofibre Arrays. *Scientific Reports* **4**, (2014).
8. V Merkulov, D Lowndes, Y Wei, G Eres, E Voelkl, Patterned growth of individual and multiple vertically aligned carbon nanofibers. *Applied Physics Letters* **76**, 3555-3557, (2000).
9. MK Debe Field emission device having nanostructured emitters. Google Patents, 1998.
10. KBK Teo, SB Lee, M Chhowalla, V Semet, VT Binh, O Groening, M Castignolles, A Loiseau, G Pirio, P Legagneux, D Pribat, DG Hasko, H Ahmed, GAJ Amaratunga, WI Milne, Plasma enhanced chemical vapour deposition carbon nanotubes/nanofibres - how uniform do they grow? *Nanotechnology* **14**, 204-211, (2003).

11. PR Schwoebel, JM Boone Stationary x-ray source for tomographic medical imaging. 2006; pp 61423N-61423N-61423.
12. WI Milne, KBK Teo, E Minoux, O Groening, L Gangloff, L Hudanski, J-P Schnell, D Dieumegard, F Peauger, IYY Bu, MS Bell, P Legagneux, G Hasko, GAJ Amaratunga, Aligned carbon nanotubes/fibers for applications in vacuum microwave amplifiers. *Journal of Vacuum Science and Technology B* **24**, 345-348, (2006).
13. E Minoux, O Greening, KBK Teo, SH Dalai, L Gangloff, JP Schnell, L Hudanski, IYY Bu, P Vincent, P Legagneux, GAJ Amaratunga, WI Milne, Achieving high-current carbon nanotube emitters. *Nano Letters* **5**, 2135-2138, (2005).
14. B Gao, GZ Yue, Q Qiu, Y Cheng, H Shimoda, L Fleming, O Zhou, Fabrication and electron field emission properties of carbon nanotube films by electrophoretic deposition. *Advanced materials* **13**, 1770-1773, (2001).
15. GZ Yue, Q Qiu, B Gao, Y Cheng, J Zhang, H Shimoda, S Chang, JP Lu, O Zhou, Generation of continuous and pulsed diagnostic imaging x-ray radiation using a carbon-nanotube-based field-emission cathode. *Applied Physics Letters* **81**, 355-357, (2002).
16. JL Silan, DL Niemann, BP Ribaya, M Rahman, M Meyyappan, CV Nguyen, Carbon nanotube pillar arrays for achieving high emission current densities. *Applied Physics Letters* **95**, -, (2009).
17. P Rai, DR Mohapatra, KS Hazra, DS Misra, SP Tiwari, Nanotip formation on a carbon nanotube pillar array for field emission application. *Applied Physics Letters* **93**, 131921-131921-131923, (2008).
18. F Charbonnier, Developing and using the field emitter as a high intensity electron source. *Applied Surface Science* **94**, 26-43, (1996).
19. R Forman, Evaluation of the emission capabilities of Spindt-type field emitting cathodes. *Applications of Surface Science* **16**, 277-291, (1983).
20. J-M Bonard, C Klinke, KA Dean, BF Coll, Degradation and failure of carbon nanotube field emitters. *Physical Review B* **67**, 115406, (2003).
21. WI Milne, KBK Teo, GAJ Amaratunga, P Legagneux, L Gangloff, JP Schnell, V Semet, VT Binh, O Groening, Carbon nanotubes as field emission sources. *Journal of Materials Chemistry* **14**, 933-943, (2004).
22. C Spindt, I Brodie, L Humphrey, E Westerberg, Physical properties of thin-film field emission cathodes with molybdenum cones. *Journal of Applied Physics* **47**, 5248-5263, (2008).
23. M Doytcheva, M Kaiser, Nd Jonge, In situ transmission electron microscopy investigation of the structural changes in carbon nanotubes during electron emission at high currents. *Nanotechnology* **17**, 3226, (2006).
24. S Itoh, Current status of the Spindt-type field emitter. *Proc. ISDEIV* **2**, 875-876, (2006).
25. MT Cole, C Li, Y Zhang, SG Shivareddy, JS Barnard, W Lei, B Wang, D Pribat, GAJ Amaratunga, WI Milne, Hot Electron Field Emission *via* Individually Transistor-Ballasted Carbon Nanotube Arrays. *ACS Nano* **6**, 3236-3242, (2012).

26. C Li, Y Zhang, MT Cole, SG Shivareddy, JS Barnard, W Lei, B Wang, D Pribat, GAJ Amaratunga, WI Milne, Hot Electron Field Emission via Individually Transistor-Ballasted Carbon Nanotube Arrays. *ACS Nano* **6**, 3236-3242, (2012).
27. C Li, Y Zhang, M Mann, P Hiralal, HE Unalan, W Lei, BP Wang, DP Chu, D Pribat, GAJ Amaratunga, WI Milne, Stable, self-ballasting field emission from zinc oxide nanowires grown on an array of vertically aligned carbon nanofibers. *Applied Physics Letters* **96**, 143114-143113, (2010).
28. Y Sun, DA Jaffray, TW Yeow, The Design and Fabrication of Carbon-Nanotube-Based Field Emission X-Ray Cathode With Ballast Resistor. *IEEE Transactions on Electron Devices* **60**, 7, (2013).
29. S Fujii, S-i Honda, H Machida, H Kawai, K Ishida, M Katayama, H Furuta, T Hirao, K Oura, Efficient field emission from an individual aligned carbon nanotube bundle enhanced by edge effect. *Applied Physics Letters* **90**, -, (2007).
30. JL Killian, NB Zuckerman, DL Niemann, BP Ribaya, M Rahman, R Espinosa, M Meyyappan, CV Nguyen, Field emission properties of carbon nanotube pillar arrays. *Journal of Applied Physics* **103**, -, (2008).
31. Y Liu, L Gao, A study of the electrical properties of carbon nanotube-NiFe<sub>2</sub>O<sub>4</sub> composites: Effect of the surface treatment of the carbon nanotubes. *Carbon* **43**, 47-52, (2005).
32. J Madsen, Focal spot size measurements for microfocus X-ray sets. *NDT international* **22**, 292-296, (1989).
33. Z Liu, G Yang, YZ Lee, D Bordelon, J Lu, O Zhou, Carbon nanotube based microfocus field emission x-ray source for microcomputed tomography. *Applied Physics Letters* **89**, 1-3, (2006).
34. W Ehrenberg, WE Spear, An Electrostatic Focusing System and its Application to a Fine Focus X-Ray Tube. *Proceedings of the Physical Society. Section B* **64**, 67, (1951).
35. BM Moores, P Brubacher, Focal spot studies and electron focusing in a demountable X-ray tube. *Physics in Medicine and Biology* **19**, 605, (1974).
36. ASfTaM Philadelphia, Standard Test Method for Measurement of Focal Spots of Industrial X-Ray Tubes by Pinhole Imaging. Annual book of ASTM standards **ASTM-E-1165-12**, (2010).
37. SH Heo, A Ihsan, SO Cho, Transmission-type microfocus x-ray tube using carbon nanotube field emitters. *Applied Physics Letters* **90**, 183109-183103, (2007).
38. Z Liu, J Zhang, G Yang, Y Cheng, O Zhou, J Lu, Development of a carbon nanotube based microfocus x-ray tube with single focusing electrode. *Review of Scientific Instruments* **77**, 054302-054306, (2006).
39. S Sultana, X Calderón-Colón, G Cao, O Zhou, J Lu Design and characterization of a carbon-nanotube-based micro-focus x-ray tube for small animal imaging. 2010; pp 76225G-76225G-76229.
40. A Reyes-Mena, C Jensen, E Bard, DC Turner, K Erdmann, Q Qiu, B Gao, J Lu, O Zhou, Miniature X-ray tubes utilizing carbon-nanotube-based cold cathodes. *Advances in X-ray Analysis* **48**, 204-209, (2005).

41. Y Cheng, O Zhou, Electron field emission from carbon nanotubes. *Comptes Rendus Physique* **4**, 1021-1033, (2003).
42. J-W Kim, J-W Jeong, J-T Kang, S Choi, J Choi, S Ahn, Y-h Song A digital compact x-ray tube with carbon nanotube field emitters for advanced imaging systems. In *SPIE Medical Imaging*; International Society for Optics and Photonics, 2013; pp 861-866.
43. P Legagneux, P Ponard, L Gangloff, S Xavier, C Bourat, J Martinez, CS Cojocar, A Gohier, JP Mazellier, JP Schnell, D Pribat, KBK Teo Carbon nanotube photocathodes for optically driven multiple X-ray sources.
44. J Zhang, Y Cheng, YZ Lee, B Gao, Q Qiu, WL Lin, D Lalush, JP Lu, O Zhou, A nanotube-based field emission X-ray source for microcomputed tomography. *Review of Scientific Instruments* **76**, -, (2005).
45. Y Sakai, A Haga, S Sugita, S Kita, S-I Tanaka, F Okuyama, N Kobayashi, Electron gun using carbon-nanofiber field emitter. *Review of Scientific Instruments* **78**, -, (2007).
46. W Sugimoto, S Sugita, Y Sakai, H Goto, Y Watanabe, Y Ohga, S Kita, T Ohara, A fine-focusing X-ray source using carbon-nanofiber field emitter. *Journal of Applied Physics* **108**, -, (2010).
47. J Zhang, G Yang, YZ Lee, S Chang, JP Lu, O Zhou, Multiplexing radiography using a carbon nanotube based x-ray source. *Applied Physics Letters* **89**, -, (2006).
48. F Sprenger, X Calderon, E Gidcumb, J Lu, X Qian, D Spronk, A Tucker, G Yang, O Zhou Stationary digital breast tomosynthesis with distributed field emission x-ray tube. 2011; pp 79615I-79615I-79616.
49. P Sarrazin, D Blake, L Delzeit, M Meyyappan, B Boyer, S Snyder, B Espinosa, Carbon-nanotube field emission x-ray tube for space exploration XRD/XRF instrument. *Advances in X-ray Analysis* **47**, 8, (2004).
50. A Haga, S Senda, Y Sakai, Y Mizuta, S Kita, F Okuyama, A miniature x-ray tube. *Applied Physics Letters* **84**, 2208-2210, (2004).
51. SH Heo, HJ Kim, JM Ha, SO Cho, A vacuum-sealed miniature X-ray tube based on carbon nanotube field emitters. *Nano Research Letters* **7**, 5, (2012).
52. J-W Jeong, J-T Kang, S Choi, J-W Kim, S Ahn, Y-H Song, A digital miniature x-ray tube with a high-density triode carbon nanotube field emitter. *Applied Physics Letters* **102**, (2013).
53. P Sarrazin, D Blake, L Delzeit, M Meyyappan, B Boyer, S Snyder, B Espinosa, Carbon-nanotube field emission X-ray tube for space exploration XRD/XRF instrument. *Advances in X-ray Analysis* **47**, 232-239, (2004).
54. H Sugie, M Tanemura, V Filip, K Iwata, K Takahashi, F Okuyama, Carbon nanotubes as electron source in an x-ray tube. *Applied Physics Letters* **78**, 2578-2580, (2001).
55. S Senda, M Tanemura, Y Sakai, Y Ichikawa, S Kita, T Otsuka, A Haga, F Okuyama, New field-emission x-ray radiography system. *Review of Scientific Instruments* **75**, 1366-1368, (2004).
56. HS Kim, D Quang, JH Kim, HJ Lee, DM Yoon, SS Shin, JW Ha, KJ Lee, YG Hwang, CH Lee, Field-Emission Electron Source using Carbon Nanotubes for X-ray Tubes. *Journal of Korean Physical Society* **52**, 3, (2008).

57. S Kita, Y Watanabe, A Ogawa, K Ogura, Y Sakai, Y Matsumoto, Y Isokane, F Okuyama, T Nakazato, T Otsuka, Field-emission-type X-ray source using carbon-nanofibers. *Journal of Applied Physics* **103**, -, (2008).
58. J-W Kim, J-W Jeong, J-T Kang, S Choi, S Ahn, Y-H Song, Highly reliable field electron emitters produced from reproducible damage-free carbon nanotube composite pastes with optimal inorganic fillers. *Nanotechnology* **25**, (2014).
59. X Qian, R Rajaram, X Calderon-Colon, G Yang, T Phan, DS Lalush, J Lu, O Zhou, Design and characterization of a spatially distributed multibeam field emission X-ray source for stationary digital breast tomosynthesis. *Medical Physics* **36**, 4389-4399, (2009).
60. TT Tan, HS Sim, SP Lau, HY Yang, M Tanemura, J Tanaka, X-ray generation using carbon-nanofiber-based flexible field emitters. *Applied Physics Letters* **88**, -, (2006).
61. Y Cheng, J Zhang, YZ Lee, B Gao, S Dike, W Lin, JP Lu, O Zhou, Dynamic radiography using a carbon-nanotube-based field-emission X-ray source. *Review of Scientific Instruments* **75**, (2004).
62. X Qian, A Tucker, E Gidcumb, J Shan, G Yang, X Calderon-Colon, S Sultana, J Lu, O Zhou, D Spronk, F Sprenger, Y Zhang, D Kennedy, T Farbizio, Z Jing, High resolution stationary digital breast tomosynthesis using distributed carbon nanotube x-ray source array. *Medical Physics* **39**, 2090-2099, (2012).
63. J Zhang, G Yang, YZ Lee, Y Cheng, B Gao, Q Qiu, JP Lu, O Zhou A multi-beam x-ray imaging system based on carbon nanotube field emitters. 2006; pp 614204-614204-614208.
64. G Yang, R Rajaram, G Cao, S Sultana, Z Liu, D Lalush, J Lu, O Zhou, Stationary digital breast tomosynthesis system with a multi-beam field emission x-ray source array. 69131A-69131A, (2008).
65. J Shan, P Chtcheprov, AW Tucker, YZ Lee, X Wang, D Foos, MD Heath, J Lu, O Zhou Stationary chest tomosynthesis using a CNT x-ray source array. 2013; pp 86680E-86680E-86612.
66. SX Chang, O Zhou Carbon Nanotubes Field Emission X-ray for Research and Clinical Applications in Radiation Oncology - <http://amos3.aapm.org/abstracts/pdf/77-22629-310436-91429.pdf> [Online]. University of North Carolina at Chapel Hill, (accessed 19/08/2014, 2014).
67. E Quan, DS Lalush Three-dimensional imaging properties of rotation-free square and hexagonal micro-CT systems. 2009; pp 72580I-72580I-72510.
68. IA Guzilov, KV Kuzmich, OY Maslennikov, EV Smirnova, PV Minakov, AY Poroykov, AT Rakhimov, B Seleznev, VV Sen Multi beam X-ray tube with the field emitter on the base of nanocrystalline graphite for computer tomography. In *Vacuum Electronics Conference, 2009. IVEC '09. IEEE International*, 2009; pp 289-291.
69. F Sprenger, X Calderon-Colon, Y Cheng, K Englestad, J Lu, J Maltz, A Paidi, X Qian, D Spronk, S Sultana, G Yang, O Zhou, Distributed source x-ray tube technology for tomosynthesis imaging. 76225M-76225M, (2010).
70. S Xray, <http://www.source1xray.com/index-2.html>. (2000).
71. Amptek Miniature X- Ray Source. 2013.
72. J-T Kang, J-W Kim, JW Jeong, S Choi, J Choi, S Ahn, Y-H Song, Analysis of Failure in Miniature X-ray Tubes with Gated Carbon Nanotube Field Emitters. *ETRI Journal* **35**, 1164-1167, (2013).

73. RJ Parmee, CM Collins, WI Milne, MT Cole, X-ray generation using carbon nanotubes. *Nano Convergence* **2**, 1, (2015).
74. MT Cole, RJ Parmee, WI Milne, Nanomaterial-based x-ray sources. *Nanotechnology* **27**, 082501, (2016).
75. C Li, MT Cole, W Lei, K Qu, K Ying, Y Zhang, AR Robertson, JH Warner, S Ding, X Zhang, B Wang, WI Milne, Highly Electron Transparent Graphene for Field Emission Triode Gates. *Advanced Functional Materials* **24**, 1218-1227, (2014).
76. L C., et al, Stable, self-ballasting field emission from zinc oxide nanowires grown on an array of vertically aligned carbon nanofibers. *Applied Physics Letters* **96**, 143114, (2010).
77. S Ding, C Li, W Lei, Y Zhang, K Qasim, H Cui, X Zhang, B Wang, Stable and uniform field emission from zinc oxide nanowires grown on carbon nanotube mesh template. *Thin Solid Films* **524**, 245-248, (2012).
78. X. Yuan, Y. Zhang, M. T. Cole, Y. Yan, X. Li, R. Parmee, J. Wu, N. Xu, W. I. Milne & S. Deng A Truncated-Cone Carbon Nanotube Cold-Cathode Electron Gun. *Carbon* 2017

# 5 ENCODED APERTURE

## 5.1 Introduction

The purpose of this part of the work is to evaluate a novel way of obtaining x-ray images of moving objects, for use in contaminant detection. It is intuitive that, when a moving object is scanned at a rate at which its movement is greater than the pixel dimension of the resulting image, this will normally create a reduction in resolution, or blurring. However there are recently published techniques for resolving such problems. This chapter describes a proof-of-concept study, to establish the viability of applying an Encoded Aperture method, implemented by means of a controlled generator, to the problem of imaging a moving object [1].

This section of the project simulates the use of a gated X-ray source, in which the data is acquired in a pseudo random sequence by means of combining a series of delayed static images of the object. In this, I have captured a set of images of a sample object, in different positions by translating it on a linear slide, and then accumulating them to produce a single image with a well defined blur. By applying a deconvolution algorithm, it has been possible to restore the image sharpness. Such an image represents the output of a detector when irradiated using an X-ray source that is sequentially pulsed, or “fluttered” in real time.

## 5.2 Objectives

- To create an interface for operating the motorised slide using an object oriented interface, so that the object may be moved to known locations.
- To create a program that can grab, save, and display images from an x-ray detector.
- To create a program capable of taking a series of images with the sample in different positions, combine them, to produce a blurred image of with the characteristics that represent a fluttered Xray source.
- To perform deconvolution to rebuild the original sharp image that can be further analysed to find artefacts such as foreign bodies.
- To obtain sharp images of these features at different heights relative to the detector.

## 5.3 Methodology

In a conventional single acquisition image, moving objects will create blur due to the time-based piece-wise constant filter that smears the image across the image. By applying a pseudo-random binary sequence to the source radiation, the resultant image will contain the high frequency spatial information which will allow the sharpness to be restored to the image by deconvolution.

In order to simulate this, a sequence of images is captured as the object is linearly translated at defined increments. These images will be selectively combined to produce a resultant that replicates the effect of the gated radiation source. A deconvolution algorithm has been devised so as to restore the sharpness to this combined image.

## 5.4 Apparatus

The equipment comprises a motorised linear slide, with an X-ray transparent tray on which an object is placed, as show in **Figure 18**. A static X-ray generator is supported above the slide and a detector is located below the level of the tray, so that the object can pass through the X-ray beam, as close to the detector as practicable. The entire equipment is mounted in a shielded test cabinet, to provide a safe working environment.

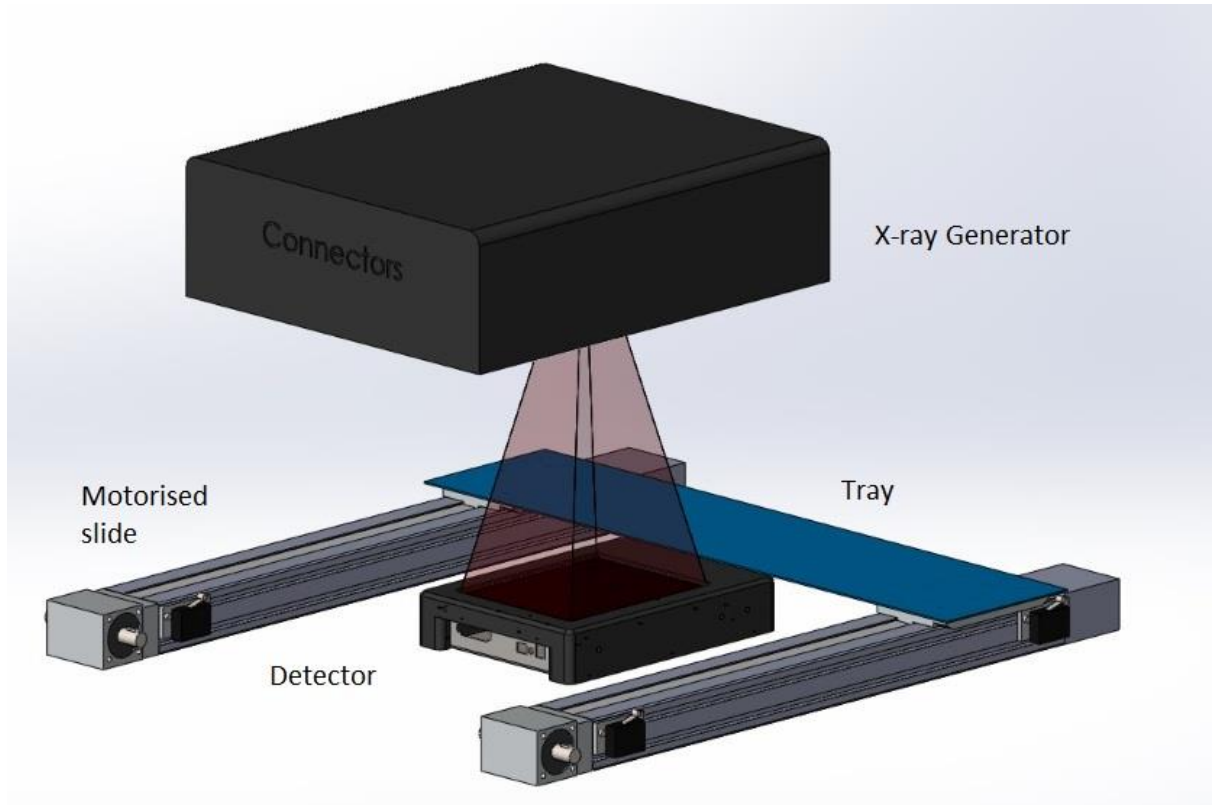


*Figure 18: Layout of equipment used*

## 5.5 The Program

The program, created in an object oriented programming environment (Delphi XE), serves as an interface for the motor controller, using RS232 serial communications protocol. The same program also interfaces with the detector (using Dexela and Epix Cameralink libraries). The main feature of the program is to execute a sequence of commands which bring the object into set locations and captures an image at each position. These images are then recombined, to form a single blurred image, by adding them. The program provides a means of tracking the progress of the sequence through the Status indicators. A screenshot of the user interface is shown in **Figure 19**.

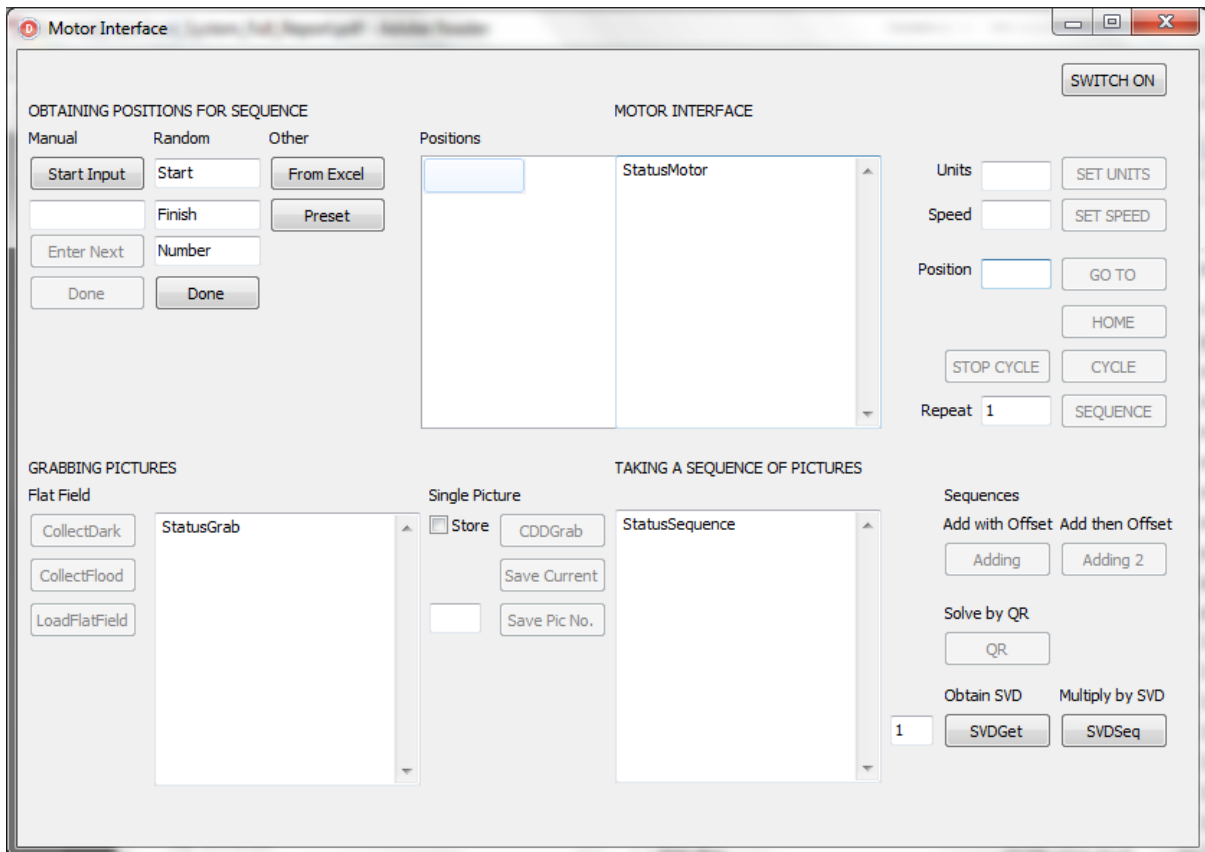


*Figure 19: Screenshot of the Motor Interface Program*

### 5.5.1 Motor interface features

The motor interface comprises a stepper motor drive card with a microprocessor, which executes a simple interpreted program. The program will move the tray to the desired positions by writing commands to the RS232 serial output, or COM port. The firmware in the motor controller allows the speed to be set, returning the carriage to the “home” position as defined by a limit switch, to repeatedly cycle or follow a preset sequence, as shown in **Figure 20**. The positions to which the carriage is moved can be entered manually or transferred from a spreadsheet.

The program sends a “home” command to the motor when first initialised. By entering the length of the sequence, a series of test positions may be generated and uploaded to the controller. In each case, while executing a sequence the program waits until motor has stopped moving before acquiring the image and progressing to the next position.

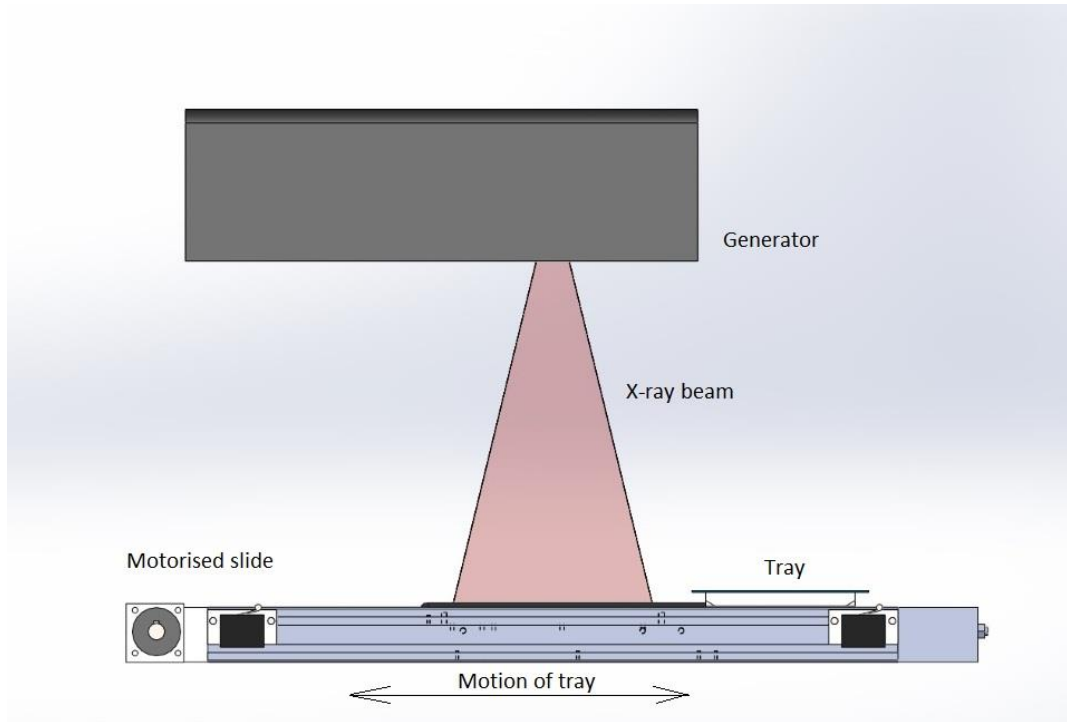


**Figure 20: Movement of the object through the X-ray beam**

### 5.5.2 Detector interface features

A detector comprises a large array of photosites, each of which can be addressed and read by the internal electronics. Within the detector, a sensor comprises an array of photosites, or diodes, which are primarily sensitive to visible light – this is created when X-rays from the generator strike a scintillator material which is placed on top of the sensor. A typical area sensor, such as the one used in this work, will comprise up to 5 million diodes.

Each diode in the sensor array will have a different sensitivity and dark current, so that a calibration process is required to normalise the output of each diode.

In order to normalise the array, it is first necessary to collect and store data for the dark condition, when X-rays are off, and the data for the X-rays on condition, which will be used to calculate the gain for flat field correction. These two images are stored in files to obviate the necessity of going through a calibration procedure each time the program is used. In order to normalise the data, the program is used to grab images from the detector, convert them from 14 to 16 bit, unscramble them, and apply flat field correction. The resultant image is then saved to a .png file.

### 5.5.3 Sequences section

The program can perform different sequences that use different methods to combine pictures. The deconvolution can be performed using the QR decomposition [2] or Singular Value Decomposition (SVD). The Point Spread Function (PSF), which is defined by the pseudo random sequence, is loaded from a txt file. Any length of PSF can be accommodated, but the selection requires optimisation, as explained later. Also, the program allows for scaling to produce a longer blur than the PSF (usually a factor 2, 4, or 6 times the PSF). To do this, the accumulated image is shrunk to match the blur and then expanded again. However, this reduces the portion of the image that is deblurred correctly and also the quality of the obtained image is reduced. This feature is useful in obtaining a sharp image at different heights, as described in section 5.9.

### 5.5.4 Dexela 1512CL-Detector

The images are captured using an area X-ray detector, with a native pixel resolution of 0.075mm. The overall active area of the detector is 145 x 115mm and outputs images with 14 bit resolution.

### 5.5.5 Control of X-ray Generator

The X-ray generator is controlled through a X-ray Generator Control Circuit (or “XGEN”) which performs the functions of controlling the generator, monitoring safety interlocks, operating indicator lamps and other outputs. It is the same unit that is described later in chapter 7. The main program will pass commands to the XGEN software via messages in a shared memory map file (SM MAP).

### 5.5.6 Stepper motor

The motor controller incorporates a microprocessor which executes a program onboard that can be edited and loaded using BASIC software functions. The motor is controlled by sending simple commands via the serial communications (COM) port. The stepper motor controls a belt-driven slide with a tray mounted on it, made from a sheet of Mylar, a material which is transparent to X-rays.

## 5.6 Method and Description

The acquisition of a sequence of images consists of several steps, explained below.

### 5.6.1 Moving to position

The motor will cycle through a sequence of positions determined by a pseudo random sequence. At each step, there is a simple handshaking procedure implemented via serial commands and responses, which causes the operation to pause until the mechanical movement has been completed.

### 5.6.2 Converting to a 16 bit picture

Since high speed is not an important requirement for this study, for the purposes of this Proof of Concept study, at each position four 14 bit images are acquired and accumulated, effectively averaging the result, thereby improving the signal to noise level. The resultant data is stored into a one dimensional array, of some 3 million 16 bit words.

### 5.6.3 Unscrambling

In order to achieve the fastest data speeds, the architecture of the detector is such that there are multiple (6) analog output channels from the sensor array, and in order to minimise the bandwidth, and hence noise level, the outputs are read in a scrambled sequence.

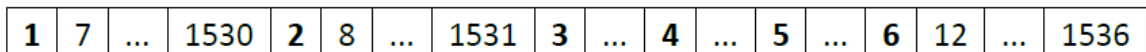


*Figure 21: Diagram of scrambling in columns*

Because of this, the data is scrambled in such a way that it is collected from the sensor from 6 vertical strips of equal width. To start, the pixel in the first column of the first strip is read, then the pixel in the first column of the second strip. The seventh pixel read is from the second column of the first strip and so on, as shown in **Figure 21** above.

Appendix 5, page 3 shows the fragment of the code used to unscramble the data from an array of words called Snap [1] into a similar array Snap [2]. Stride is equal to 3072, which is the pixel width of the detector x 2 bytes/pixel.

## 5.7 Flat field correction

As previously mentioned, the detector will have a non-uniform response, due to differing diode responses and X-ray levels. To compensate for this, the system will record calibration data for the entire array of photo-sites. When the system is initialised, because this calibration data is volatile, the dark and gain images need to be acquired for the flat field correction. This is a standard technique used in image processing systems, that removes any non-uniformity from the detector itself. With the tray indexed to its home position, and hence no object in the beam, with the X-rays turned off the ‘Dark’ picture is captured. Following that, the X-rays are enabled and the ‘Gain’ image is taken. After unscrambling, the raw image is corrected using the Flat Field Correction formula given in Equation 3.

$$C(x,y) = \frac{(R(x,y) - D(x,y)) \cdot m}{(G(x,y) - D(x,y))} \quad \text{Equation 3.}$$

where, C is the corrected image, R is the raw image, D is the ‘Dark’ image, G is the ‘Gain’ image, and m is the average value of (G(x,y) – D(x,y)). This is repeated for all pixel coordinates x, y.

The technique is illustrated below with two pictures. **Figure 22** is without the correction, **Figure 23** is with the correction. After the correction there are no artefacts from the detector present.

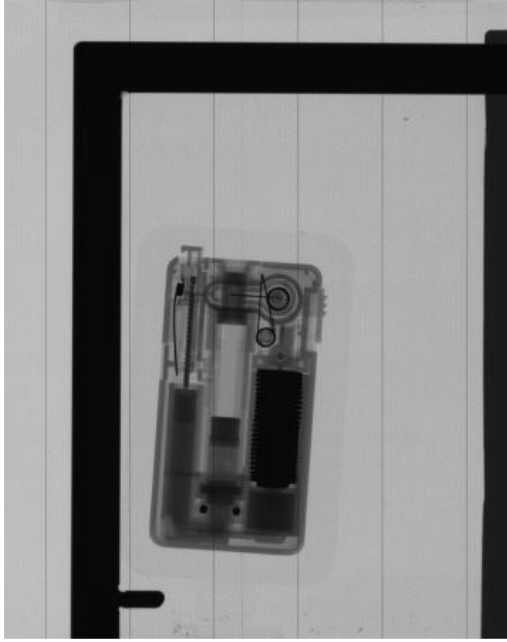


*Figure 22: No flat field correction*

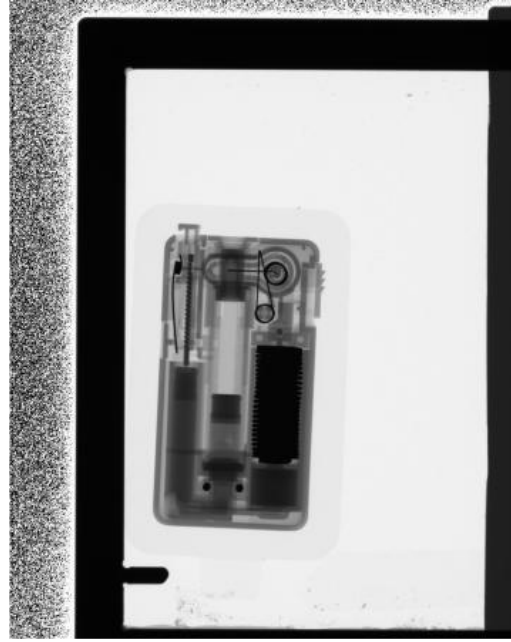


*Figure 23: Flat field correction*

## 5.8 Deconvolution

In the Encoded Aperture system, during the total exposure time the source of X-rays is ‘fluttered’, meaning it is alternately enabled and disabled in a pseudo random, predetermined sequence. This is the core concept of this study. The resultant image will contain a coded blur. The accumulation of the individual exposures will contribute to the final blurred image. The exposures of the sample in different positions are added together to form a single, blurred image; the process is shown in **Figure 24**.



*Figure 24: Overview of the algorithm*

### 5.8.1 Deblurring an image via deconvolution.

The aim is to estimate the signal  $S(x)$  that was blurred by a linear system's point spread function  $P(x)$  from the measured signal  $I(x)$ .  $I(x)$  is known to be:

$$I(x) = P(x) * S(x); \quad \text{Equation 4}$$

where ‘ $*$ ’ symbolises convolution

However, in our case the deconvolution problem can be simplified and solved by an overdetermined linear least squares problem [3], where  $\mathbf{A}$  is the smearing matrix,  $\mathbf{B}$  is the obtained added image and  $\mathbf{X}$  is the deblurred image that we are looking for:

$$\mathbf{AX} = \mathbf{B} \quad \text{Equation 5}$$

$$\mathbf{X} = \mathbf{A}_+ \mathbf{B}; \quad \text{Equation 6}$$

where  $\mathbf{A}_+$  denotes the Moore-Penrose[4] pseudoinverse of the smearing matrix  $\mathbf{A}$ .

The problem is illustrated in **Figure 25**.

Matrix  $\mathbf{A}$  is a circulant sparse matrix and is formed by entering the elements of the PSF into the first column. Each next column is obtained from the previous one, by shifting the entries one row down each time. The size of the matrix  $\mathbf{A}$  is important, as its number of rows must be equal to the height of the detector in pixels plus the (blur – 1) and its number of columns is to be equal to the height of the detector in pixels.

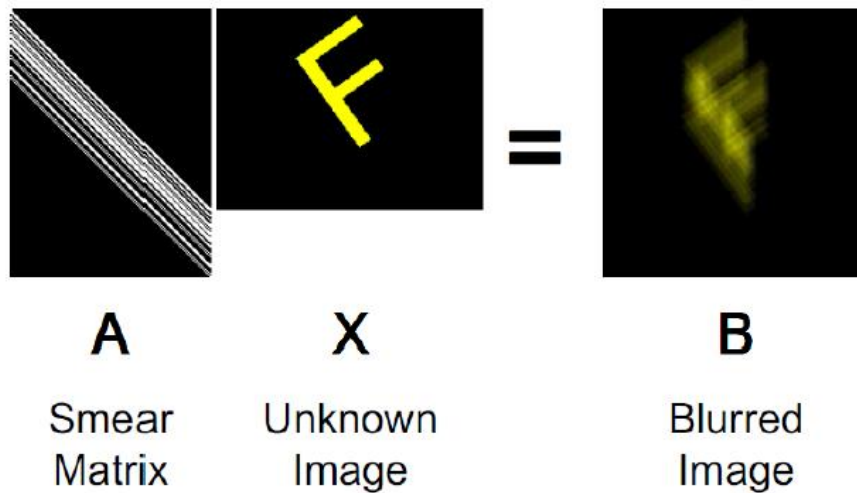


*Figure 25: Linear Least Squares problem in image deblurring*

### 5.8.2 Code selection

The contributing short exposure pictures are taken in a pseudo random sequence determined by the Point Spread Function (PSF). The elements of the PSF represent the positions at which the images are to be taken, where the separation between the consecutive elements is equal to a distance of 1 pixel. The PSF used can be found in the **Figure 26**. The PSF is selected so that the invertibility of the circulant matrix created from the PSF is improved, and has been taken from reference [1]. The invertibility of the smearing matrix **A**, in the presence of uncertainty and noise, can be optimised by minimising the condition number of the matrix (the ratio of the largest to the smallest singular value), which indicates the sensitivity of the solution **X** to the noise in the input image.

1010000111000001010000110011110111010111001001100111

*Figure 26: PSF used in tests (length 52) - from [1]*

### 5.8.3 Singular Value Decomposition:

The linear least squares involves calculating the pseudoinverse of the circulant smear matrix  $\mathbf{A}$ . However, obtaining the matrix using the explicit formula is not efficient. A better approach is to use the Singular Value Decomposition (SVD) of  $\mathbf{A}$ . Matrix  $\mathbf{A}$  is a  $\mathbf{m}$  by  $\mathbf{n}$  matrix with  $m \geq n$ . Thus,  $\mathbf{A}$  can be factorised as  $\mathbf{A} = \mathbf{U}\mathbf{\Sigma}\mathbf{V}_T$ , where  $\mathbf{U}$  is a  $\mathbf{m} \times \mathbf{m}$  unitary matrix and  $\mathbf{V}_T$  is a  $\mathbf{n}$  by  $\mathbf{n}$  matrix. Matrix  $\mathbf{\Sigma}$  is a rectangular diagonal matrix with singular values in decreasing order along its main diagonal. Now, the pseudoinverse can be expressed by  $\mathbf{A}_+ = \mathbf{V}\mathbf{\Sigma}_+\mathbf{U}_T$ .  $\mathbf{\Sigma}_+$  is straightforward to obtain, all the nonzero values of  $\mathbf{\Sigma}$  are replaced with their reciprocals, and the resultant matrix is transposed. In the case of implementing this into an x-ray inspection system, where speed is essential, the pseudoinverse can be pre-computed and only the final multiplication ( $\mathbf{X} = \mathbf{A}_+\mathbf{B}$ ) will have to be performed each time an image is to be reconstructed. This is due to the fact that the matrix  $\mathbf{A}$  is always the same, for any image.

## 5.9 Results

**Figure 27(a)** shows the results of the test of the algorithm that uses SVD to obtain the deblurred image. The blur is 52 pixels. **Figure 27(b)** shows the resultant image indicating a good reconstruction of the sharpness. The artefacts at the top and bottom of the deblurred picture are present because there was insufficient information about them in the blurred picture. These areas were not present in all of the constituent images, so it was impossible to deblur them. The constituent images were flat field corrected. The execution of the program to restore the sharpness of the blurred image, took several seconds, using a pre-computed pseudoinverse.

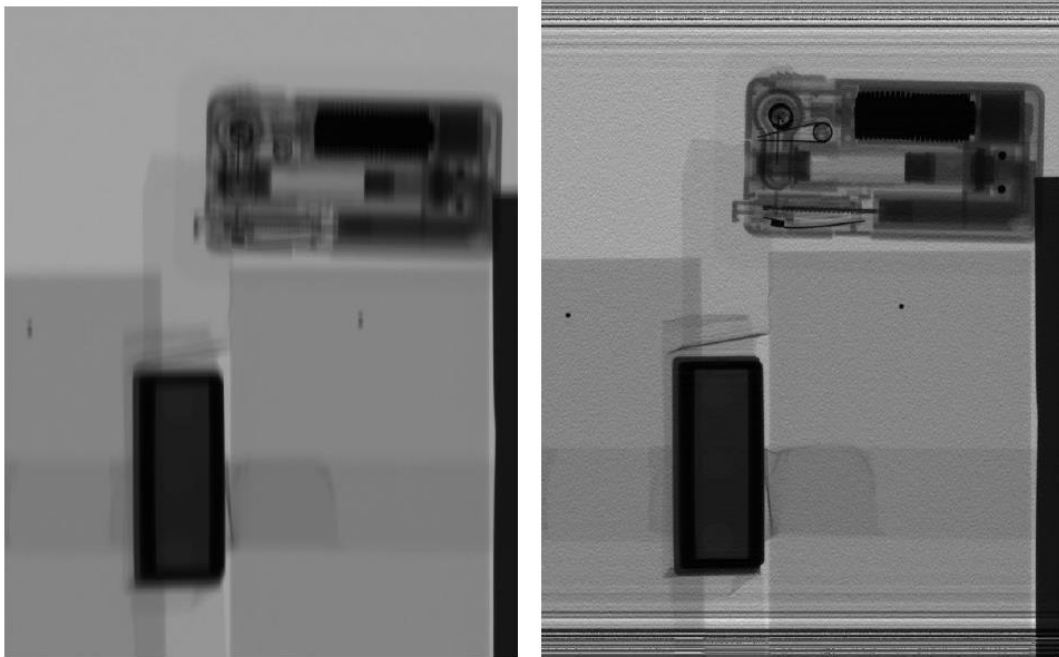


*Figure 27: (a) Blurred image. (b) Results of the deconvolution*

The accumulation algorithm used at the moment suffers from a problem that as more pictures are added, the contrast artefact progressively reduces, making the artefact hard to distinguish from the blur created by adding images, as shown below in **Figure 28**.

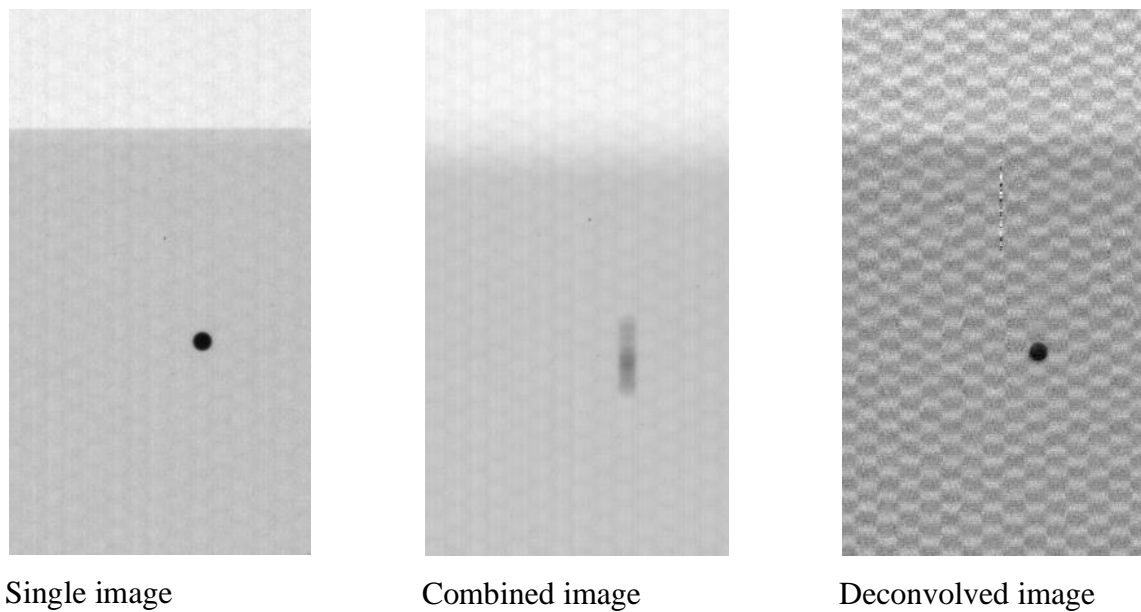


*Figure 28: Detailed images showing artefacts*

## 5.10 Discussion on Tomography

Due to the fact that X-rays do not fall on the detector at the same angle everywhere (since the x-ray tank is mounted at a given height above the detector and can be treated as a point source) the deconvolution makes only the artefacts at a specific height appear sharp on the final image. This could in principle allow for scanning an object in horizontal slices. Sharp pictures can be obtained for any given height by slightly *shrinking* or *expanding* the image and adjusting the size of the corresponding circulant matrix for each slice. In this way, all features located at other heights appear as blurred. The pseudoinverse matrices for all the desired heights would be pre-computed and then applied, at the expense of the processing time for the image of each object.

Using a single area detector in this context, leads to a problem with features lying directly on top of each other, as there is a possibility of them appearing as a single artefact on the combined images. This opens up a potential need for more than one sensor to be used at the same time.

To fully take advantage of the size of the detector a longer point spread function could be beneficial. This will allow a larger blur to be obtained, which will in turn allow the program to detect features at different heights. However, a longer blur will result in greater boundary conditions, since the features at the top and bottom of the image will cover a greater proportion of the deblurred image (see **Figure 29**). Hence, unless the artefact problem is solved, there is an upper limit to the achievable blur.

Solving the deconvolution can be made both faster and more accurate. The method used was simple and far from optimal, which suggests that the program's speed can be improved. The reconstruction of the image introduced noise, which was due to the simplification of the deconvolution to a linear least squares problem. This would mean that solving the deconvolution using a better algorithm would reduce the amount of the noise present.

The purpose of this Proof of Concept study, however is to demonstrate the achievement of an objective for the randomly pulsed X-ray source that is the primary object of this work. Further considerations will be discussed in Chapter 7 (discussion on the temporal response of the FE generator) and in Chapter 10 (the effect of non-ideal detector response).

## 5.11 Conclusions

The current results demonstrate that the general concept is viable. Blurred images have been created and then deconvolution has been successfully applied to reconstruct the sharpness of the image. The main advantages of the deconvolution method is that it will allow the use of an area sensor with a long exposure time for imaging continuously moving objects, while needing less X-ray generator power than conventional pulse Xray systems, which facilitates a system with lower emissions and higher reliability.

The most evident effect in the final images, is the presence of artefacts that produce a background noise level. This can be seen below, in **Figure 29**.

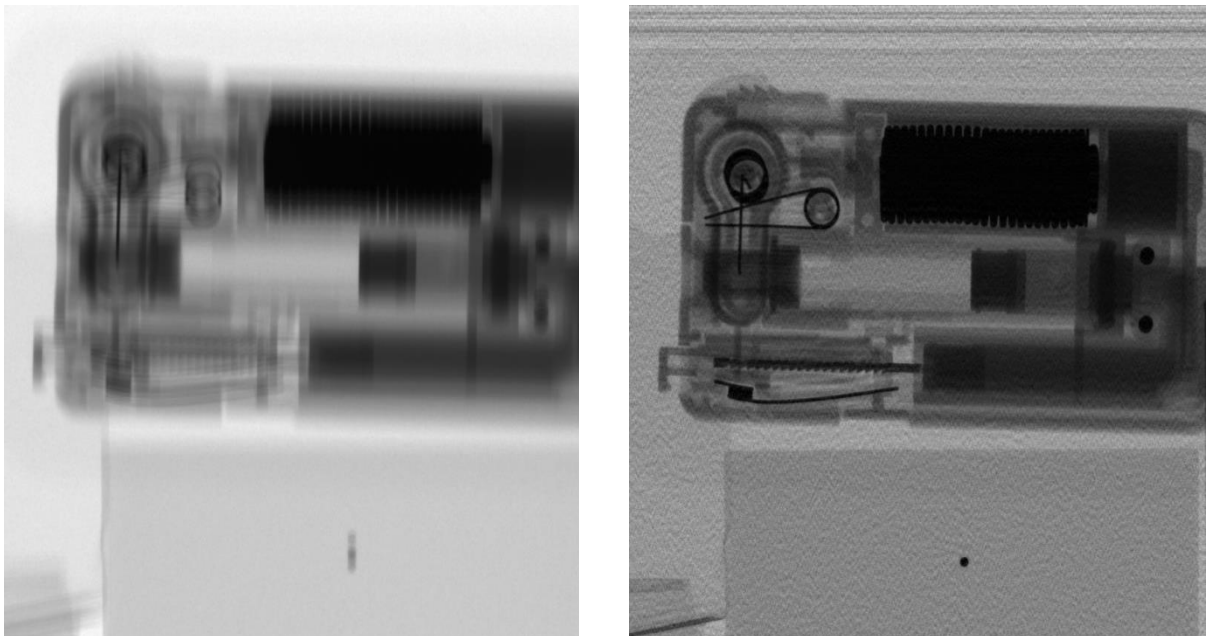


*Figure 29: Blurred and final processed images*

## 5.12 References

1. Raskar, A Agrawal, J Tumblin, Coded exposure photography: motion deblurring using fluttered shutter. *ACM Trans. Graph.* **25**, 795-804, (2006).
2. WH Press Numerical recipes : the art of scientific computing ; source code CD-ROM v 3.0. Cambridge Univ. Press; Cambridge, 2007.
3. Lee Do Q, Numerically efficient methods for solving least squares problems. (2012).
4. Penrose, A generalized inverse for matrices. *Mathematical Proceedings of the Cambridge Philosophical Society* **51**, 406-413, (2008).

# 6 EVALUATION OF SEALED INSERTS

## 6.1 Introduction

Most conventional X-ray tubes utilise thermionic emission (TE) which can stimulate appreciable current densities that are capable of giving rise to X-ray emission. **Figure 30(a)** shows examples of static and rotating anode TE X-ray sources, which are essentially based on the Coolidge tube [3], as shown as **Figure 10** in **Chapter 3**. The core components of these systems are illustrated in **Figure 30(b)** which also outlines the principle mode of operation. Here, the device is sealed in an inexpensive and easily fabricated evacuated glass or ceramic envelope, and the electrons are liberated from a metallic filament, such as Tungsten, Joule heated to in excess of 1000°C [3]. Since the emission is directly dependent on the filament temperature [4] – as increasing the emitter temperature allows for much of the electron population to pass over the surface barrier – such tubes readily enable analogue control over the magnitude of the emission current. In TE sources this beam current is controlled by monitoring the anode current and adjusting the inferred filament temperature using a closed-loop control system.

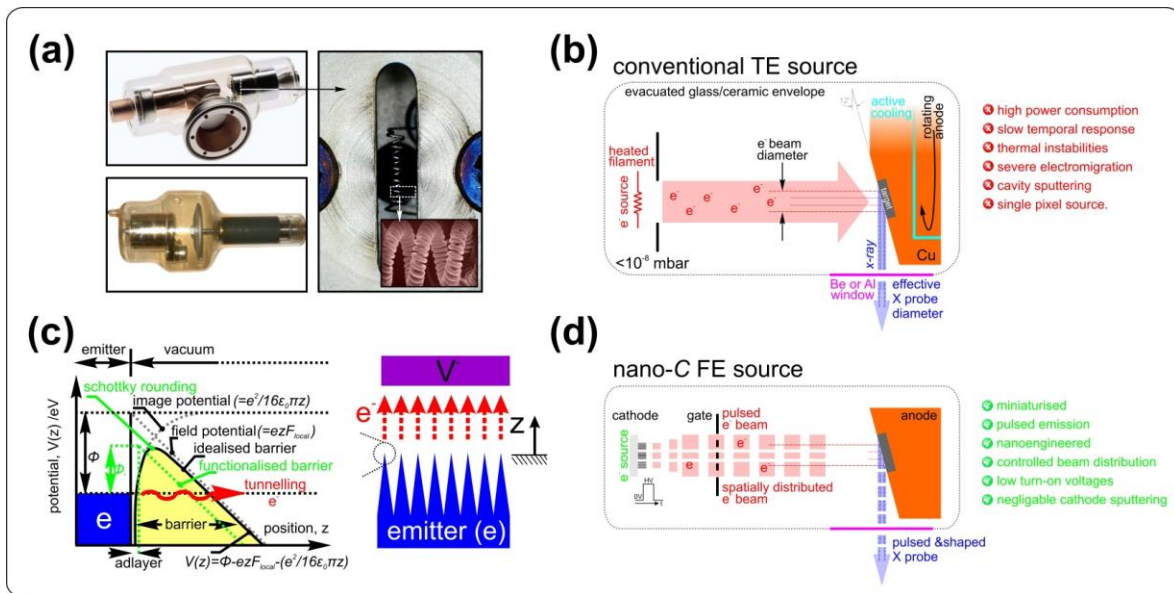


**Figure 30: Thermionic and Field X-ray emission technologies.**

(a) Images of micro-coil and rotating anode thermionic emission (TE) electron sources. (b) Schematic depiction of the operation principles of a thermionic emission (TE) electron emitter based X-ray source. Note the active anode cooling. (c) Band diagram illustrating the routes to thermionic, photo, and field emission as means to stimulate an electron beam by overcoming the surface potential barrier. (d) Schematic depiction of the operation of a field emission (FE) X-ray source. Adapted from [5].

Since these “glass inserts” form the basis for a very high proportion of the industrial Xray sources produced today, they are manufactured in large volumes, with well understood manufacturing methods, and are hence very cost effective.

## 6.2 Construction of cathode assembly

It was for the reasons of low cost and ready accessibility, that initially this method of construction was selected for the first experimental studies in my field emission work. Using the concept show in **Figure 30(c), (d)**, a CNT field emission electron source was designed in a form that was physically similar to the conventional filament assembly used in standard thermionic emission (TE) X-ray tube, and the process of mounting the cathode unit into the evacuated tube was sub-contracted to a conventional TE X-ray tube manufacturer. As shown in **Figure 31**, this comprised :

- A field emission source utilising Multi Wall Carbon Nanotubes (MWCNTs), applied as a screen printed paste to the cathode area, onto a conductive stage.

- A gate assembly manufactured as an array of circular holes in a Molybdenum sheet. The manufacturing process involved photo lithography patterning and etching, with the hole size being approximately 100 microns diameter.
- The gate assembly is spaced off from the printed cathode by a mica insulator, approximately 1000 microns thick. It is the thickness of this insulator that defines the electric field at the surface of the emitters, combined with the cathode voltage.

The cathode is connected to a negative high voltage supply, whilst the gate assembly is grounded. The cathode voltage is controllable, and provides a means of generating the electric field needed to extract the electrons from the CNT emitters.

The resultant electrons will partially pass through the holes in the gate assembly, and thence be attracted towards the anode. At the point that they strike the target material of the anode, an X-ray photon will be released.

The resultant assembly was incorporated into a sealed glass insert (**Figure 32(a)**), similar to that used in a conventional thermionic X-ray tube.

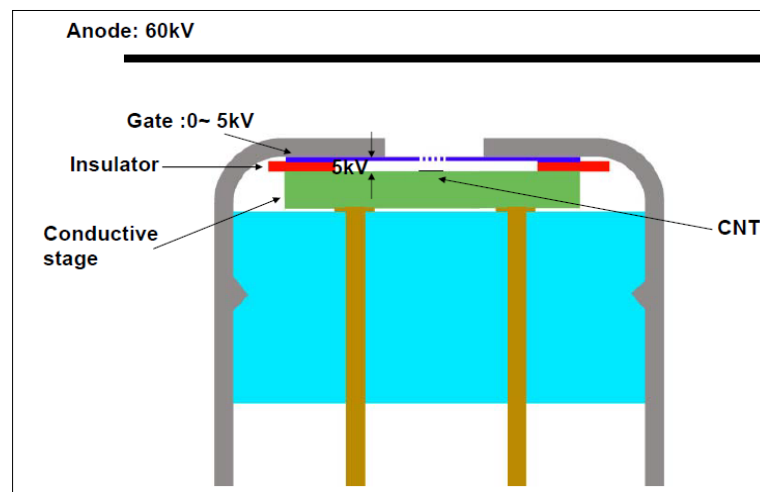


**Figure 31: Schematic of the construction of CNT field emission X-ray tube.**

This type of X-ray tube requires two high voltage multiplier stages. One stage of up to +60 kV is used to supply the anode, and a second stage of up to – 8 kV is used to provide the cathode to gate extraction voltage. Both high voltage stages are controlled by mean of an analog control system, which is adjusted either by analog potentiometers, or by a computer via digital-to-analog convertors.

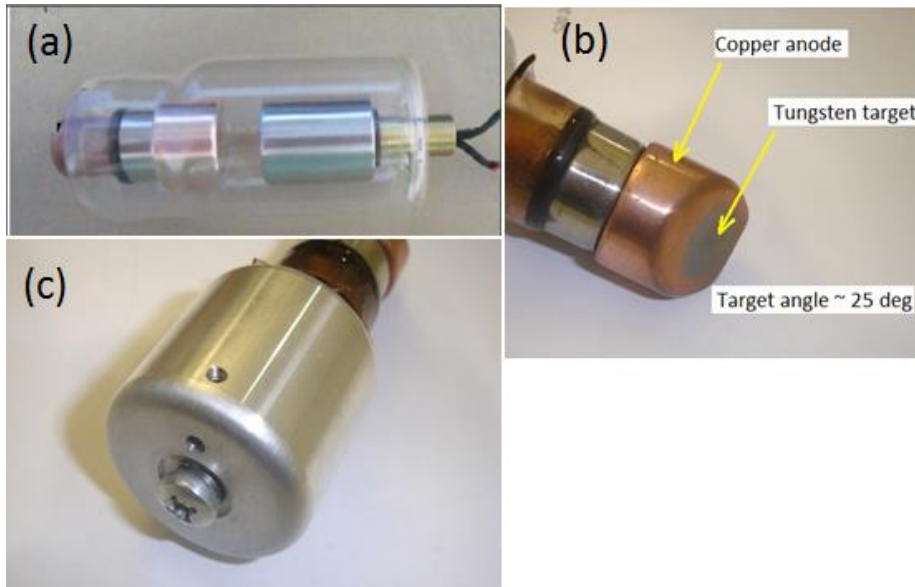


**Figure 32: Components of Sealed Xray tube**

Tube components (a) CNT tube assembly, (b) Anode and target, (c) Anode radiator

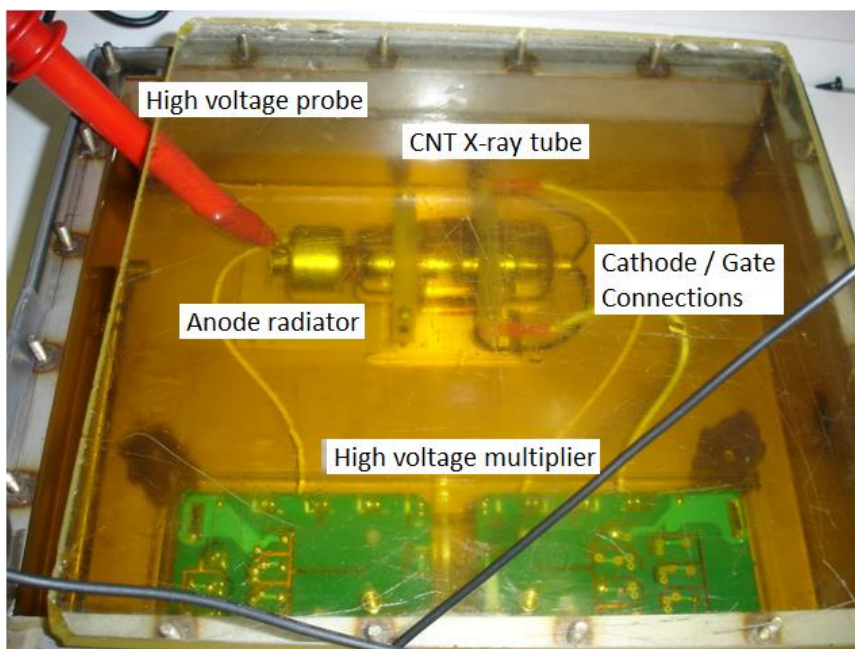


**Figure 33: Assembled tank, with leaded glass plate for viewing.**

### 6.3 Generator design

The X-ray generator requires these two controllable elements, being the cathode which creates the electron beam, and the supply of high voltage to the anode, which ultimately determines the X-ray photon energy. In the case of a field emission tube, this requires two sources of high voltage.

The Xray generator is built into an oil filled “tank”. The silicone oil employed serves two purposes – it provides an insulating medium for the high voltages present, and it also can conduct away the significant amounts of heat generated by the circuitry and the anode.

The conversion of electrons to X-ray photons occurs at the point that the electrons impinge on the anode, known as the “target”. A target is a material such as tungsten, which is cast into the copper body of the anode. The process of converting the electron beam to X-ray photons is an inefficient one, with typically only about 1% of the power of the electron beam being converted into photons. The remainder will be dissipated as heat. The anode contact of the tube, therefore has to conduct away this heat in order to prevent the temperature of the surface of the anode becoming excessive, as in **Figure 32(b)**. To assist in the transfer of the heat to the oil within the tank, the exterior end of the anode is connected to an Aluminium radiator that increases its area of contact with the cooling oil. This can be seen in the photograph in **Figure 32(c)**.

In order to view the interior of the tank, whilst testing is being conducted, the top cover of the tank is replaced with a sheet of leaded glass. This glass plate, which is about 15mm thick, has an equivalent radiation protection level of 3mm of lead (referred to as 3.0LE). In **Figure 33**, the glass plate has been positioned to allow a small gap to insert a high voltage probe, which is in contact with the anode.

In the case of the initial experimental work, the voltage sources are derived from a pair of conventional high voltage single phase multiplier circuits. This high voltage source has been designed by the author, and the block diagram is shown in **Figure 34** while the schematics are attached in **Figure 35**.

The multipliers operate at a switching frequency of around 50kHz and are powered from a high frequency power circuit external to the tank, which is in turn controlled by a closed loop circuit on the adjacent control board. The firmware for the control circuit, adapted to operate with the CNT high voltage multiplier, is included in **Appendix 5**. In this case, the control circuitry may be set by analog voltages, one for the anode voltage,  $V_a$ , and one for the cathode – gate voltage,  $V_g$ . The control circuit also provides a means of monitoring the voltage, current and temperature levels within the generator, in order to provide for a safe working environment.

Xray Generator - Simplified Block Diagram

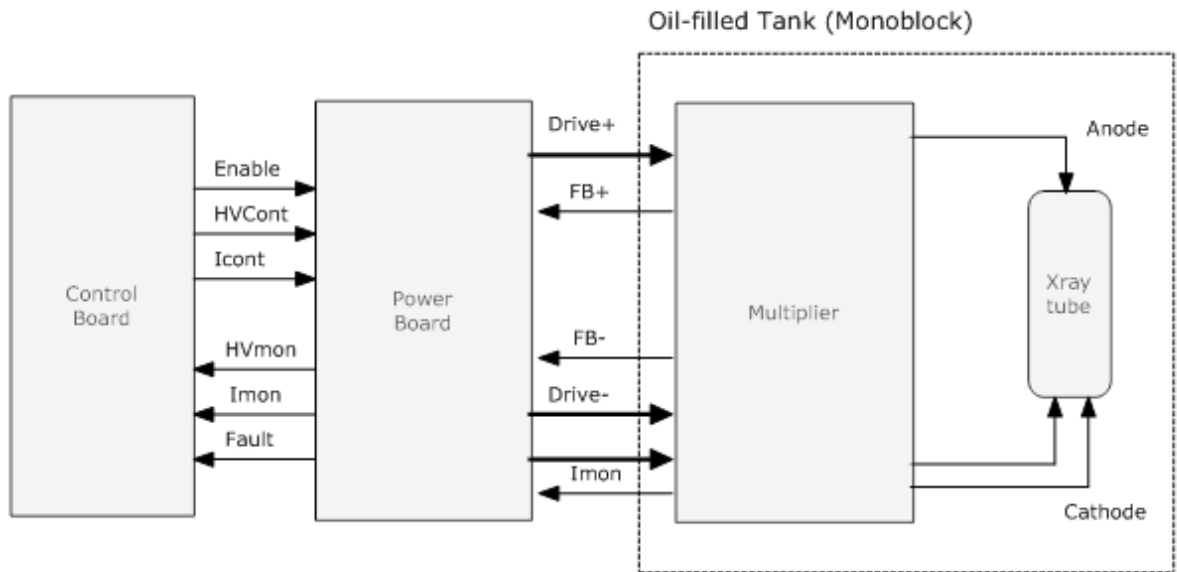


Figure 34: Block diagram of generator and control electronics.

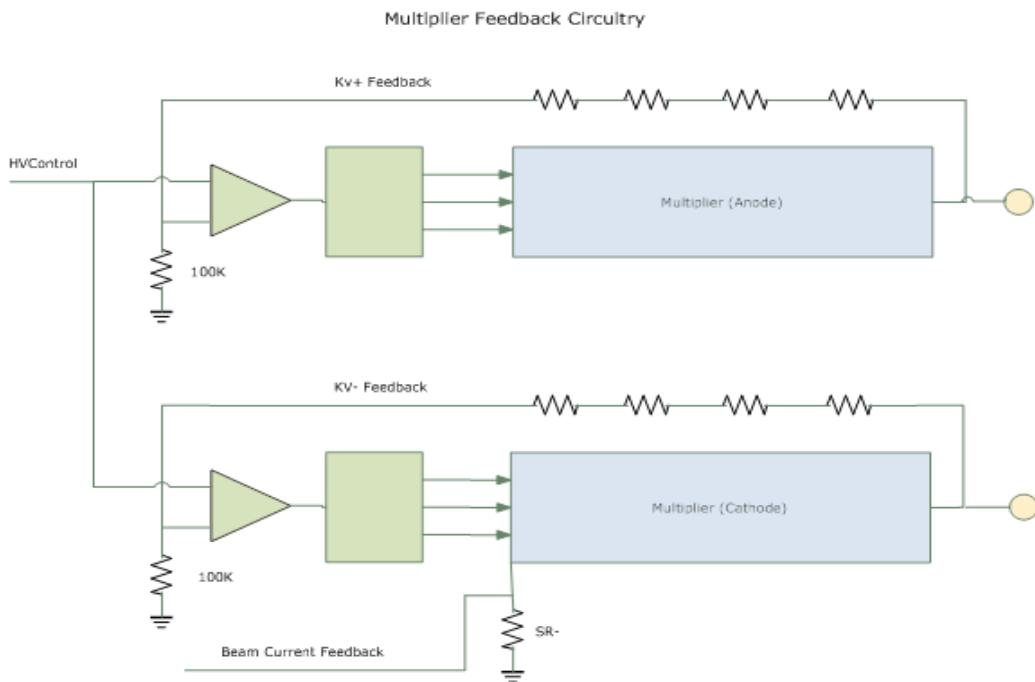


Figure 35: Simplified high voltage multiplier schematic.

## 6.4 Safety considerations

X-rays are a form of ionising radiation, and therefore potentially hazardous. Great care was taken in the design and construction of the test tank, to ensure safe operation. In particular, the exterior of the tank was lined with 3mm (code 5) lead, welded along each corner. The primary beam from the tube was oriented downwards, onto 6mm lead sheet. The leaded glass plate was positioned so as to minimise the opening for the high voltage probe, as this gap would permit the direct emission of X-rays.

The author is qualified as a Radiation Protection Supervisor (RPS) and took all necessary steps to minimise the risk during this work. A radiation meter (GM tube) was on hand at all times, and the test rig was surveyed regularly, and on any physical movement of the component parts.

## 6.5 Results

As an initial test, the CNT X-ray tube was set up to image a circuit board, by way of demonstration. The detector used was a Dexela 1512 APS CMOS detector, with 75 micron pixel size. The object being imaged is an assembled circuit board. The associated software has incorporated a normalisation procedure to ensure a uniform image response over the area sensor, with the result shown in **Figure 36**.

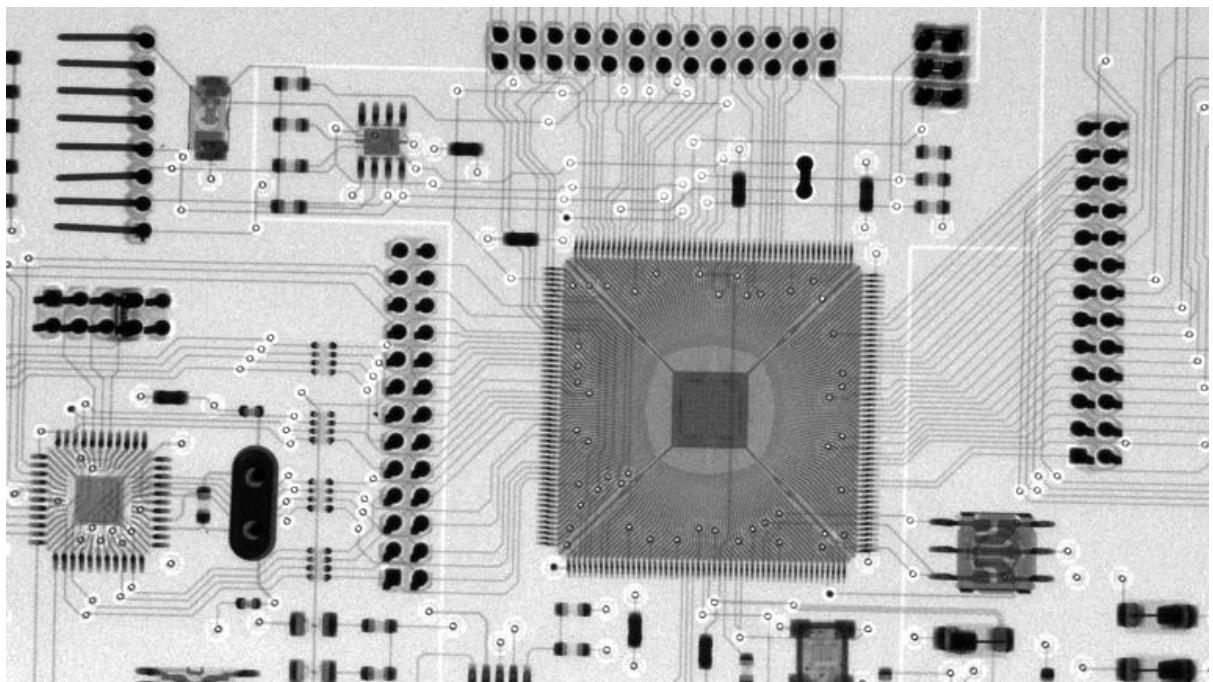


*Figure 36: Image taken with X-ray generator using sealed CNT insert.*

The purpose of this stage of the work is to understand the relationship between the operation of the field emission electron source and the generation of X-rays by the tube. The generator was set up to sweep through a range of gate voltages and recorded the anode current. This was repeated at various anode voltage settings. Sample results are shown in **Figure 37**.

To achieve this, the control system was configured to operate as a closed loop system, with the control of the gate voltage ( $V_g$ ) forming part of the feedback circuit, to maintain a constant anode current ( $I_a$ ). A computer was connected to a control circuit with several analog and digital inputs and outputs. It was programmed to execute a sequence of cycles with different demand settings, as defined in a database table. The gate current ( $I_g$ ) and gate voltage ( $V_g$ ) were monitored every 100ms and an average of 100 readings was recorded at intervals of approximately 10 seconds, while sequentially stepping the anode voltage. This averaging was found to be necessary in view of the high noise level experienced. The results for individual values of  $V_a$  are shown in **Figures 38** and **39**. The results for all kV settings are shown in **Figures 40** and **41**. The software written for this is recorded in **Appendix 3**, together with examples of the database tables used to control the sequence.

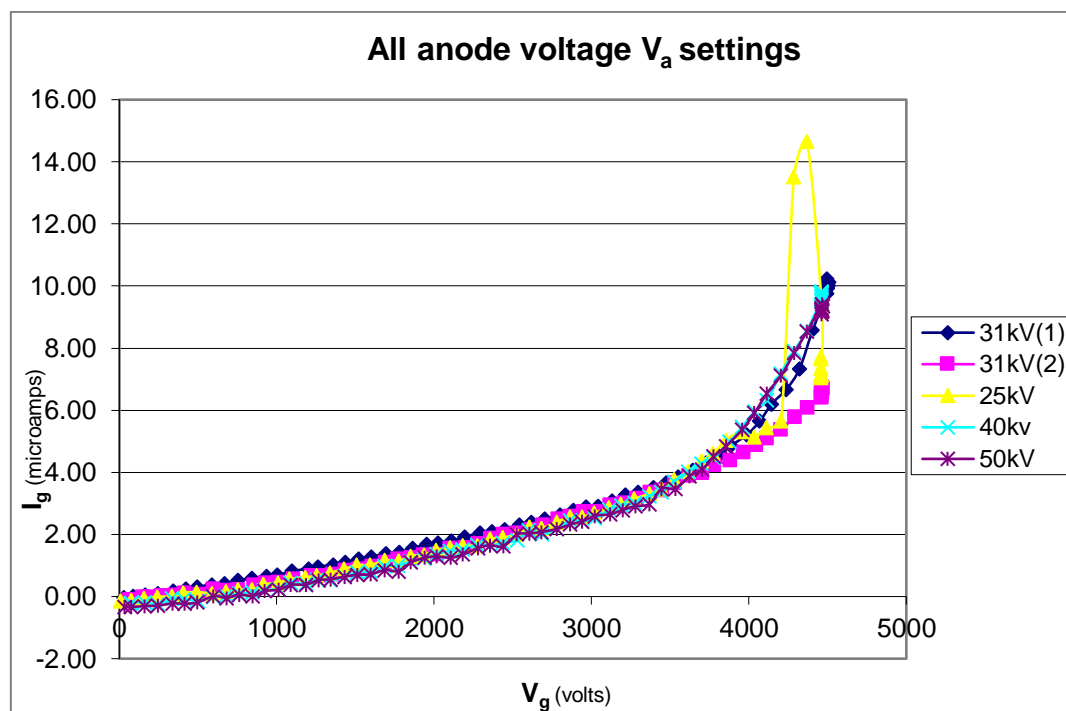


**Figure 37: Gate characteristics at various settings of anode voltage,  $V_a$ .**

It can immediately be seen that there is significant instability on the following charts.

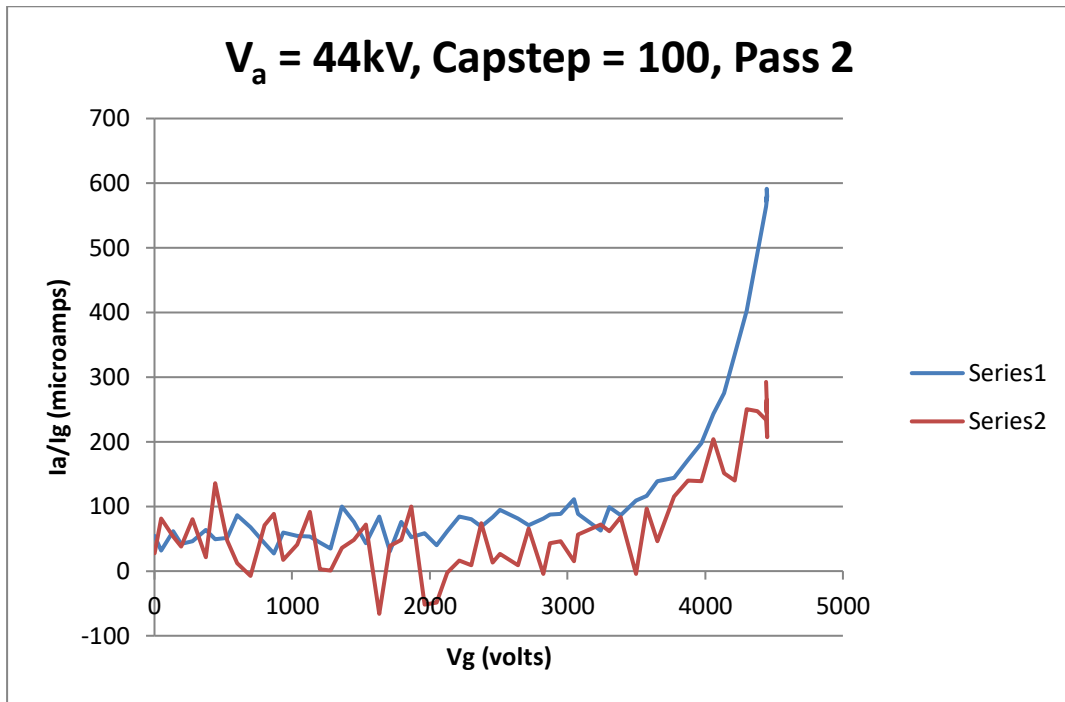


Figure 38:  $I_g$  and  $I_a$  as a function of  $V_g$  for  $V_a = 44\text{kV}$ .

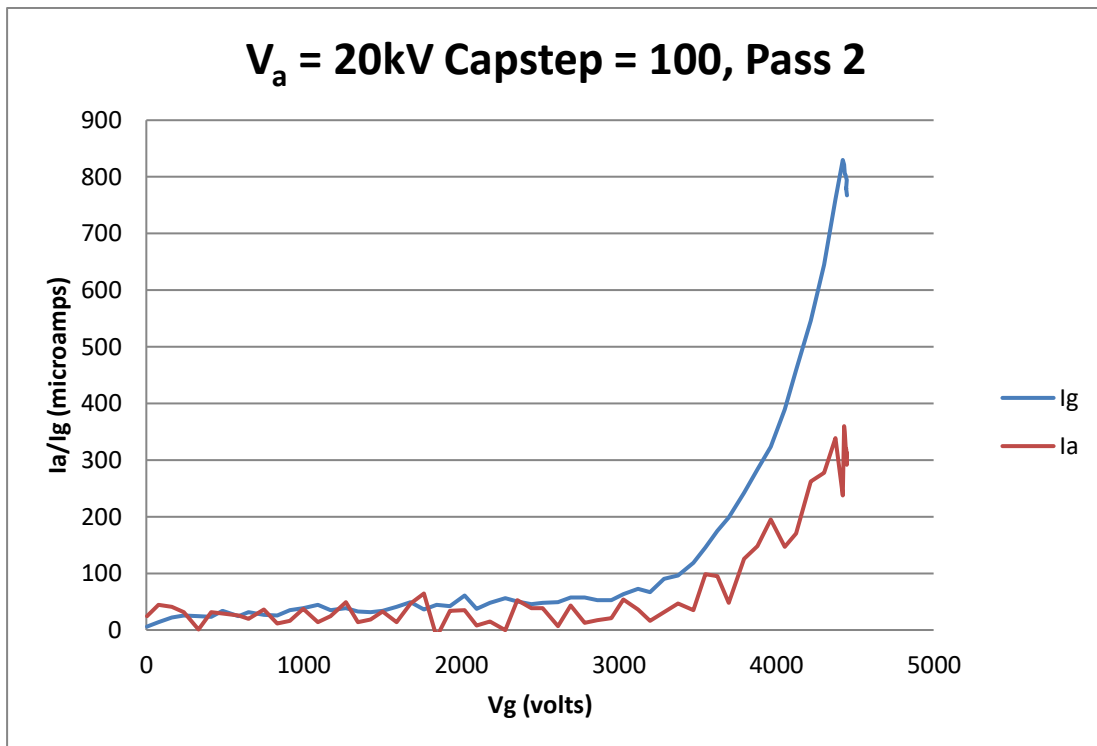


Figure 39:  $I_g$  and  $I_a$  as a function of  $V_g$  for  $V_a = 20\text{kV}$

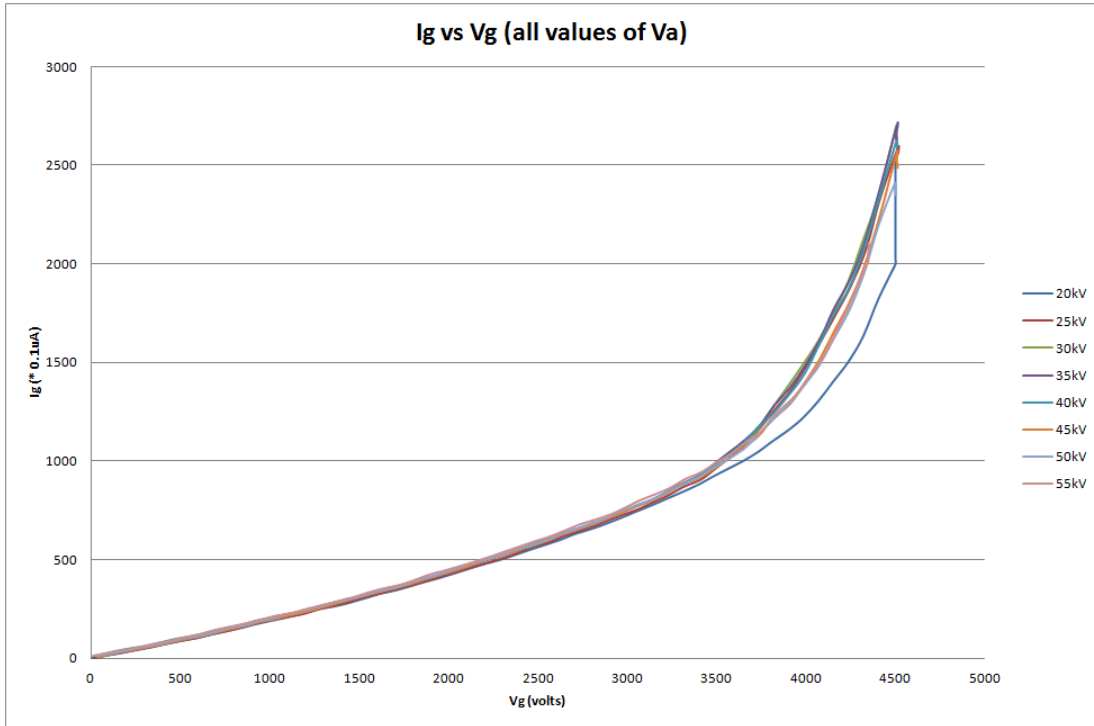


Figure 40:  $I_g$  as a function of  $V_g$  for all values  $V_a$

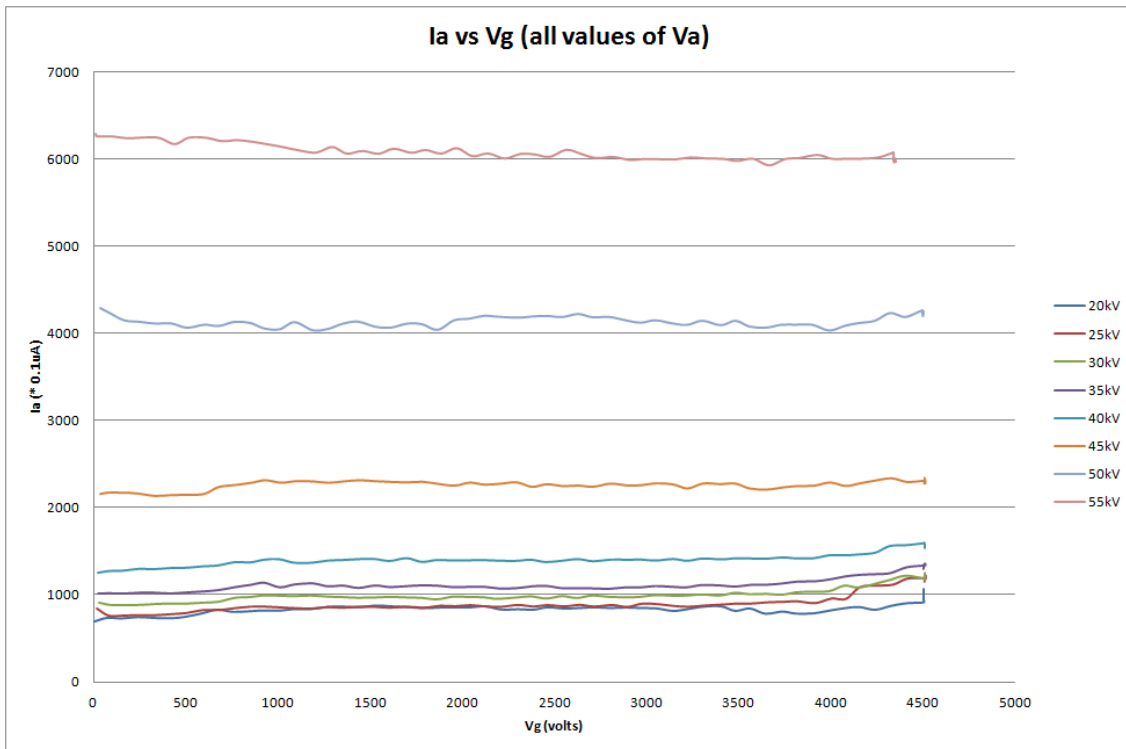


Figure 41:  $I_a$  as a function of  $V_g$  for all values  $V_a$

The final measurements taken with tube 5 suggest a failed tube. The anode current appears to be virtually unaffected by the gate voltage, but bears a direct relationship to anode voltage. However the gate current,  $I_g$  bears a constant relationship to  $V_g$ ,

irrespective of anode voltage,  $V_a$ . Upon reviewing this, it must be assumed a major manufacturing fault has occurred within this tube.

## 6.6 Failure modes

The experiments were repeated with five X-ray tubes, that had been manufactured in this way. During the period of this work, a number of issues were encountered and addressed.

The initial tube suffered failure after about 40 minutes. This was due to excess gate voltage  $V_g$  as the negative high voltage supply had the capability to provide an output of up to  $-8$  kV, and the closed loop control system could, in principle, permit this to happen. This was clearly excessive, given the cathode geometry. As a result the control circuit firmware was modified to clamp the maximum output voltage to  $-5$  kV.

The following tests were conducted on the remaining tubes, with each one exhibiting failure after a certain period. Tube 3 provided little useful data. Tube 4 lasted the longest period, a little over 5 hours.

It became clear that it was necessary to consider the causes of these failures. A review of the literature has shown reports that the non-uniform nature of the emission sites in a paste printed cathode can give rise to preferential conduction from the longest and/or highest aspect ratio CNTs, resulting in potential damage.

As a result of this, with tube 5, an attempt was made to season it by running continuously at lower levels, as described below in section 6.8.

During this work, it has been assumed that the vacuum level is high enough to support field emission. However, there is no means of verifying this with a sealed glass insert, and measurements in chapter 9 of this work suggest that for a pressure greater than  $2e-6$  millibar, the field emission tails off and ion emission becomes dominant.

In order to investigate the failure mode, the cathode assembly from tube 4 was removed and examined under an SEM. The conclusions were :

Perturbed cathode and gate surfaces seem to stimulate arcing as evidenced by the blue hues on the cathode, as can be seen clearly in **Figures 42 and 43**. Arcing is most likely occurring between gate and the cathode.

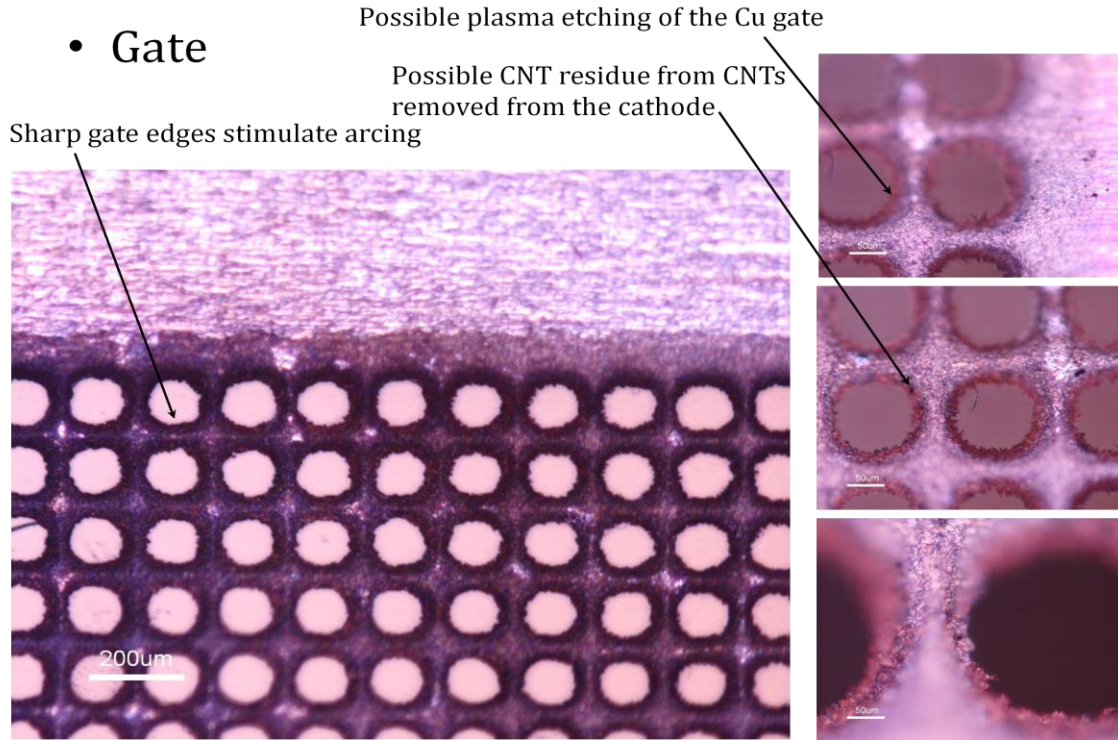


*Figure 42: SEM of gate of failed sealed insert*

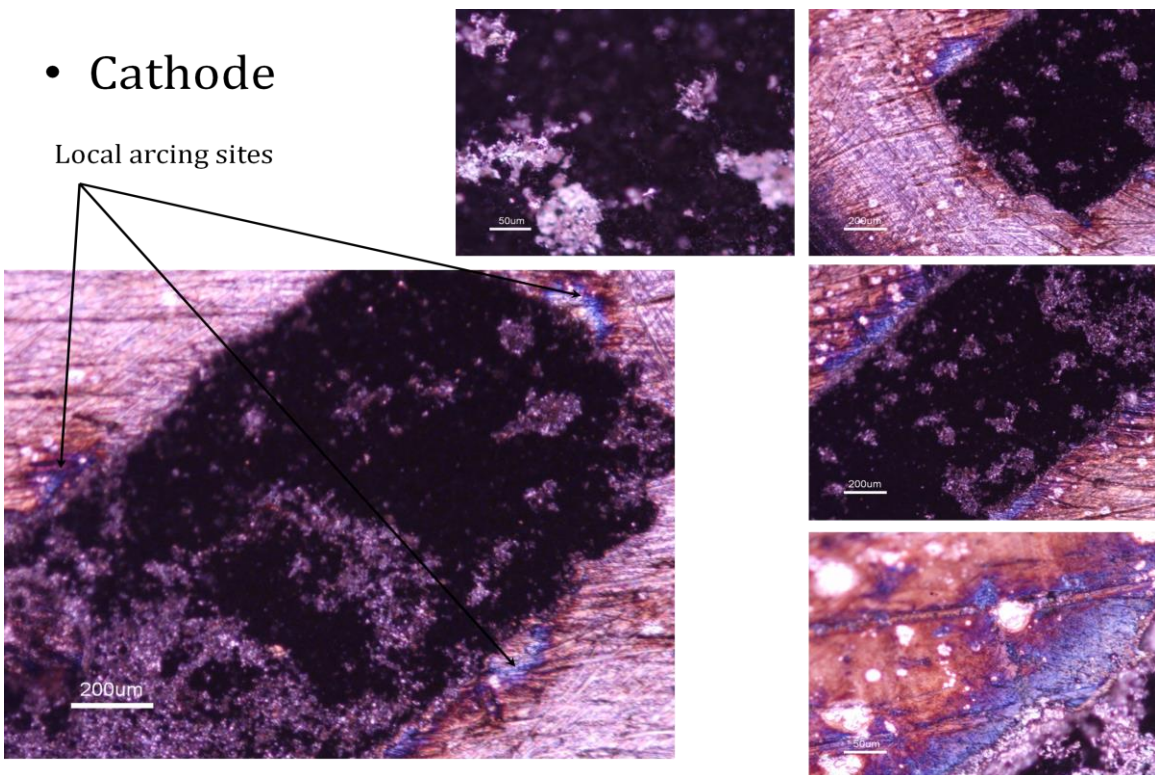


*Figure 43: Failure mode of Sealed Insert*

## 6.7 Annealing and Seasoning of the cathode in paste printed devices.

The method of construction of these cathodes, by vacuum filtration and screen printing, gives rise to an irregular array of emitters with many long features, as indicated in **Figure 44**, which may well have contributed to the observed instabilities in the measured data. In particular, excess conduction in the emitters having the highest aspect ratio would lead to selective conduction and ultimately damage as these would burn away.

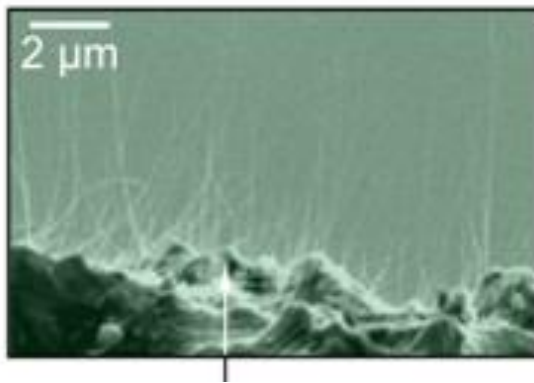


**Figure 44: SEM of Paste Printed CNT emitter**

Adapted from [6] – copyright American Institute of Physics

There have been various methodologies proposed which attempt to reduce temporal instabilities. Thermal annealing or electrostatic seasoning, to remove residual surfactants and non-uniform emitter profiles, are perhaps the most common, and certainly the most simple and readily implemented [1]. During thermal annealing the cathode assemblies are heated to temperatures in excess of 300°C under high vacuum conditions. This out-gases the emitter, removing weakly surface bound chemisorbed species which increases the work function uniformity across the surface of the emitter. Such out-gassing techniques are also useful in emitter recovery following an arcing event. Arcing events stimulate high current flow which heats and subsequently out-gases the emitter. This out-gassing can lead to further transient arcs which, if allowed to continue, will degrade the emitter. If the emitter is initially well out-gassed any local arcs will only marginally increase the cavity pressure and the emitter will stabilise more rapidly.

Annealing is also employed to enhance the pressure of the vacuum cavity, making local plasma formation increasingly unlikely. In the case of electrostatic seasoning, the

extraction electric field is slowly ramped up to around 80% of the nominal emission voltage. The emitters are then left emitting for tens to hundreds of hours to increase the surface smoothness of the emitter and hence, stabilise the emission current. Such approaches are critical in achieving intrinsic emitter stability, as can be seen in **Figures 38 and 39**, and though feedback techniques have been employed to artificially control the stability, engineering intrinsic stability remains central to the formation of a long-term stable emitter. In feedback based systems, such as has been implemented here, in the same way as conventional TE generator designs, the anode current is monitored and the extraction voltage adjusted accordingly to maintain a known, safe, emission current. Though this is a viable and widely adopted approach to ensuring emitter stability, the slow response times of the feedback loop cannot entirely remove transient effects, such as arcing events, and only careful design of the electron source can facilitate this.

Seasoning is a well known technique employed in conventional sealed TE X-ray tubes. When commencing the running of a brand new tube, manufacturers will recommend that it is “run-up” slowly. A typical profile would be to operate the tube while increasing the anode voltage in 10% steps at 60 minute intervals. This is known to prevent flashovers, by improving the vacuum levels present in the tube. It is a method that is also known to work when a tube has been seen to exhibit instability, especially after a long period when it has not been operational.

Tests on tube 5 did show increasing levels of instability as tests progressed over a period of about 4 hours. In addition, the peak beam current declined over this period.

Information from Xintek, a spin-out company from the group of Otto Zhou in North Carolina, indicated that they considered that it is beneficial to season a CNT tube for up to 5 days.

In this experiment, the tube has been run at  $V_a = 30\text{kV}$ ,  $V_g = 3800$ , firstly for about 24 hours, with the results shown in **Figure 45 and 46**. Whilst this is different from thermal annealing, it was hoped that the process of seasoning by running the tube for a long period, would improve the temporal stability. In fact the results of this were inconclusive, and therefore, after that, it was run at the same levels for a further 48 hours with monitoring enabled (as shown in **Figure 47**). This process was then continued for several days to see if the tube recovered, but this was without any further improvement.

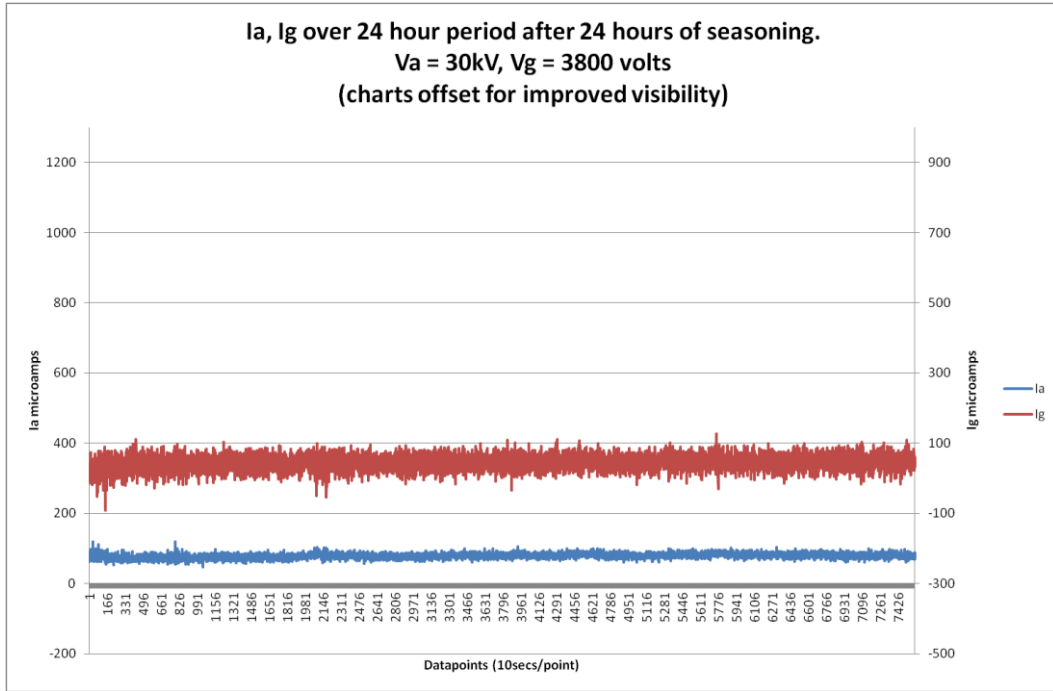


**Figure 45: Plot of attempted re-seasoning of tube**

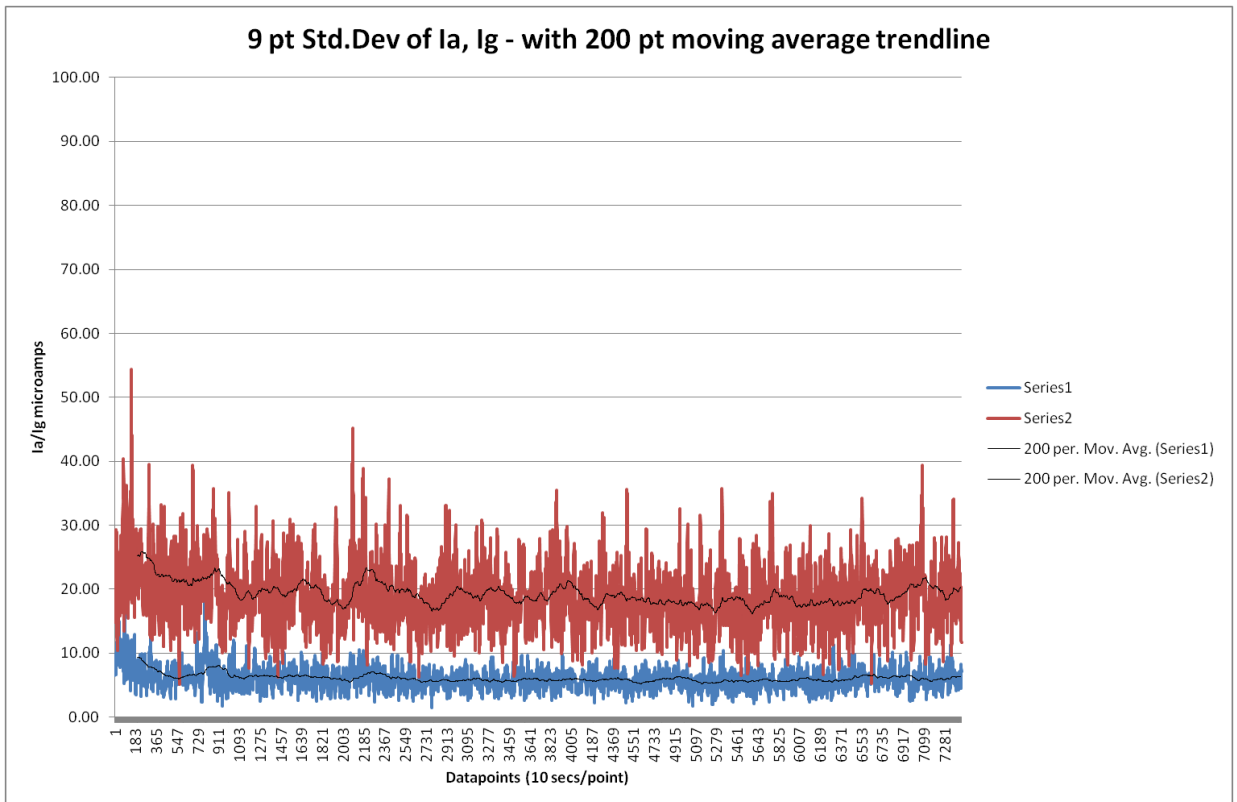


**Figure 46: Plot of attempted re-seasoning**

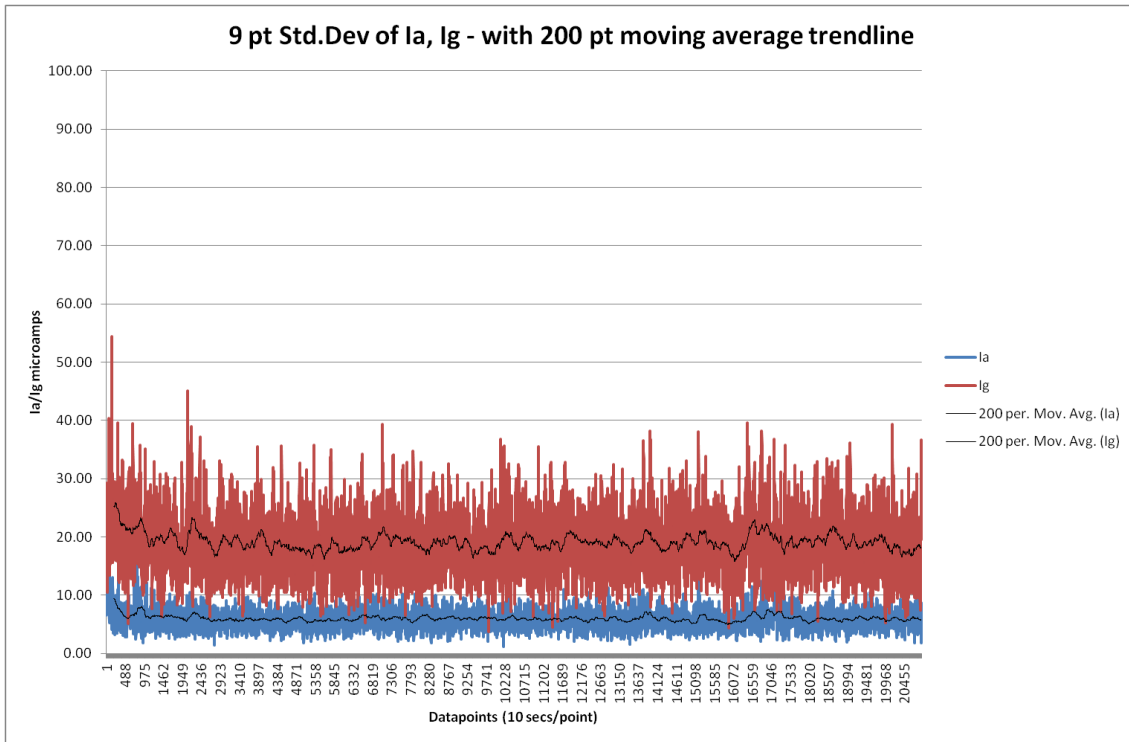


**Figure 47: Plot of attempted re-seasoning 48 hours**

## 6.8 Conclusions

It can be seen from **Figures 39** and **40**, that the variation in Grid Voltage ( $V_g$ ) is indeed controlling the anode current ( $I_a$ ). However, the anode current represents only about 50% of the associated cathode current. This suggests that a large proportion of the cathode current is as a result of electrons captured on the grid, rather than passing through the grid to the anode.

**Figure 42**, indeed does show that the grid has a low ratio of aperture to solid grid area. It also shows that the periphery of each hole exhibits sharp edges, which will preferentially attract electrons. This situation should be compared with the results from the triode study in **Chapter 9**.

The results of the work described in the chapter, make it clear that the failure modes require detailed study. Furthermore, it is necessary to understand the optimum parameters for the physical construction of a FE Xray tube and to select the best cathode construction methods.

In addition, the manufacturing process for sealed inserts, does not produce vacuum levels which are either well defined, or as high as can be achieved using a conventional vacuum

chamber utilising a turbo pump, and indeed which cannot be readily measured. This is introducing additional unquantifiable variables.

As a result of this, the method of fabrication using paste printed cathodes, was discarded in favour of Chemical Vapour Deposition. Chemical vapour deposition (**Chapter 3, Figure 11(f)**) provides a more controllable means of growing CNTs. The CNTs self-assemble from atomic units in a highly parallelised process, which when coupled with high resolution lithographic techniques, allows for near nano-scale engineering of the CNTs and CNFs. Such CVD techniques mediate the growth of chemically untreated disordered or aligned CNT thin films depending on the substrate, catalyst and growth precursors employed. In a typical implementation, Silicon is coated with a physical vapour deposited metal catalyst which can be patterned *via* lithographic or masking techniques by either additive or subtractive process, such as magnetron sputtering, or plasma etching, respectively. The substrate is then heated to temperatures often in excess of 500°C, and the growth of the CNTs on these sites is initiated by supplying a hydrocarbon feedstock gas, such as CH<sub>4</sub> or C<sub>2</sub>H<sub>2</sub>, combined with an *a*-C etching gas species, typically H<sub>2</sub> or NH<sub>3</sub> both of which readily pyrolyse to give a constant supply of carbon and atomic hydrogen. In situ plasma can also be employed to enhance the catalysis and align the CNTs during growth. [2].

In addition, the significant costs and manufacturing delays involved in the use of glass inserts, combined with the inability to measure or control the vacuum, have led to the conclusion that the optimisation process would be expedited by developing a special purpose vacuum chamber, or “demountable” tube. This permits the rapid repair and replacement of components, the means to monitor pressure levels accurately and provides the ability to explicitly analyse failures. In traditional TE generators, such tubes have often been used in applications where internal components may need to be replaced, such as micro focal X-ray tubes, where the current density through a very small area of the anode creates significant erosion, and hence degradation of the target.

The following **Chapter 7** will deal with the design and construction of such a device, and in particular its adaptation for CVD grown CNT arrays.

## 6.9 References

- 1 CALDERÓN-COLÓN, X., GENG, H., GAO, B., AN, L., CAO, G. & ZHOU, O. 2009. A carbon nanotube field emission cathode with high current density and long-term stability. *Nanotechnology*, 20, 325707.
- 2 COLE, M. T., COLLINS, C., PARMEE, R., LI, C. & MILNE, W. I. 2015. NanoCarbon Electron Emitters: Advances & Applications. *Chemical Functionalisation of Carbon Nanomaterials: Chemistry & Applications - Structure & Synthesis* Taylor & Francis.
- 3 COOLIDGE, W. D. 1913. A Powerful Röntgen Ray Tube with a Pure Electron Discharge. *Physical Review*, 2, 409-430.
- 4 MURPHY, E. L. & GOOD, R. H. 1956. Thermionic emission, field emission, and the transition region. *Physical Review*, 102, 1464-1473.
- 5 PARMEE, R. J., COLLINS, C. M., MILNE, W. I. & COLE, M. T. 2015. X-ray generation using carbon nanotubes. *Nano Convergence*, 2, 1.
- 6 J Ryu, J Kang, K Park, Carbon Nanotube Electron Emitter for X-ray Imaging. *Materials* 5, 2353-2359, (2012).

# 7 DEMOUNTABLE ASSEMBLY

## 7.1 Background

In the previous section, an early stage of the development of CNT cathode Xray tube has been described. Paste printed cathode assemblies have been produced and mounted into sealed glass inserts (see section 6.2). Since the process of mounting the cathode unit into the evacuated tube was sub-contracted to a conventional TE X-ray tube manufacturer, the turn-around time for this process was several months. During testing of these devices, early failure of the cathode has been seen to result in the catastrophic destruction of the tube, in all cases within several hours.

As a result of this, a demountable tube has been designed, together with an adjustable cathode assembly which allows the evaluation of tube performance at various geometries, voltages and dimensional parameters.

## 7.2 Design of Motorised Cathode Assemblies

An essential part of the design of the demountable tube, is the ability to vary parameters within the device. This becomes necessary in order to undertake a rigorous analysis of the performance of the device under a wide range of dimensional conditions, in a methodical and automated way, and is therefore necessary to create a design in which various features are hence controlled by computer. Most importantly, these should be adjustable without having to compromise the vacuum.

The two important dimensions are :

- Gate/Cathode assembly to anode distance
- Cathode to gate dimension within the cathode assembly.

The first of these is relatively straightforward. The Gate/Cathode assembly can be mounted onto a stage that is external to the vacuum chamber. The motorisation is therefore not in a high vacuum environment and the position of the stage can be readily monitored by an electronic scale.

However, the second stage is considerably more involved. The motorisation must be located within the vacuum chamber, and activated by signals introduced through feed-throughs. The chamber volume needs to be minimised to allow for rapid evacuation of the chamber. This therefore precludes incorporating a significant level of instrumentation internal to the chamber.

The design and prototyping of the cathode assembly consists of the following stages :

- Concept design of the motion stage
- Detailed design and 3D model
- 3D Printed prototype
- Final prototype manufactured from machined Aluminium
- High voltage wiring – thermo setting adhesive
- Motor selection, suitable for high vacuum operation
- Unit assembled and motor tested
- Develop techniques of attaching and removing TEM grids
- Develop techniques of attaching silicon chips

### 7.3 Cathode concept design - motorisation

From the initial work, one of the most important of these is the cathode-gate separation. This has been achieved by mounting the cathode on a motorised stage within the assembly. The motorisation is achieved by means of a jacking screw, which is rotated by means of a stepper motor, as shown in **Figure 48**.

## 7.4 Detailed 3D model and design

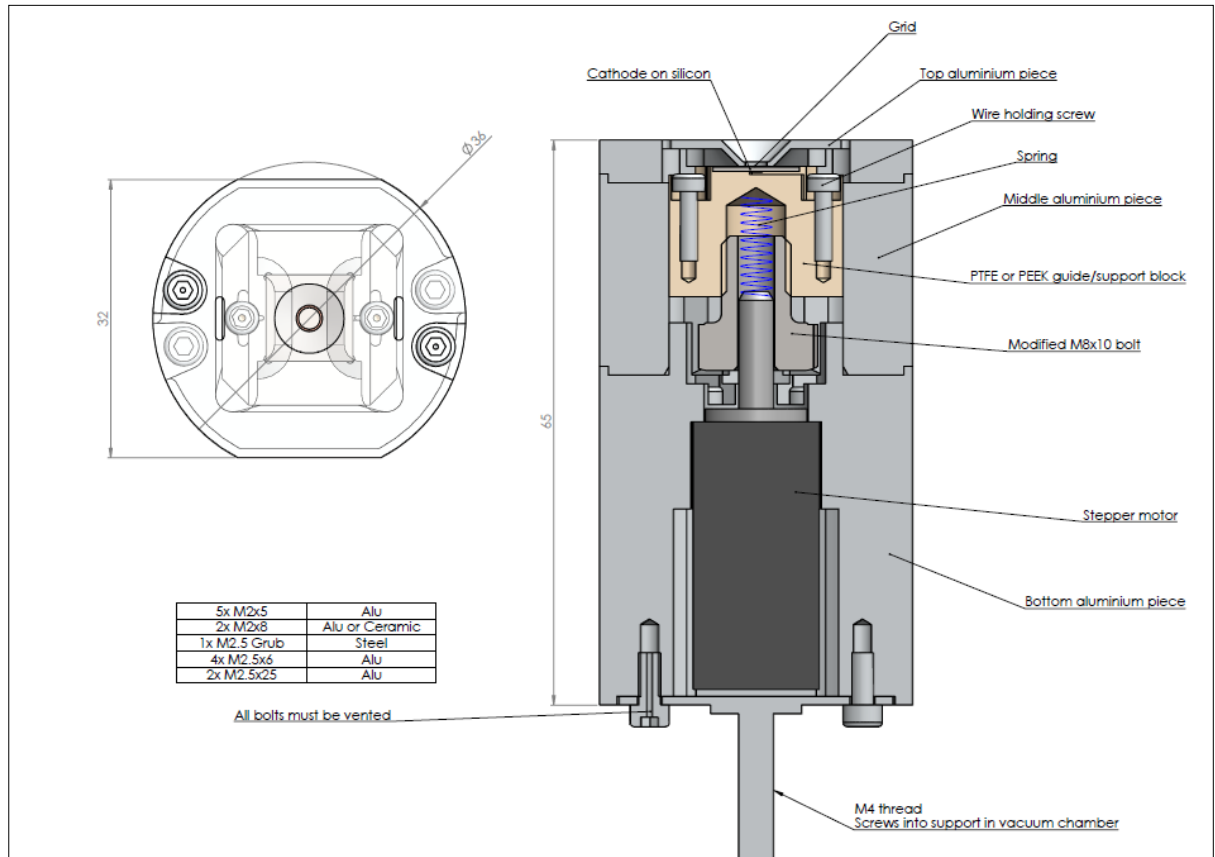


**Figure 48: Detail of the Cathode assembly showing Jacking screw.**

The jacking screw is rotated by means of a miniature stepper motor. The stepper motor is driven by means of an external bipolar drive card, requiring 4 wires to pass into the chamber. The complete cathode assembly is shown in **Figure 49**.

The motor is driven in half-step mode, which causes a rotation of 0.9 degrees per step, or 400 steps per revolution. The movement per step is therefore defined by the pitch of the jacking screw. In this case, the screw is a standard M8 course pitch bolt with a pitch of 1.25mm. Hence the expected linear movement is about 3 microns / step.

Because of the small size of the assembly, it becomes necessary to estimate the position of the cathode relative to the gate, by dead-reckoning. The process of setting up a cathode-gate dimension is therefore :

- Drive the motor vertically upwards (say) 500 steps, so that the carriage bottoms out on the lower face of the gate top-piece.
- Drive the motor in reverse, at low speed, for N steps, where :
- $N = d * 400 / 1250$  steps

- Execute measurement cycle.

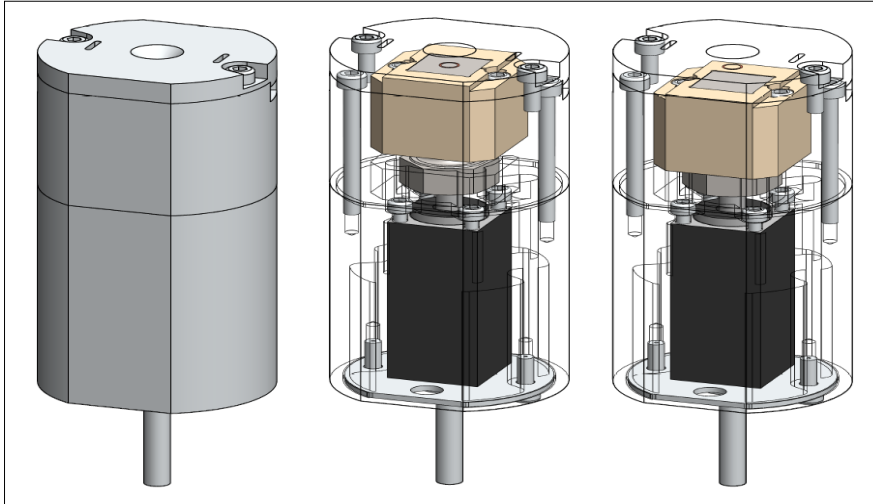


*Figure 49: Rendered drawing of Cathode assembly.*

## 7.5 Cathode concept design – chip carrier

The chip carrier is the vertically sliding part of the cathode assembly. It is machined to be a sliding fit within the body of the assembly, constructed of PEEK [1], which combines high radiation resistance and a very high insulation resistance over a broad temperature range. The machined rebate locates the silicon chip which carries the CNT emitters. The chip is located and secured with silver DAG and conductive adhesive. The rear of the chip is connected by means of a Kapton wire to a high voltage feed-through, which can set the voltage of the cathode – relative to the body of the assembly, and gate assembly at a high voltage.

## 7.6 Cathode concept design – electrical

Supporting the cathode/gate voltage of up to 5000 volts, the rear of the silicon chip which carries the CNT emitter array, is connected to high voltage feed-throughs. There is the provision for a second high voltage connection to facilitate a connection to a separate plane of control electrodes which would contact through the front face of the chip (see section 8.8). Particular attention has been given to material within the chamber that might out-gas or otherwise compromise the vacuum integrity. High voltage compatible Kapton wire has been used with appropriate connections, and insulation is maintained by using herring bone ceramic stand-offs.

## 7.7 Cathode concept design – Gate

The gate cap of the cathode assembly carries the grid which provides the transparent window through which the emitted electrons pass. The assembly has been designed to accept a standard TEM grid, secured by thermo plastic adhesive, or a graphene window [2, 3]. This provides a means of interchanging grids, as a further key optimisation parameter.

## 7.8 3D Printed prototype

The design was initially evaluated by mean of 3D printing, shown in **Figure 50**, to ensure the correct alignment of the parts.

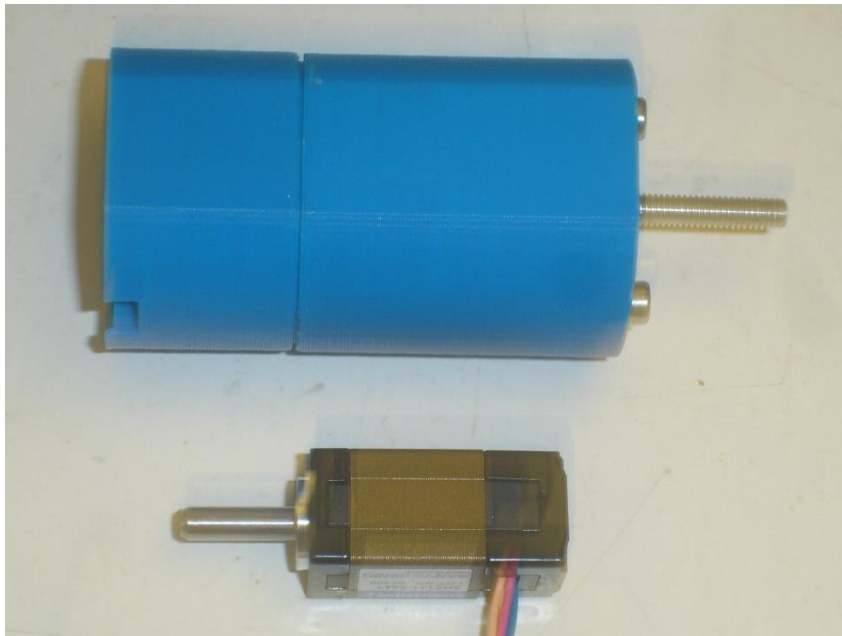


*Figure 50: Stepper motor used to operate jack*

At the top of the assembly, there is a plate that supports the gate, shown in **Figure 51**. The purpose of the gate is to draw electrons away from the cathode, by setting up the extraction E-field. The gate initially comprised a standard TEM grid which was attached to a rebate in the rear of the top cap of the cathode assembly.

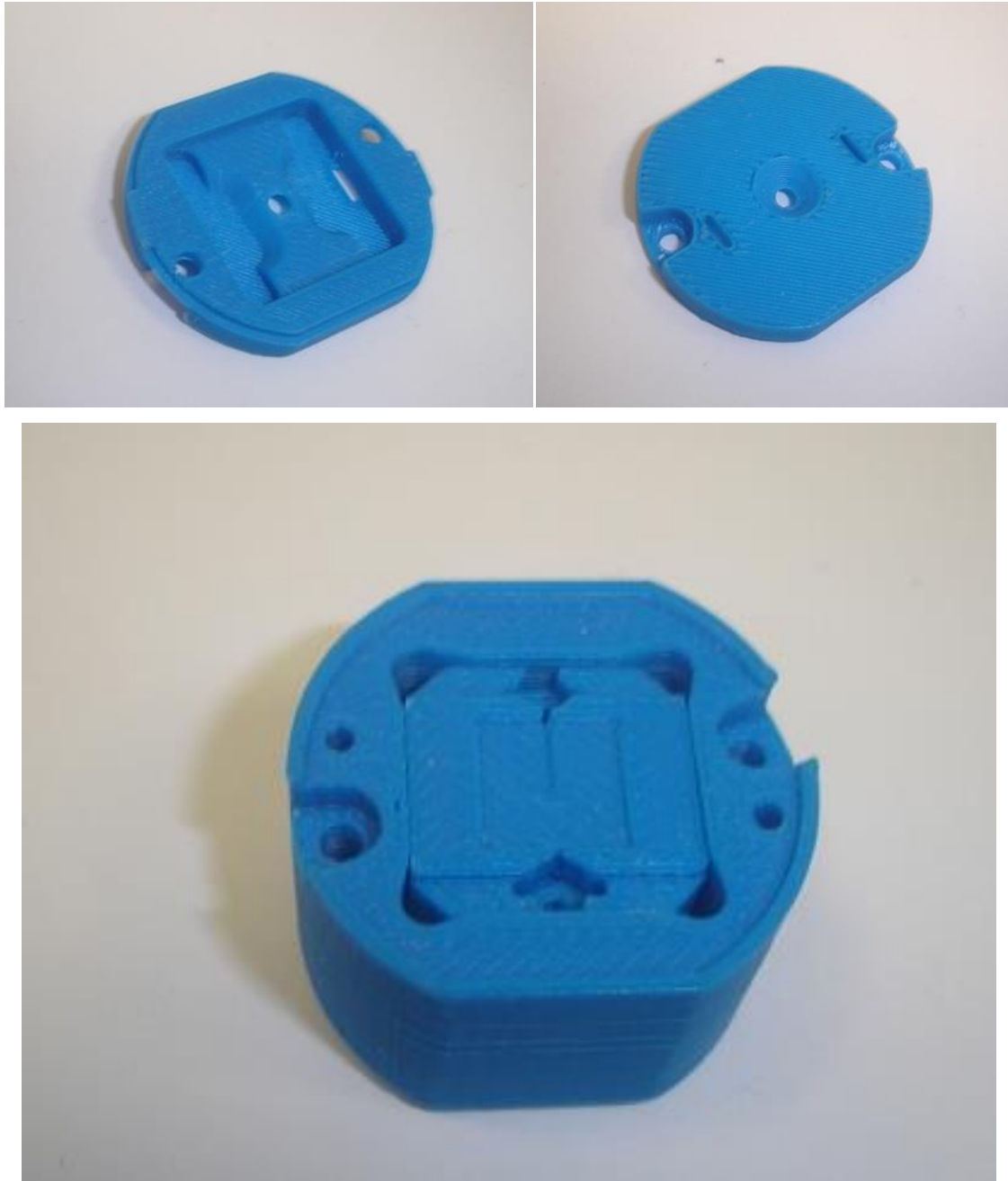


*Figure 51: 3-D printed Cathode assembly components.*

## 7.9 Cathode-Anode assembly motorisation

The entire cathode assembly is mounted on the end of a stepper motor driven slide. This allows the distance between the cathode assembly and the anode of the tube to be adjusted.

The detail of the interior of the vacuum chamber is shown in **Figure 52**. To the right is the anode of the triode, with high voltage feed-throughs, capable of supporting up to 20kV in air and 50kV in oil

In the centre is the cathode assembly as described above

At the left is a cross-piece that provides access to the chamber via feed-throughs and supports the cathode mount which is motorised by the external slide.

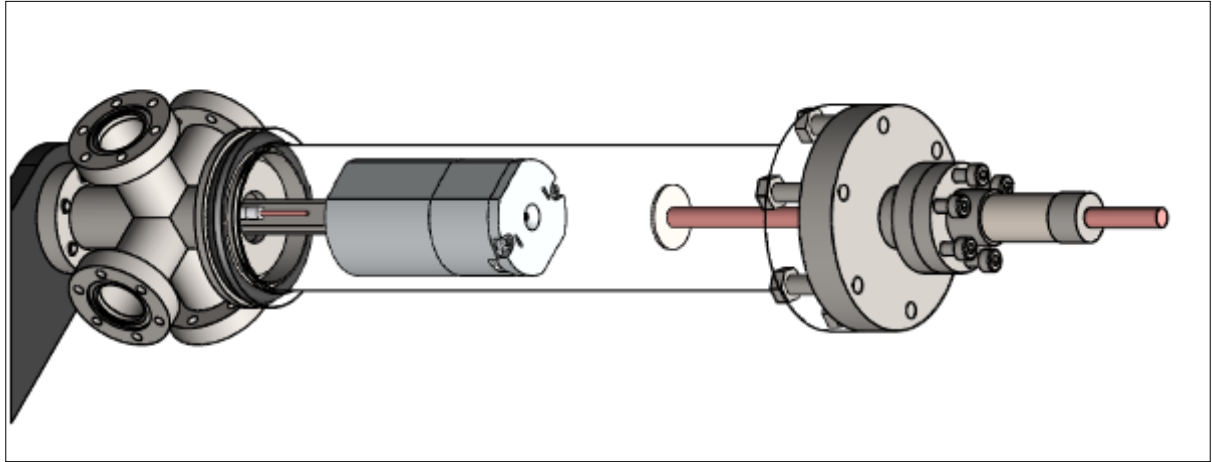


*Figure 52 : Vacuum chamber layout.*

## 7.10 Vacuum system

The stages in the design of the vacuum chamber are as follows :

Vacuum chamber

- First phase - basic chamber with flat anode for cathode development – 10kV
- Full chamber with Be window for XR generation – 50kV
- Detailed design of phase 1 chamber and 3D modelled
- Design of special high voltage FT and cathode support
- RFQ submitted to suppliers – MDC and Lesker
- Slide with bellows used for cathode positioning – anode fixed
- Detail design of phase 2 chamber

The vacuum system is shown in **Figure 53**, and comprises a roughing pump, with a turbo pump to provide a capability to pump down to a vacuum of  $1e-7$  millibar. A Pirani gauge is used on the roughing side, and a full range Pfeiffer gauge is used on the high vacuum side. These were calibrated against standard gauges, with the results shown in **Figure 54**. The final design of the vacuum system is shown in **Figure 55**.

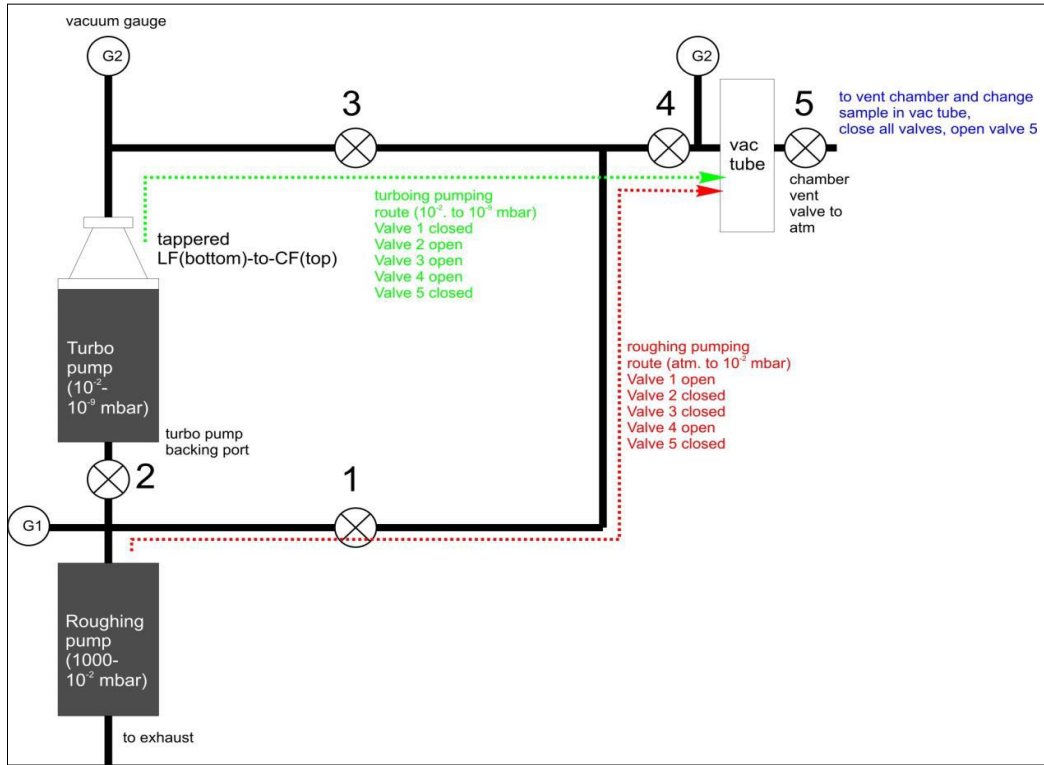


Figure 53 : Schematic of the Vacuum circuit

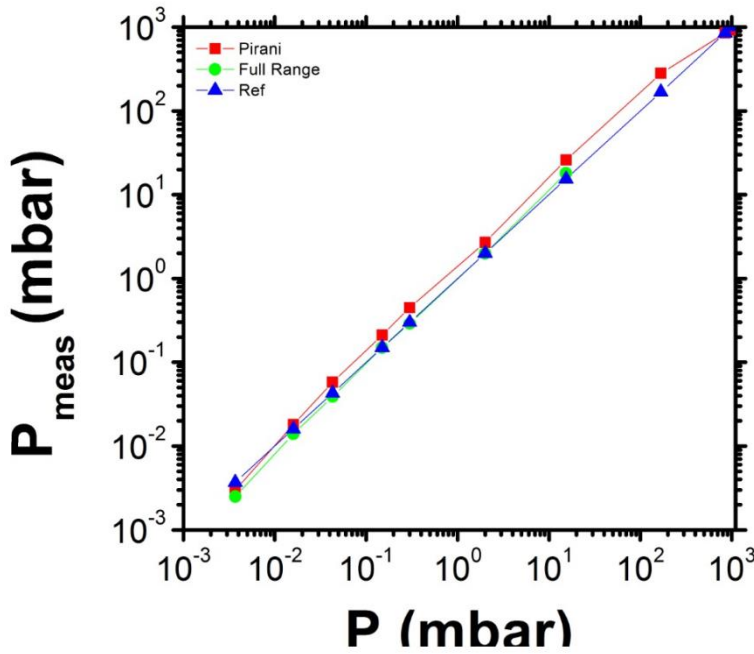
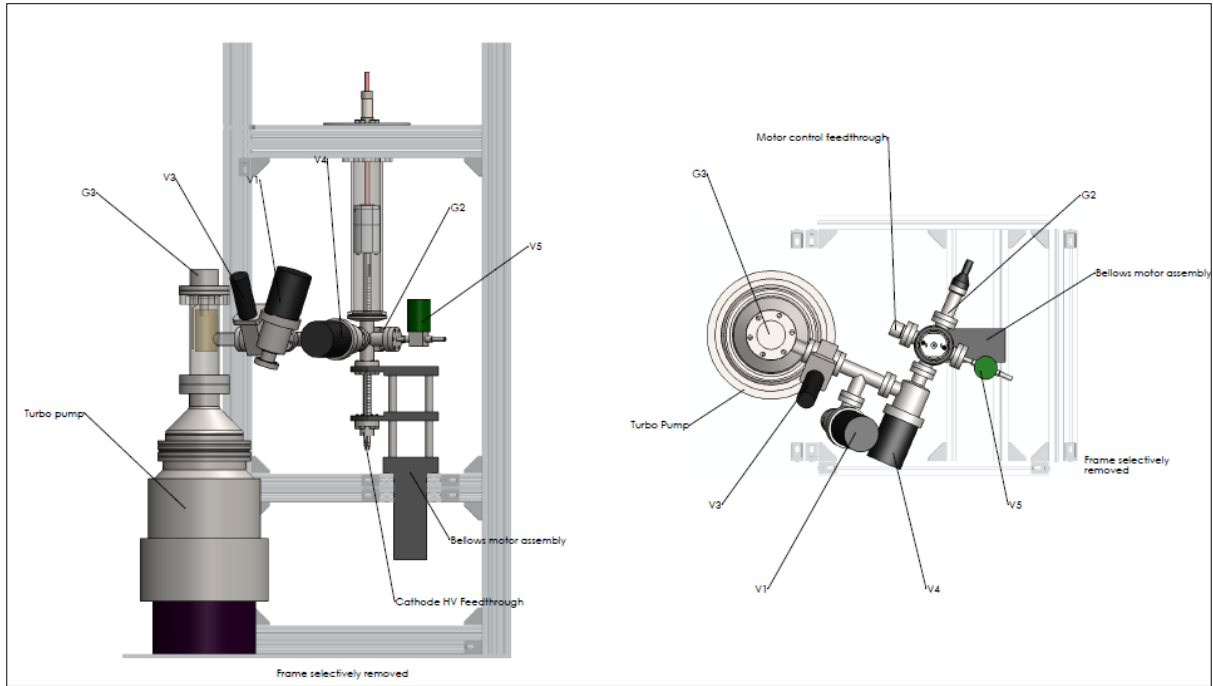


Figure 54 : Calibration of pressure gauges



*Figure 55 : Construction of CNT field emission X-ray tube.*

## 7.11 Vacuum Testing

Initially the vacuum system required some time to pump down and a bake-out procedure was needed to improve the base vacuum down to  $1e-7$  millibar. This process accelerates out-gassing and removal of water vapour in the vacuum system with a view to reducing the time taken to pump-down.

The process of bake-out involves wrapping the key vacuum components in an electrically heated tape, to raise the temperature. This was run over a period of 24 hours.

## 7.12 Interchange of Parts

During the research testing protocol, it is necessary to open the vacuum chamber to exchange parts, such as the silicon chips, which have different growth profiles and emitter patterns, and the grids in the gate assembly.

The chamber is removed by means of the KF40 vacuum fitting at the lower end of the chamber. This allows the body of the chamber to be withdrawn over the cathode assembly. In its open condition the cathode top cap may be removed, which exposes the chip location. This is shown in **Figure 56**, with the chip clearly visible in the centre of the PEEK carrier. **Figure 57** shows the connections to the stepper motor, used to adjust the position of the chip carrier relative to the top cap and grid.

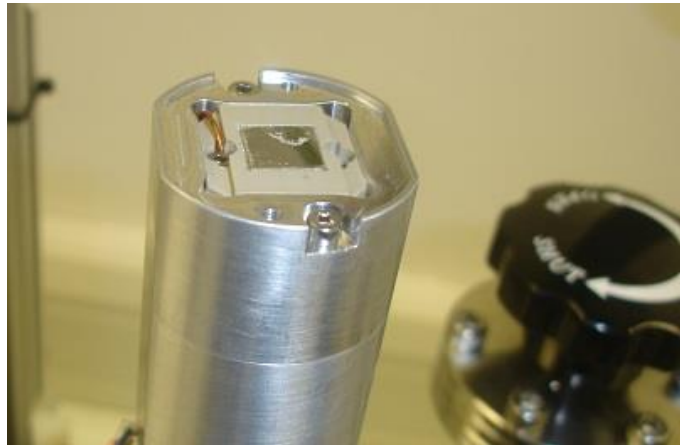


*Figure 56 : Vacuum chamber opened to view emitter chip.*

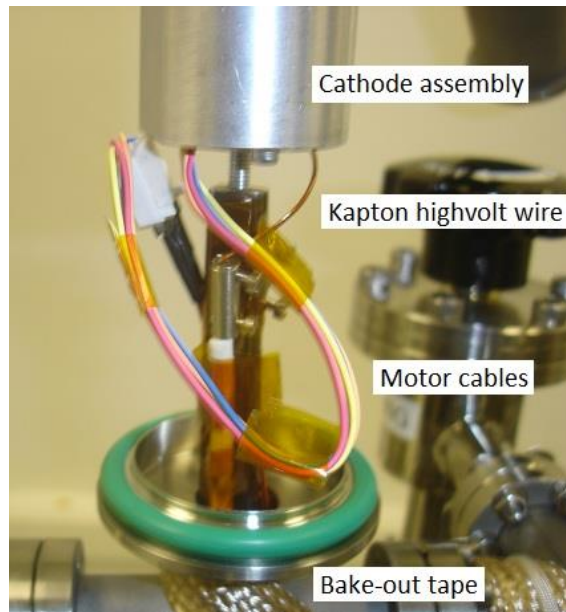


*Figure 57 : Open chamber showing connections and KF40 fitting.*

### 7.13 Research vacuum chamber assembly

The unit was constructed from an open aluminium profile framework, to support the vacuum circuit and associated valve, as shown below in **Figure 58**.

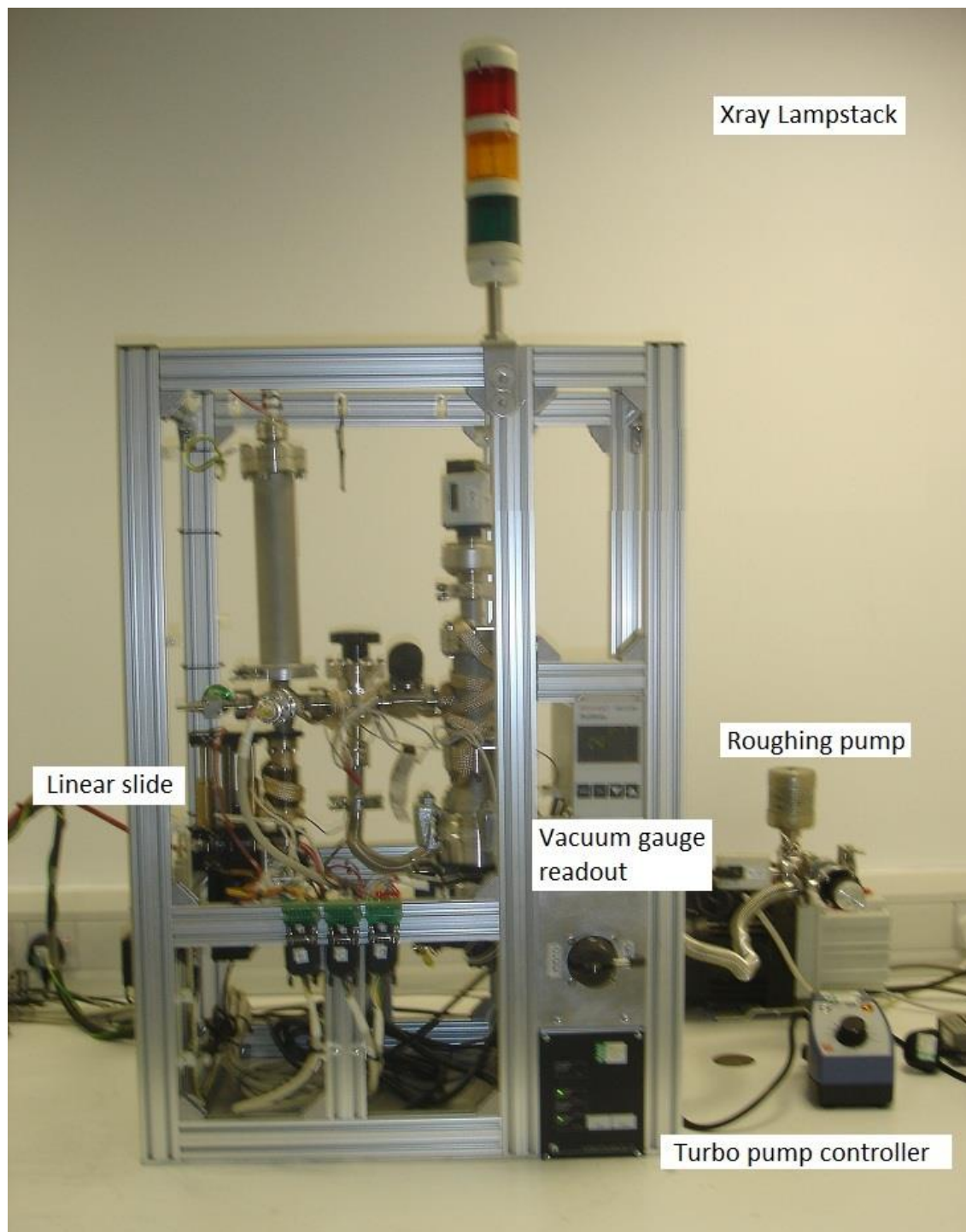


*Figure 58 : Vacuum chamber test rig*

The lamp-stack, indicating the Xray status is a mandatory requirement.

Included are the turbo pump and controller, gauges and vacuum chamber, as indicated in **Figure 59**, below.

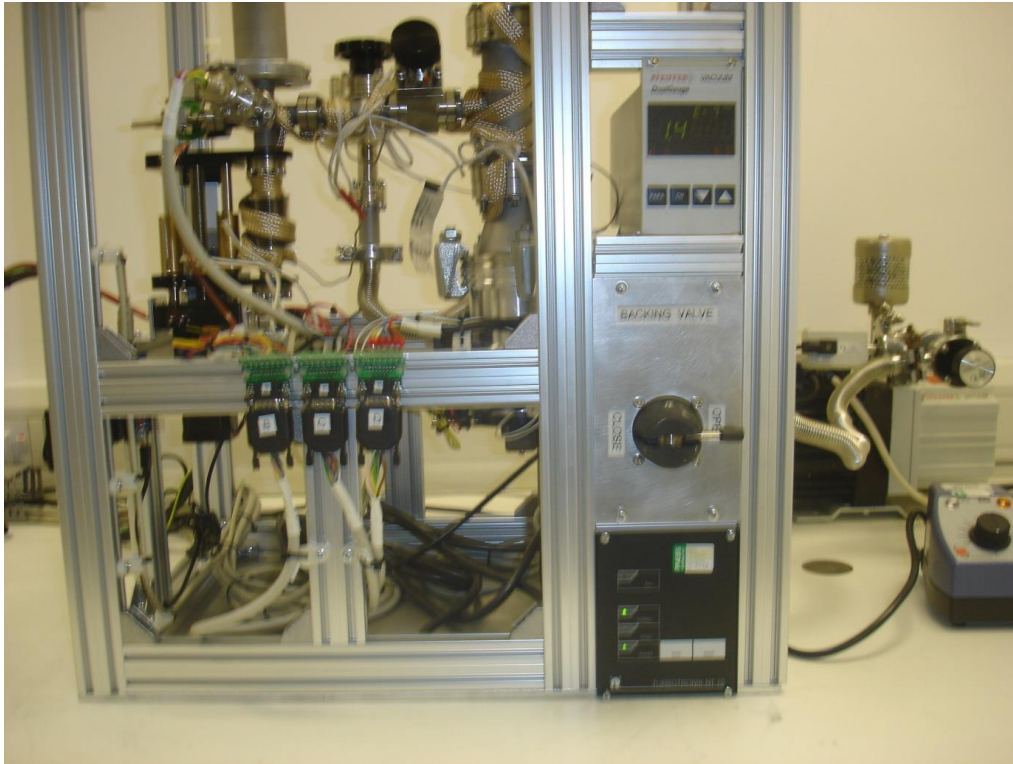


*Figure 59 : Detail of Vacuum test rig*

## 7.14 Control electronics

The control of the system is made through a commercially used “Xray Generator Control System” or “XGEN” module, designed and programmed by the author, and shown in **Figure 60**. The XGEN modules incorporates all of the interface and safety requirements generally needed in an industrial Xray system.

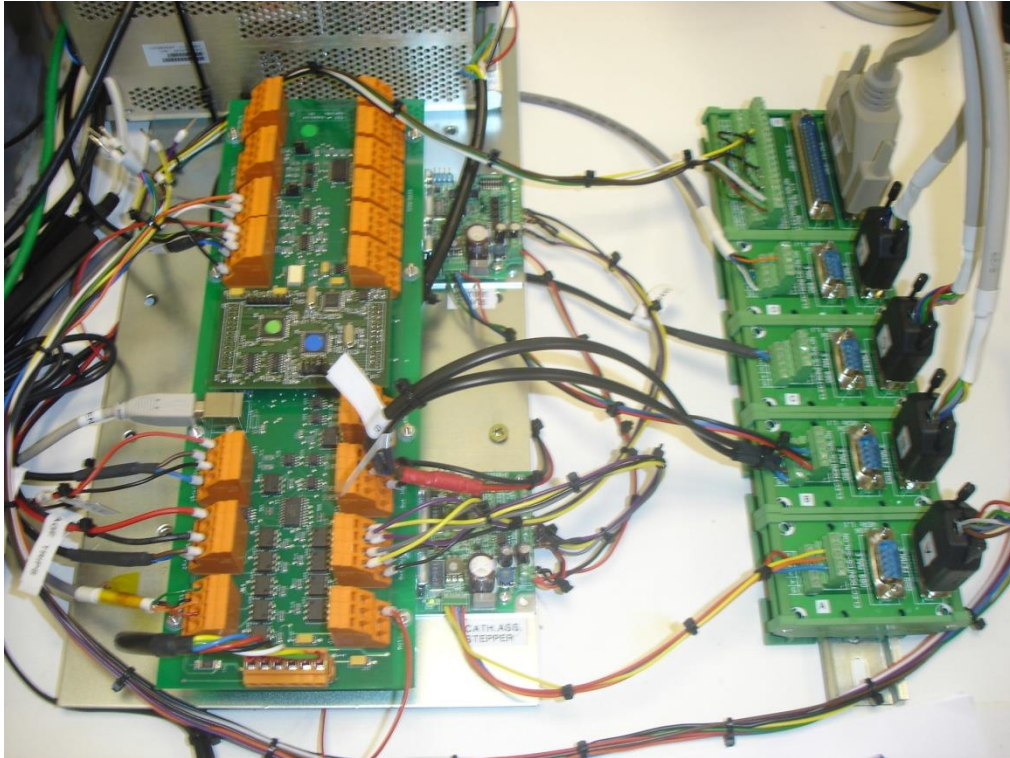


*Figure 60 : Control circuitry for test rig*

*adapted from electronics designed and made by the author.*

The Xray Generator Control Module is responsible for the following functions :

- Control of the high voltage power supply
- Operation of the lamps and outputs
- Monitoring of interlock and fault condition circuits
- USB communications with the main computer
- Control of the conveyors and motors

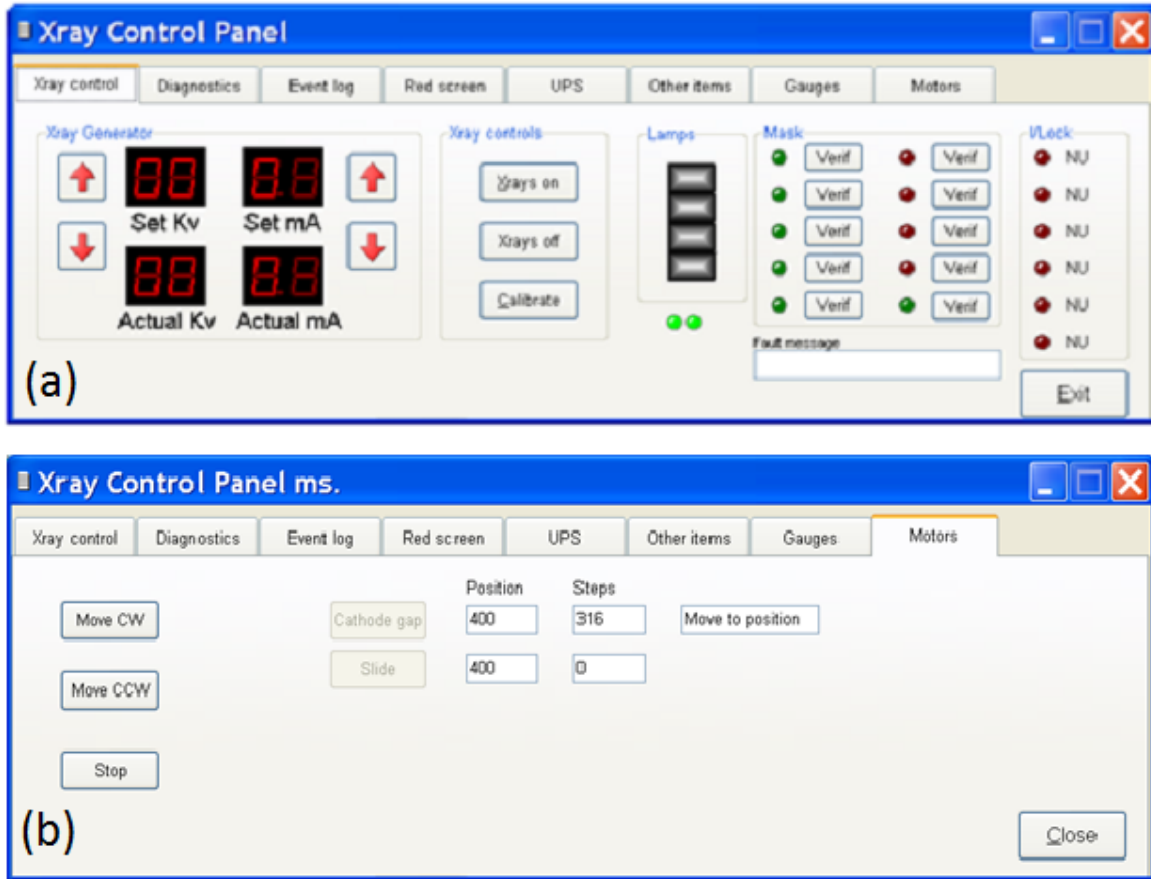


*Figure 61 : SDK interface for the XGEN control module.*

SDK user interface screens. (a) main user interface showing Xray controls and fault status indicators. (b) motor control tab.

Each function can be accessed by single letter commands, via a USB port.

The unit is connected via USB to a windows based computer. It is controlled via a SDK interface program, as shown in **Figure 61(a)**.

## 7.15 Special XGEN control functions

### 7.15.1 Motor control functions

The Field Emission unit requires the Cathode/Gate assembly to be moved to different positions within the chamber, as well as adjustment of the cathode/gate gap . This is done by moving the carriage assembly by means of a stepper motors activating a linear slide. The section of the user interface that controls this is shown in **Figure 61(b)**.

Limit switches, where applicable are PNP. This feature can be configured as an option in the XGEN configuration parameter :

Configuration

Set Option “Motor drive”     **O8**

Connections :

Function	Port	Direction	Connection
Output for “direction”	11	Output	J12/3 → J12/4
Output for “enable motor 1”	10	Output	J12/1 → J12/2
Output for “enable motor 2”	12	Output	J12/5 → J12/6
Output for “run motor”	13	Output	J12/7 → J12/8
Input for “slide home”	2	Input	J13/5 → J13/6
Input for “slide out”	3	Input	J13/7 → J13/8

Notes :

- The speed and ramp characteristics are set in the motor controller.
- There are no limit switches for the internal jacking screw.

The schematic is shown in **Figure 62**. The motion time-out can be set in timer counts (20 milliseconds). Motion will continue until the time-out or the appropriate slide sensor is activated. The default motion time is 5 seconds. To set the reverse direction, add 1000 to the parameter value. Example commands :

**H300**                      Set “motion” output on for 6 seconds

**H1500**                     Set “motion reverse” output on for 10 seconds

## Xray Generation by Field Emission

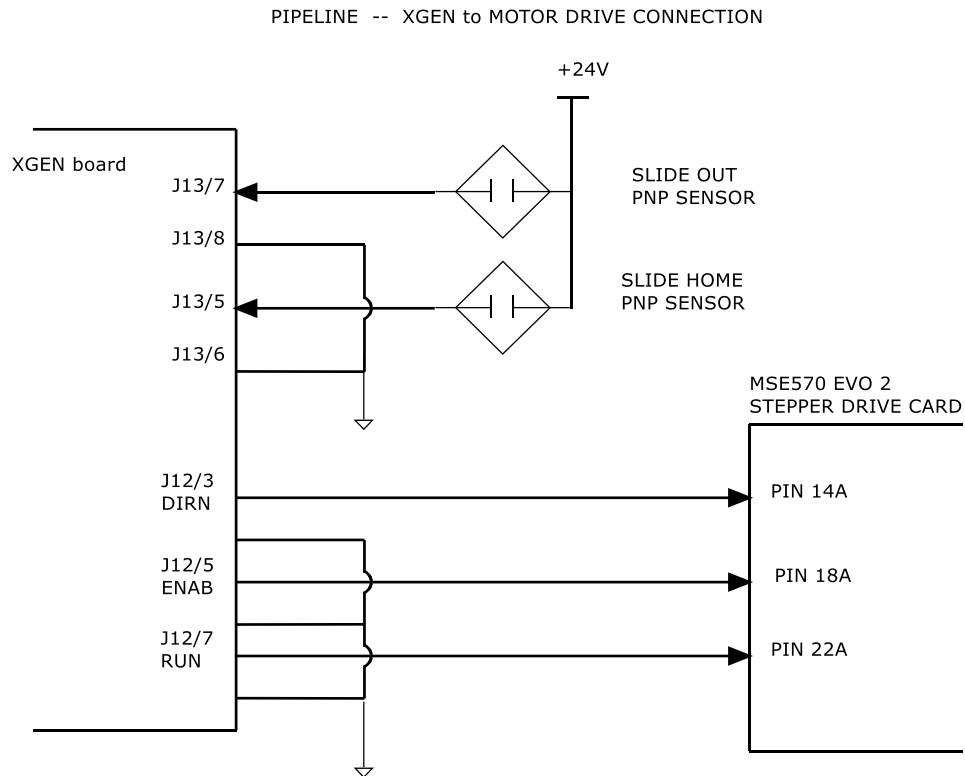


**Figure 62 : Control circuitry for driving stepper motors**

### 7.15.2 Alternative drive via high level commands

The program has been adapted to accept a series of high level commands which will explicitly control the motors. The command details are entered in the “Command” box in the Diagnostics tab, or can be passed to the program from another process via a shared memory map file (SMMAP).

The following commands are available :

Command	Function	Argument
Cathode+	Move cathode closer to gate	Distance (3μm) steps
Cathode -	Move cathode away from gate	Distance (3μm) steps
Slide+	Move cathode closer to anode	Distance
Slide -	Move cathode away from anode	Distance

The section of the software that executes these commands is listed in Appendix 3. The speed of stepping defaults to constants *stepspd* and *stepspd1* in the declarations.

### 7.15.3 Calibration of motors

In order to confirm the correct operation of the motors, and establish the relationship between the number of steps demanded and the physical distance moved, the motor assemblies were calibrated against a dial gauge, using the arrangement shown below :

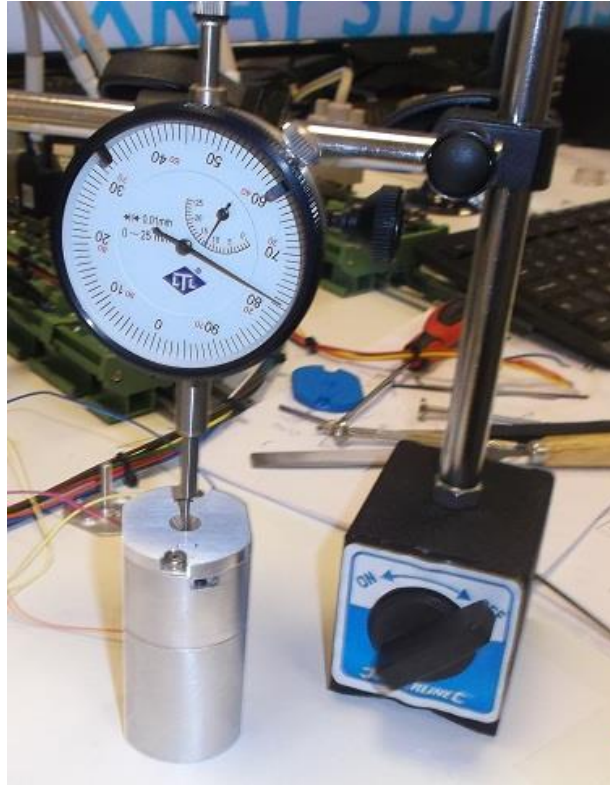


*Figure 63 : Calibration of movement of stepper motors*

### 7.15.4 Cathode Gap Calibration

It is clearly critical that the Cathode Gap motorisation is accurate and well understood, as the assembly is located within the vacuum chamber with no means of measuring the position other than by dead-reckoning.

The sequence used to position the cathode relative to the gate comprises the following steps:

- Advance the cathode in an upwards direction until its bottom is out on the cap of the cathode assembly. Referring to **Figure 48** it can be seen that the cap has pads which provide the cathode a surface on which to locate. The force applied will be

limited by the Dynamic Torque of the motor. The number of steps programmed was 2,500 which allows for a maximum movement of 3.0 mm.

- The step rate of the stepper motor is reduced, to increase the dynamic torque, and the motor is moved a further 10 steps in the upwards direction.
- With the reduced step rate, the motor is driven 10 steps in the downwards direction. This prevents the cathode assembly, driven by the jacking screw, from “lock-nutting” against the top cap of the assembly.
- The motor is then driven to its required position, in a downwards direction.

In order to determine the relationship between the position of the components and the command used by the software, a dial gauge was used to calculate and by repeatability, confirm the accuracy of the positioning system. This arrangement is show in **Figure 63**. The plot of the physical position versus the number of steps shows a movement per step of 1.4 microns, which is determined by the thread pitch of the jacking screw, as shown in **Figure 64**. The underlying data is shown in Appendix 6, from which the mean standard deviation of the repeat measurements is calculated as 11 microns.

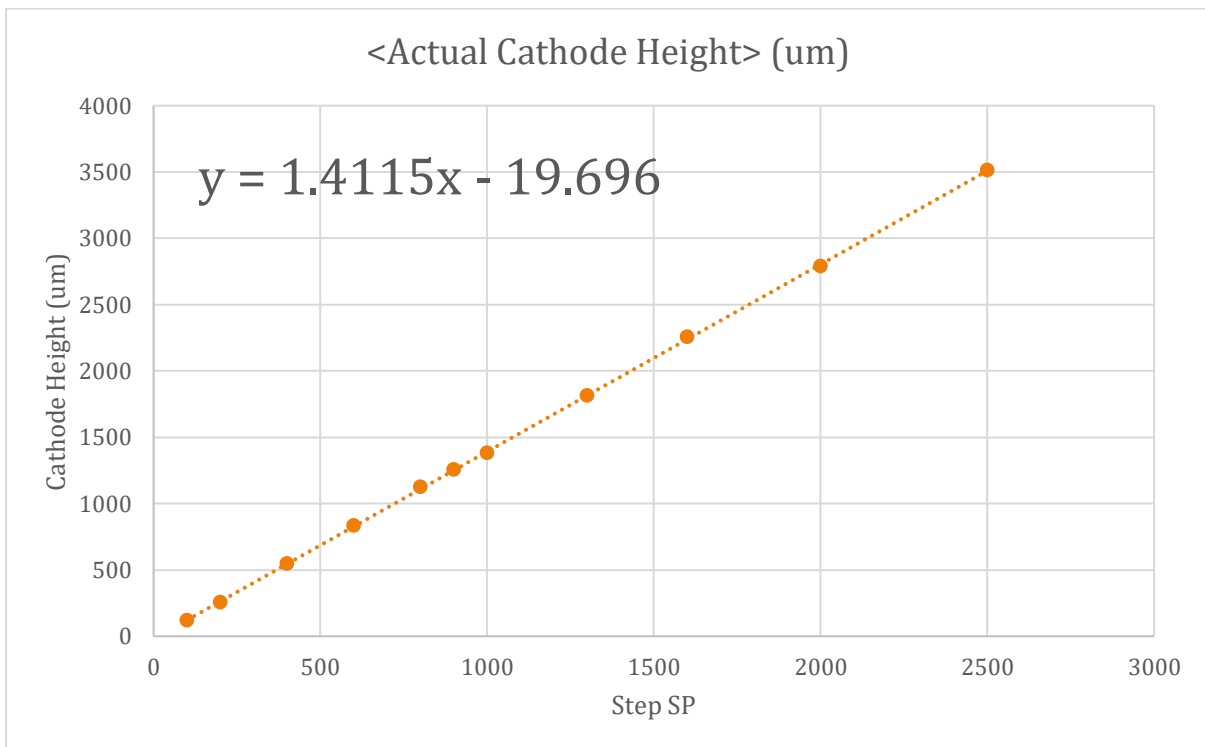


**Figure 64 : Calibration chart for the cathode stepper motor.**

### 7.15.5 Anode Position Calibration

The Anode to Gate position is adjusted by means of the motorised slide, which is outside of the chamber. As such, it is a much easier procedure, as the home position of the slide can be determined by a limit switch, and the assembly is accessible and visible.

A similar sequence was programmed, except that in this case, it is possible to explicitly determine when the slide carriage activates the limit switch. The plot of the physical position versus the number of steps shows a movement per step of 0.79 microns, which is determined by the pitch of the lead screw, as shown below in **Figure 65**. The underlying data is shown in Appendix 6, from which the mean standard deviation of the repeat measurements is calculated as 20 microns.

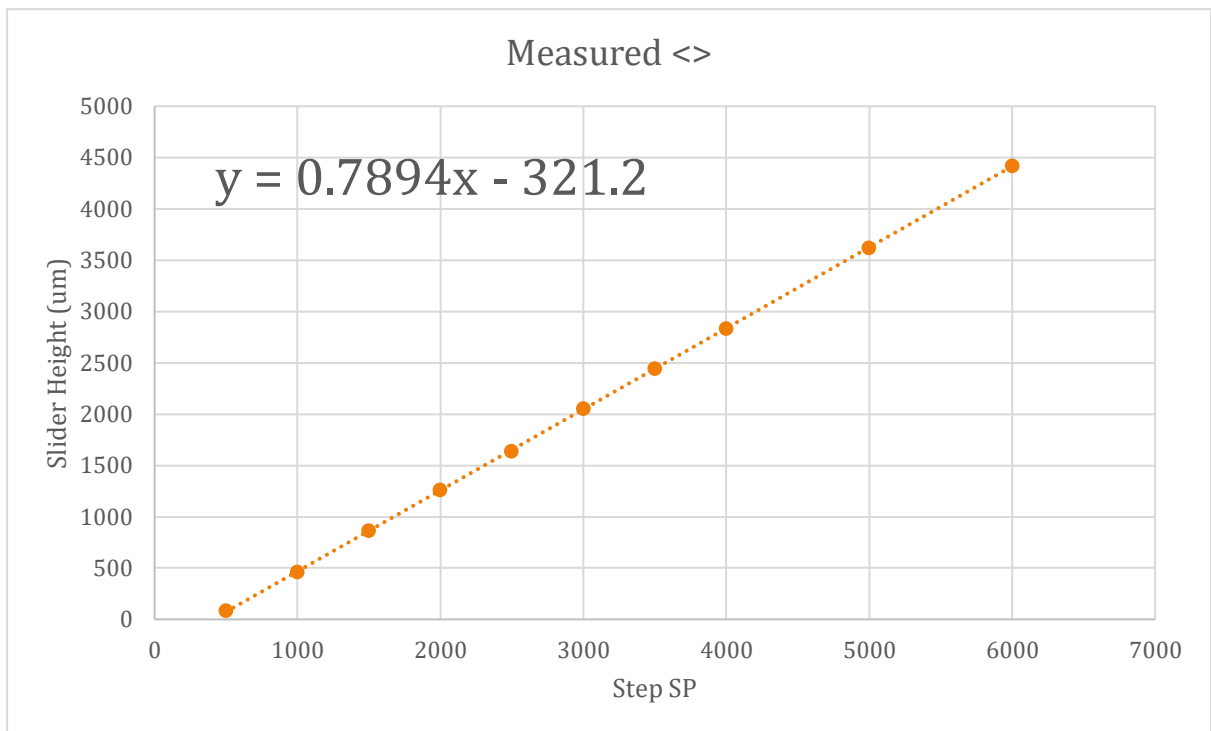


*Figure 65 : Calibration chart for the assembly stepper motor.*

### 7.15.6 Pressure gauge monitoring and Pump interlock

The XGEN module also provides the means of monitoring the pressure gauges, and controlling the pumps. Certain controls and interlocks are important when operating a turbo pump. For example, the pump may be damaged unless the roughing pump has already reduced the vacuum level to less than 1.0e-2 millibar.

The software, described in Appendix 3, sends alternately requests to read the Pirani gauge and Full range gauge, once every 250ms. The response is parsed, and any error condition is displayed, as shown below in **Figure 66**. The turbo pump may be enabled providing there is no error status from the Pirani (other than “UR”=under-range) and the exponent is less than -2. The pump may be over-ridden by pressing the appropriate buttons, as long as the safety conditions are met.

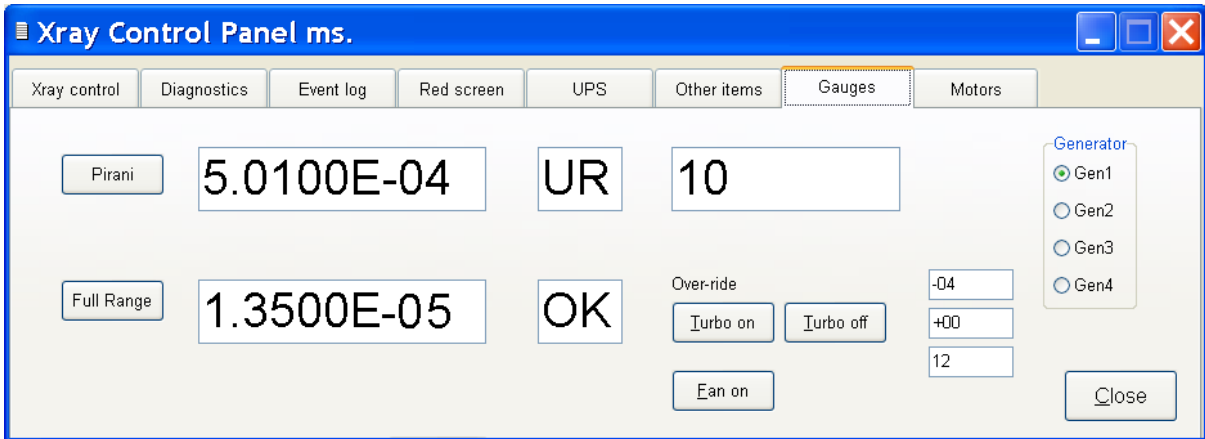


*Figure 66 : Pressure gauge monitoring in normal running condition.*

The turbo pump is equipped with a water cooling system, with a radiator and fan. The cooling fan may be turned on and off by touching the button on the user interface. An example of the situation where the Turbo pump is inhibited due to insufficient internal vacuum is show in **Figure 67**.

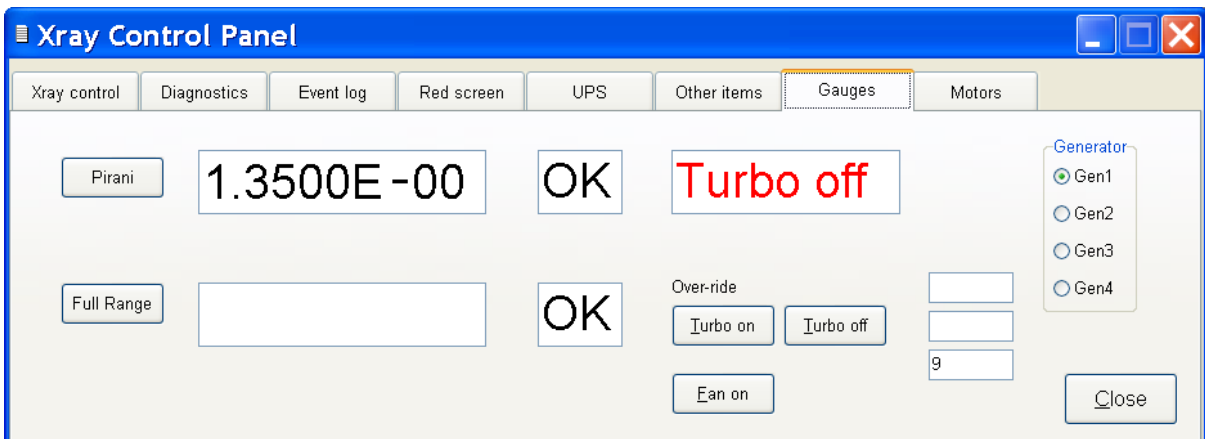


*Figure 67 : Pressure gauge monitoring with roughing pump inactive.*

## 7.16 Modifications to the Chamber

The demountable test rig previously described, was designed with a basic vacuum chamber, incorporating the cathode assembly, and a planar anode. There was no provision to direct any X-ray emission away from the direction of the electron beam, or to allow those X-rays to emerge from the chamber. This was done for reasons of simplicity and safety.

Here, I describe the modifications that may be made to the chamber to permit the X-rays to pass from the chamber. This requires several steps.

### 7.16.1 Beryllium window.

A suitable port in the chamber is needed to allow the Xrays to pass out of the chamber, but retain the vacuum. Since Xrays are strongly attenuated by materials with a high atomic number, the conventional approach is to create a window of a material such a beryllium. Beryllium is stable and may be easily worked, while having an atomic number of 4. A typical beryllium window assembly comprises a steel foot with a thin beryllium sheet attached to it – typically 250 to 500 microns in thickness.

### 7.16.2 Thermal dissipation.

In a conventional Xray tube, while there is thermal dissipation from the filament that represents the cathode, the majority of the heat generated is from the anode. This is because the efficiency of the conversion from the beam current to Xray photons is generally of the order of 1%. So, at a beam current of 2mA and an anode voltage of 50kV, at least 99W of heat will be generated in the anode.

Since the anode will usually comprise a large block of copper, this heat is normally conducted away to the exterior of the tube. At this point it is transferred to a radiator, which may conduct the heat away by air cooling. A preferable solution is to immerse the radiator in oil, since this will perform the dual function of thermal transfer, and electrical insulation.

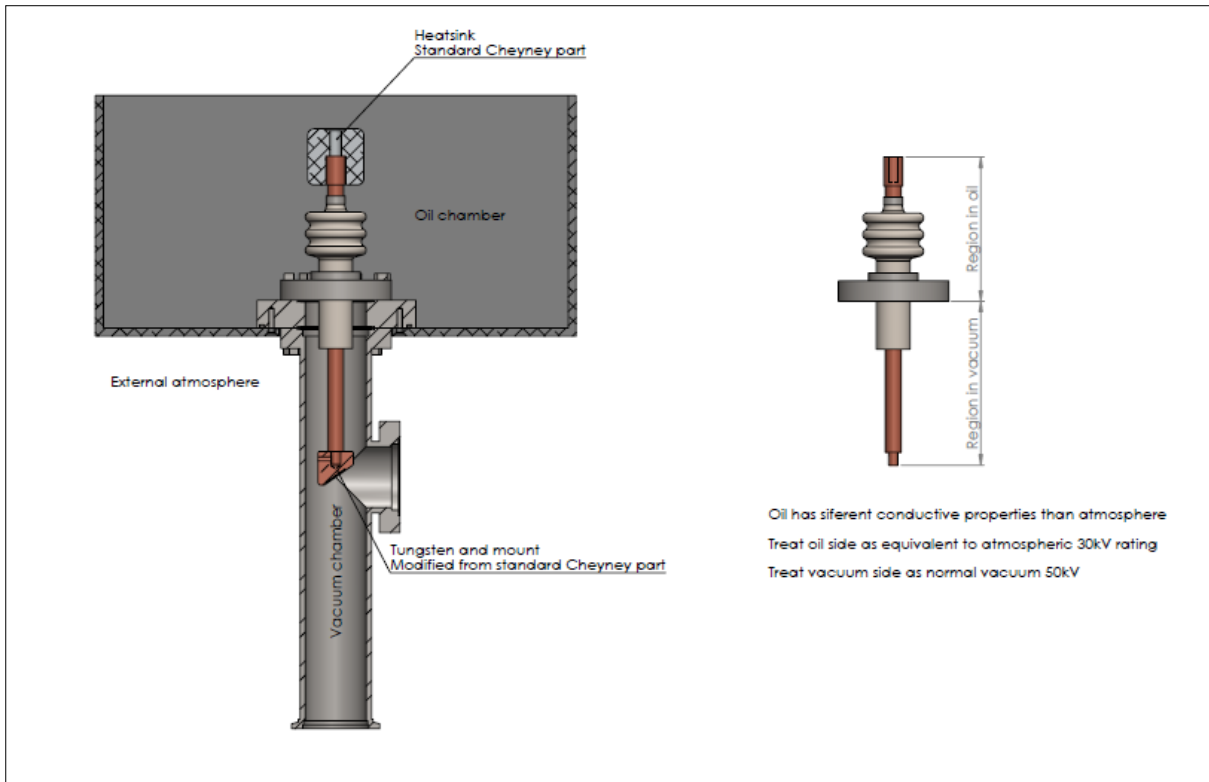


**Figure 68 : Drawing of Phase 2 Vacuum chamber with X-ray port.**

In the **Figure 68**, the following features can be seen :

- Beryllium port, on the right side of the vacuum chamber.
- Angled anode, so that the Xrays are deflected through the port.
- The anode is cast copper, with a tungsten insert. The tungsten insert forms a target for the electron beam, with the spectrum of Xrays created, being characterised by the target material. Various materials are used in this situation, common materials being Copper, Molybdenum and Tungsten.
- The upper end of the anode assembly extends beyond the chamber and is immersed in oil, in the surrounding tank.

## 7.17 Practical construction

The design of the chamber called for the use of a Beryllium window, which was found to be prohibitively expensive. Many commercial X-ray inserts incorporate such a window, and so a foot assembly was recovered from a non-functioning tube, and welded to a KF50 blank. A chamber was produced with a corresponding fitting, and the two items were clamped together as shown, in **Figure 69**.

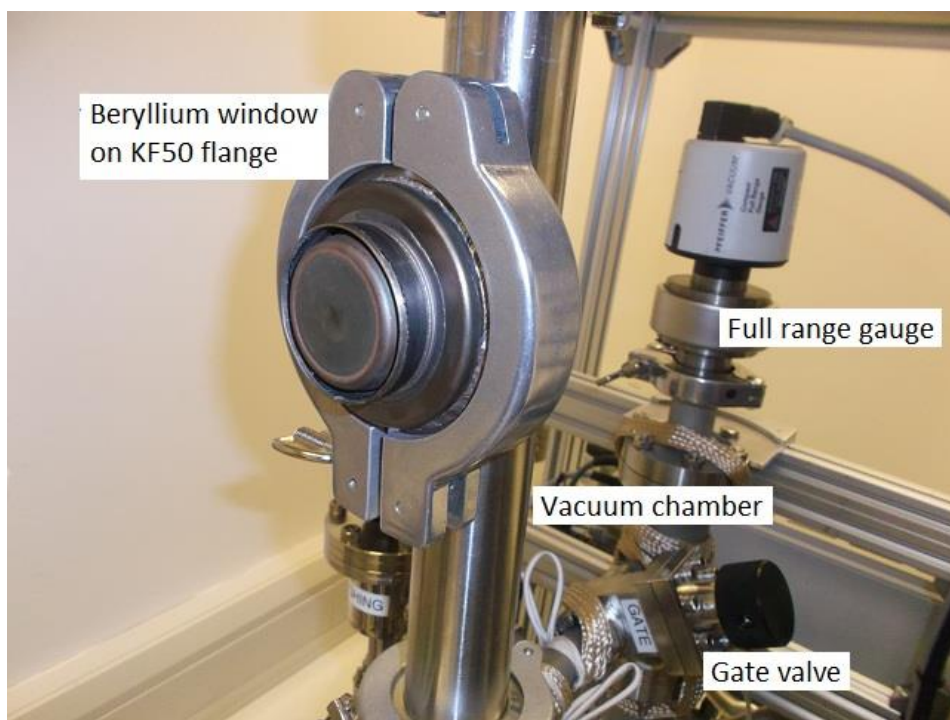


*Figure 69 : Recovered beryllium window to create X-ray port.*

The anode assembly was similarly recovered from non-functioning tube and mounted to the end of a high voltage feed-through, show in **Figure 70**.

Subsequent work has shown that the KF50 flange may not be appropriate to the UHV vacuum conditions that we are seeking.

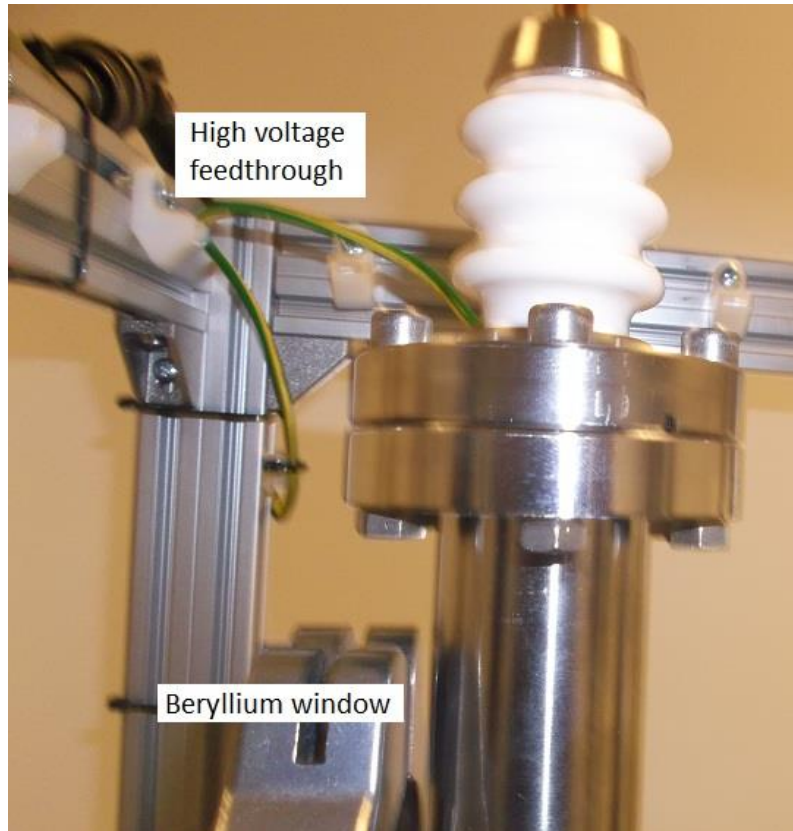


*Figure 70 : HVfeed-through with recovered anode (internal to chamber)*

## 7.18 Options for creating Pulse X-ray source

Pulse Xray sources have been a source of research interest and investigation for some time [4]. A pulse Xray source may be created by :

- Gating or shuttering a CP (constant potential) source such as a thermionic or field emission Xray tube.
- Using a resonant pulse power supply which may be capable of producing pulses ca. 50ns at 300kVp
- Using a laser-produced plasma source with electron injection.
- Sub-nanosecond pulses
- Synchrotron sources

The interest in this work is in the application of gated CP sources. In this case the source is a field emission tube controlled by a gate electrode.

The gate signal is typically 4 – 5000 volts at up to 2mA. It is assumed that a voltage change of perhaps 10% of this will be needed to fully modulate the beam current (to be confirmed after tests). Power devices [MTD1N50E] are available with  $t_{on}$ ,  $t_r$  and  $t_{off}$  times of the order of 10ns, and small signal devices somewhat faster.

The output signal level will be limited by the photon flux integrated over the pulse period. So to get a measurable signal (i.e. significantly above the detector noise level), it is necessary to have a proportionately high photon flux. Photon flux may be controlled by :

- Beam current. This will result from higher field emission current density, and is therefore likely to be a limiting factor
- Accelerating potential. A higher photon flux will occur as a result of higher kV, but this will modify the characteristics of the emitted radiation. The relationship between the kV and photon flux is nominally a square law. In addition, the construction of the tube, and the containment around the tank will limit the maximum operating kV of the generator.

Pulse Xray generators of this type have been used for several decades. However, due to the above-mentioned limitations, as well as those of the detector, the applications will normally be restricted to pulse durations of ca. 1ms [5]

Other descriptions of this type of pulsing, as applied to field emission X-ray sources may be found in [6], [7]

## 7.19 Conclusions

A “demountable” chamber has been designed in which CVD emitters may be mounted. This work has highlighted a series of important aspects associated with the design of such a piece of equipment. The most important factor has been the careful design of the high vacuum system, including consideration of the materials used, and the effects of power dissipation, and hence temperature, on out-gassing. In order to improve the efficiency of the studies, the chamber and cathode assembly were designed to be mechanically adjustable, so that key parameters such as cathode-gate distance and emitter-anode may be varied whilst under vacuum.

## 7.20 References

- 1 ALLECTRA. 2013. *PEEK datasheet* [Online]. Available: <http://www.allectra.com/images/Downloads/Datasheets/311-PEEKM-035-10M.pdf> [Accessed].
- 2 JEON, H., CHOI, Y. C., PARK, S., KANG, J.-T., GO, E., LEE, J.-W., KIM, J.-W., JEONG, J.-W. & SONG, Y.-H. 2017. Very large suspended graphene as an efficient electron-transparent gate electrode. *Carbon*, 119, 371-377.
- 3 LI, C., COLE, M. T., LEI, W., QU, K., YING, K., ZHANG, Y., ROBERTSON, A. R., WARNER, J. H., DING, S., ZHANG, X., WANG, B. & MILNE, W. I. 2014. Highly Electron Transparent Graphene for Field Emission Triode Gates. *Advanced Functional Materials*, 24, 1218-1227.
- 4 1990. Repetitive flash x-ray generator utilizing a simple diode with a new type of energy-selective function. *Review of Scientific Instruments*, 61, 2343-2348.
- 5 RADICON\_IMAGING\_CORP. 2001. *Imaging with Pulsed X-Ray Sources* [Online]. Available: <http://ebookbrowse.com/radicon-an04-pdf-d46857665> [Accessed].
- 6 WANG, S., CALDERON, X., PENG, R., SCHREIBER, E. C., ZHOU, O. & CHANG, S. 2011. A carbon nanotube field emission multipixel x-ray array source for microradiotherapy application. *Applied Physics Letters*, 98, 213701-213701-3.
- 7 YUE, G. Z., QIU, Q., GAO, B., CHENG, Y., ZHANG, J., SHIMODA, H., CHANG, S., LU, J. P. & ZHOU, O. 2002. Generation of continuous and pulsed diagnostic imaging x-ray radiation using a carbon-nanotube-based field-emission cathode. *Applied Physics Letters*, 81, 355-357.

# 8 FIELD EMISSION MODELLING

## 8.1 Introduction

The first examples of X-ray sources using FE electron sources employed diode configurations which comprised only a cathode and an anode. However, in such devices the emission current is a function only of the anode voltage. As a result, such diode configurations give rather limited adjustment over the magnitude of the emission current for most applications. To more accurately control the emission current, whilst also providing a degree of protection, it is now standard procedure to introduce a third electrode. This gate electrode gives rise to a triode configuration. Early in the development of CNT-based FE X-ray sources, Sugie *et al.* [12] introduced a counter-electrode wire. Since this naturally produced an anisotropic beam, the control mechanism of choice became a perforated grid, or gate electrode. The purpose of the gate is to create a local electric field that draws the electrons away from the principal emission beam. However, in practice a significant proportion of the emitted electrons will be attracted towards the gate electrode. The gate must therefore be sufficiently transparent to allow the maximum number of electrons to pass to the anode. It is normal that  $> 50\%$  of the cathode current is directed to the gate, thereby limiting the efficiency of such devices. However, there has been recent interesting work on improving the transparency of the gate by incorporating graphene layers. This has shown a substantial improvement in

efficiency to around 60% [8] although the technique has yet to be applied to X-ray sources.

The construction of the cathode assembly suitable for a triode configuration X-ray source comprises of the following structure, previously shown in **Figure 31** and shown again here for clarity, as **Figure 71**, below :

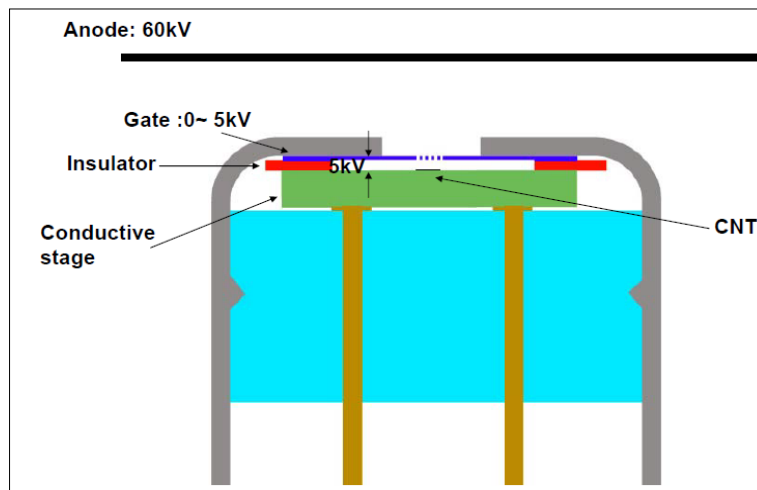


*Figure 71: Schematic of a basic triode assembly*

It is clear that relative positions of the structure of the CNT array and the associated grid is critical to the efficiency and reliability of the electron emission source.

## 8.2 Comsol modelling

It is possible to conceive of many options for the construction of this assembly – these options would include varying geometry, particularly cathode-gate and gate-anode dimensions, varying applied voltages to adjust electric field strengths, studying the effects of non-ideal vacuum levels, etc.

The work involved with evaluating and comparing these options practically, is a very long process. In the case of using sealed inserts, the steps of cathode/gate fabrication, assembly into a glass tube and testing is an extensive series of functions, absorbing considerable elapsed time, and at a substantial cost. By comparison, when using a demountable vacuum chamber, simply the time taken to strip down and re-assemble the test equipment, pump down the chamber to a suitable level of vacuum, and execute the tests, would make the project impracticably long for all but the most limited range of experiments.

Fortunately tools exist for studying and evaluating the electrostatic parameters, such as electric fields, electron trajectories and emission characteristics of the various components in the tube. Several options are commercially available, including Comsol Multiphysics and Computer Simulation Technology (CST).

A number of others have published examples of simulations related to the E-field characteristics associated with CNTs and silicon tips. Crossley [5], R.C.Smith [11], and others have all modelled individual emitters or arrays, demonstrating the shielding effects, in reducing the aspect ratio of the structures. Dall’Agnol [6] modelled arrays of differing heights, spacings and diameters, a somewhat theoretical concept. Silan [1] considered toroids as a means of increasing the aspect ratio of CNT pillar arrays, by creating additional edge regions – this can be seen in **Figure 72**. Prommesburger has modelled electron trajectories of silicon nano-tips [10].

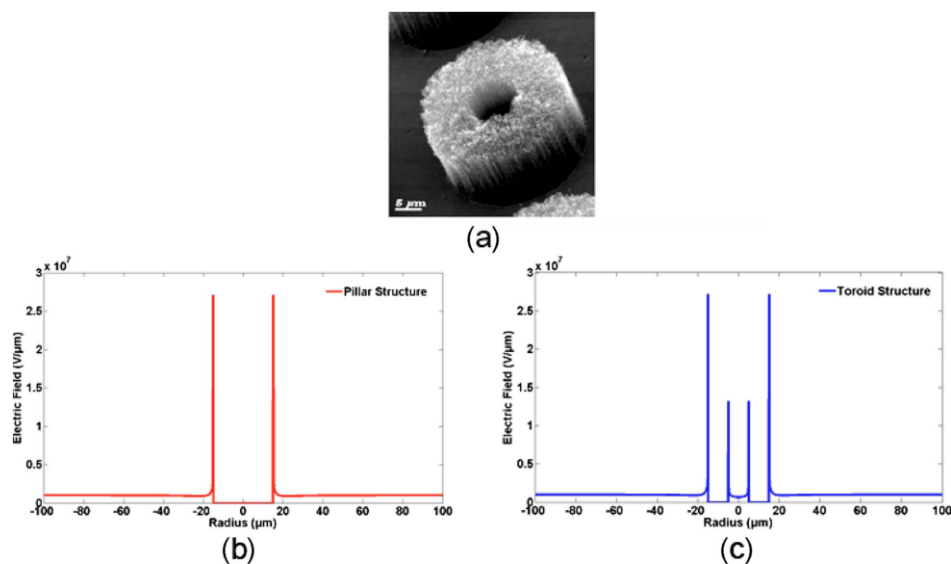


**Figure 72 :** (a) SEM image of a tCPA. (b) and (c) Simulated e-field

Simulated e-field plotted against radial distance for both arrays of solid CNT pillar array and the tCPA toroid structures, using COMSOL MULTIPHYSICS. Cut line for electric field vs radius plot was taken to be at the maximum electric field for each of the two structures. Both structures are 5 μm in height and have the same 30 μm diameter.

The study of modelling has comprised a series of stages :

- The modelling of the electric fields associated with an individual emission source, which may be a single CNT or CNF, a CNT Pillar Array (CPA).
- The modelling of the field distribution associated with an array of emitters

- The modelling of irregular arrays, to understand the effects and benefits of annealing.
- The modelling of emitters with control electrodes
- The modelling of the emission characteristics of extended geometrical structures.
- The modelling of the macro cathode assembly, in particular taking due regard of the structure of the gate. Of particular interest in this section, is estimating the size of the focal spot, and the ability to make adjustments to the design of the cathode/gate assembly to assist in focussing.

Of course, a further consideration is the orientation of the axis of the CNT. This will be affected by the means of growing the emitters, for example – paste printing – where the orientation is essentially random, electrophoresis – where there can be a broad degree of alignment, and CVD – which generally produces well ordered and aligned structure. As a result of the conclusions from the experimental work in chapter 6, this simulation work will be restricted to emitters that are normal to the substrate – in other words, those that typify CNTs grown by chemical vapour deposition.

### 8.3 Modelling of individual source

The theory behind the emission from carbon nanotube is well described by Forbes [7] and Bocharov [3]. Considering the emission from an individual CNT, it is necessary to study the I-V characteristics of the emitter [2]. As previously mentioned, this is defined by the Fowler Nordheim equation, at least to a first order. This relates the emission current to the electric field strength near the CNT tip, at a given cross section and work function of the CNT.

$$I = \left( \frac{A\beta^2 V^2}{\phi} \right) \exp\left( \frac{-B\phi^{3/2}}{\beta V} \right) \quad \text{Equation 7}$$

Here the parameters A and B are expressed through the magnitude of the electron work function  $\phi$  for the conductor under consideration,  $\beta$  is the field enhancement factor and the basic constants (the charge and the mass of electron  $e$  and  $m$  and the Plank constant  $h$ ):

The FN equation represents a 1D situation, and as such is very straightforward to simulate. The first element to consider relates to the shape of the tip, which will affect

the field enhancement factor,  $\beta$ . One can conceive a range of tip morphologies which can be built into the simulation, shown in **Figure 73**, for which this can be calculated.

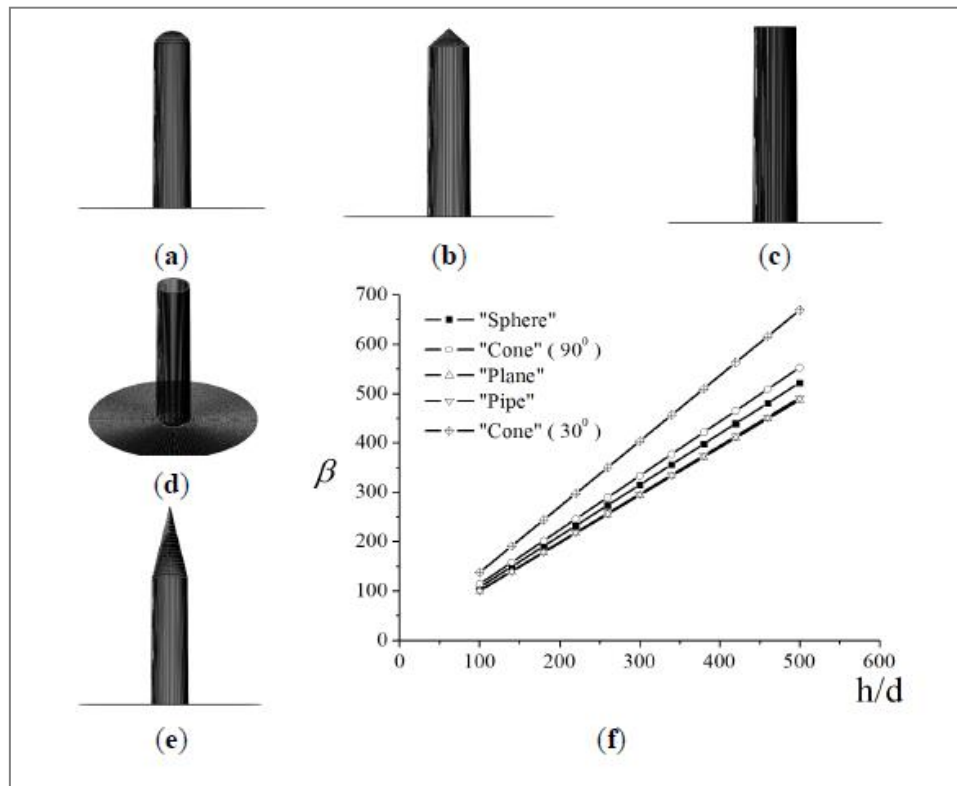


**Figure 73 : Various shapes of the carbon nanotube) tip.**

(a)–(e) Various shapes of the carbon nanotube (CNT) tip for which the field enhancement factor versus the aspect ratio was calculated. Curves 1–5 in panel (f) correspond to panels (a)–(e). The inter-electrode spacing and the applied voltage are 200  $\mu\text{m}$  and 1000 V, respectively [2].

Selecting a typical tip shape, such as a hemisphere (**Figure 73(a)**), we can then proceed to model the effect of arrays of emitters, both in 1D and 2D.

## 8.4 Modelling of array of emitters

The electric field strength,  $E$ , will be ultimately determined by, in the case of a diode configuration, the voltage between the anode and the tip of the CNTs, and the distance between them. Again these factors may be parameterised, and included in the model. The study of an individual emitter, is the limiting case of an array in which the inter-electrode distance is very much greater than the height of the CNT. If the separation between individual members of a set of emitters approaches the height, then the field

enhancement factor will become dependent on the inter-electrode spacing. This is created as a result of the electrostatic “shielding” effect that is described in many papers [11, 9].

In a 1D example, the simplest model is an array of 3 emitters, as shown in **Figure 74**, and it is quite intuitive that the effect of the field enhancement depends on the distance between emitters. In the case of a large separation between tips, the form of the electric potential in the vicinity of the tips is very similar to an isolated emitter, as it is not disturbed by its neighbours. However, if the array is closely packed, it leads to a situation where the electric field at or near each tip is effectively screened by the neighbouring emitters. Of course, the overall current emitted is a function of both the screening effect, when there are many emitters in close proximity, and also the number of emitters in a given area.

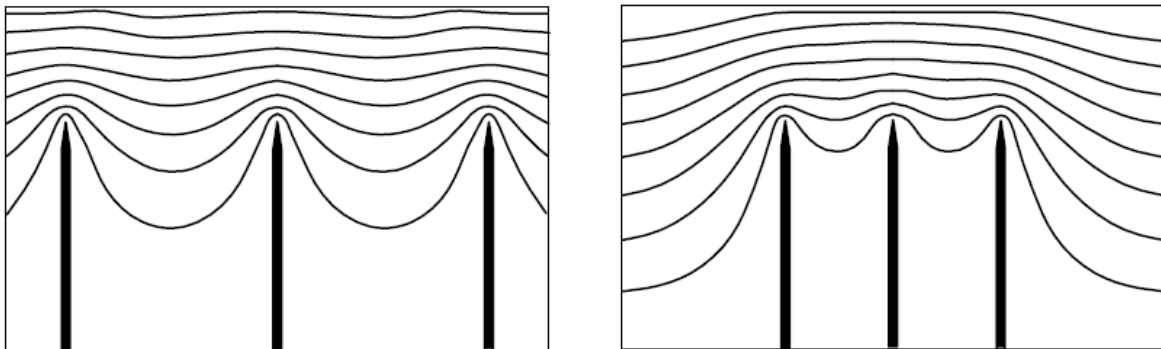


**Figure 74 : Spatial distribution of CNT electric potential.**

Spatial distribution of the electric potential in a vicinity of three CNTs calculated for various inter-tube distances (arbitrary units) [28]. It can be seen that the closer the nanotubes, the lower will be the electrical field enhancement factor.

Repeating this process for a 2D array of emitters, we can see the effect of the shielding in **Figures 75 and 76**.

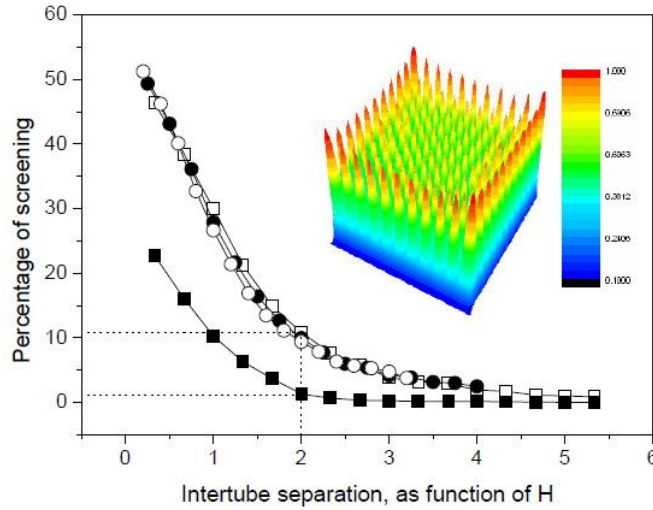


**Figure 75 : Spatial distribution of 2D CNT electric potential.[11]**

The upper traces show the percentage of screening calculated by the difference in local electric field between an isolated CNT to the middle CNT of an array of 11 x 11. The CNT height of 3, 4 and 5  $\mu\text{m}$  is shown. At  $S = 2h$ , the middle CNT is screened by approximately 11%. However 3 CNTs each spaced by 3  $\mu\text{m}$  at a similar spacing,  $S = 2g = h$ , the screening factor is less than 2%, as shown in the lower trace.

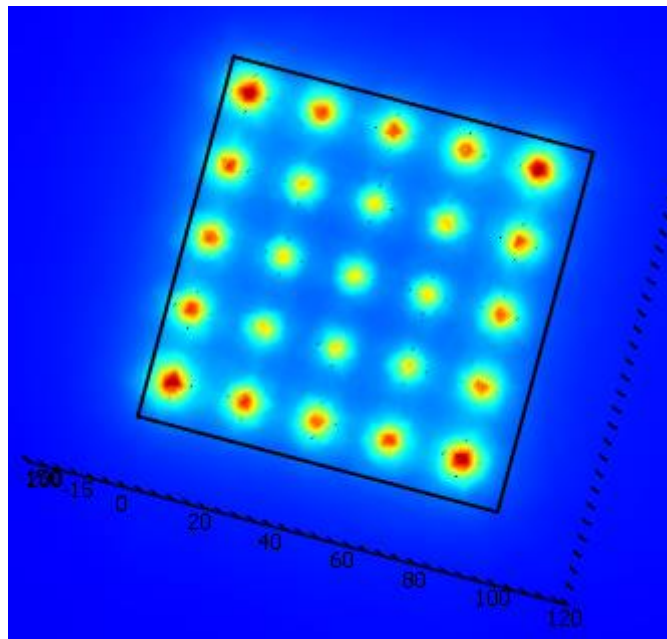


**Figure 76 : Spatial distribution of CNT electric potential.**

Electric field strength in the plane parallel to the tips of the arrays, for a 5 x 5 array. The shielding effect is clearly visible.

## 8.5 Modelling irregular arrays

There is the potential for irregularity in the arrays of CNTs that are grown. This is particularly important when considering arrays of individual CNTs (as opposed to CNT pillar arrays). Variation in the length, diameter and sharpness of tips will give rise to preferential conduction, and which could cause exposed tips to become damaged or destroyed.

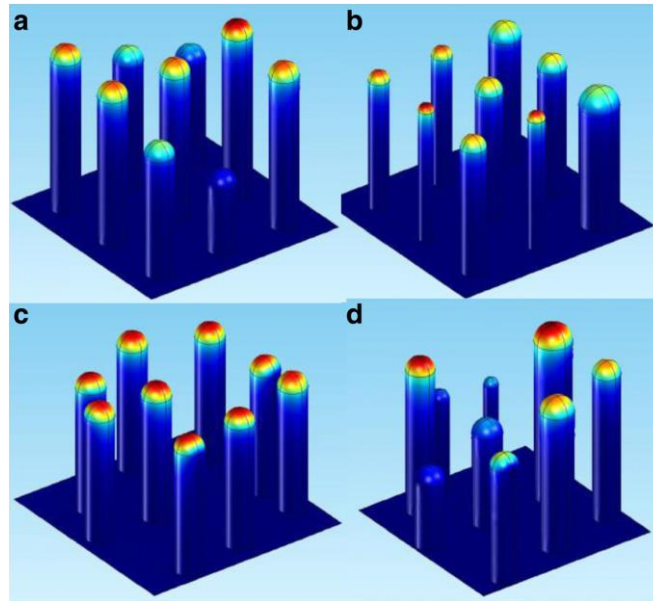


**Figure 77 : Various forms of CNT electric potential.**

Examples of modelling irregular arrays (a) varying CNT heights, (b) varying diameters, (c) varying separation, (d) all parameters varied. Adapted from [6]

## 8.6 Simulation of Triode configuration

The previous simulations have all been made by modelling a diode configuration – that is an arrangement where the substrate of the CNTs is grounded, and an anode at a higher potential is used to create the electric field.

However, as discussed in the introduction to this chapter, the diode arrangement does not represent a practical controllable assembly. To achieve this requires a triode assembly in which the electrons are extracted from the cathode by means of a gate. An aperture in the gate electrode is covered by a conductive material or a grid which allows the electrons to pass through, to be attracted towards the anode.

This, of course, adds complexity to the model, which results in significantly greater computational requirements. In the initial stages, one way of representing this is to show the CNT cathode array as a single block. This can be seen as a valid compromise, because from the simulations of 2D arrays, the largest part of the emission occurs at the edges and interstices (corners) of the array, as seen in **Figure 78**. The gate assembly is shown as an open aperture, and incorporates a bevel to minimise emission directly between the gate and the anode. This structure is broadly along the lines of the demountable tube design described in Chapter 6.

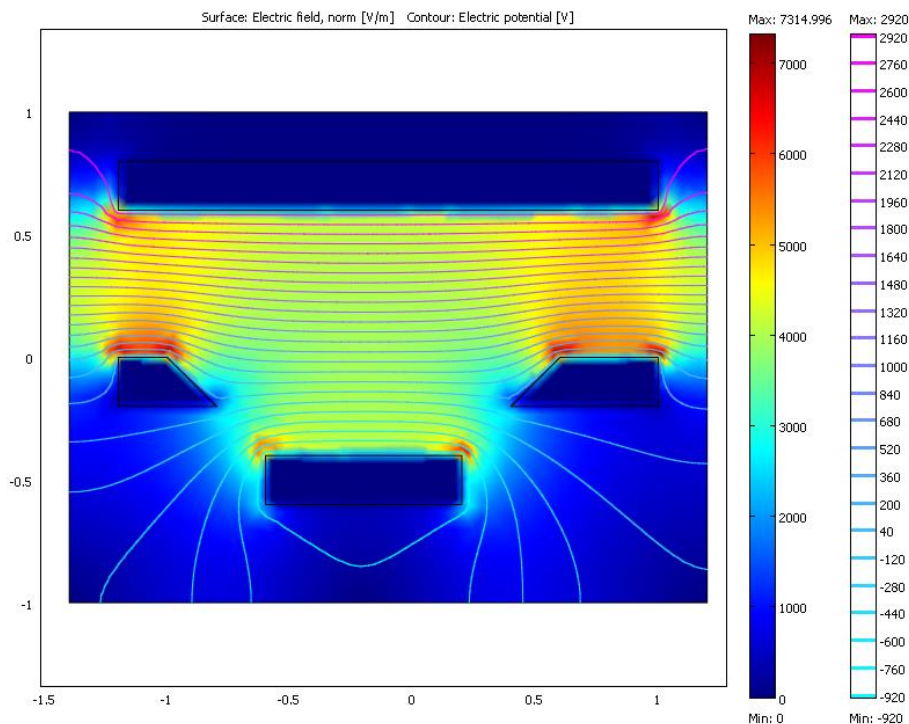


**Figure 78 : Simple simulation of a triode configuration**

This simulation models the CNT cathode array as a single block, shown at the bottom of the image, with a plate anode at the top and a grounded gate assembly.

## 8.7 Modelling emitters with control electrodes

As an alternative means of controlling the emission current between the cathode and the anode, consideration has also been given to controlling the electron flow with an additional electrode incorporated onto the substrate. A structure in which each emission source is encircled by a hexagonal control electrode has been proposed by my team members, Bill Milne and Matt Cole, shown in **Figure 79**. In this case the emission may

be controlled by maintaining a differential voltage between the control electrode and the central CNT pillar array.

Modelling this initially as a 1D array of alternating emitters and control electrodes, we can immediately see the impact of varying the voltage applied to the control electrodes. This work remains unpublished due to the difficulty of growing an array of significant size that is free from short circuits between the electrodes. However it is perfectly feasible to model the ideal situation.

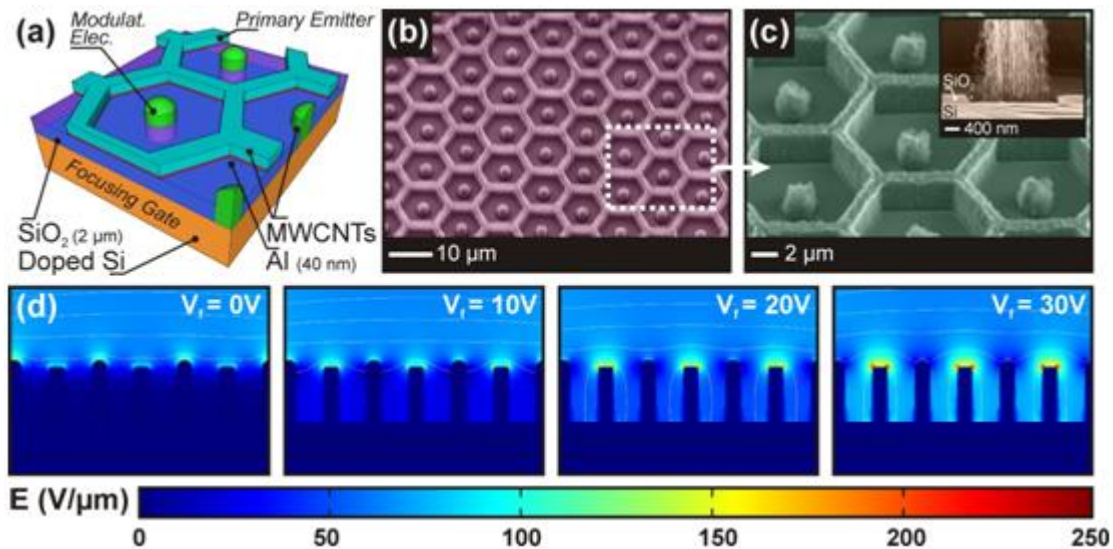


**Figure 79 : Effect of Control Electrodes.**

Surface electric field of a 1D array of alternating cathode emitters and control electrodes as a function of inter-electrode voltage. (a) description of control electrodes. (b), (c) SEM images of the hexagonal control electrodes and CPAs, (d) field strength as a function of control electrode voltage.

## 8.8 Modelling extended geometrical structures

A fellow member of our research group, Clare Collins has been working on potential improvements to the maximum current output of the cathode structures, by researching various emitter morphologies. This has comprised of designing, creating and studying the performance of a series of surface geometries, both as arrays of CNT pillar arrays (CPAs) and inverse arrays. The inverse arrays have some similar characteristics to those proposed by Chen *et al.* [4].

The various patterns were used to create emitters by chemical vapour deposition. The steps in this included application of a photo-resist to a silicon substrate, using electron beam lithography to etch the patterns, DC Magnetron sputtering to apply a suitable catalyst, and finally the use of thermal CVD to grow the CNT arrays.

The purpose of this work was to understand and to create emitters with higher output current capacity. Typical results of this process are shown in **Figure 80**.

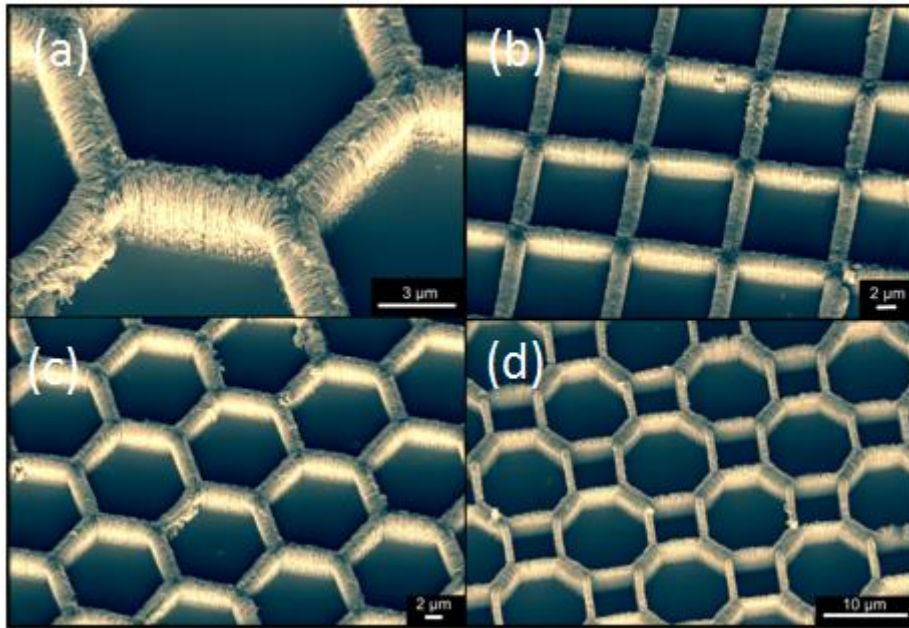


*Figure 80 : Inverse pillar variants.*

Scanning electron micrographs of inverse pillar parallel plate samples in (a), (c) hexagon, (b) square and (d) octagon variants.

Extending the concept of the previous simulation work, geometrical structures have been produced and modelled by CVD on patterned silicon substrates.

Such a simulation is best performed by establishing repetitive boundary conditions, to effectively create a model of infinite extents. The version of Comsol Multiphysics that was available does not support this functionality, and therefore a simulation was conducted with a manual replication of the cell features. This has resulted in much larger structures, and a limit to the capability to process these.

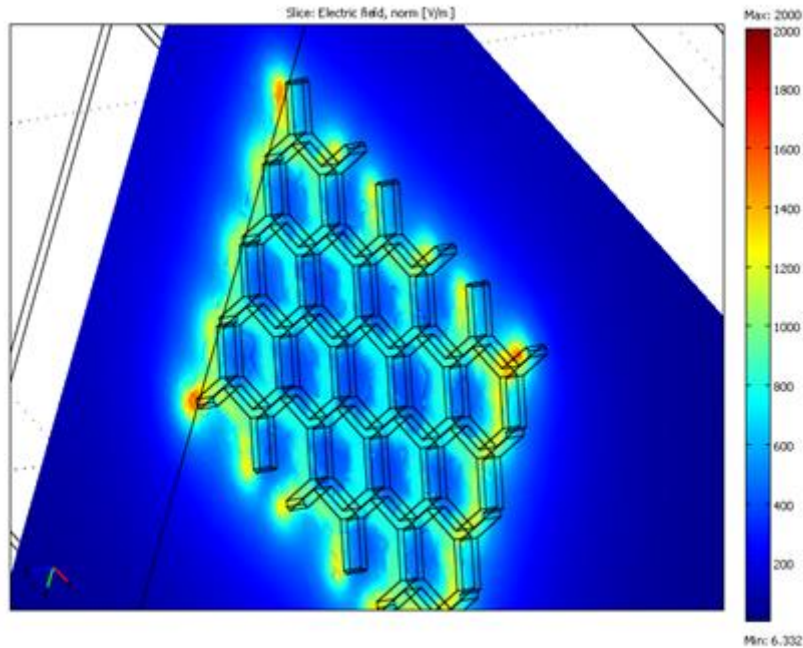


*Figure 81 : Surface electric field of a 2D hexagonal array.*

The results, in **Figure 81**, predictably show that there is little field emission occurring at the interstices, other than that associated with the normal edge of the CNT pillar patterns. Indeed, it can be argued that a non-inverse structure would represent a considerably better solution.

## 8.9 Modelling of macro cathode assembly (CST)

In an X-ray tube, a source of electrons impinges on the positively charged anode. At that point the interactions between the electrons and the material of the target, which is cast into the anode, will cause the emission of X-ray photons of characteristic wavelengths, which are a function of the electron energy (anode kV).

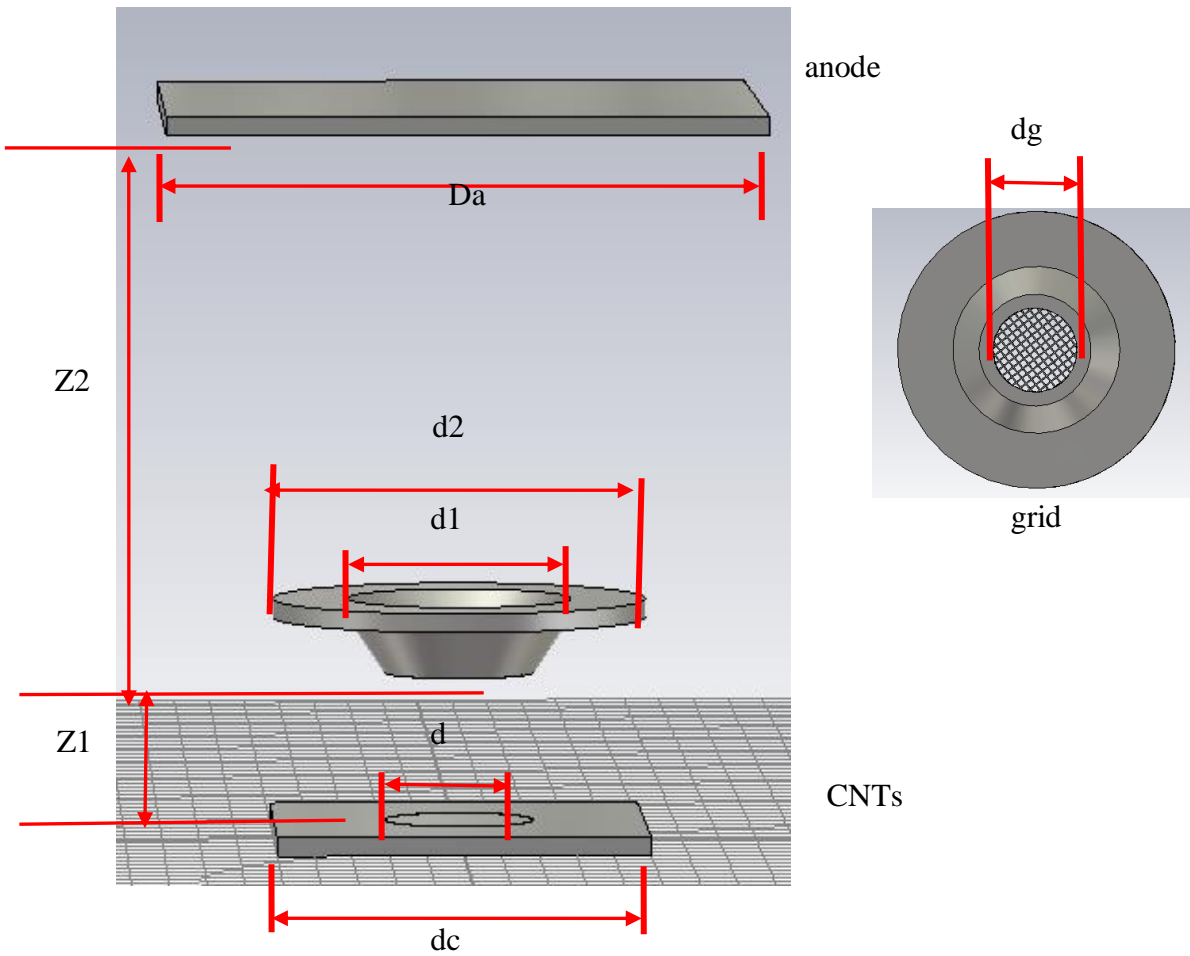
It is a very desirable characteristic of the X-ray tube, that the focal spot size is as small as possible. Conventional tubes would have a focal spot size of typically around 1 mm, with the electron beam becoming divergent as it approaches the anode, as a result of repulsion due to coulombic effects. In a practical implementation of the cathode/gate assembly, the design would incorporate a “focussing cup” which would have the effect of minimising the divergence of the electron beam. For special applications, much smaller focal spots have been achieved by focussing with Einzel lenses, as has been described in Chapter 4.

In order to study the effects of this, it is necessary to simulate the electron trajectories, as they pass from the cathode, through the gate towards the anode. The cathode assembly described in Chapter 6, comprises of a top cap, supporting the gate structure which is adapted from a TEM grid. The grid forms a semi-transparent conductive electrode, which will pull the electrons away from the cathode emission sites, towards the anode. This model describes the electron trajectories between the cathode, via the gate towards the anode.

Whilst this model describes a basic structure, it is quite possible to conceive other arrangements of the top cap which can offer benefits regarding focussing and the inhibition of uncontrolled emission from the cathode assembly.

It is interesting to model the dispersion of the electrons from the CNT array, as they pass through the TEM grid, and proceed to the anode. This model is based upon the design of the demountable X-ray source as shown in chapter 6. The modeling software is CST (Computer Simulation Technology). For the purposes of modelling, all dimensions are parameterized. The objective of this is to determine, firstly the optimum Cathode-Grid distance,  $Z1$ , and the Grid-Anode distance  $Z2$ . Then secondly the optimum grid size,  $G$  is determined.

Xray Generation by Field Emission



Details:

Da	d2	d1	Dg	D	dc
16	10.05	6.05	3.05	4	10

(Units:mm)

A).Simulation results of effect of Z1 and Z2 on the electron trajectories,

Distance (Units:mm)		Voltage (Units:kV)	
Z1	Z2	grid	anode

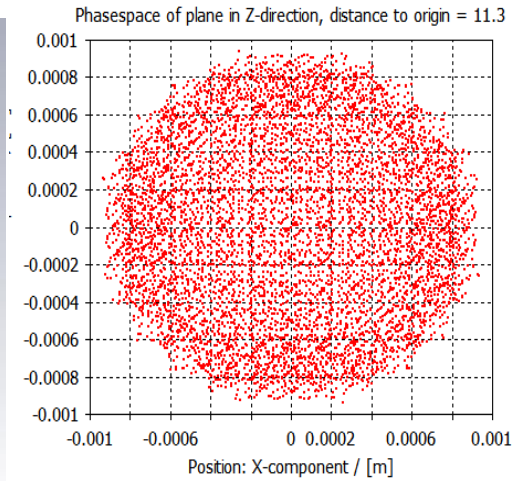
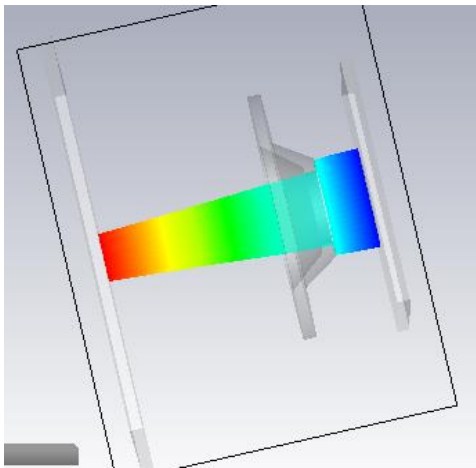
1.8	9	2.8	10
3	12	4.5	13
4	15	6	16

***Table 1: Summary of electron trajectory simulation***

Whilst the dimensions selected are not entirely representative of those anticipated in the final assembly, this represents an interesting exercise, for which I acknowledge the help of Xuesong Wang, who assisted with the electron trajectory simulation work in CST.

# Xray Generation by Field Emission

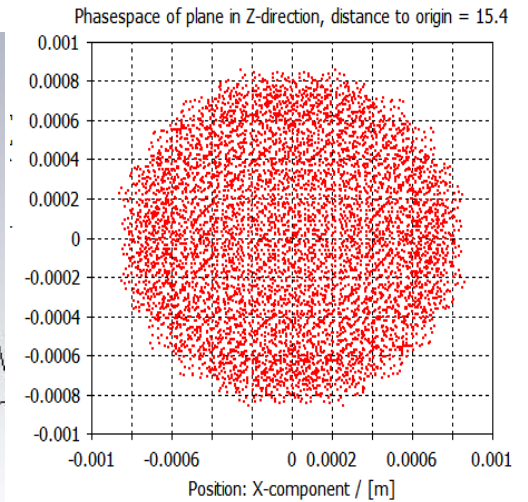
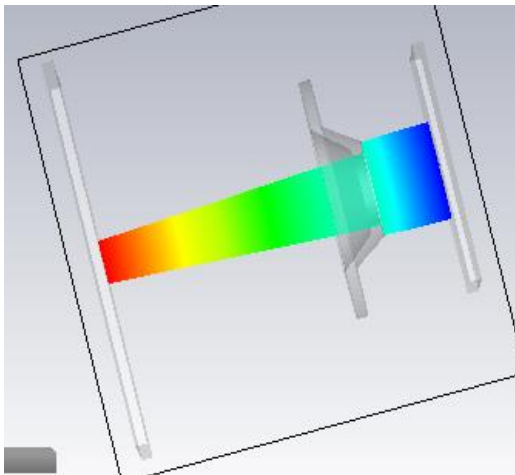
Iteration 1 : Z1=1.8 Z2=9



Electron beam trajectories

Electron beam spots on the anode

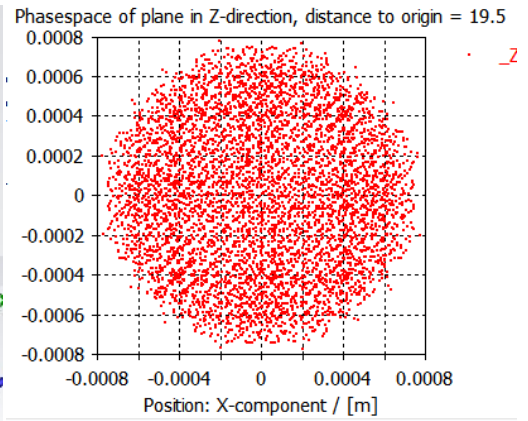
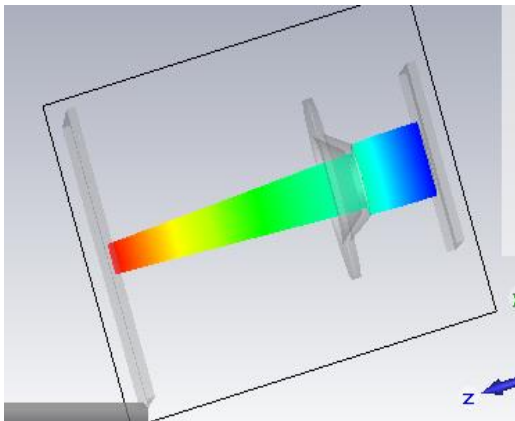
Iteration 2 : Z1=3 Z2=12



Electron beam trajectories

Electron beam spots on the anode

Iteration 3 : Z1=4 Z2=15



Electron beam trajectories

Electron beam spots on the anode

b) Simulation results of effect of TEM grid (gate) openness on the electron trajectories

We chose  $Z1=4$ ,  $Z2=15$

Optimisation of grid size, G.

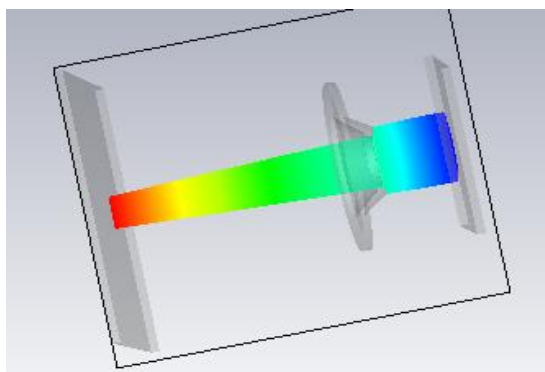
The grid dimensions were selected from a catalog of TEM grids :

[http://www.2spi.com/catalog/grids/regular\\_grids\\_tem.php](http://www.2spi.com/catalog/grids/regular_grids_tem.php)

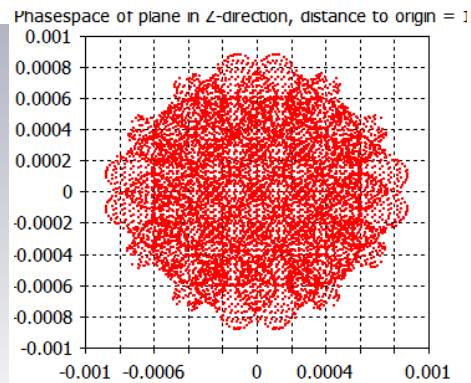
From this the following mesh apertures were selected, where the aperture is in microns:

G50 G75 G100 G150 G200

Iteration 1 : G50

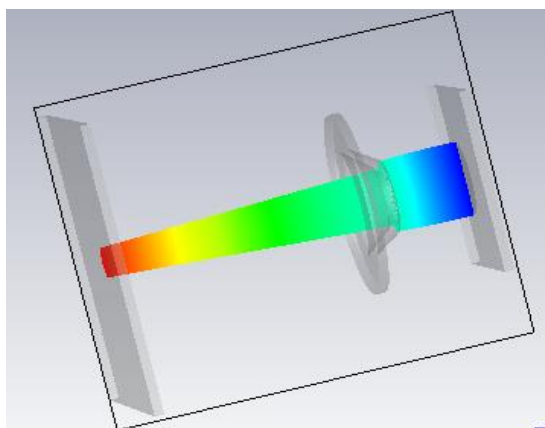


Electron beam trajectories

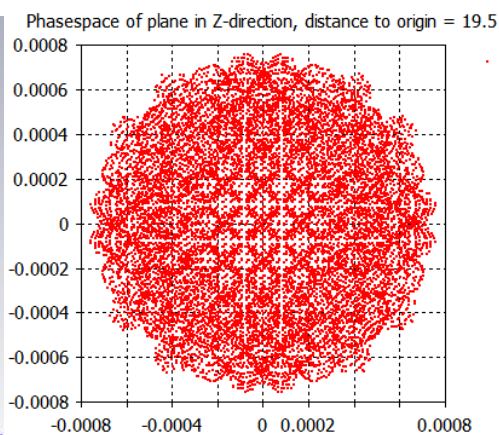


Electron beam spot on the anode

Iteration 2 : G75

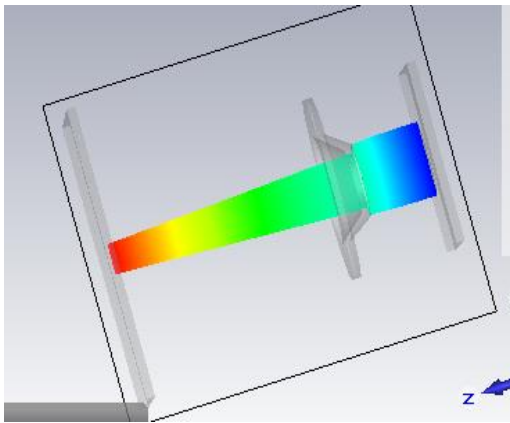


Electron beam trajectories

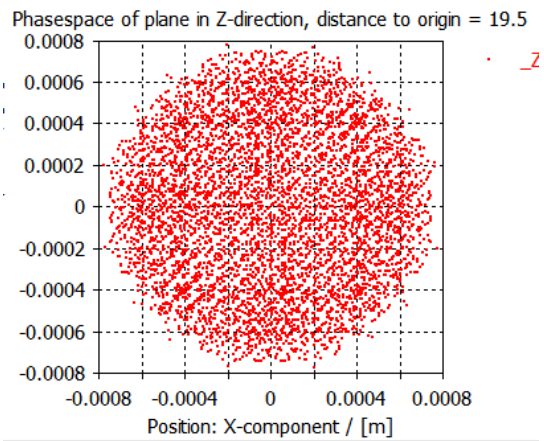


Electron beam spot on the anode

Iteration 3 : G100

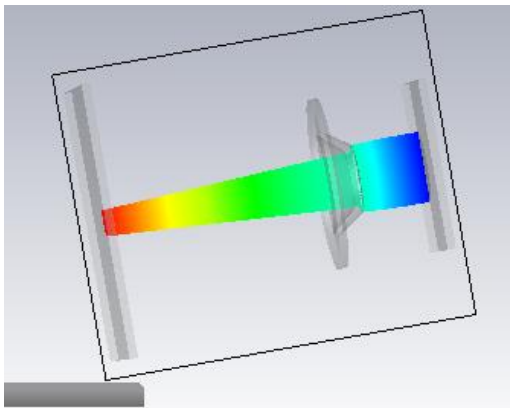


Electron beam trajectories

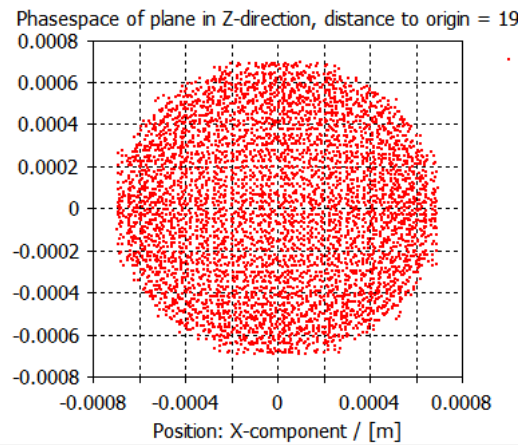


Electron beam spot on the anode

Iteration 4 : G150

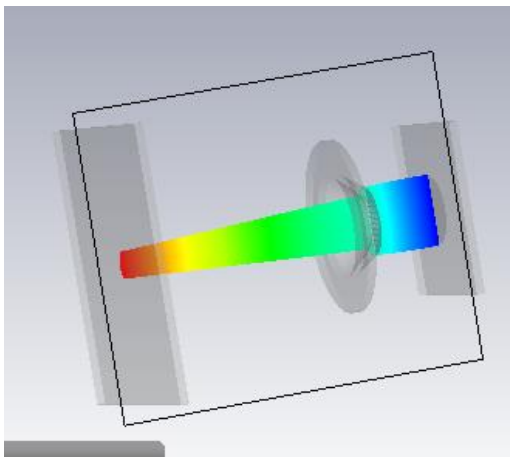


Electron beam trajectories

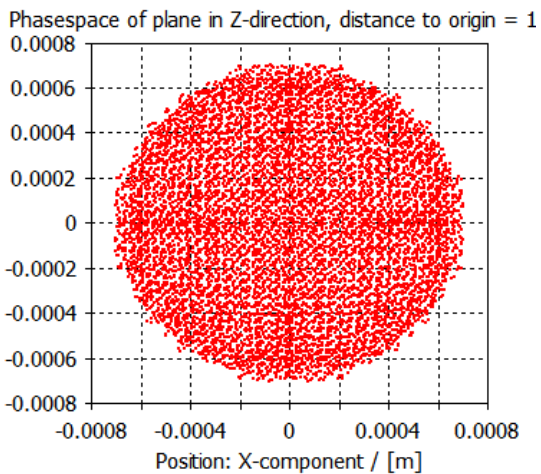


Electron beam spot on the anode

Iteration 5 : G200



Electron beam trajectories



Electron beam spot on the anode

## 8.10 Conclusion

There can be no doubt that modelling represents a very powerful tool in the development of field emission sources. The ability to experiment with different geometries, and parameterise the structures is especially valuable given the long development cycle in physically prototyping and evaluating design options.

In particular, the results of the modelling allow the investigation of features that cannot readily be measured or analysed within the high vacuum environment. This, combined with the extended time required to design, prototype and assemble vacuum components, and even the delays required to pump down the vacuum chamber, mean that many iterations may be modelled, and non-ideal situations considered, in a fraction of the time needed for experimental work. But, of course, the benefits of modelling rely on the completeness of the model itself, and ultimately this is only a step on the way to achieving a viable, engineered, working solution.

## 8.11 References

- 1 AL, J. L. S. E. 2009. Carbon nanotube pillar arrays for achieving high emission current densities. *Applied Physics Letters*, 95, 133111.
- 2 ALEKSANDR, V. E. 2010. Carbon nanotube-based electron field emitters. *Physics-Uspokhi*, 53, 863.
- 3 BOCHAROV, S. G. & ELETSKII, V. A. 2013. Theory of Carbon Nanotube (CNT)-Based Electron Field Emitters. *Nanomaterials*, 3.
- 4 CHEN, J., LI, C., ZHAO, D. W., LEI, W., ZHANG, Y., COLE, M. T., CHU, D. P., WANG, B. P., CUI, Y. P., SUN, X. W. & MILNE, W. I. 2010. A quantum dot sensitized solar cell based on vertically aligned carbon nanotube templated ZnO arrays. *Electrochemistry Communications*, 12, 1432-1435.
- 5 CROSSLEY, B. L. Year. Optimization of Carbon Nanotube Field Emission Arrays. *In: COMSOL Conference, 2009* 2009.
- 6 DALL'AGNOL, F. F. & DEN ENGELSEN, D. 2013. Field emission from non-uniform carbon nanotube arrays. *Nanoscale Research Letters*, 8, 319-319.
- 7 FORBES, R. G. 1999. Field emission: New theory for the derivation of emission area from a Fowler–Nordheim plot. *Journal of Vacuum Science & Technology B: Microelectronics and Nanometer Structures Processing, Measurement, and Phenomena*, 17, 526-533.
- 8 LI, C., COLE, M. T., LEI, W., QU, K., YING, K., ZHANG, Y., ROBERTSON, A. R., WARNER, J. H., DING, S., ZHANG, X., WANG, B. & MILNE, W. I. 2014. Highly Electron Transparent Graphene for Field Emission Triode Gates. *Advanced Functional Materials*, 24, 1218-1227.

- 9 MINOUX, E., GROENING, O., TEO, K. B. K., DALAL, S. H., GANGLOFF, L., SCHNELL, J.-P., HUDANSKI, L., BU, I. Y. Y., VINCENT, P., LEGAGNEUX, P., AMARATUNGA, G. A. J. & MILNE, W. I. 2005. Achieving High-Current Carbon Nanotube Emitters. *Nano Letters*, 5, 2135-2138.
- 10 PROMMESBERGER, C., DAMS, F., LANGER, C., SCHREINER, R., RUTKOWSKI, S., BORNMANN, B. & MUELLER, G. Year. Simulation of electron trajectories of a field emission electron source in triode configuration by using finite element methods. *In: 2011 24th International Vacuum Nanoelectronics Conference, 18-22 July 2011* 2011. 115-116.
- 11 SMITH, R. C., CAREY, J. D. & SILVA, S. R. P. Year. Simulation of field enhancement effects in carbon nanotubes. *In: Technical Digest of the 17th International Vacuum Nanoelectronics Conference (IEEE Cat. No.04TH8737), 11-16 July 2004* 2004. 176-177.
- 12 SUGIE, H., TANEMURA, M., FILIP, V., IWATA, K., TAKAHASHI, K. & OKUYAMA, F. 2001. Carbon nanotubes as electron source in an x-ray tube. *Applied Physics Letters*, 78, 2578-2580.

# 9 FIELD EMISSION ELECTRON SOURCE

During the course of this work, it has emerged that the principle challenge is the development of a viable field emission cathode assembly. Whilst this was not intended to be the initial direction of the project underlying this thesis, it has become clear that a critical part of the work involves the understanding of the complexities and limitations of this component. In particular there are conflicting requirements associated with the operation of the field emitter at power levels that create high temperatures, and the attendant problems of compromised vacuum caused by out-gassing.

In this chapter, I will describe the attempts made to resolve these problems. Whilst not entirely successful, this will serve as a narrative which might be of benefit to others working in this field.

## 9.1 Cathode Assembly

The ideal cathode assembly is an array of field emission sites arranged over a small area behind an extraction gate. The data in appendix 2 suggests that Carbon Nanotubes (CNTs) represent a promising material for these emitters because of their high electrical conductivity, their high aspect ratio “whisker-like” shape for optimum geometrical field enhancement, and remarkable thermal stability. The array is designed to maximise the field enhancement factor,  $\beta$ , by means of the CNT surface geometry. This is controlled by the pattern of CNT structures that can be grown, as discussed in **Chapter 3**.

## 9.2 Fabrication methods

The emitters are grown by Chemical Vapour Deposition, CVD, allowing for selective growth patterns as well as aligned growth [5, 6]. The objective was to grow arrays of CNT Pillar Arrays (CPAs) of varying lengths, thereby providing a range of enhancement factors. This was to be achieved by varying the duration of the growth cycle.

The CNTs are grown on a catalyst which is deposited on a silicon substrate, that is patterned by electron beam lithography, and then deposited by DC magnetron sputtering. This took place in the clean room in the Electrical Division Building, with the assistance of Clare Collins, a PhD candidate in my group.

The electron beam photolithography (EBL) involves deposition of a photoresist by spin coating, at a patterning accuracy of typically 100nm. The resist which is exposed to the electron beam becomes soluble in a photo developer solution, and thus provides a means of selectively coating the substrate with catalyst. A .dxf file is used to create the pattern which is then used to control the XY table in the EBL machine.

After development, the catalyst material is sputtered over the entire surface of the silicon, adhering to the regions where the photoresist has been removed, with the remaining resist being stripped with acetone. After annealing, the catalyst breaks down to form nano-particle nucleation, on which the CNTs will self-assemble[7].

## 9.3 CNT growth

The CNTs are grown in an Aixtron “Black Magic” reactor, using thermal CVD. The silicon substrate is mounted on a raised platform and ammonia and acetylene are fed into the chamber, while the substrate is heated through a graphite stage, to a temperature of several hundred degrees C. The parameters of this process are selected according to previously-determined recipes, including chamber pressure and stage temperature.

## 9.4 Design of the emitter

Initially, the design of the emitter utilised 2 micron diameter CPAs or unit cells, on a cartesian matrix with a pitch of 10 microns, as shown in **Figure 82**. The total area covered is 2mm x 2mm. Previous discussion, in chapter 3 indicates, and simulation work described in chapter 8 suggests strongly that emission will occur at the periphery of the

CPA. The aspect ratio,  $\beta$ , will be closely related to the height,  $h$ , of the CPA, assuming that there are not significant screening effects from adjacent structures.

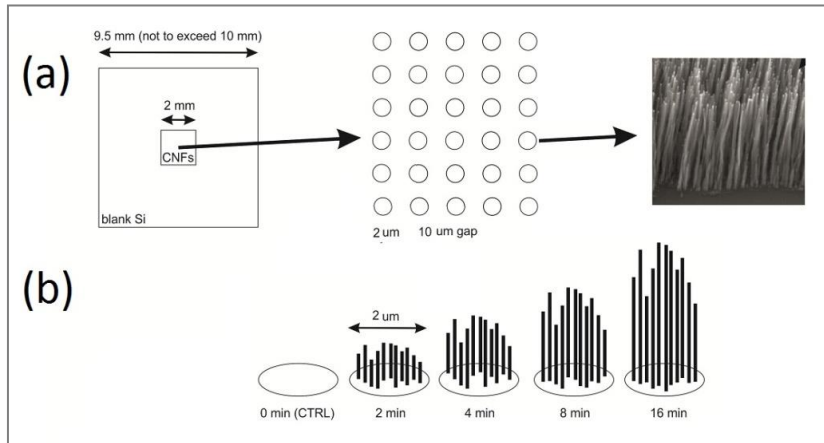


**Figure 82 : Emitter design on 10mm Si chip**

As a result, the growth period was varied to control the height,  $h$ , with CPAs produced for periods of 20 seconds, 40 seconds, 80 seconds and 160 seconds. It was anticipated that there would be a relationship between this period and the height of the CPA, and thereby affecting the aspect ratio and hence emitter characteristics.

### 9.5 Scanning Electron Microscope results

The substrates carrying the emitter arrays were examined with a scanning electron microscope (SEM).

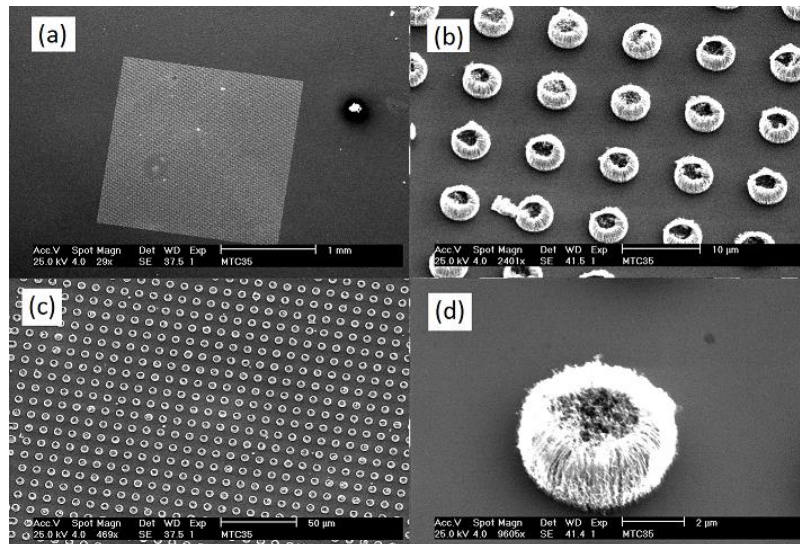


**Figure 83 : SEM of array of CNT pillars, on silicon substrate**

- (a) Overall area of emitter array is 2mm x 2mm, (b), (c) shows CNTs on 10  $\mu\text{m}$  pitch,
- (d) CPA diameter approx 3  $\mu\text{m}$ .

The results show that the low growth period emitters were as expected. However the longer intervals produced CPAs that collapsed onto themselves, producing a morphology that resembled a ring doughnut.

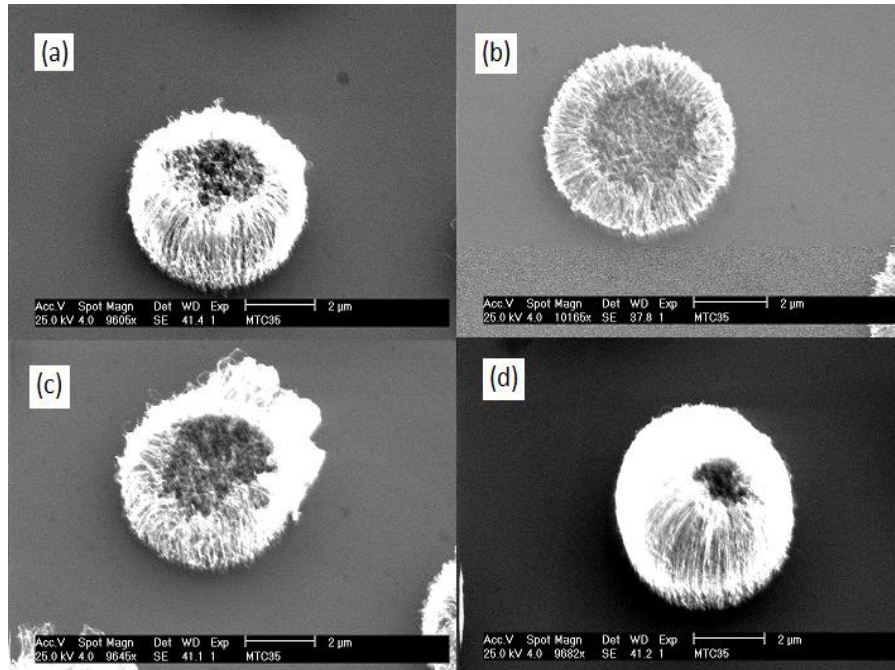


**Figure 84 : SEM of CNT pillars, different growth periods**

Individual CPAs, with growth periods of (a) 20 seconds, (b) 40 seconds, (c) 80 seconds, (d) 160 seconds. Collapsing of the CPA at higher growth periods is in evidence.

In **Figure 84**, it can be seen that the morphology of the CPA, rather than growing taller as expected, is collapsing in on itself to form a “doughnut”. This has been attributed to the growth technique, in particular premature removal of power from the heated stage.

In growing the CPAs, there is a choice when the heat is applied and when the various gases are introduced. If the heater in the CVD reactor is turned off too early, and the gas supply remains on, then instead of forming graphitic carbon deposits or extending the length of the CNTs, it is seen that amorphous carbon is deposited on the CNT surfaces, particularly the catalyst rich tips. This can cause quite a significant mass build up at the tips which then in turn causes the CNT tips to fold over, which would give rise to the unusual CPA shapes.

A potential solution to this problem, would be to increase the growth temperature and then to ensure all the growth gases are evacuated (back to a base pressure of  $1e-2$  mbar) prior to allowing the chamber to cool down. Alternatively, the process could be modified

to slightly augment the growth catalyst such that the areal packing density is increased, which would restrict the available space for such folding to occur, which would result in straight CNT forests. Unfortunately, these characteristics were not observed until SEM images were taken, but insufficient time was available to optimise the process.

In an attempt to achieve some improvement in the emission characteristics, they were further processed by application of methanol or IPA to create “tepee” structures, as shown in **Figure 85**. This has the advantage that, in the region within the CPA, many CNTs can contribute to the emission current of a single Tepee, and the separation of the tips is increased, thereby reducing the electrostatic screening effects.

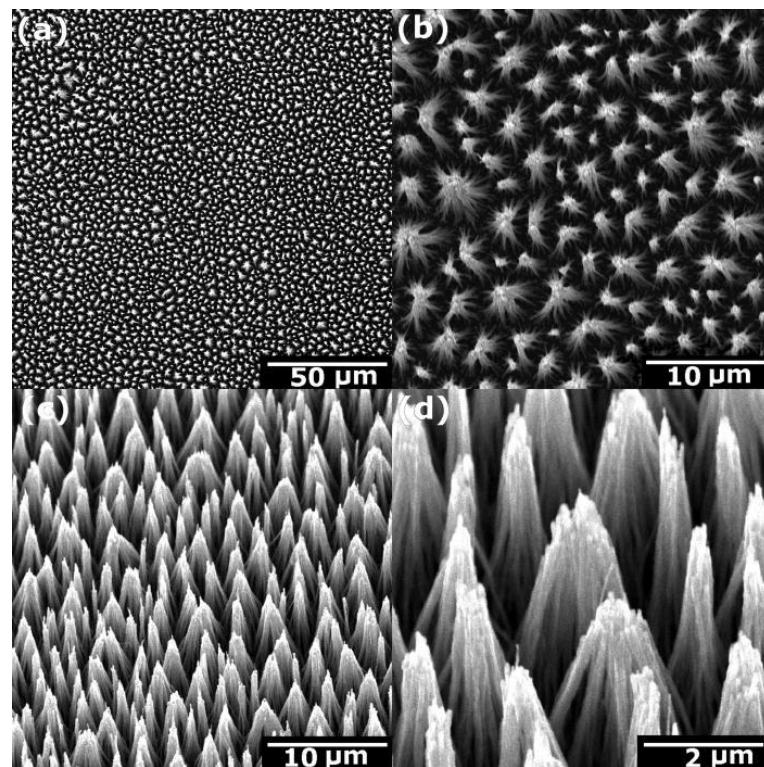


**Figure 85 : SEM of array of Densified tepees.**

Individual CNTs, densified into tepees, with IPA, etc. shown at scales of (a) 50 $\mu\text{m}$ , (b) 10 $\mu\text{m}$ , straight on, and (c) 10 $\mu\text{m}$ , (d) 2 $\mu\text{m}$ , at 30 degree view. These would form the ideal emitter morphology. The effects are probably as a result of the high forest density. Acknowledgements to : [8]

## 9.6 Parallel Plate Measurements

Because of the unusual nature of the CPA arrays that had been grown, as seen from the SEM images, it is advantageous to establish a base-line of the expected emission characteristics. Parallel Plate Field Emission measurement provides a good representation of the mechanisms present within the cathode assembly. In the Demountable design, the emitters are located at a given distance from the gate, which can be adjusted by means of the internal stepper motor. The combination of cathode-gate distance and cathode-gate voltage will largely define the electric field that is present at the tips of the CPA emitters.

Parallel plate type of measurement is quite common in field emission studies. A metallic anode is located parallel to the CPA array at the cathode, and a voltage applied between them, liberating electrons from the field emitters, which are attracted to the anode, resulting in a current flow. Any conductive material can be used for the anode, which in this case comprised a patterned nickel conductor on a glass substrate.

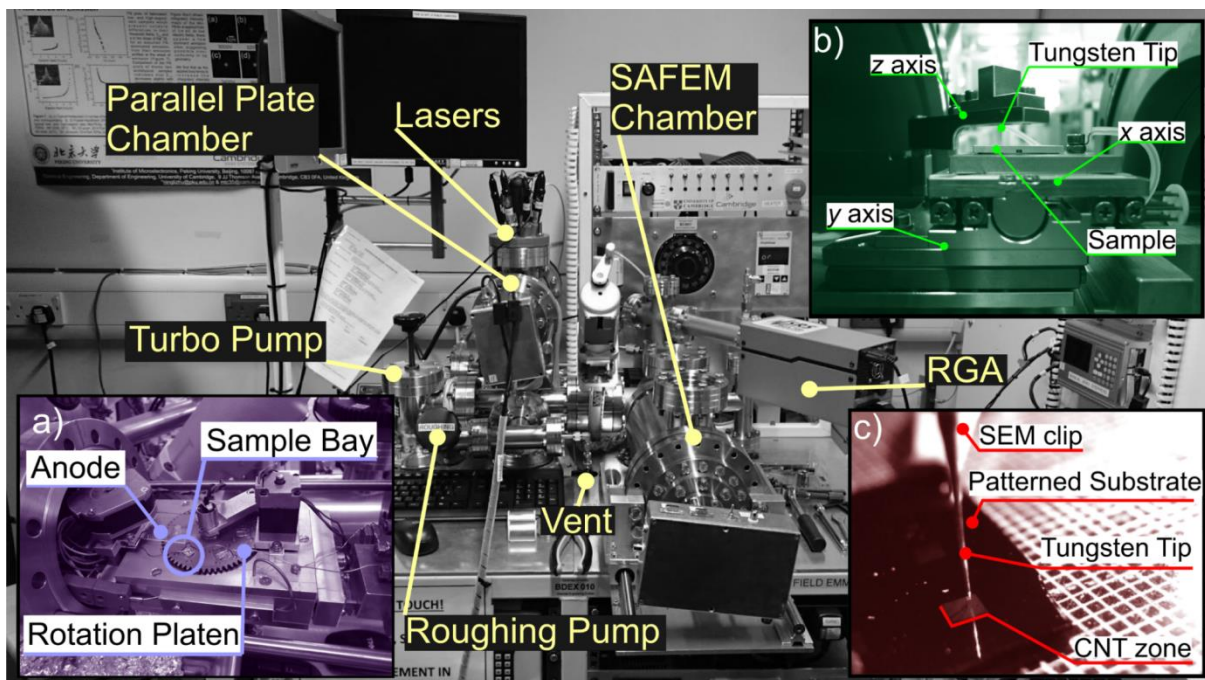


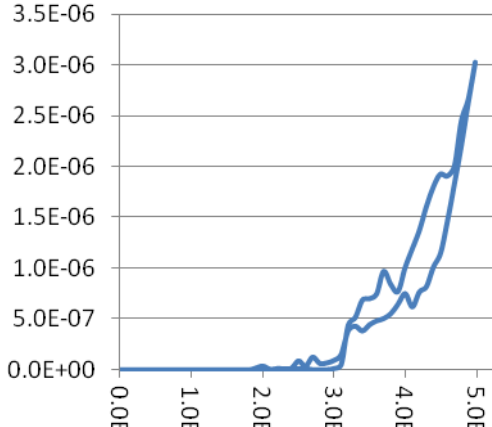
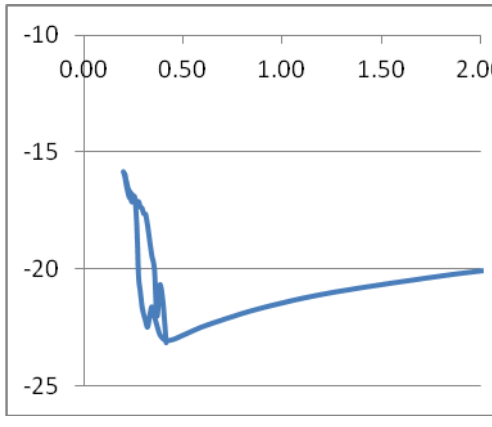
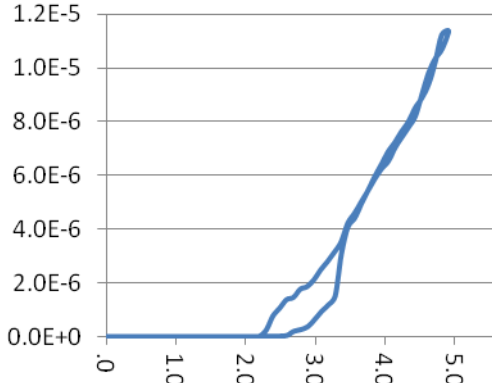
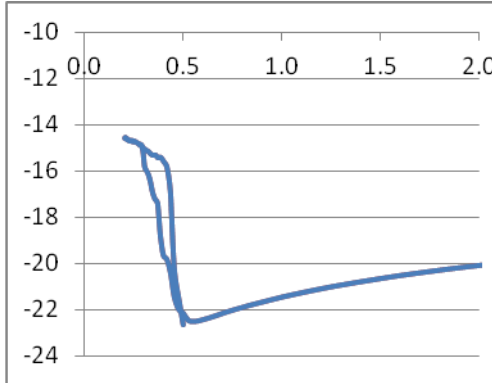
**Figure 86 : Scanning Anode Field Emission Microscope**

**Figure 86** shows the layout of the SAFEM, which includes a Parallel Plate measurement chamber. The samples are loaded onto a rotational stage as shown in **Figure 86(a)**, enabling up to six emitters to be measured in sequence. In this case, four sample sets had been prepared and mounted, as shown in **Figure 86(c)**, after which the stage was loaded

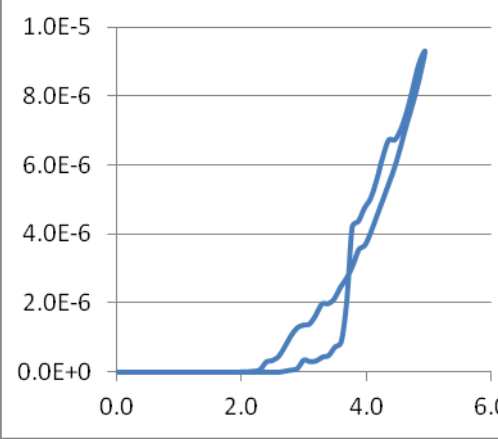
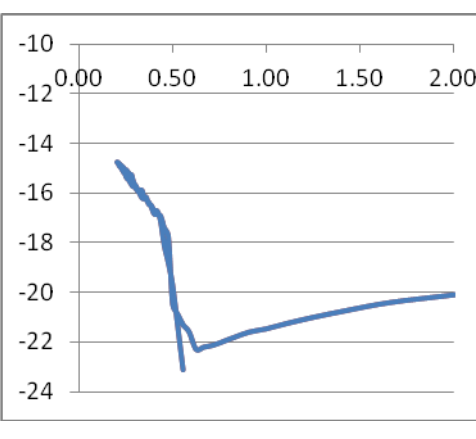
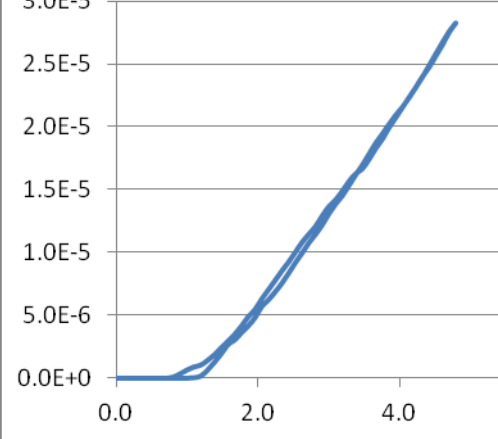
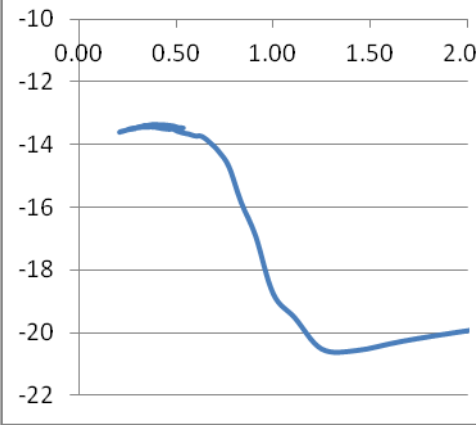
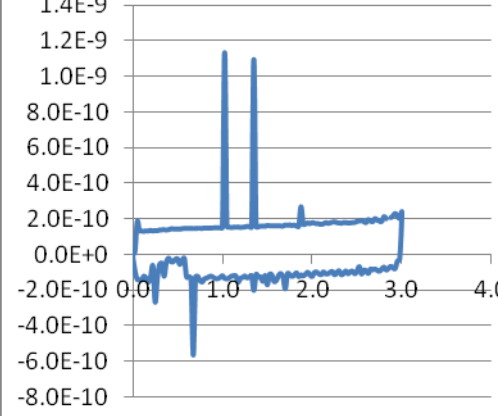
into the chamber, and the cathode-anode distance set to 600 microns. The chamber was then pumped down to a vacuum of  $< 1e-6$  millibar. Once the level of vacuum had been achieved, the measurement process comprised a voltage sweep from 0 to 5000 volts, at 50 volt intervals, following which the sweep returned to 0 volts. The equipment has the additional functionality of being able to position the measurement stage, by means of nano-stepping stages as shown in **Figure 86(b)**.

### 9.7 Results from Parallel Plate rig

The following results, in **Table 2**, were taken from the parallel plate measurements of the emitters described above. These results were “as grown” and after densification by dropping with IPA. Sample 6 was a control sample of silicon. Each curve is an average of 3 passes. For the control samples, the Fowler Nordheim was not plotted.

Reference	I-V curve	F-N plot
Clare BC1		
Clare BC2		

Xray Generation by Field Emission

<p>Clare BC3</p>		
<p>Clare BC4</p>		
<p>Control BC6 (Bare Si)</p>		

*Table 2 : Summary of Clare emitter performance*

In the case of the FN plots, the hysteresis is very much in evidence.

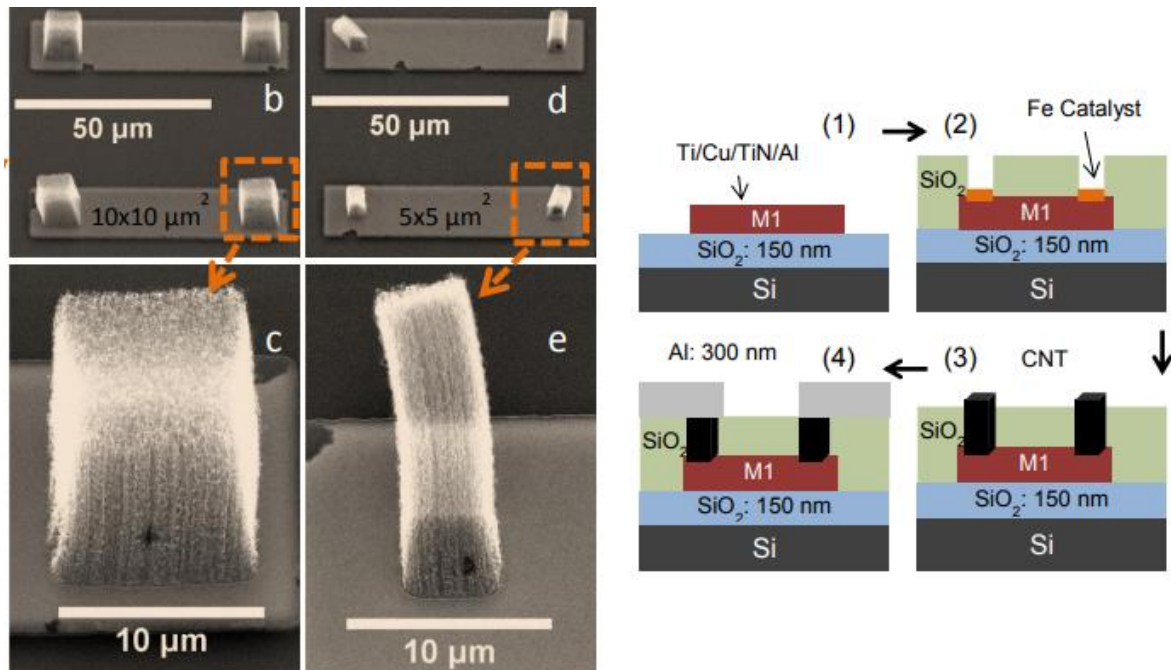
The fliers in the V-I curve for the control sample are believed to be instrumentation issues.

## 9.8 Samples from Surrey

In view of the problems with the original CPA samples, an alternative source of these items was located, by way of a comparison. A series of dense CNT forests were obtained from Prof. Ravi Silva, grown by his team at Surrey University. These were on silicon chips, irregular in size and measuring between 6 and 10 mm across.

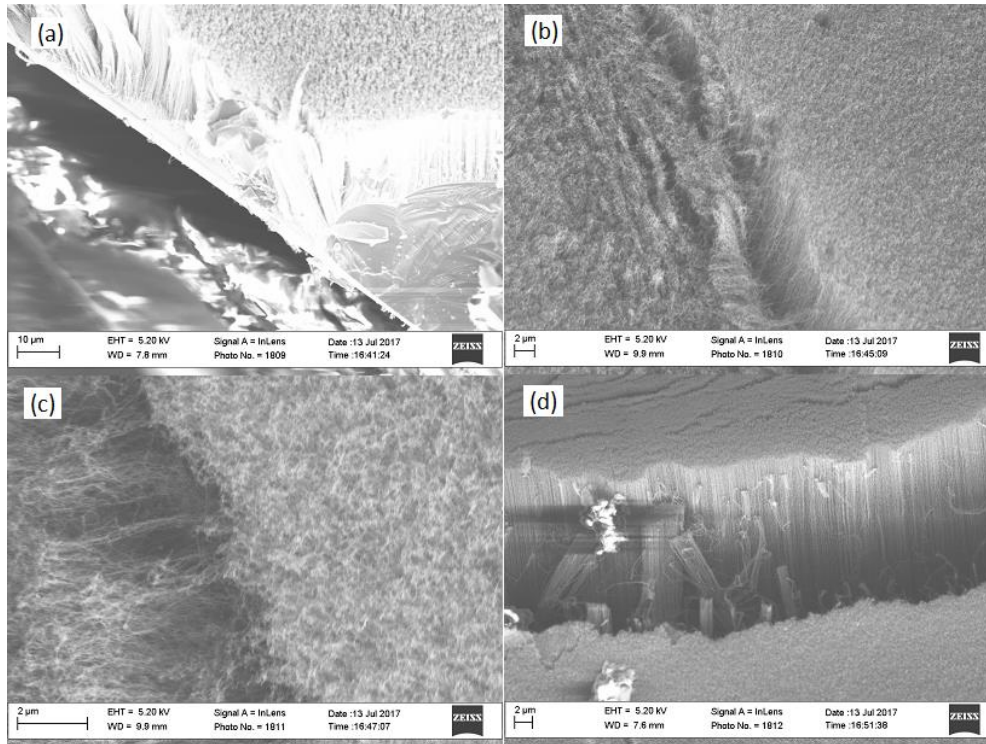
The team at the University of Surrey has developed a technique of growing the CNTs at a lower substrate temperature. In particular, one example uses no heating of the stage that carries the substrate [1], but rather heats the gases, by means of an array of radiant heaters above the substrate. Other techniques utilised include the use a gradual low temperature, below 450°C, in order to maximise the quality of the CNT growth [2-4].

Published images of CNT pillar arrays show very good vertical alignment, such as would be needed in the application for field emission X-ray sources :



**Figure 87 : Low temperature CPA growth.**

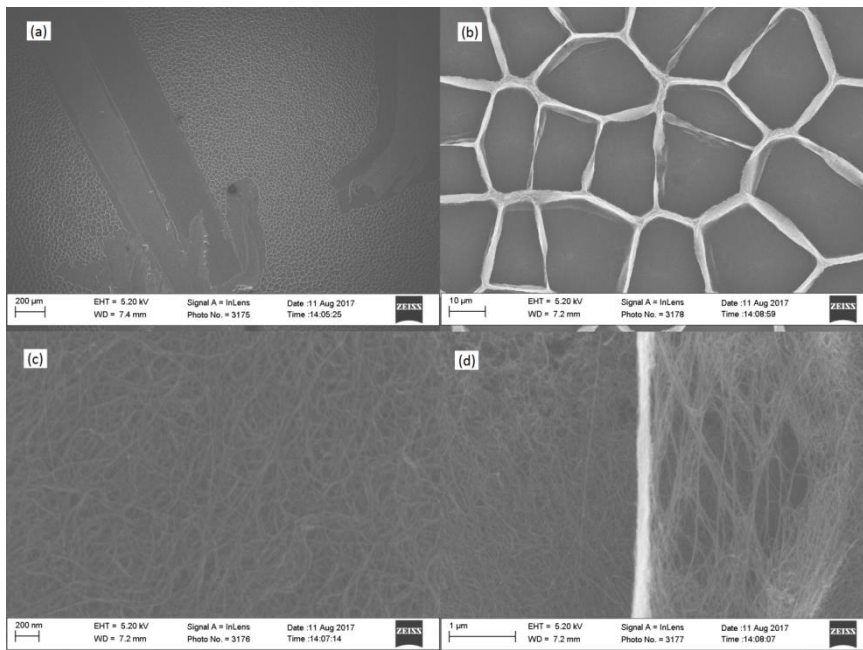
(b – e) Magnified images for the CNTs grown in vias of  $10 \times 10 \mu\text{m}^2$  and  $5 \times 5 \mu\text{m}^2$  sizes on M1. Process flow for the fabrication of CNT based vias. A layer stack of Ti/Cu/TiN (50/200/50 nm) is sputter deposited on a 150 nm  $\text{SiO}_2$  coated Si substrate and patterned lithographically using lift-off process (step 1). After this a 300 nm  $\text{SiO}_2$  film is grown and patterned to define via holes (step 2). A layer stack of Al/Fe (10/3 nm) is sputter deposited as catalyst for CNT growth. CNT growth is conducted in a PTCVD system and a 300 nm Al film (M2) is sputter deposited and patterned to form top contact. Adapted from [1].



**Figure 88 : Dense forests “as grown”**

CNT dense forests provided by University of Surrey – (a) sample 1, (b) sample 1 part 2, (c) sample 3 (d) sample 5. Viewing angle 30 degrees.

These chips were processed “as-grown”, and then densified by dropping on IPA.

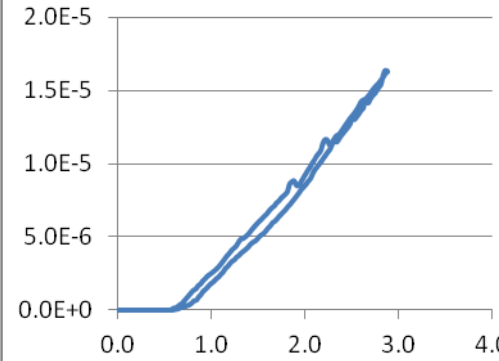
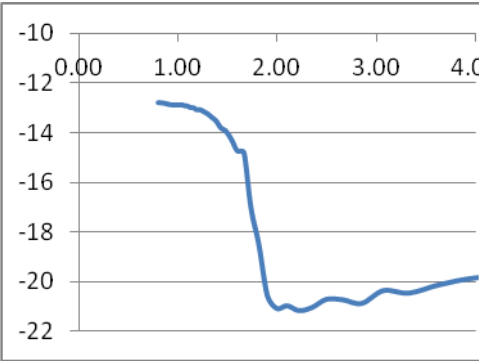
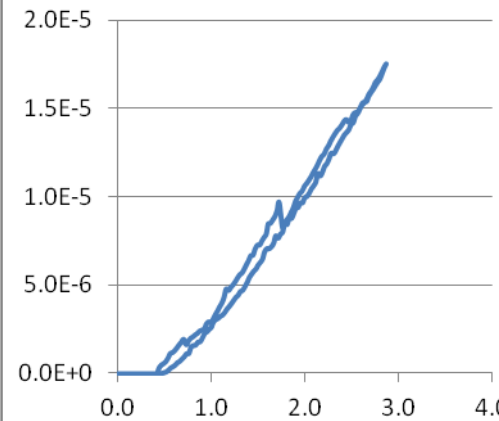
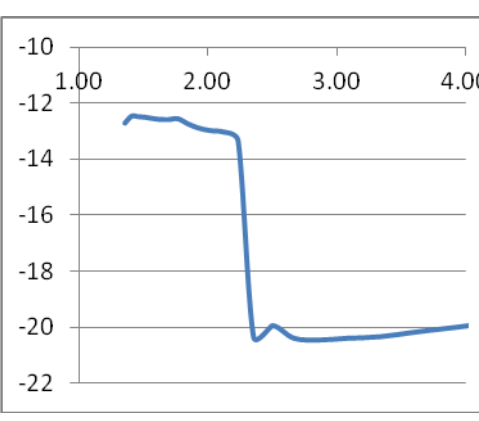
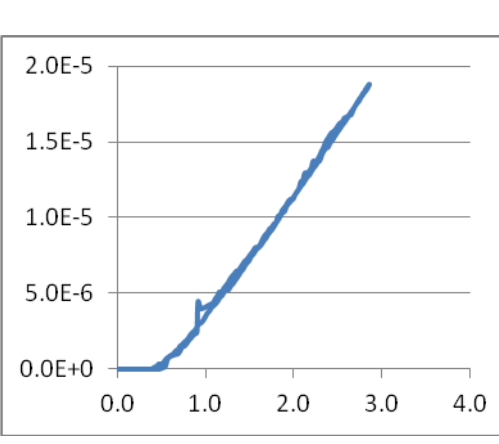
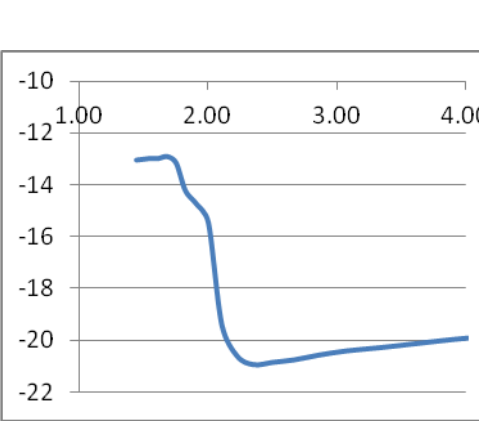


**Figure 89 : Dense forests post densification**

Dense forests from University of Surrey after densification – straight on view

### 9.9 Surrey “as-grown” plots

The following results in **Table 3** were taken from the parallel plate measurements of the emitters described above. These results were “as grown”. Sample 6 was a control sample of silicon. Each curve is an average of 3 passes.

Reference	I-V curve	F-N plot
Surrey BR1a	 <p>The I-V curve for Surrey BR1a shows current density (A/cm²) on the y-axis (0.0E+0 to 2.0E-5) versus electric field (kV/cm) on the x-axis (0.0 to 4.0). The curve starts at zero and begins to rise around 0.5 kV/cm, showing a characteristic field emission behavior with a sharp increase in current density above 1.5 kV/cm.</p>	 <p>The F-N plot for Surrey BR1a shows ln(J/E²) on the y-axis (-22 to -10) versus electric field (kV/cm) on the x-axis (0.00 to 4.00). The plot shows a characteristic field emission behavior with a sharp decrease in ln(J/E²) around 1.5 kV/cm, indicating a transition to field emission.</p>
Surrey BR1b	 <p>The I-V curve for Surrey BR1b shows current density (A/cm²) on the y-axis (0.0E+0 to 2.0E-5) versus electric field (kV/cm) on the x-axis (0.0 to 4.0). The curve starts at zero and begins to rise around 0.5 kV/cm, showing a characteristic field emission behavior with a sharp increase in current density above 1.5 kV/cm.</p>	 <p>The F-N plot for Surrey BR1b shows ln(J/E²) on the y-axis (-22 to -10) versus electric field (kV/cm) on the x-axis (1.00 to 4.00). The plot shows a characteristic field emission behavior with a sharp decrease in ln(J/E²) around 2.0 kV/cm, indicating a transition to field emission.</p>
Surrey BR3a	 <p>The I-V curve for Surrey BR3a shows current density (A/cm²) on the y-axis (0.0E+0 to 2.0E-5) versus electric field (kV/cm) on the x-axis (0.0 to 4.0). The curve starts at zero and begins to rise around 0.5 kV/cm, showing a characteristic field emission behavior with a sharp increase in current density above 1.5 kV/cm.</p>	 <p>The F-N plot for Surrey BR3a shows ln(J/E²) on the y-axis (-22 to -10) versus electric field (kV/cm) on the x-axis (1.00 to 4.00). The plot shows a characteristic field emission behavior with a sharp decrease in ln(J/E²) around 2.0 kV/cm, indicating a transition to field emission.</p>

Xray Generation by Field Emission

<p>Surrey BR3b</p>		
<p>Surrey BR5</p>		
<p>Control BC4 (Bare Si)</p>		<p style="text-align: center;">7</p>

**Table 3: Summary of Surrey”as grown” emitter performance**

### 9.10 Surrey “after densification” plots

The following results in **Table 4** were taken from the parallel plate measurements of the emitters described above. These results were “after densification” by dropping with IPA. Sample 6 was a control sample of silicon. Each curve is an average of 3 passes.

Reference	I-V curve	F-N plot
Surrey BR1a		
Surrey BR3a		
Surrey BR5		

**Table 4 : Summary of Surrey “densified” emitter performance**

## 9.11 Summary of measurements

Chip	From	Identification	$E_{on}$	$I_{max}$	at (kV max)
			@ $i=1e-7$		
BC1	Clare	20 secs growth	3.10	3.00E-06	5.0
BC2	Clare	40 secs growth	2.55	1.13E-05	5.0
BC3	Clare	80 secs growth	2.30	9.30E-07	5.0
BC4	Clare	160 secs growth	1.00	2.80E-05	5.0
BR1	Surrey	Std [TiNAIFe]	0.63	1.65E-05	3.0
BR2	Surrey	Std [TiNAIFe]	0.47	1.70E-05	3.0
BR3	Surrey	Al(i)684 [long CNTs]	0.47	1.90E-05	3.0
BR4	Surrey	Al(i)684 [long CNTs]	0.86	1.55E-05	3.0
BR5	Surrey	Ag774 [long CNTs]	0.17	2.40E-05	3.0
BR1_dens	Surrey	Std [TiNAIFe]	0.80	1.45E-05	3.0
BR3_dens	Surrey	Al(i)684 [long CNTs]	0.77	1.60E-05	3.0
BR5_dens	Surrey	Ag774 [long CNTs]	0.17	2.40E-05	3.0
BC4	Bare Si			2.00E-10	3.0
Notes :					
Clare samples had 2 x 2 mm emitting area					
Surrey samples were a full forest covering chip approx 6 x 6 mm					

**Table 5 : Summary of all emitter performance**

Notes :

- The samples from Surrey were dense forests and thus would be expected to exhibit electrostatic screening.
- It is noticeable that the densified samples produced results that are very similar to the “as grown” items.
- The sample BR5, referred to as Ag774 shows exceptional characteristics, of very low  $E_{on}$  and high  $J_{max}$ . Thoughts on what might be causing this :

- (i) Some kind of adlayer effect, as a result of materials used during the growth
- (ii) The “Ag” catalyst refers to silver, so there could be a plasmonic effect as a result of residual silver atoms on the CNT tips. This is analogous to recent work on CNTs with gold nanoparticles [9].

## 9.12 Additional unpatterned samples

The growth of the first samples from Cambridge were disappointing, both in terms of the morphology and the measured emission performance.

A second batch of samples were grown, on a silicon substrate with ITO (Indium Tin Oxide) conductive layer. In this case, the structure of the emitter was affected by the heating of the substrate which caused poor adhesion of the ITO layer to the silicon. In order to resolve the effects of heating, the sample was replaced with unpatterned samples on silicon with 1.3nm oxide. The growth is shown in **Figure 90**, below.

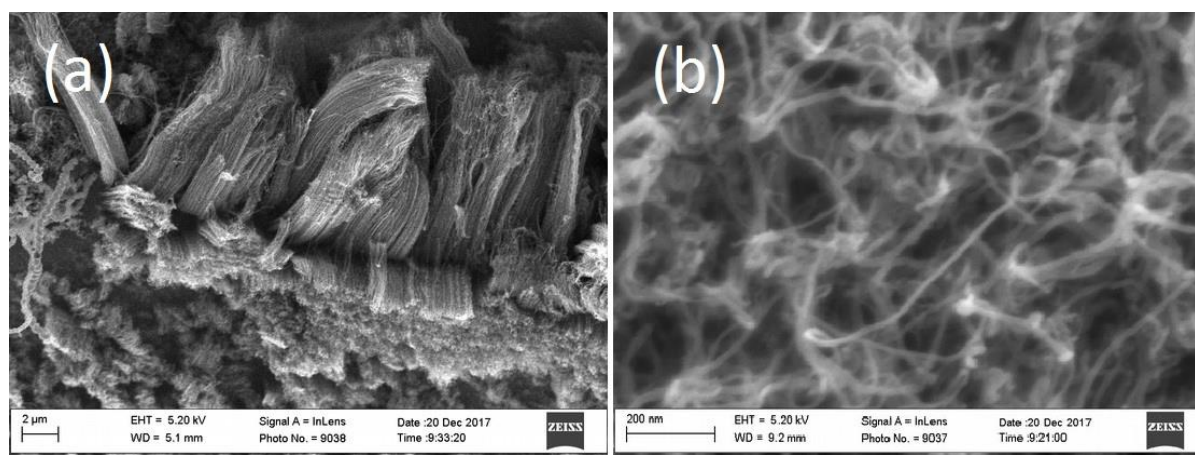


**Figure 90 : Unpatterned samples**

- (a) The forest appears to consist of an accumulation of bundles of nanotubes, typically 10-20nm in diameter, which thins out at the top edge. (b) there is a wide range of sizes and orientations present .

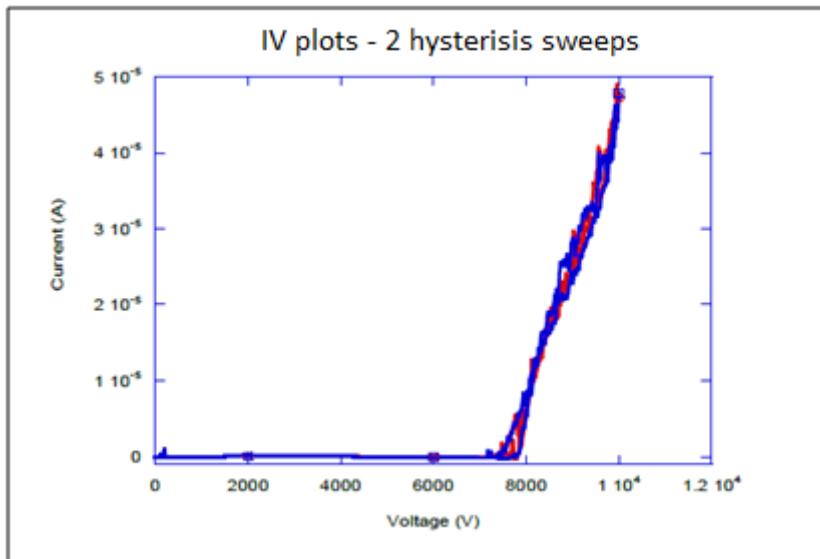


**Figure 91 : Unpatterned sample IV plot**

Testing was carried out in a UHV system at a background pressure of 5e-7mbar measured on the side of the sample away from the ion pump. Significant current starts to appear at applied voltages of greater than about 8kV, although the indicated voltage may be misleading.

In **Figure 91**, the results shown are from two hysteresis sweeps i.e. a sweep from 0V to -10kV and back to 0V. As can be seen the sweeps are very consistent apart from some stochastic noise. This behaviour was found to be stable over a considerable period of testing (several hours) once the extractor electrode had outgassed. At the higher currents there was a significant increase in the pressure, despite the system having been baked previously. The load on the extractor electrode is hundreds of mWs at the higher voltages and as this assembly only weighs a few grams it seems likely that it was getting hot.

There was no detectable current on the remote anode, but this is no surprise as this is an unpatterned sample, with primary emission occurring around the edge of the forest. Most of the emission will see a blank metal surface. Only emission close to the nickel TEM grid can be extracted into the space beyond, but as this corresponds to only a few percent of the emission area, there is little available current to detect. The conclusion was therefore that clearly, a patterned sample is needed.

The gap was set by the difference between a ceramic spacer of thickness 1.19mm and the thickness of the silicon wafer 0.79mm, giving a nominal gap of 0.4mm. This gap would

be increased if the ceramic and silicon pieces were not parallel and reduced by the thickness of the nickel grid.

Based on this gap estimate, the electric field for the onset of significant current appears to be about 20V/micron, which seems somewhat high, although perhaps not unexpected for field emitters of this type. Further interpretation is complicated by the uncertainty of the number/size of the emitters, however a FN type plot from a single hysteresis sweep (see **Figure 92**) shows behaviour above this threshold that is consistent with field emission.

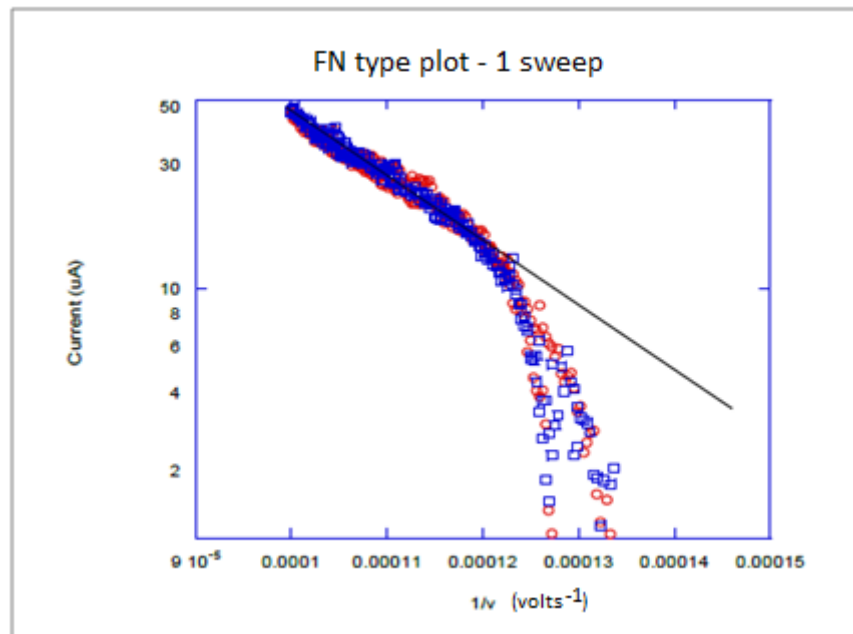


**Figure 92 : Unpatterned sample FN type plot**

Blue points show increasing sweep voltage, red points are decreasing sweep voltage.

### 9.13 Results from a patterned array

From the foregoing, it is clear that a successful solution requires a patterned array. After further modifications, the following results were achieved, with a patterned mask. The patterned area covers about 2mm by 2mm, with nominally 3 micron diameter dots on a 50 micron pitch, ie a total of 1600 dots. This matches well with the patterned area of a standard 3mm TEM grid, if aligned well, as described in section 9.15.

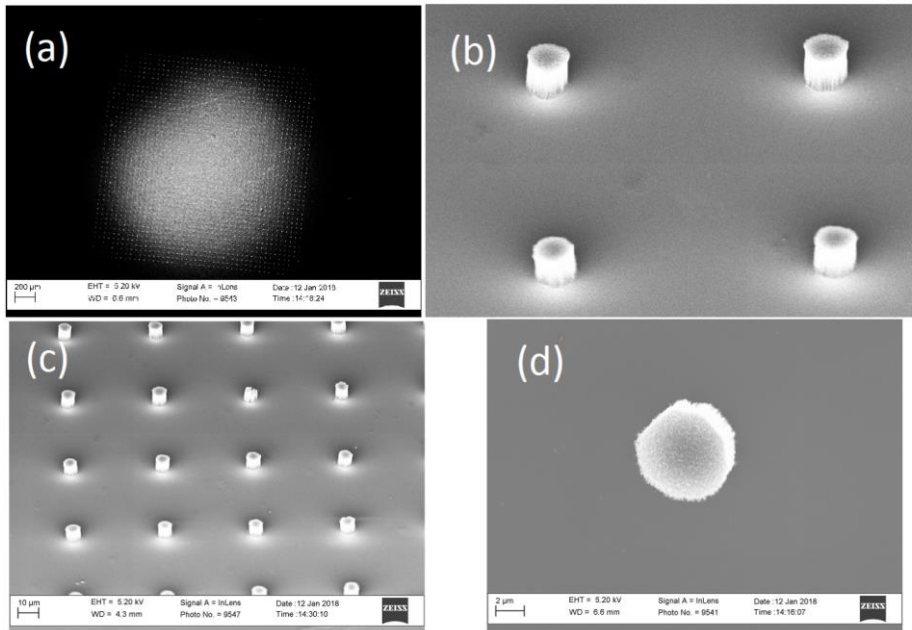


**Figure 93 : SEM of Patterned sample**

(a) Plan view SEM image of a patterned dot array after CNT growth. (b), (c) 45 degree tilted SEM image showing dense nanotube growth over the dot area. The pillar height is about 10 microns. (d) Each dot covers a disc of about 5 microns diameter with a dense bundle of CNTs. These are more separated at the top outer edge, where many fine tips can be seen.

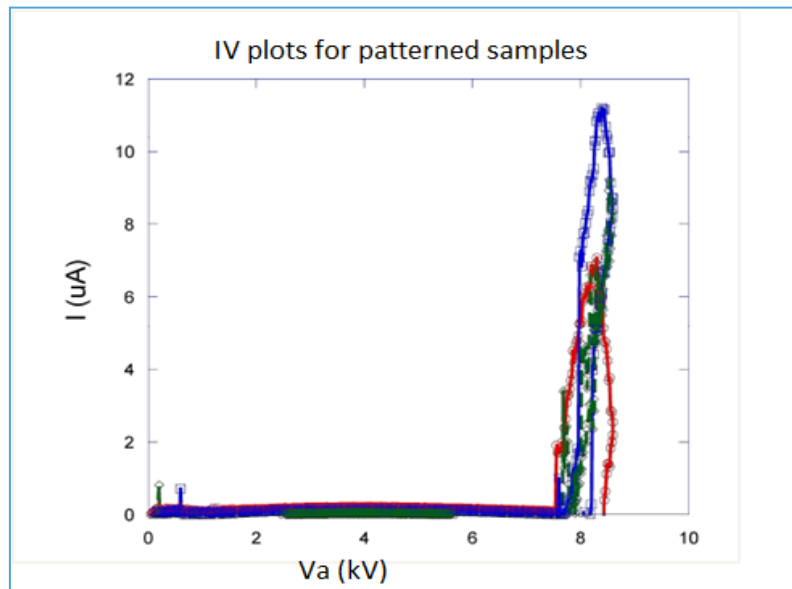


**Figure 94 : Patterned sample - IV plots- 3 sweeps**

Electrical measurements were taken in the same way as with the unpatterned array. The pressure was about  $5e-7$  mBar, with a small rise in pressure during emission. The onset of emission occurs at almost 2kV lower voltage than with the unpatterned array, but shows significantly more hysteresis, as a result of residual photoresist.

The results of three IV sweeps are shown in **Figure 94**. Since the active area is now 2mm by 2mm compared to the 8mm by 8mm for the unpatterned array, the current levels here represent a 16 fold increase in current density. Significant increases in pressure are seen at the higher currents, probably due to outgassing of the anode. This therefore requires additional cooling.

### 9.14 Further Surrey samples

A set of masked samples were prepared to send to Surrey. In this case they were lithographically patterned, to leave a 2mm x 2mm array of 2 micron growth sites on a 10 micron pitch, centred on a 10mm silicon chip.

The initial batch of samples showed poor adhesion of the CNTs to the catalyst. It was surmised that the cause of this was the thickness of the photoresist – when the resist was removed, it left a thin layer of material on top of the catalyst, thereby preventing the attachment of the CNTs.

### 9.15 Construction of a prototype triode assembly.

In order to create a controllable source, it is necessary to assemble a triode configuration. In this, the cathode emitter is mounted adjacent to an extraction grid. It is necessary to have a grid that is relatively transparent, and for this purpose a Transmission Electron Microscope (TEM) grid has been used, TAAB Laboratories type ‘Micron’ GT001/c, with 100 $\mu$ m hole width, 25 $\mu$  bar width and 64% transmission. Photographs are shown in **Figure 95**.

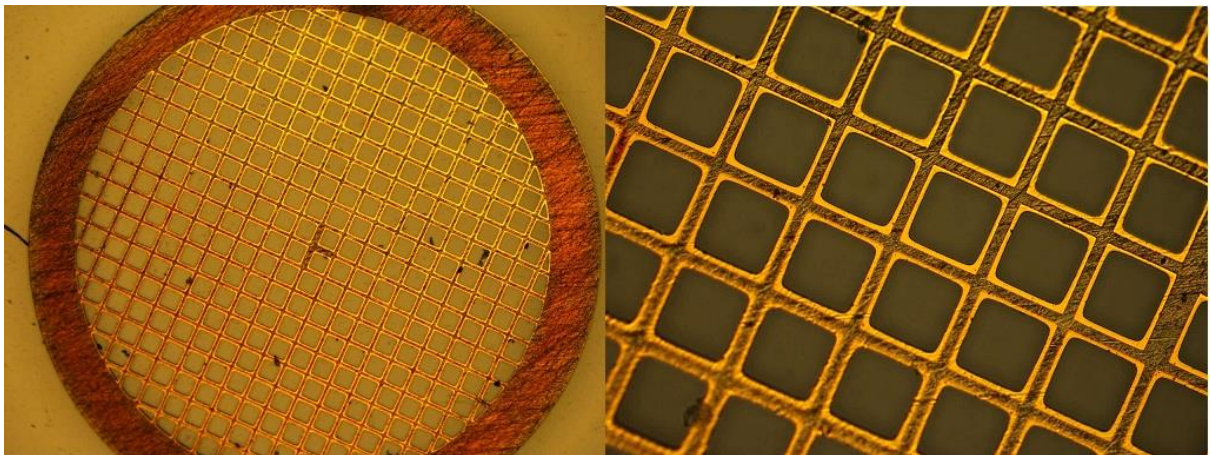


*Figure 95 : TEM grid with mesh dimension of 100 microns*

The triode structure, shown in **Figure 96**, is based on a different UHV feed-through from that used for the field emission measurements described in the previous section. This feed-through is equipped with two large copper terminals and two small ferrous terminals. The anode and cathode terminals use the copper feed-throughs so that improved cooling is available. The extractor grid uses the ferrous terminals, which can be switched faster than the larger conductors. This has involved the fabrication of a number of ceramic and phosphor bronze parts to enable the CNT array to be clamped in position and spaced from the extractor grid. Other parts are stainless steel or OHFC copper. The construction and assembly is shown in **Figure 97**.

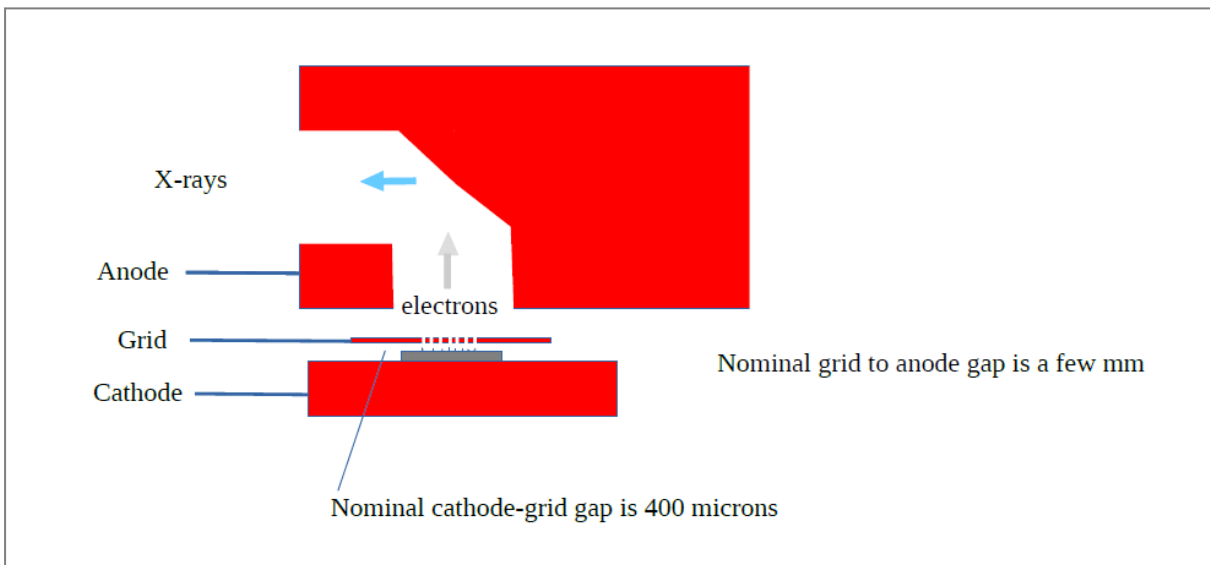


**Figure 96 : Schematic of the final triode assembly**

Parts as fabricated are shown below in **Figure 97**.

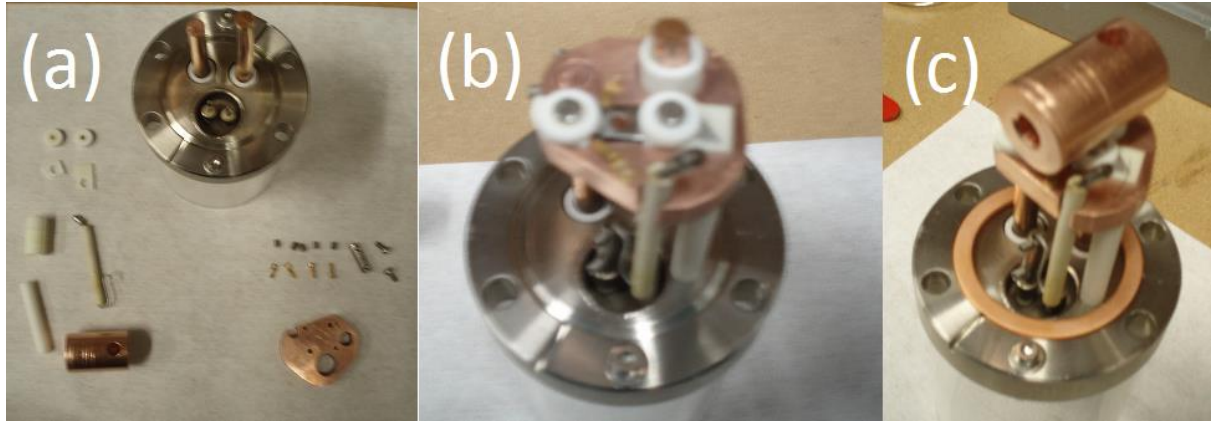


**Figure 97 : Stages of Triode assembly**

(a) Prior to mounting the CNT array and extractor grid. (b) After mounting onto the feed-through flange and connecting the extractor grid to one of the small feed-throughs. The CNT array is connected to the LHS copper feed-through. (c) After mounting the anode onto the RHS copper feed-through. The anode is cylindrical with a hole at one end face (lower left in the image). This is connected via a radial hole through to the extractor grid with an angled wall so that electrons landing in this region can give X-ray emission along the axis of the cylinder.

### 9.16 Two terminal testing of the cathode/grid section.

The extractor grid current was measured using a Keithley 236 which provides much better sensitivity and dynamic range than the power supply current monitor. In addition, the grid voltage can be changed in order to explore gating. The base pressure after baking was  $1.5 \times 10^{-7}$  mbar. Measurements were made using the anode and grid grounded in order to check for FN behaviour. The graphs in **Figure 98** show the data from six successive sweeps from 0V up to -2kV and back again. There is very consistent behaviour with each sweep (possibly as a result of the improved pressure) and the turn-on voltage is around 1000V corresponding to a nominal electric field of around 2V/micron.

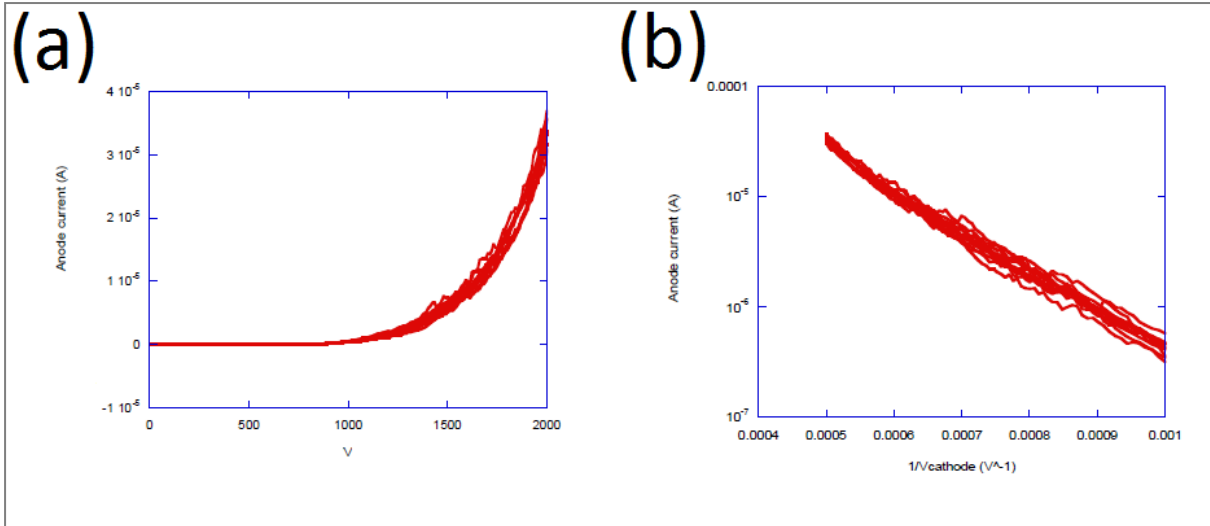


**Figure 98 : Triode assembly – IV and FN type plots**

Results from six successive sweeps, from 0 to 2kV and back, as described in 9.16. (a) IV response and (b) FN-type plot for cathode/grid section of the triode assembly

### 9.17 Three terminal testing

The effectiveness of the cathode/grid assembly in controlling the beam current (anode current) of the triode assembly was measured by stepping the grid voltage, and sweeping the cathode voltage whilst measuring the grid current. This is repeated for different values of anode voltage. One would expect to see a relationship similar to the results of the two terminal testing.

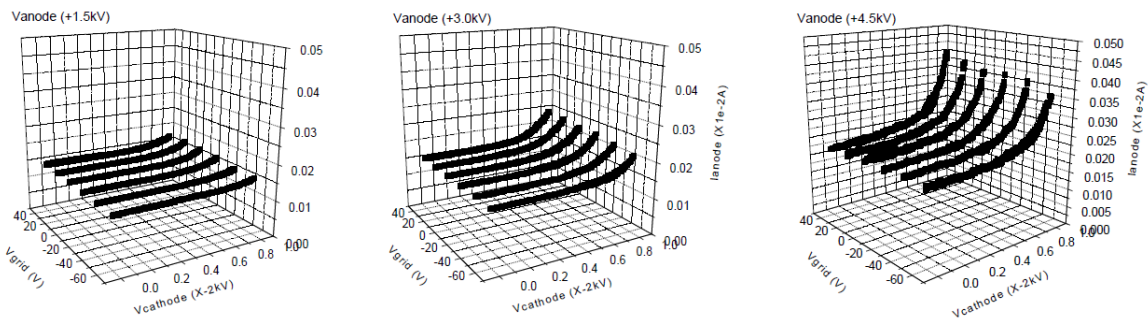


**Figure 99 : Anode response for swept cathode and stepped gate voltage**

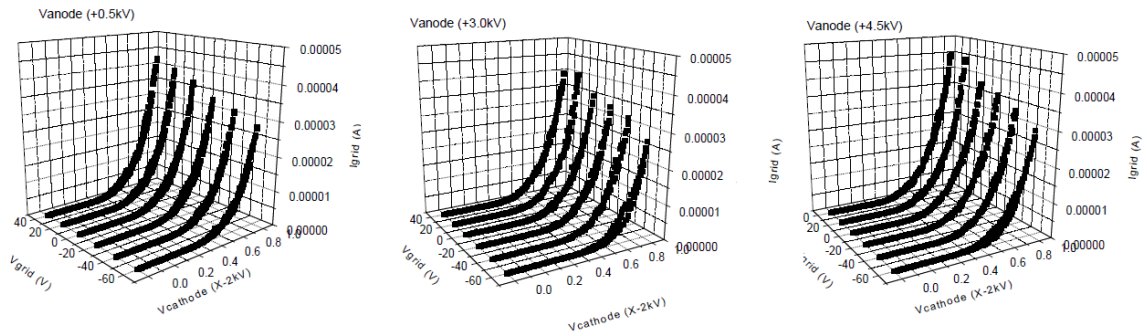


**Figure 100 : Gate response for swept cathode and stepped gate voltage**

Considering the data in **Figures 99 and 100**, it can be seen that the anode current is strongly influenced by the cathode voltage, as expected. This replicates the results seen with the sealed inserts in chapter 6, albeit at a much lower anode voltage. Therefore it is possible to assume that the grid current is arising as a result of field emission from the cathode.

Below the level at which there is the threshold grid current, there is a significant anode current of around 150µA, which is almost independent of anode voltage, as long as the anode voltage is greater than about 1.5kV. This is suggesting that there is an effect analogous to the cold cathode emission seen in thermionic X-ray tubes.

When the grid current increases, it can be seen that, at 4.5kV substantially more of the cathode current is flowing to the anode. This suggests that the anode current may be effectively controlled by the cathode-grid voltage, and that a large proportion of the cathode emission passes to the anode.

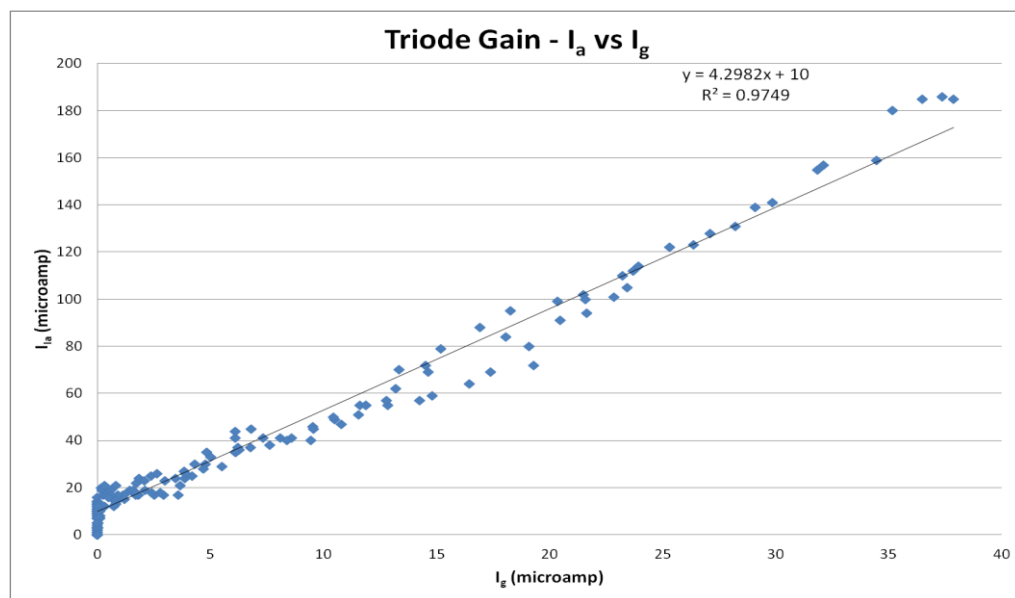


**Figure 101: Triode gain plot –  $I_a$  vs  $I_g$**

Indeed, in **Figure 99**, for an anode voltage of 4.5kV and gate voltage of 0V, a differential anode current of  $(380 - 150) = 230\mu\text{A}$  is created by a differential grid current of  $35\mu\text{A}$ , as seen in **Figure 100**. This should be compared with the efficiency of the sealed insert cathode assembly measured in Chapter 6, in which the grid current is approximately equal to the anode current. The triode gain is plotted in **Figure 101**.

It must be noted that the anode voltages are significantly below those that are normally used for useful X-ray generation.

## 9.18 Conclusions

The major elements associated with a good field emission electron source, such as that needed in a X-ray generator are, a high quality patterned CNT pillar array, high transparency extraction grid and very good quality vacuum with minimal out-gassing, with particular attention given to thermal management. Giving due regard to all of these aspects it has been possible to produce a triode assembly with the potential to deliver a source with the performance needed to continue with other aspects of this project.

This work has led to an understanding of the cause of the failures in the sealed inserts, recorded in chapter 6. As a result of the lessons learnt during this period, it is clear that it will be necessary to make substantial modifications to the test rig, before proceeding to optimise the physical and electrical parameters of the X-ray source.

## 9.19 References

- 1 AHMAD, M., ANGUIA JOSE, V., STOLOJAN, V., CORLESS, T., CHEN, J. S., CAREY, J. D. & SILVA, S. R. P. 2015. High Quality Carbon Nanotubes on Conductive Substrates Grown at Low Temperatures. *Advanced Functional Materials*, 25, 4419-4429.
- 2 ANGUIA JOSÉ, V., COX DAVID, C., AHMAD, M., TAN, Y. Y., ALLAM, J. & SILVA, S. R. P. 2013. Highly Transmissive Carbon Nanotube Forests Grown at Low Substrate Temperature. *Advanced Functional Materials*, 23, 5502-5509.
- 3 CHEN, G. Y., JENSEN, B., STOLOJAN, V. & SILVA, S. R. P. 2011. Growth of carbon nanotubes at temperatures compatible with integrated circuit technologies. *Carbon*, 49, 280-285.
- 4 CHEN, J.-S., STOLOJAN, V. & SILVA, S. R. P. 2015. Towards type-selective carbon nanotube growth at low substrate temperature via photo-thermal chemical vapour deposition. *Carbon*, 84, 409-418.
- 5 COLE, M., HIRALAL, P., YING, K., LI, C., ZHANG, Y., TEO, K., FERRARI, A. & MILNE, W. 2012. Dry-Transfer of Aligned Multiwalled Carbon Nanotubes for Flexible Transparent Thin Films. *Journal of Nanomaterials*.

- 6 COLE, M. T., DOHERTY, M., PARMEE, R., DAWSON, P. & MILNE, W. I. 2014. Ultra-broadband Polarisers Based on Metastable Free-Standing Aligned Carbon Nanotube Membranes. *Advanced Optical Materials*, 2, 929-937.
- 7 SOHN, J. I., NAM, C. & LEE, S. 2002. Vertically aligned carbon nanotube growth by pulsed laser deposition and thermal chemical vapor deposition methods. *Applied Surface Science*, 197, 568-573.
- 8 ZOU, Y., MAY, P. W., VIEIRA, S. M. C. & FOX, N. A. 2012. Field emission from diamond-coated multiwalled carbon nanotube “teepee” structures. *Journal of Applied Physics*, 112, 044903.
- 9 WILLIAMSON, CHRIS. 2017. Private conversation. Electrical Division, Engineering Department, Cambridge



# 10 DETECTOR AND SCINTILLATOR CHARACTERISTICS

## 10.1 Introduction

In its simplest form, the application of the Encoded Aperture algorithm for restoration of image sharpness assumes that the acquisition and accumulation of images, will be produced in a known binary pseudo random time sequence. The resultant image incorporates all of the additional information needed to restore the sharpness to the original image, by means of the deconvolution. In the version of the implementation as described in the Proof of Concept work in Chapter 5, the assumption is that each pulse of the sequence is represented by a box filter, and that this therefore requires effectively zero switching time of the source, as well as a zero lag time in the detector.

The switching time of the source has been considered in Chapter 7. In order for the system as a whole to work, the response time of the detector element, both in terms of delay, or lag, and in terms of non instantaneous transition from light to dark, must be considered.

## 10.2 Temporal performance of X-ray detectors

An Xray detector will normally comprise a photo-sensing element, on top of which, a scintillator is superimposed [4]. It is the function of this scintillator to convert the incident Xray photons into visible light. That visible light is then picked up by the photo-sites of the detector to produce the output signal. A typical construction is shown in **Figure 102**.

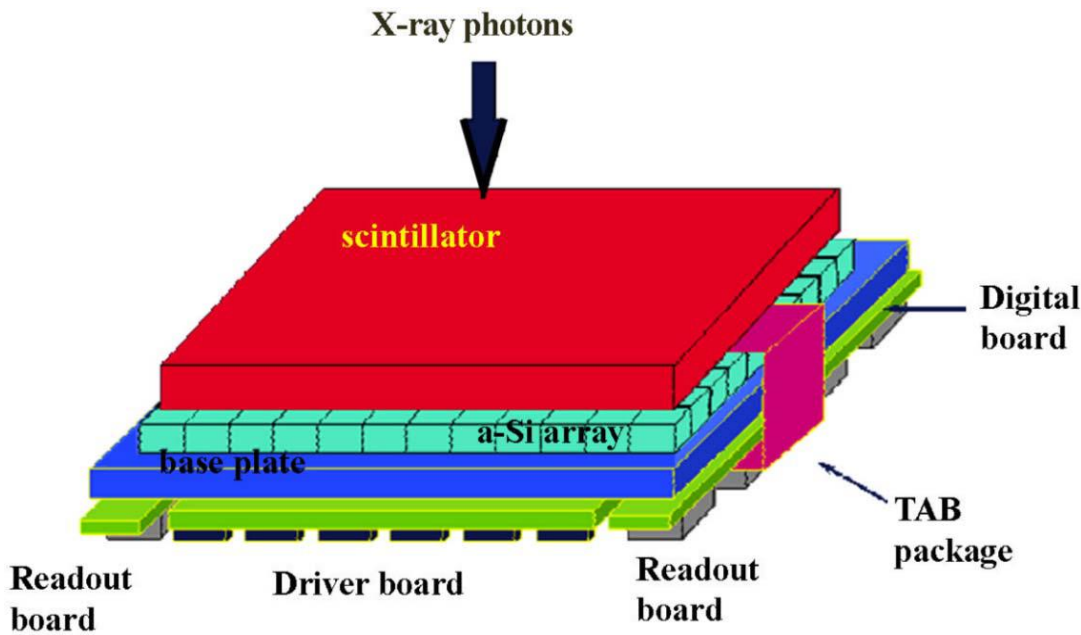


*Figure 102 : Construction of a X-ray area sensor.*

The silicon photodiode array may be amorphous silicon, as shown in **Figure 102**, or more commonly nowadays, an APS (active pixel sensor) array produced using CMOS technology [5]. The sensor is generally manufactured in “tiles” of a size that produces an acceptable yield from the silicon wafers employed. These tiles may then be abutted to create a sensor of the required size [9]. Since X-rays are generally not able to be refracted in the same way that is possible with visible light, there are no readily available equivalents to the optical lens. As a result, most X-ray systems rely on direct imaging of the object on to the detector, which usually limits the spatial resolution to the native pixel size of the detector. In irradiating the detector with a given photon flux,  $\Phi$ , the number of photons arriving at a given pixel during the integration period is clearly a function of the area of the pixel, as well as the duration of the acquisition. It is necessary to achieve a compromise to get the optimum combination of high resolution, and sensitivity, or speed of acquisition.

The number of photons,  $N$  arriving at a pixel is shown by

$$N = K \cdot \Phi \cdot d^2 \cdot t \quad \text{Equation 8}$$

where  $\Phi$  is the photon flux,  $d$  is the linear dimension of the photo-site,  $t$  is the integration time of the detector, and  $K$  relates to physical constants. The resulting output from the detector will be

$$V(x,y) = C \cdot N(x,y) + v_n \quad \text{Equation 9}$$

where  $V$  is the output voltage,  $v_n$  is the noise level arising from the circuitry,  $x$  and  $y$  are the pixel coordinates in the array, and  $C$  is related to physical constants. Clearly, we want the signal-to-noise ratio to be as high as possible. Under normal circumstances, a higher output,  $V$  requires a larger pixel, therefore limiting spatial resolution, or a longer acquisition time resulting in more motion blur when imaging a moving object, thereby limiting response time.

In practice, the response time of the silicon array will vary but may typically be 0.5 to 0.7 milliseconds. In comparison the response time of the scintillator may well be several hundred microseconds.

### 10.3 Requirement for Encoded Aperture implementation

At this point, it is necessary to consider the requirements for an encoded aperture system in relation to the practical requirements for a real-world application. Consider a typical requirement :

- A product is to be imaged on a continuously moving conveyor.
- The linear speed of the conveyor is 60m/min (1.0m/sec)
- The size of the object is 100mm in the direction of motion
- The point spread function (smear matrix) will have 52 point
- The number of “on” pulses will therefore be 26.
- The improvement in noise level is expected to be  $\sqrt{26} \approx 5$ .
- The length of the detector will be 2 x the length of the object = 200mm
- The period over which the encoded data will be acquired will be (200 – 100)mm
- This movement of 100mm will correspond to 52 pulses
- Each pulse will correspond to 2mm of travel of the object
- Each pulse will therefore correspond to a time interval of  $(2 * 1000 / 1000) \text{ ms} = 2.0\text{ms}$

- We therefore need a rise/fall time of the resulting signal to be significantly less than 2.0ms

## 10.4 Scintillator response time

A literature search has revealed relatively little specific temporal response data for developmental or commercial scintillators. Most publications referring to X-ray detectors focus of the performance of the sensor array [2, 8] in which static performance is the main criterion, while papers that specifically refer to scintillator screens appear to relate to neutron detection performance [1]. Direct contact with a series of manufacturers has similarly produced little in the way of detail, and data provided appears to be quite inconsistent with expected results.

It is clear that the scintillator response time is likely to be a significant factor in the implementation of an encoded aperture system. The importance of this can be seen from the following images, in which the bell actuator is being blurred by the longer integration time :

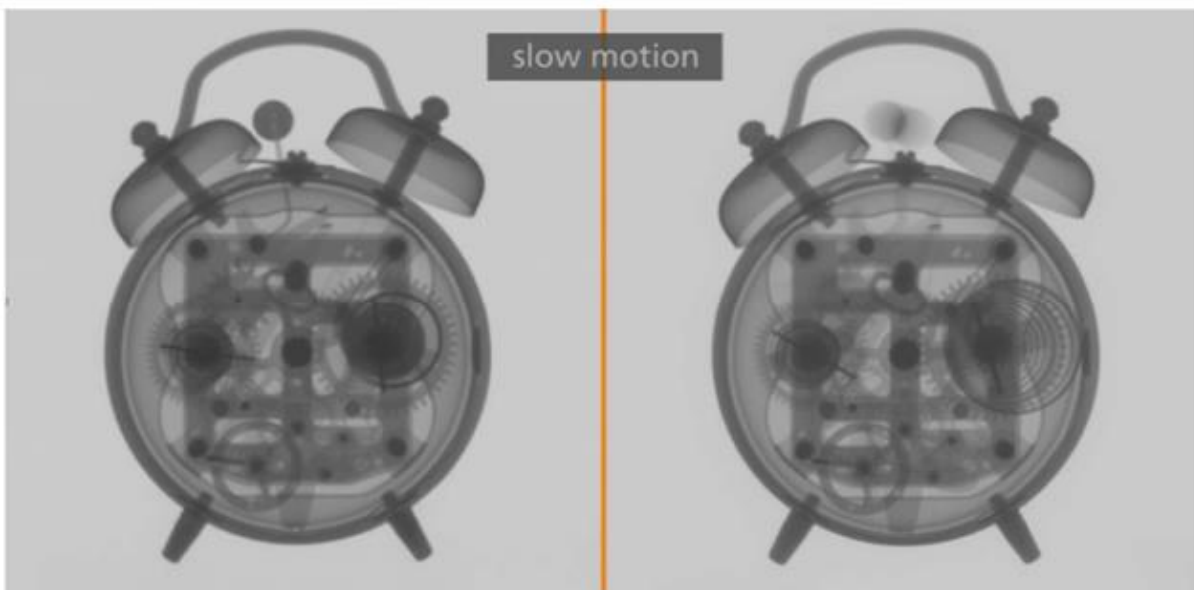


***Figure 103 : Demonstration of the effect of motion blur in X-ray images.***

Adapted from [3]

Different scintillator materials will have varying lag and response profiles. Materials such as Caesium Iodide (CsI) whilst having a fast response, to perhaps 3% of the normal irradiated output, but will continue to produce an output for a significant time thereafter –

known as “burn-in”. A method of examining and recording these characteristics is required.

## 10.5 Manufacturers data

Relatively little data is published by manufacturers of the response time of scintillator material. An example of the data that is required, is the unpublished information from several makers of X-ray detectors. Hamamatsu Photonics is a large Japanese producer of optical and X-ray sensors. As a result of the author’s close working relationship with them, the following data was obtained, on Caesium Iodide (CsI) and Lanex which is a form of Gadox.

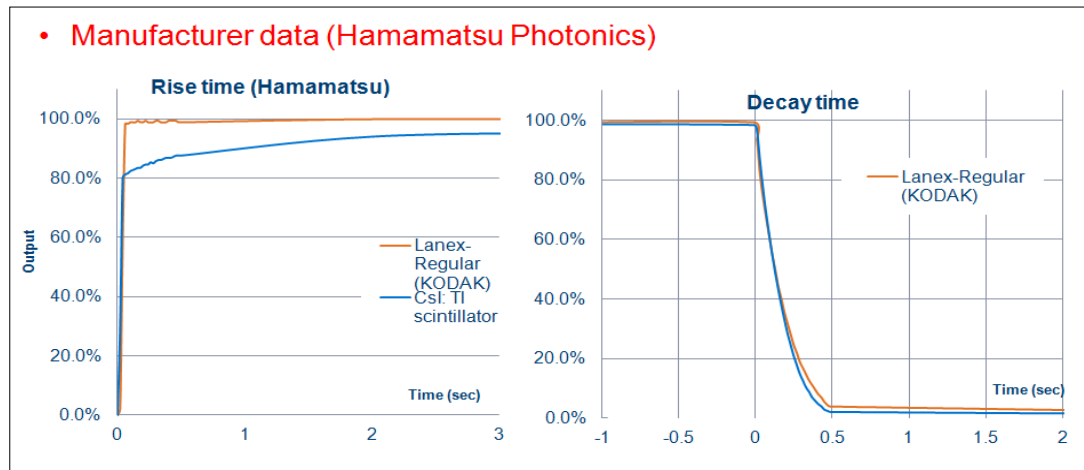


**Figure 104 : Temporal response of scintillator.**

This information shows certain expected characteristics, but clearly the decay time data is implausible.

The Fraunhofer Institute [3] is a quasi academic organisation, in Nurnberg, Germany, with activities in the area of optical and X-ray imaging techniques. The data provided shows similar features, particularly the incomplete saturation in CsI (XRD0840), relative to Gadox and the long apparent delay.

- Long term lag (Fraunhofer)

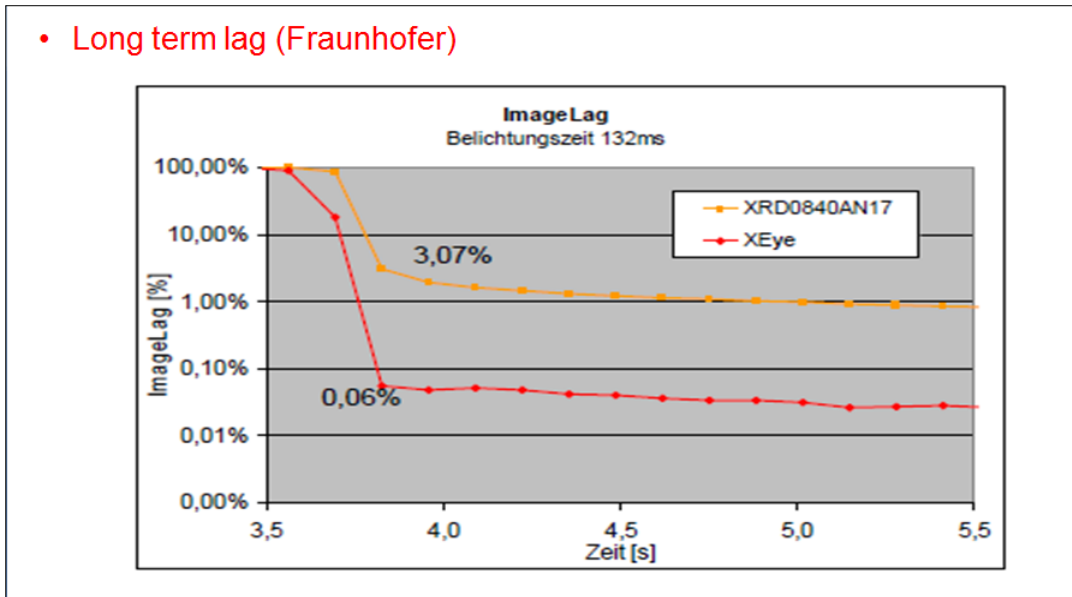


*Figure 105 : Temporal response of scintillator [3].*

The implausibility of this data lies in the fact that these scintillator materials are also used in conjunction with linear diode array detectors, which operate in a line-scan mode, with maximum scanning rates in the range of 2000 to 5000 scans per second. Clearly a decay time of the order of several tenths of a second would render the material unusable in this application.

Since the scintillator response time is a critical part of the Encoded Aperture implementation, it was important to devise a method of gaining independent data on the temporal characteristics of the scintillators that were available to this project.

## 10.6 Development of scintillator testing rig

The scintillator response time is to be measured by subjecting the detector assembly to X-rays of a known pulse duration. The most straightforward way to achieve this is by shuttering a continuous X-ray source with a rotating disc, as shown in **Figure 106**. The disc has an aperture with radial sides, so that the time of incidence of the radiation is constant at all points across the detector element. In addition the X-ray beam is collimated by a slot so that the transition, from fully shuttered to fully open, is as short as possible.

In the following example, the disc has 2 slots, on opposite sides of its rotational axis to maintain a balanced assembly. The slots are on a pitch circle diameter of 283mm (750mm circumference). The disc can rotate at up to 3000 revolutions per minute (50

revs per second). The collimation slot is 2mm, giving a minimum rise time of 53 microseconds.

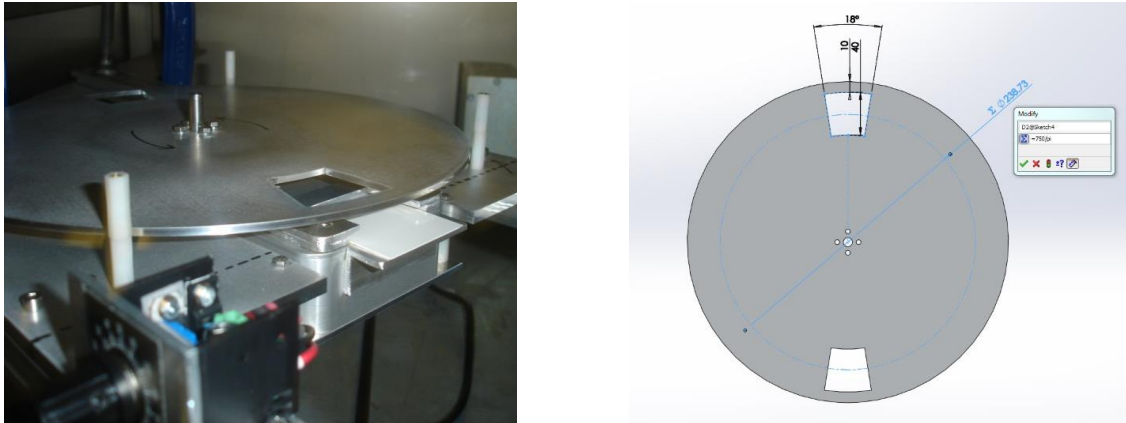


**Figure 1066 : Rotating shutter to test scintillator temporal response.**

### 10.7 Methodology

The detector under test was a Hamamatsu S1227-BR PIN photodiode [6], directly connected to a high gain amplifier stage with a balanced line output. This sensor chip comprises of a silicon device which is 500 microns thick and is therefore sensitive to low energy Xrays by direct conversion. The detector has been located in the Xray beam below the slot. The output of the amplifier stage was connected to a Picoscope USB oscilloscope [11] and recorded.

The detector was initially tested without scintillator, as a control, and then with a range of scintillator types provided by Hamamatsu Photonics [7] and Scintacor [10].

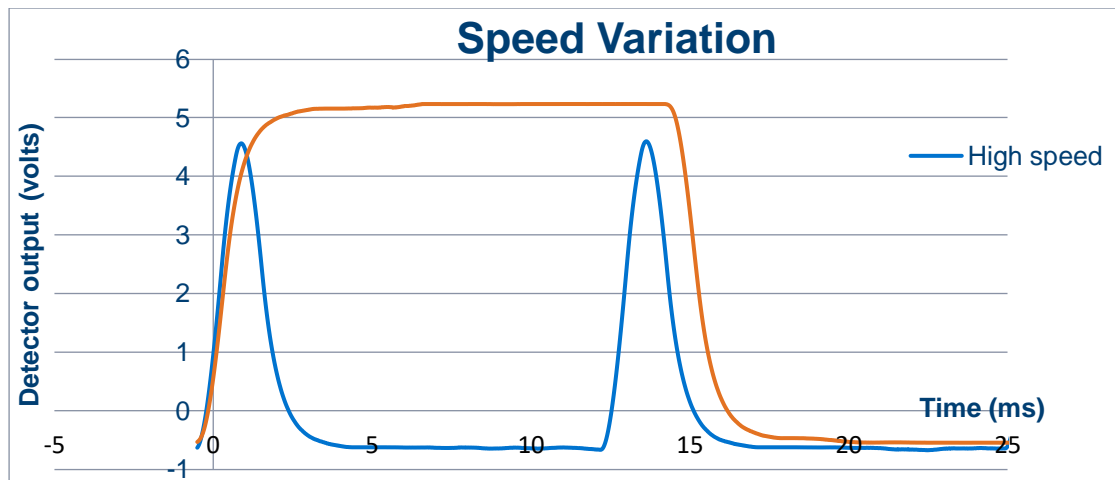


**Figure 1077 : Scintillator test - detector output (bare silicon)**

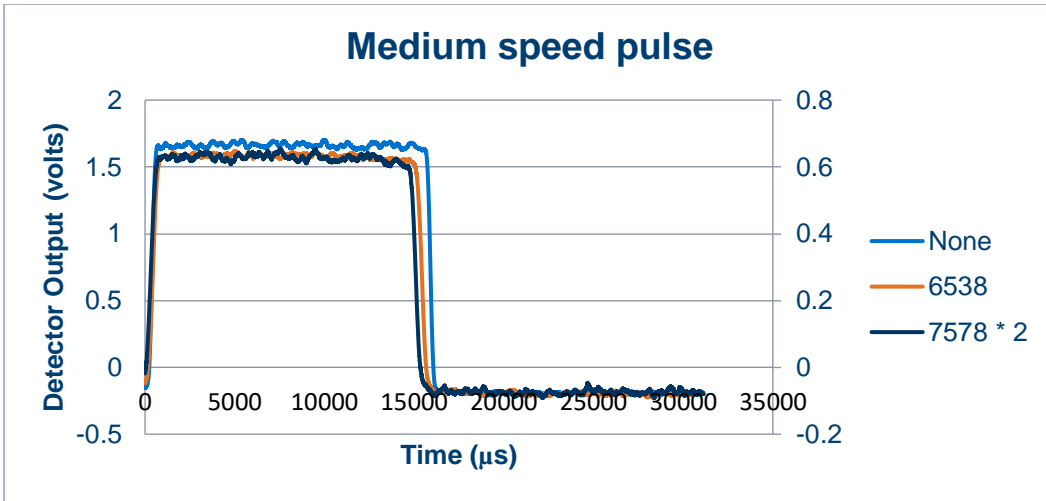


Figure 108 : CsI scintillator with fibre-optic plate

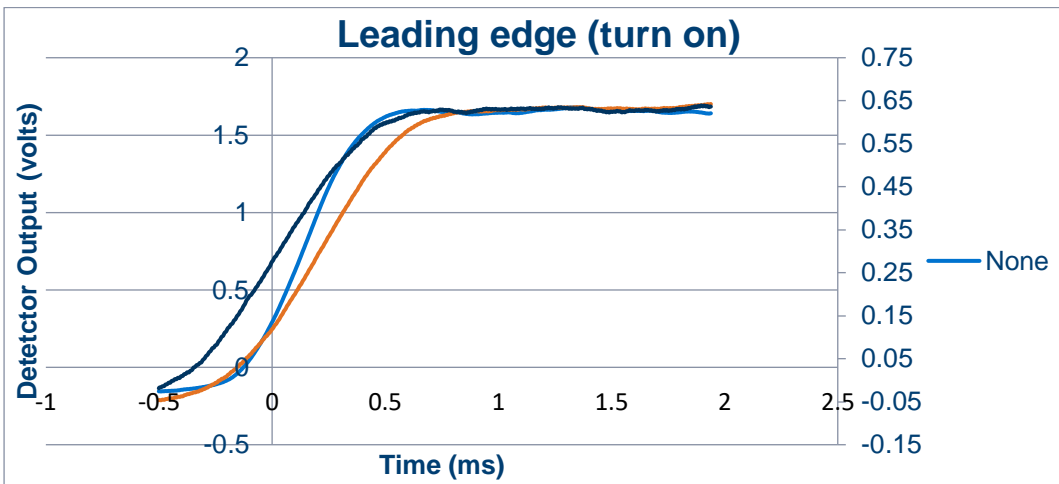


Figure 109 : CsI scintillator leading edge with Fibre-optic plate

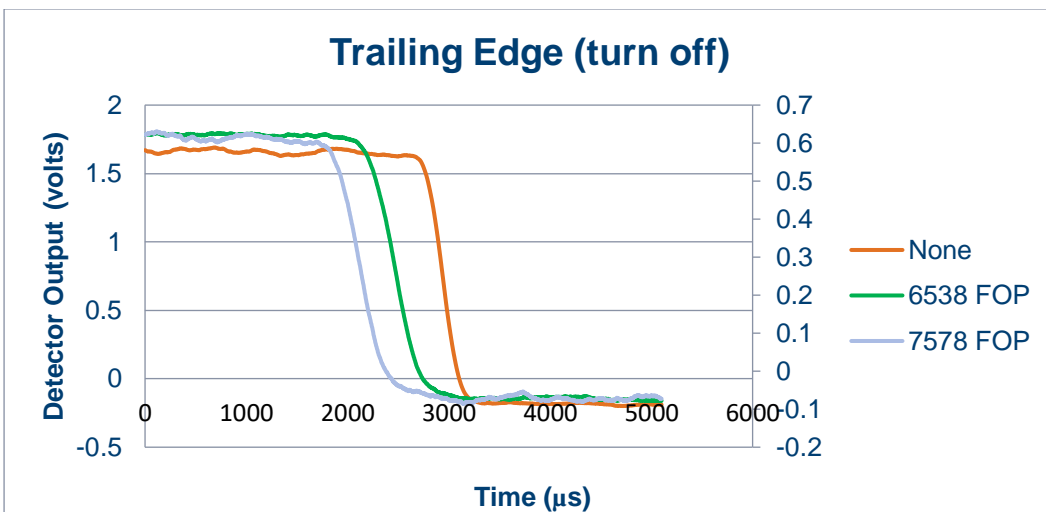


Figure 110 : CsI scintillator trailing edge with Fibre-optic plate

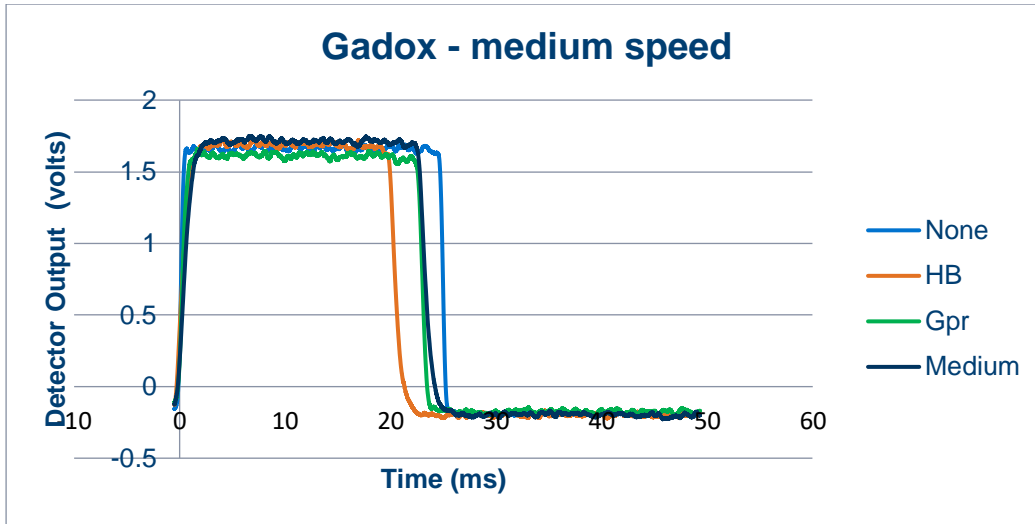


Figure 111 : Gadox with Fibre-optic plate – porous side

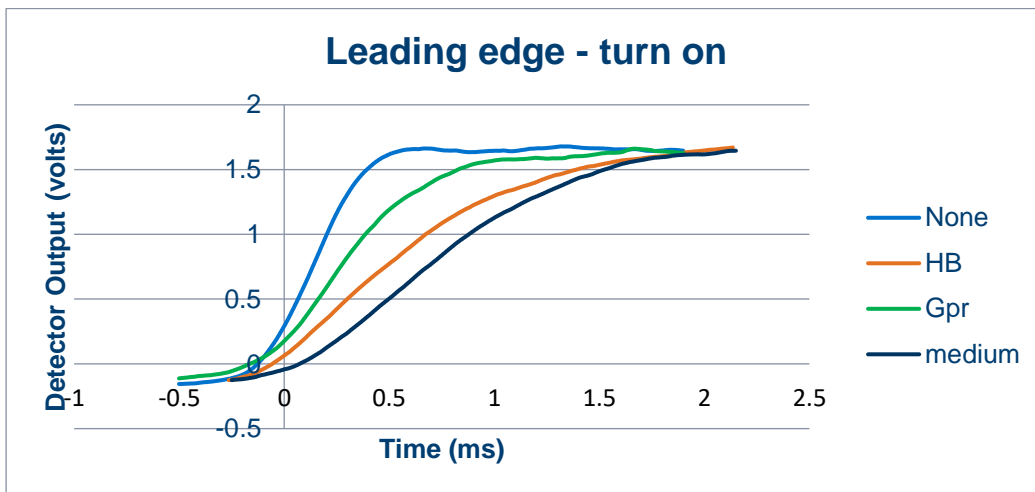


Figure 112 : Gadox with Fibre-optic plate – leading edge – porous side

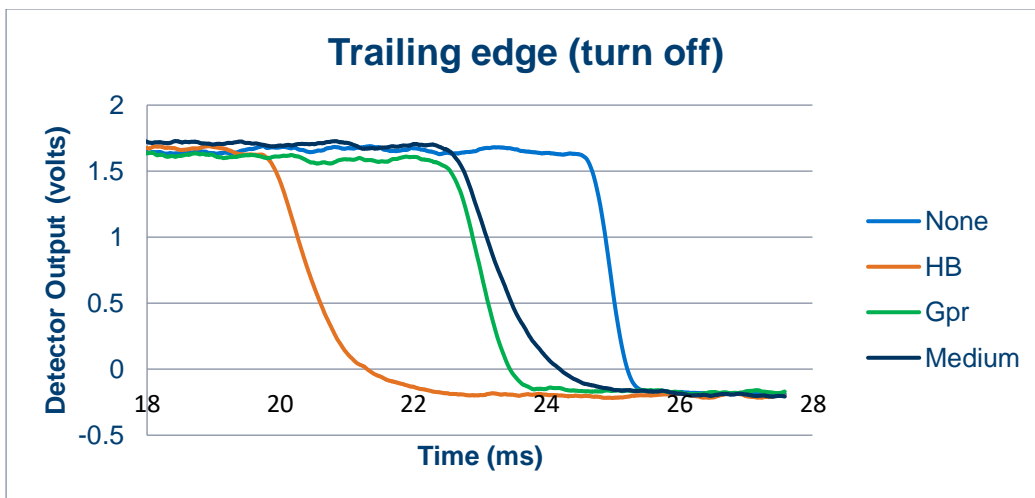


Figure 113 : Gadox with Fibre-optic plate – trailing edge – porous side

The summary of the results on the preceding pages is :

Summary of data					
Calculated from 10% to 90% points in milliseconds					
Gadox		None	HB	Gpr	Medium
	Leading	0.54	1.58	0.98	1.60
	Trailing	0.55	1.48	0.88	1.57
CsI		None	6735	7578	
	Leading	0.54	0.87	0.94	
	Trailing	0.55	0.89	0.96	

**Table 6 : CsI scintillator with fibre-optic plate**

## 10.8 Conclusions

The conclusions of this study are :

- CsI gives good high level response but long term lag or burn-in of ~ 3%
- Gadox is slower, but with less lag.
- For both type of scintillator, turn-on responses ca. 0.75 – 1.6 ms
- For both type of scintillator, turn-off responses ca. 1.0 – 1.6 ms

This delay is a limiting factor and therefore a further deconvolution will be required to take account of the non-ideal response time of the detector.

As we have seen in Chapter 5, the advantage offered by Encoded Aperture, is the increase in total acquisition time, thereby improving the signal to noise ratio.

## 10.9 Impact of non-ideal scintillator response

The effect of the detector response on the deconvolution used in the Encoded Aperture solution, would be to replace the ideal Box Filter with a Trapezoidal function. This will have the consequence of lower frequency bands in the deconvolved data, which will limit the degree of sharpness that can be restored.

## 10.10 References

- 1 CHA, B. K., KIM, J. Y., KIM, T. J., SIM, C., CHO, G., LEE, D. H., SEO, C. W., JEON, S. & HUH, Y. 2011. Use and imaging performance of CMOS flat panel imager with LiF/ZnS(Ag) and Gadox scintillation screens for neutron radiography. *Journal of Instrumentation*, 6, C01064.
- 2 FRANCO, L., GÓMEZ, F. & BADANO, A. 2008. Characterization and simulation of linear scintillator arrays for low-energy x-ray detection. *Measurement Science and Technology*, 19, 115504.
- 3 FRAUNHOFER 2014. X-eye presentation. Fraunhofer Institute.
- 4 FRÖJDH, C., ANDERSSON, J., BATES, R., HEUKEN, M., IRSIGLER, R., PETERSSON, C. S., O'SHEA, V., SMITH, K., STAMATAKIS, H. & WELANDER, U. 1999. New sensors for dental X-ray imaging. *Nuclear Instruments and Methods in Physics Research Section A: Accelerators, Spectrometers, Detectors and Associated Equipment*, 434, 18-23.
- 5 GREIG, T., CASTELLI, C., HOLLAND, A. & BURT, D. 2007. The design of an active pixel sensor test structure optimised for the read out of scintillator screens. *Nuclear Instruments and Methods in Physics Research Section A: Accelerators, Spectrometers, Detectors and Associated Equipment*, 573, 30-33.
- 6 HAMAMATSU. 2010. *Si photodiode S1227-1010BR* [Online]. Available: <http://www.hamamatsu.com/jp/en/product/category/3100/4001/4103/S1227-1010BR/index.html> [Accessed].
- 7 HAMAMATSU. 2016. *Company website* [Online]. Available: <http://www.hamamatsu.com/> [Accessed].
- 8 NAGARKAR, V. V., GUPTA, T. K., MILLER, S. R., KLUGERMAN, Y., SQUILLANTE, M. R. & ENTINE, G. 1998. Structured CsI(Tl) scintillators for X-ray imaging applications. *IEEE Transactions on Nuclear Science*, 45, 492-496.
- 9 SCHEFFER, D. Year. A Wafer scale active pixel CMOS image sensor for generic x-ray radiology. *In*, 2007. 651000-651000-9.
- 10 SCINTACOR. 2017. *Company website* [Online]. Available: <https://scintacor.com/> [Accessed].
- 11 TECHNOLOGY, P. 2014. *Pico Oscilloscope Range* [Online]. Available: <https://www.picotech.com/products/oscilloscope> [Accessed].



# 11 CONCLUSIONS

The project that is the subject of this thesis has been ambitious, and evolved to be far more wide ranging than anticipated at the outset. It has relied on a series of steps which, at the beginning have assumed a degree of maturity, but was subsequently found not to be the case. The original objective involved the development of a new technique for creating X-ray images of fast moving objects. In particular this would address long known issues of emissions, power consumption and unreliability, and comprise of software methods used in combination with new, controllable X-ray sources.

## 11.1 Summary of work completed

A detailed literature review was undertaken covering, in Chapter 2, the historical perspective of X-ray discovery and development, followed by the methods of applying field emission elements to X-ray sources, in Chapter 3 and the beneficial enhancements that can be achieved, in Chapter 4.

In order to accomplish the objectives of the project, a proof of concept study on Encoded Aperture has been successfully completed, and described in chapter 5. In this, the sharpness of a predictably blurred image has been restored by means of deconvolution with the blurring function. This lays the groundwork for being able to acquire high resolution images at a far lower instantaneous X-ray power level than is possible by using conventional means.

In chapter 6, the study of sealed inserts which incorporate electron sources, comprising paste-printed field emission cathodes, has been demonstrated to operate as a viable source of X-rays. However, this work has shown that the devices had uncontrollable failure modes, which lead to catastrophic destruction of the Xray tubes. In addition, the initial choice of CNT paste printing as a means of creating a field emission electron source has highlighted the limitations associated with the random orientation and selective conduction of the emission sites. The results showed that the anode current of the tubes was indeed controllable by the gate voltage, but that, in this case, the gain was limited due to the poor transparency of the grid.

Due to the high failure rate and long turnaround time of these devices, I decided to construct a unit in which the components could be replaced in the event of failure. A “demountable” chamber was designed into which CVD emission sources could be mounted, and the chamber pumped down to a high vacuum, as described in Chapter 7. This has highlighted a series of important factors. Chief among these has been the careful design of high vacuum systems, including the effects of power dissipation, and hence temperature, on out-gassing. The chamber and cathode assembly were designed to be mechanically adjustable, so that key parameters such as cathode-gate distance and emitter-anode distance could be adjusted by means of motorised stages, which could be varied without opening up the vacuum system.

A range of emitters, of different morphologies, may be mounted within the demountable chamber. In anticipation of this, in Chapter 8, a study of the potential performance of the field emitters was conducted by simulation. This comprised both static field analysis and electron trajectory studies, which were used to calculate the likely focal spot size of the resulting source.

Based upon the results of the simulation, a series of emitters was prepared, comprising of CNT pillar arrays, created by CVD growth. Prior to use within the chamber, these were imaged using a Scanning Electron Microscope, which revealed that the geometry of the emitters was sub-optimal. This in turn lead to a study of the growth methods of field emitters suitable for this work, by several methods, and the subsequent performance analysis on parallel plate field emission measurement equipment, which has been reported in Chapter 9.

A simplified chamber was constructed and a triode arrangement assembled, which ultimately demonstrated a field emission electron source in which the cathode voltage controlled the anode current of the device. An important aspect of this work was to

ensure high transparency of the grid electrode, for which a Transmission Electron Microscope grid was used. This showed a significant gain, and therefore provides a good basis for a controllable X-ray tube.

Finally, in Chapter 10, a study of the temporal response of the detector scintillator was undertaken, in order to understand the likely response time and hence switching rate of the overall system.

The problems encountered in the project have led to a number of beneficial developments. In particular, a test rig has been designed to provide a stable base from which to optimise the geometry of the internal structures of the X-ray source in a systematic way. This will ultimately lead to a way of validating the initial premise of rapid pulsing of the X-ray beam to facilitate an encoded aperture imaging capability, which has been demonstrated at a proof-of-concept level.

## 11.2 Further work

The project has reached an interesting phase, in which a series of key elements have been identified. Test equipment has been developed to the point that further objective studies can progress efficiently. The next aspects of the project to be addressed are :

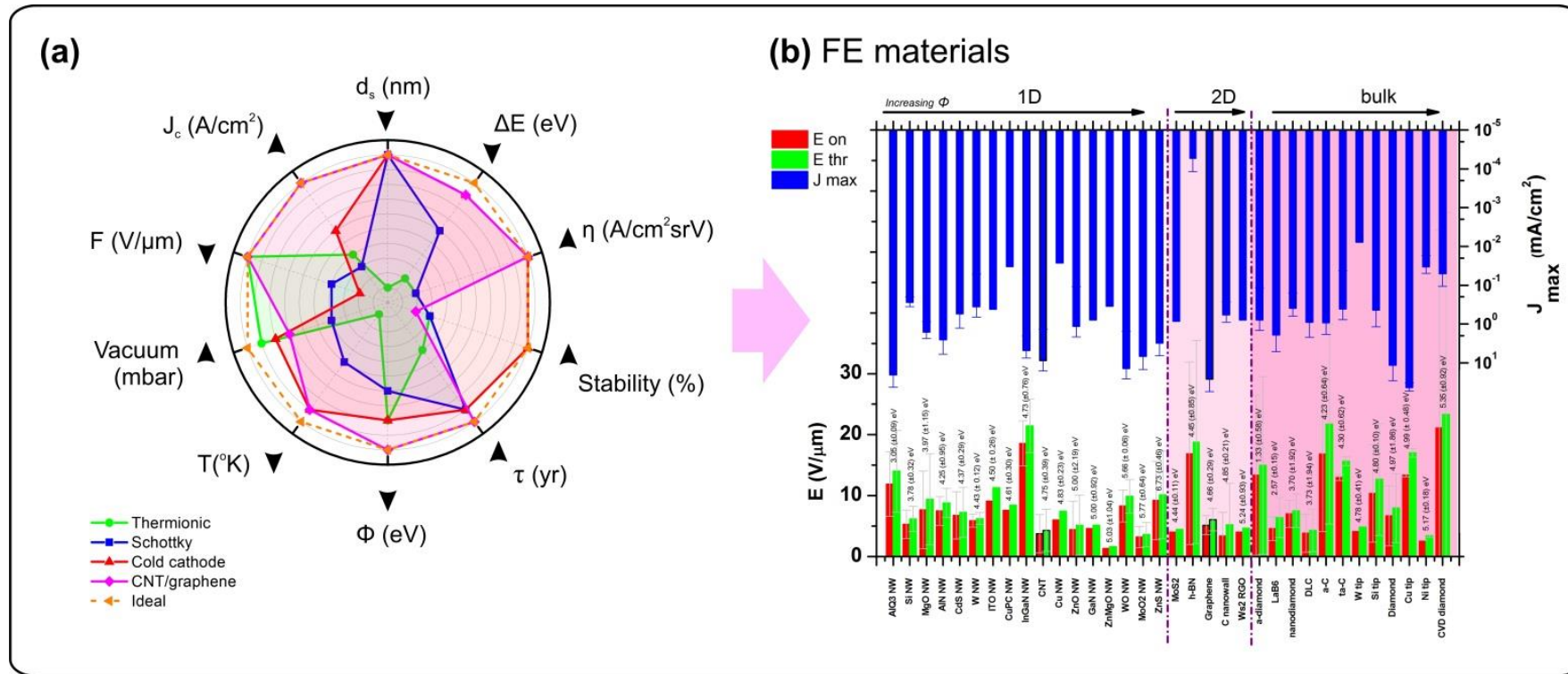
- Development of the triode assembly to allow operation at higher anode voltages. Whilst the sealed insert study was conducted with anode voltages up to 60kV, and represented a viable X-ray source, the subsequent triode work operated at a much lower voltage for reasons of safety and simplicity. In a high vacuum environment, it should be a straightforward matter to increase this, by use of high voltage feed-throughs as illustrated in Chapter 7.
- Improvement of emitter morphology. The efficiency of the source is related to the design of the field emission cathode assembly. The initial studies conducted during this work have indicated that samples produced by the techniques used by University of Surrey can give rise to lower turn-on fields, less hysteresis and greater current density. Patterned samples of chips with photo-resist were prepared to allow the production of CNT pillar arrays using these techniques, but initially this resulted in low adhesion of the CNT to the substrate, as a result of a residual layer of resist on the growth sites. To resolve this, it is planned to use a more dilute photo-resist, which would leave a thinner deposit.

- Upgrading of the demountable test rig. The current test rig, as described in Chapter 7 requires improvement to allow vacuum levels of  $1e-7$  millibar to be consistently achieved. These modifications include the replacement of KF vacuum fittings with CF fittings, which are more suitable for UHV situations. In addition, the physical layout of the vacuum circuit will be changed to reduce the potential pressure gradients, between the turbo-pump and the vacuum chamber.
- The modified test rig can then be used to evaluate the improved emitter morphology, and also optimise the relative locations of the internal components of the source, using the motorised stages that have been incorporated into the design.
- The test rig incorporates fast high voltage switches. By using PIN diodes as detection elements (such as those used in the scintillator study described in Chapter 10), it will be possible to determine the switching range of the gate-cathode voltage necessary to achieve the fastest pulsed X-ray output.
- The output of the demountable chamber may be directed towards an area detector, such as that used in Chapter 6, to image a moving object mounted on a translation stage. This will create real time blurred images similar to those described in Chapter 5.
- Finally, the resultant images will be subject to the deconvolution algorithms, also described in Chapter 5. These will be modified to take account of non-ideal switching conditions arising as a result of the temporal response of the scintillator that is employed in the detector.

# 12 APPENDICES

APPENDIX 1 – FIELD EMISSION CHARACTERISTICS .....	214
APPENDIX 2 – LITERATURE SUMMARY .....	225
APPENDIX 3 – DATA CAPTURE PROGRAM .....	231
APPENDIX 4 – XGEN SOFTWARE .....	239
APPENDIX 5 – FIRMWARE FOR CNT GENERATOR .....	245
APPENDIX 6 – SOFTWARE FOR ENCODED APERTURE .....	253
APPENDIX 7 – MOTOR CALIBRATION .....	271

## APPENDIX 1– FIELD EMISSION CHARACTERISTICS



**Appendix 1:** (a) Polar plot for the various common-place electron emitters. CNT and graphene based field emitters out-perform such sources across most metrics, where  $J_{max}$  the current density,  $E_{on}$  is the turn-on electric field, ‘Vacuum’ denotes the operating vacuum,  $T$  the typical operating temperature,  $\Phi$  the emitter work function,  $\tau$  the lifetime, ‘Stability’ is the temporal stability,  $\eta$  the electron-optical brightness,  $\Delta E$  the energy spread of the emitted electrons,  $d_s$  the virtual source size. Adapted from [1]. (b) Overview of the on and threshold electric fields ( $E_{on}$  and  $E_{thr}$ , respectively) and maximum current density,  $J_{max}$ , for various materials used for field emission to date, in order of dimensionality (1D, 2D and bulk) and increasing work

function ( $\Phi$ ), including 1D nanowires - AlQ<sub>3</sub> [2, 3], Si [4-6], MgO [7, 8], AlN [9-12], CdS [13-16], W [17-19], ITO [20], CuPC [21, 22], InGaN [23-25], CNTs [26-30] Cu [31-33], ZnO [34-39], GaN [40, 41], ZnMgO [37, 42], WO [43-46], MoO<sub>2</sub> [47-49], and ZnS [4, 50], the 2D platelets - MoS<sub>2</sub> [51], h-BN [52-55], graphene [56-59] [60-64], C nanowall [65-67], WS<sub>2</sub> RGO [68], and the bulk materials - a-diamond [38, 69], LaB<sub>6</sub> [70-73], nanodiamond [74, 75], DLC [76, 77], a-C [78-80], ta-C [81-83], W [84], Si [85-87], diamond [88-92], Cu [32, 33, 93], Ni [94-97], and CVD diamond [79, 98-100]. Adapted from [101].

1. MT Cole Dry-Transfer of Chemical Vapour Deposited Nanocarbon Thins Films for Functionally Enhanced Flexible Transparent Electronics Applications. University of Cambridge, Cambridge, 2011.
2. JJ Chiu, WS Wang, CC Kei, CP Cho, TP Perng, PK Wei, SY Chiu, Room temperature vibrational photoluminescence and field emission of nanoscaled tris-(8-hydroxyquinoline) aluminum crystalline film. *Applied Physics Letters* **83**, 4607-4609, (2003).
3. C-P Cho, T-P Perng, On the dendritic growth and field emission of amorphous AlQ<sub>3</sub> nanowires. *Organic Electronics* **11**, 115-122, (2010).
4. X Fang, Y Bando, UK Gautam, C Ye, D Golberg, Inorganic semiconductor nanostructures and their field-emission applications. *Journal of Materials Chemistry* **18**, 509-522, (2008).
5. FCK Au, KW Wong, YH Tang, YF Zhang, I Bello, ST Lee, Electron field emission from silicon nanowires. *Applied Physics Letters* **75**, 1700-1702, (1999).
6. Y Hung, Jr., S-L Lee, LC Beng, H-C Chang, Y-J Huang, K-Y Lee, Y-S Huang, Relaxing the electrostatic screening effect by patterning vertically-aligned silicon nanowire arrays into bundles for field emission application. *Thin Solid Films* **556**, 146-154, (2014).
7. LA Ma, ZX Lin, JY Lin, YA Zhang, LQ Hu, TL Guo, Large-scale growth of ultrathin MgO nanowires and evaluate their field emission properties. *Physica E* **41**, 1500-1503, (2009).
8. H Tan, N Xu, S Deng, Synthesis and electron emission properties of MgO nanowires. *Journal of Vacuum Science and Technology B* **28**, C2B20-C2B23, (2010).
9. JH He, RS Yang, YL Chueh, LJ Chou, LJ Chen, ZL Wang, Aligned AlN nanorods with multi-tipped surfaces - Growth, field-emission, and cathodoluminescence properties. *Advanced Materials* **18**, 650+, (2006).

10. X Ji, P Chen, J Deng, W Zhou, F Chen, Field Emission Properties of AlN Nanostructures. *Journal of Nanoscience and Nanotechnology* **12**, 6531-6533, (2012).
11. J Pelletier, D Gervais, C Pomot, Application of wide-gap semiconductors to surface ionization: Work functions of AlN and SiC single crystals. *Journal of Applied Physics* **55**, 994-1002, (1984).
12. W Sun, Y Li, Y Yang, Y Li, C Gu, J Li, Morphology inducing selective plasma etching for AlN nanocone arrays: tip-size dependent photoluminescence and enhanced field emission properties. *Journal of Materials Chemistry C* **2**, 2417-2422, (2014).
13. PG Chavan, MA More, DS Joag, SS Badadhe, IS Mulla Photo-enhanced field emission studies of tapered CdS nanobelts. In *Proceedings 27<sup>th</sup> International Vacuum Nanoelectronics Conference*, Engelberg, Switzerland pp 83-84.
14. P Chavan, R Kashid, S Badhade, I Mulla, M More, D Joag, CdS nanowires: Ultra-long growth and enhanced field emission properties. *Vacuum* **101**, 38-45, (2014).
15. T Ge, L Kuai, B Geng, Solution-phase chemical route to branched single-crystalline CdS nanoarchitectures and their field emission property. *Journal of Alloys and Compounds* **509**, L353-L358, (2011).
16. Y Lin, Y Hsu, S Lu, S Kung, Non-catalytic and template-free growth of aligned CdS nanowires exhibiting high field emission current densities. *Chemical Communications*, 2391-2393, (2006).
17. YH Lee, CH Choi, YT Jang, EK Kim, BK Ju, NK Min, JH Ahn, Tungsten nanowires and their field electron emission properties. *Applied Physics Letters* **81**, 745-747, (2002).
18. S Wang, Y He, X Fang, J Zou, Y Wang, H Huang, PMFJ Costa, M Song, B Huang, CT Liu, PK Liaw, Y Bando, D Golberg, Structure and Field-Emission Properties of Sub-Micrometer-Sized Tungsten-Whisker Arrays Fabricated by Vapor Deposition. *Advanced Materials* **21**, 2387-+, (2009).
19. KS Yeong, JTL Thong, Field-emission properties of ultrathin 5 nm tungsten nanowire. *Journal of Applied Physics* **100**, (2006).
20. N Wan, J Xu, G Chen, X Gan, S Guo, L Xu, K Chen, Broadband anti-reflection and enhanced field emission from catalyst-free grown small-sized ITO nanowires at a low temperature. *Acta Materialia* **58**, 3068-3072, (2010).
21. AS Komolov, EF Lazneva, SA Pshenichnyuk, AA Gavrikov, NS Chepilko, AA Tomilov, NB Gerasimova, AA Lezov, PS Repin, Electronic properties of the interface between hexadecafluoro copper phthalocyanine and unsubstituted copper phthalocyanine films. *Semiconductors* **47**, 956-961, (2013).

22. WY Tong,ZX Li,AB Djuricic,WK Chan,SF Yu, Field emission from copper phthalocyanine and copper hexadecafluorophthalocyanine nanowires. *Materials Letters* **61**, 3842-3846, (2007).
23. S-H Jang,J-S Jang, Schottky Barrier Characteristics and Carrier Transport Mechanism for Ohmic Contacts to Strained p-Type InGaN/GaN Superlattice. *Electrochemical and Solid State Letters* **13**, H403-H405, (2010).
24. TH Seo,KJ Lee,TS Oh,YS Lee,H Jeong,AH Park,H Kim,YR Choi,E-K Suh,TV Cuong,VH Pham,JS Chung,EJ Kim, Graphene network on indium tin oxide nanodot nodes for transparent and current spreading electrode in InGaN/GaN light emitting diode. *Applied Physics Letters* **98**, (2011).
25. F Ye,XM Cai,XM Wang,EQ Xie, The growth and field electron emission of InGaN nanowires. *Journal of Crystal Growth* **304**, 333-337, (2007).
26. J Lee,Y Jung,J Song,JS Kim,G-W Lee,HJ Jeong,Y Jeong, High-performance field emission from a carbon nanotube carpet. *Carbon* **50**, 3889-3896, (2012).
27. JM Bonard,JP Salvetat,T Stockli,L Forro,A Chatelain, Field emission from carbon nanotubes: perspectives for applications and clues to the emission mechanism. *Applied Physics A* **69**, 245-254, (1999).
28. DD Nguyen,Y-T Lai,N-H Tai, Enhanced field emission properties of a reduced graphene oxide/carbon nanotube hybrid film. *Diamond and Related Materials* **47**, 1-6, (2014).
29. M Shiraishi,M Ata, Work function of carbon nanotubes. *Carbon* **39**, 1913-1917, (2001).
30. H Ago,T Kugler,F Cacialli,WR Salaneck,MSP Shaffer,AH Windle,RH Friend, Work functions and surface functional groups of multiwall carbon nanotubes. *Journal of Physical Chemistry B* **103**, 8116-8121, (1999).
31. K Zheng,X Li,X Mo,G Chen,Z Wang,G Chen, Enhanced field emission and patterned emitter device fabrication of metal-tetracyanoquinodimethane nanowires array. *Applied Surface Science* **256**, 2764-2768, (2010).
32. O Auciello,JC Tucek,AR Krauss,DM Gruen,N Moldovan,DC Mancini, Review of synthesis of low-work function Cu-Li alloy coatings and characterization of the field emission properties for application to field emission devices. *Journal of Vacuum Science and Technology B* **19**, 877-883, (2001).
33. T Glatzel,H Steigert,S Sadewasser,R Klenk,MC Lux-Steiner, Potential distribution of Cu(In,Ga)(S,Se)(2)-solar cell cross-sections measured by Kelvin probe force microscopy. *Thin Solid Films* **480**, 177-182, (2005).

34. S Ding, H Cui, W Lei, X Zhang, B Wang Stable field emission from ZnO nanowires grown on 3D graphene foam. In *Proceedings 27<sup>th</sup> International Vacuum Nanoelectronics Conference*, Engelberg, Switzerland, pp 178-179.
35. F Jamali Sheini, DS Joag, MA More, Field emission studies on electrochemically synthesized ZnO nanowires. *Ultramicroscopy* **109**, 418-422, (2009).
36. X Sun Designing efficient field emission into ZnO using morphological and electronic design techniques, low-threshold, high-emission current densities have been obtained with ZnO. SPIE.; *Nanotechnology*, 2006.
37. H Tampo, H Shibata, K Maejima, TW Chiu, H Itoh, A Yamada, K Matsubara, P Fons, Y Chiba, T Wakamatsu, Y Takeshita, H Kanie, S Niki, Band profiles of ZnMgO/ZnO heterostructures confirmed by Kelvin probe force microscopy. *Applied Physics Letters* **94**, (2009).
38. YH Yang, CX Wang, B Wang, NS Xu, GW Yang, ZnO nanowire and amorphous diamond nanocomposites and field emission enhancement. *Chemical Physics Letters* **403**, 248-251, (2005).
39. ZP Zhang, WQ Chen, YF Li, J Chen Defect-Assisted Field Emission from ZnO nanotrees. In *Proceedings 27<sup>th</sup> International Vacuum Nanoelectronics Conference*, Engelberg, Switzerland, pp 78-79.
40. DKT Ng, MH Hong, LS Tan, YW Zhu, CH Sow, Field emission enhancement from patterned gallium nitride nanowires. *Nanotechnology* **18**, (2007).
41. YQ Wang, RZ Wang, MK Zhu, BB Wang, B Wang, H Yan, Structure and surface effect of field emission from gallium nitride nanowires. *Applied Surface Science* **285, Part B**, 115-120, (2013).
42. R Yousefi, FJ Sheini, MR Muhamad, MA More, Characterization and field emission properties of ZnMgO nanowires fabricated by thermal evaporation process. *Solid State Sciences* **12**, 1088-1093, (2010).
43. A Agiral, JGE Gardeniers On-Chip Tungsten Oxide Nanowires Based Electrodes for Charge Injection, 2010).
44. K Huang, Q Pan, F Yang, S Ni, D He, The catalyst-free synthesis of large-area tungsten oxide nanowire arrays on ITO substrate and field emission properties. *Materials Research Bulletin* **43**, 919-925, (2008).
45. Y Kojima, K Kasuya, T Ooi, K Nagato, K Takayama, M Nakao, Effects of oxidation during synthesis on structure and field-emission property of tungsten oxide nanowires. *Japanese Journal of Applied Physics* **46**, 6250-6253, (2007).

46. S Yue, H Pan, Z Ning, J Yin, Z Wang, G Zhang, Amazing ageing property and in situ comparative study of field emission from tungsten oxide nanowires. *Nanotechnology* **22**, (2011).
47. A Khademi, R Azimirad, AA Zavarian, AZ Moshfegh, Growth and Field Emission Study of Molybdenum Oxide Nanostars. *Journal of Physical Chemistry C* **113**, 19298-19304, (2009).
48. J Zhou, Large-Area Nanowire Arrays of Molybdenum and Molybdenum Oxides: Synthesis and Field Emission Properties. *Advanced materials (Weinheim)* **15**, 1835-1840, (2003).
49. J Liu, Z Zhang, C Pan, Y Zhao, X Su, Y Zhou, D Yu, Enhanced field emission properties of MoO<sub>2</sub> nanorods with controllable shape and orientation. *Materials Letters* **58**, 3812-3815, (2004).
50. X Fang, Y Bando, G Shen, C Ye, UK Gautam, PMFJ Costa, C Zhi, C Tang, D Golberg, Ultrathin ZnS nanobelts as field emitters. *Advanced Materials* **19**, 2593-+, (2007).
51. RV Kashid, DJ Late, SS Chou, Y-K Huang, D Mrinmoy, DS Joag, MA More, VP Dravid, Enhanced Field-Emission Behavior of Layered MoS<sub>2</sub> Sheets. *Small* **9**, 2730-2734, (2013).
52. T Yamada, T Masuzawa, T Ebisudani, K Okano, T Taniguchi, Field emission characteristics from graphene on hexagonal boron nitride. *Applied Physics Letters* **104**, 5, (2014).
53. T Yamada, T Ebisudani, K Okana, T Masuzawa, Y Neo, H Mimura, T Taniguchi Field emission characteristics of graphene/h-BN structure. In *Proceedings 27<sup>th</sup> International Vacuum Nanoelectronics Conference*, Engelberg, Switzerland, pp 182-183.
54. AB Preobrajenski, AS Vinogradov, N Martensson, Monolayer of h-BN chemisorbed on Cu(111) and Ni(111): The role of the transition metal 3d states. *Surface Science* **582**, 21-30, (2005).
55. S Ohtani, T Yano, S Kondo, Y Kohno, Y Tomita, Y Maeda, K Kobayashi, Electron emission from h-BN films codoped with Mg and O atoms. *Thin Solid Films* **546**, 53-57, (2013).
56. W Chen, Y Su, H Chen, S Deng, N Xu, J Chen Temperature Dependence of the Field Emission from Monolayer Graphene. In *Proceedings 27<sup>th</sup> International Vacuum Nanoelectronics Conference*, Engelberg, Switzerland, pp 36-37.
57. T Hallam, MT Cole, WI Milne, GS Duesberg, Field Emission Characteristics of Contact Printed Graphene Fins. *Small* **10**, 95-99, (2014).

58. Z-S Wu, S Pei, W Ren, D Tang, L Gao, B Liu, F Li, C Liu, H-M Cheng, Field Emission of Single-Layer Graphene Films Prepared by Electrophoretic Deposition. *Advanced Materials* **21**, 1756-1760, (2009).
59. C Wu, F Li, Y Zhang, T Guo, Field emission from vertical graphene sheets formed by screen-printing technique. *Vacuum* **94**, 48-52, (2013).
60. A Malesevic, R Kemps, A Vanhulsel, MP Chowdhury, A Volodin, C Van Haesendonck, Field emission from vertically aligned few-layer graphene. *Journal of Applied Physics* **104**, (2008).
61. UA Palnitkar, RV Kashid, MA More, DS Joag, LS Panchakarla, CNR Rao, Remarkably low turn-on field emission in undoped, nitrogen-doped, and boron-doped graphene. *Applied Physics Letters* **97**, -, (2010).
62. L Li, W Sun, S Tian, X Xia, J Li, C Gu, Floral-clustered few-layer graphene nanosheet array as high performance field emitter. *Nanoscale* **4**, 6383-6388, (2012).
63. S Pandey, P Rai, S Patole, F Gunes, G-D Kwon, J-B Yoo, P Nikolaev, S Arepalli, Improved electron field emission from morphologically disordered monolayer graphene. *Applied Physics Letters* **100**, (2012).
64. L Jiang, T Yang, F Liu, J Dong, Z Yao, C Shen, S Deng, N Xu, Y Liu, H-J Gao, Controlled Synthesis of Large-Scale, Uniform, Vertically Standing Graphene for High-Performance Field Emitters. *Advanced Materials* **25**, 250-255, (2013).
65. ATH Chuang, J Robertson, BO Boskovic, KKK Koziol, Three-dimensional carbon nanowall structures. *Applied Physics Letters* **90**, (2007).
66. D Banerjee, S Mukherjee, KK Chattopadhyay, Synthesis of amorphous carbon nanowalls by DC-PECVD on different substrates and study of its field emission properties. *Applied Surface Science* **257**, 3717-3722, (2011).
67. YH Wu, BJ Yang, BY Zong, H Sun, ZX Shen, YP Feng, Carbon nanowalls and related materials. *Journal of Materials Chemistry* **14**, 469-477, (2004).
68. CS Rout, PD Joshi, RV Kashid, DS Joag, MA More, AJ Simbeck, M Washington, SK Nayak, DJ Late, Superior Field Emission Properties of Layered WS<sub>2</sub>-RGO Nanocomposites. *Scientific Reports* **3**, (2013).
69. M-C Kan, J-L Huang, JC Sung, K-H Chen, B-S Yau, Thermionic emission of amorphous diamond and field emission of carbon nanotubes. *Carbon* **41**, 2839-2845, (2003).
70. A Yutani, A Kobayashi, A Kinbara, Work functions of thin LaB<sub>6</sub> films. *Applied Surface Science* **70-71, Part 2**, 737-741, (1993).

71. Menaka,R Patra,S Ghosh,AK Ganguli, Manipulating the anisotropy and field emission of lanthanum hexaboride nanorods. RSC Advances **2**, 7875-7885, (2012).
72. M Jha,R Patra,S Ghosh,AK Ganguli, Vertically aligned nanorods of lanthanum hexaboride with efficient field emission properties. Solid State Communications **153**, 35-39, (2013).
73. J Xu,G Hou,H Li,T Zhai,B Dong,H Yan,Y Wang,B Yu,Y Bando,D Golberg, Fabrication of vertically aligned single-crystalline lanthanum hexaboride nanowire arrays and investigation of their field emission. NPG Asia Materials **5**, (2013).
74. S Raina,WP Kang,JL Davidson, Field emission from nanodiamond grown with 'ridge' type geometrically enhanced features. Diamond and Related Materials **17**, 790-793, (2008).
75. B-R Huang,S Jou,T-C Lin,Y-K Yang,C-H Chou,Y-M Wu, Field emission property of arrayed nanocrystalline diamond. Diamond and Related Materials **20**, 314-317, (2011).
76. HS Jung,HH Park,SS Pang,SY Lee, The structural and electron field emission characteristics of pulsed laser deposited diamond-like carbon films with thermal treatment. Thin Solid Films **355**, 151-156, (1999).
77. H Zanin,PW May,MHMO Hamanaka,EJ Corat, Field Emission from Hybrid Diamond-like Carbon and Carbon Nanotube Composite Structures. ACS Applied Materials and Interfaces **5**, 12238-12243, (2013).
78. D Banerjee,A Jha,KK Chattopadhyay, Low-temperature synthesis of amorphous carbon nanoneedle and study on its field emission property. Physica E **41**, 1174-1178, (2009).
79. RK Tripathi,OS Panwar,AK Srivastava,I Rawal,S Chockalingam, Structural, nanomechanical, field emission and ammonia gas sensing properties of nitrogenated amorphous carbon films deposited by filtered anodic jet carbon arc technique. Talanta **125**, 276-283, (2014).
80. J Robertson, Mechanisms of electron field emission from diamond, diamond-like carbon, and nanostructured carbon. Journal of Vacuum Science & Technology B **17**, 659-665, (1999).
81. A Hart,BS Satyanarayana,WI Milne,J Robertson, Effect of surface treatment and back contact material on field emission from tetrahedral amorphous carbon. Diamond and Related Materials **8**, 809-813, (1999).

82. A Ilie, A Hart, A J Flewitt, J Robertson, W I Milne, Effect of work function and surface microstructure on field emission of tetrahedral amorphous carbon. *Journal of Applied Physics* **88**, 6002-6010, (2000).
83. W I Milne, Field emission from tetrahedrally bonded amorphous carbon. *Applied Surface Science* **146**, 262-268, (1999).
84. M Setvín, J Javorský, D Turčinková, I Matolínová, P Sobotík, P Kocán, I Ošťádal, Ultrasharp tungsten tips—characterization and nondestructive cleaning. *Ultramicroscopy* **113**, 152-157, (2012).
85. K L Ng, J Yuan, J T Cheung, K W Cheah, Electron field emission characteristics of electrochemical etched Si tip array. *Solid State Communications* **123**, 205-207, (2002).
86. Z X Pan, J C She, S Z Deng, N S Xu Si Tip Arrays with Ultra-Narrow Nanoscale Charge Transfer Channel. In *Proceedings 27<sup>th</sup> International Vacuum Nanoelectronics Conference*, Engelberg, Switzerland, pp 74-75.
87. S X Chen, J J Li, C Z Gu, Ieee, Field Emission from the Composite Structure of Silicon Tips and Vertical Carbon Nanotubes. 2007 7th Ieee Conference on Nanotechnology, Vol 1-3, 367-370, (2007).
88. J W Glesener, H B Lin, A A Morrish, Field emission from cleaved diamond fibers. *Thin Solid Films* **308**, 204-208, (1997).
89. H-F Cheng, K-Y Teng, H-C Chen, G-C Tzeng, C-Y Tang, I N Lin, Bias enhanced nucleation and growth processes for improving the electron field emission properties of diamond films. *Surface and Coatings Technology* **228**, S175-S178, (2013).
90. F Zhao, D-d Zhao, S-l Wu, G-a Cheng, R-t Zheng, Diamond-like carbon decoration enhances the field electron emission of silicon nanowires. *Surface and Coatings Technology* **228**, S349-S353, (2013).
91. K Panda, K J Sankaran, B K Panigrahi, N-H Tai, I N Lin, Direct Observation and Mechanism for Enhanced Electron Emission in Hydrogen Plasma-Treated Diamond Nanowire Films. *ACS Applied Materials and Interfaces* **6**, 8531-8541, (2014).
92. P Abbott, E D Sosa, D E Golden, Effect of average grain size on the work function of diamond films. *Applied Physics Letters* **79**, 2835-2837, (2001).
93. X Song, C X Zhao, J Q Wu, J Chen, Ieee Field emission from copper micro-cones formed by ion bombardment of copper substrate using an oxide masking. In *25th International Vacuum Nanoelectronics Conference (IVNC)*; Jeju Island, South Korea, 2012; pp 376-377.

94. J Wang, L Wei, L Zhang, J Zhang, H Wei, C Jiang, Y Zhang, Controlled growth of nickel nanocrystal arrays and their field electron emission performance enhancement via removing adsorbed gas molecules. *Crystengcomm* **15**, 1296-1306, (2013).
95. E Le Shim, S B Lee, E You, C J Kang, K W Lee, Y J Choi Rapid Fabrication of Wafer Scale Patterned Nickel Nanocone Arrays for Field Emission Applications. In *25th International Vacuum Nanoelectronics Conference (IVNC)*; Jeju Island, South Korea, 2012; pp 198-199.
96. S W Joo, A N Banerjee, Field emission characterization of vertically oriented uniformly grown nickel nanorod arrays on metal-coated silicon substrate. *Journal of Applied Physics* **107**, (2010).
97. T Nakane, K Sano, A Sakai, A Magosakon, K Yanagimoto, T Sakata, Field-emission barrier height of an alloy tip: Possible effect of surface segregation. *Journal of Vacuum Science and Technology A* **15**, 1563-1567, (1997).
98. J Wang, T Ito, Improved field emission characteristics of nano-structured carbon films deposited on polycrystalline CVD diamond. *Diamond and Related Materials* **16**, 364-368, (2007).
99. J B Cui, J Ristein, M Stammler, K Janischowsky, G Kleber, L Ley, Hydrogen termination and electron emission from CVD diamond surfaces: a combined secondary electron emission, photoelectron emission microscopy, photoelectron yield, and field emission study. *Diamond and Related Materials* **9**, 1143-1147, (2000).
100. O Gröning, Properties and characterization of chemical vapor deposition diamond field emitters. *Solid-state electronics* **45**, 929-944, (2001).
101. R J Parmee, C M Collins, W I Milne, M T Cole, X-ray generation using carbon nanotubes. *Nano Convergence* **2**, 1, (2015).

## Xray Generation by Field Emission

## APPENDIX 2 – LITERATURE SUMMARY

**Table 1** below summarises the cumulative literature to-date on the progress towards the realisation of a functionally enhanced CNT-based FE X-ray source. Underlined values indicate the highest achieved standards at the time of publication. What follows is a detailed overview and assessment of some of the leading studies with regards to their functional enhancements, fabrication methods, and emission performance.

Ref	Year	CNT deposition (substrate)	Max stable beam current (A)	Max anode voltage  (kV)	Pulse frequency (Hz)	% drift in anode current in non-feedback mode (% I <sub>a</sub> )	Approx. turn-on (V/μm) (@ J <sub>a</sub> )	Focal spot size (mm)	Notes
[1]	2005	Electrophoresis	10 mA (15 V/μm)	40	DC	<5%	~2.6 (/)	0.15	micro focus
[2]	2007	PE-CVD (W and Pd wire)	50 μA ~(3 V/μA)	15	DC	/	/	0.05	micro focus
[3]	2007	PE-CVD (W wire)	26 μA (5 V/μm)	40	DC	/	1.6 (10 mA/cm <sup>2</sup> )	0.005	micro focus
[4]	2010	PE-CVD (W and Pd wire)	0.1 mA (/)	25	DC	<15%	3.2 (/)	0.0004	micro focus
[5]	2004	Solution Processed	6 mA (15 V/μm)	60	10 <sup>7-8</sup>	<±1%	~7.1 (/)	0.15 x 0.03	micro focus high pulse rate

Xray Generation by Field Emission

[6]	2002	Electrophoresis	28 mA (/)	14	$10^3$	$\pm 2-4\%$	2.0 (1 mA/cm <sup>2</sup> )	3.2	pulsed
[7]	2006	/	1 mA (/)	40	1	$\sim 50\%$	/	0.2	pulsed multi-pixel
[8]	2009	Electrophoretic	18 mA	30	$10^2$	/	$\sim 5.0$ (/)	0.5 x 0.3	pulsed multi-pixel (25x1)
[9]	2011	Screen Printing	43 mA (/)	45	5	$\pm 0.2\%$	/	0.6	pulsed multi-pixel (31x1)
[8]	2009	Electrophoresis	18 mA (/)	40	$10^3$	$< 7\%$	6.5 (/)	0.1	multi-pixel (25x1) shaped cathode
[10]	2011	Electrophoresis	3.5 mA (7.5 V/ $\mu$ m)	1.4	DC	/	3.5 (10 $\mu$ A/cm <sup>2</sup> )	2.0	multi-pixel (5x10)
[11]	2013	CVD	0.6 mA (16 V/ $\mu$ m)	40	DC	/	$\sim 8$ (/)	/	ballasted
[12]	2009	Electrophoresis	7.0 mA (8.5 V/ $\mu$ m)	50	10	$\pm 13\%$	5 (/)	0.1	shaped cathode
[13]	2012	CVD	90 mA (7.5 V/ $\mu$ m)	50	DC	/	3.0 (0.1 mA)	/	shaped cathode

[14]	2006	DC Electrophoresis	150 mA (12 V/ $\mu$ m)	40	$10^2$	/	/	0.03	shaped cathode pulsed micro focus
[15]	2004	CVD (Mo disk)	ca. 15 mA (4.6 V/ $\mu$ m)	1.1	$10^{-1}$	/	$\sim 2.0$ (/)	0.5	miniature battery operated
[16]	2004	CVD	0.3 mA (7.0 V/ $\mu$ m)	30	DC	$\pm 8\%$	/	/	miniature
[17]	2005	/	$\sim 40$ $\mu$ A (/)	/	$2 \times 10^3$	$\sim 50\%$	/	1.0	miniature
[18]	2012	Paste	0.6 mA (1.4 V/ $\mu$ m)	70	DC	$\pm 2\%$	/	3.7	miniature
[19]	2013	Paste	1.2 mA (4.7 V/ $\mu$ m)	25	10	$\sim < 1\%$	$\sim 3.5$ (/)	/	miniature
[20]	2004	CVD (Mo disk)	$\sim 2$ mA (4.65 V/ $\mu$ m)	10	$10^{-1}$	/	2.2 (10 nA)	0.5	miniature pulsed
[21]	2006	Ion bombardment (polyimide)	/	25	$6 \times 10^2$	/	1.5 (1 $\mu$ A/cm <sup>2</sup> )	/	/
[22]	2001	CVD (metal wire)	1.5 $\mu$ A (20 V/ $\mu$ m)	60	DC	$\pm 10\%$	/	/	/
[23]	2004	PE-CVD	1 mA (/)	40	DC	$\pm 8\%$	/	2.0	/

		(W and Pd wire)							
[24]	2007	CVD	2.0 mA (0.5 V/ $\mu$ m)	10	DC	~50%	~0.2 (/)	/	/
[25]	2008	PE-CVD (Pd wire)	1.0 mA (/)	50	DC	$\pm$ 10%	/	3.0	/
[26, 27]	2014	Screen Printing	15 mA (2.6 V/ $\mu$ m)	20	10	/	/	0.3	/

**Table 1: Performance of CNT-based X-ray sources**

$I_a$ : Anode current (A);

$J_a$ : Anode current density (A/cm<sup>2</sup>);

/ denotes values not given

1. J Zhang, Y Cheng, YZ Lee, B Gao, Q Qiu, WL Lin, D Lalush, JP Lu, O Zhou, A nanotube-based field emission x-ray source for microcomputed tomography. Review of Scientific Instruments **76**, 094301-094304, (2005).
2. Y Sakai, A Haga, S Sugita, S Kita, S-I Tanaka, F Okuyama, N Kobayashi, Electron gun using carbon-nanofiber field emitter. Review of Scientific Instruments **78**, -, (2007).
3. SH Heo, A Ihsan, SO Cho, Transmission-type microfocuss x-ray tube using carbon nanotube field emitters. Applied Physics Letters **90**, 183109-183103, (2007).
4. W Sugimoto, S Sugita, Y Sakai, H Goto, Y Watanabe, Y Ohga, S Kita, T Ohara, A fine-focusing X-ray source using carbon-nanofiber field emitter. Journal of Applied Physics **108**, -, (2010).

5. Y Cheng, J Zhang, YZ Lee, B Gao, S Dike, W Lin, JP Lu, O Zhou, Dynamic radiography using a carbon-nanotube-based field-emission X-ray source. *Review of Scientific Instruments* **75**, (2004).
6. GZ Yue, Q Qiu, B Gao, Y Cheng, J Zhang, H Shimoda, S Chang, JP Lu, O Zhou, Generation of continuous and pulsed diagnostic imaging x-ray radiation using a carbon-nanotube-based field-emission cathode. *Appl. Phys. Lett.* **81**, 355-357, (2002).
7. J Zhang, G Yang, YZ Lee, S Chang, JP Lu, O Zhou, Multiplexing radiography using a carbon nanotube based x-ray source. *Applied Physics Letters* **89**, -, (2006).
8. X Qian, R Rajaram, X Calderon-Colon, G Yang, T Phan, DS Lalush, J Lu, O Zhou, Design and characterization of a spatially distributed multibeam field emission x-ray source for stationary digital breast tomosynthesis. *Medical Physics* **36**, 4389-4399, (2009).
9. F Sprenger, X Calderon, E Gidcumb, J Lu, X Qian, D Spronk, A Tucker, G Yang, O Zhou Stationary digital breast tomosynthesis with distributed field emission x-ray tube. 2011; pp 79615I-79615I-79616.
10. S Wang, X Calderon, R Peng, EC Schreiber, O Zhou, S Chang, A carbon nanotube field emission multipixel X-ray array source for microradiotherapy application. *Appl. Phys. Lett.* **98**, 213701-213703, (2011).
11. Y Sun, DA Jaffray, TW Yeow, The Design and Fabrication of Carbon-Nanotube-Based Field Emission X-Ray Cathode With Ballast Resistor. *IEEE Transactions on Electron Devices* **60**, 7, (2013).
12. X Calderón-Colón, H Geng, B Gao, L An, G Cao, O Zhou, A carbon nanotube field emission cathode with high current density and long-term stability. *Nanotech.* **20**, 325707, (2009).
13. J Ryu, J Kang, K Park, Carbon Nanotube Electron Emitter for X-ray Imaging. *Materials* **5**, 2353-2359, (2012).
14. Z Liu, G Yang, YZ Lee, D Bordelon, J Lu, O Zhou, Carbon nanotube based microfocus field emission x-ray source for microcomputed tomography. *Applied Physics Letters* **89**, 1-3, (2006).
15. P Sarrazin, D Blake, L Delzeit, M Meyyappan, B Boyer, S Snyder, B Espinosa, Carbon-nanotube field emission x-ray tube for space exploration XRD/XRF instrument. *Advances in X-ray Analysis* **47**, 8, (2004).
16. A Haga, S Senda, Y Sakai, Y Mizuta, S Kita, F Okuyama, A miniature x-ray tube. *Applied Physics Letters* **84**, 2208-2210, (2004).

17. A Reyes-Mena, C Jensen, E Bard, DC Turner, K Erdmann, Q Qiu, B Gao, J Lu, O Zhou, Miniature X-ray tubes utilizing carbon-nanotube-based cold cathodes. *Advances in X-ray Analysis* **48**, 204-209, (2005).
18. SH Heo, HJ Kim, JM Ha, SO Cho, A vacuum-sealed miniature X-ray tube based on carbon nanotube field emitters. *Nano Research Letters* **7**, 5, (2012).
19. J-W Jeong, J-T Kang, S Choi, J-W Kim, S Ahn, Y-H Song, A digital miniature x-ray tube with a high-density triode carbon nanotube field emitter. *Applied Physics Letters* **102**, (2013).
20. P Sarrazin, D Blake, L Delzeit, M Meyyappan, B Boyer, S Snyder, B Espinosa, Carbon-nanotube field emission X-ray tube for space exploration XRD/XRF instrument. *Advances in X-ray Analysis* **47**, 232-239, (2004).
21. TT Tan, HS Sim, SP Lau, HY Yang, M Tanemura, J Tanaka, X-ray generation using carbon-nanofiber-based flexible field emitters. *Applied Physics Letters* **88**, -, (2006).
22. H Sugie, M Tanemura, V Filip, K Iwata, K Takahashi, F Okuyama, Carbon nanotubes as electron source in an x-ray tube. *Applied Physics Letters* **78**, 2578-2580, (2001).
23. S Senda, M Tanemura, Y Sakai, Y Ichikawa, S Kita, T Otsuka, A Haga, F Okuyama, New field-emission x-ray radiography system. *Review of Scientific Instruments* **75**, 1366-1368, (2004).
24. HS Kim, D Quang, JH Kim, HJ Lee, DM Yoon, SS Shin, JW Ha, KJ Lee, YG Hwang, CH Lee, Field-Emission Electron Source using Carbon Nanotubes for X-ray Tubes. *Journal of Korean Physical Society* **52**, 3, (2008).
25. S Kita, Y Watanabe, A Ogawa, K Ogura, Y Sakai, Y Matsumoto, Y Isokane, F Okuyama, T Nakazato, T Otsuka, Field-emission-type X-ray source using carbon-nanofibers. *Journal of Applied Physics* **103**, -, (2008).
26. J-W Kim, J-W Jeong, J-T Kang, S Choi, S Ahn, Y-H Song, Highly reliable field electron emitters produced from reproducible damage-free carbon nanotube composite pastes with optimal inorganic fillers. *Nanotechnology* **25**, (2014).
27. J-W Kim, J-W Jeong, J-T Kang, S Choi, J Choi, S Ahn, Y-h Song A digital compact x-ray tube with carbon nanotube field emitters for advanced imaging systems. In *SPIE Medical Imaging*; International Society for Optics and Photonics, 2013; pp 861-866.

## APPENDIX 3 – DATA CAPTURE PROGRAM

```

unit AteCNT;
(*=====*)
(* Test program for collecting data from CNT Xray tank *)
(*=====*)
(* 08/08/13 0.1 Cloned from CDD ATE program RJP *)
(*=====*)
//
(*=====*)

interface

uses
  Windows, Messages, SysUtils, Variants, Classes, Graphics, Controls, Forms,
  Dialogs, D2kDask, ExtCtrls, StdCtrls, DB, DBTables, Led1, TeeProcs, TeEngine,
  Chart, DbChart, TeeFunci, Series;

type
  TForm1 = class(TForm)
    Button1: TButton;
    Timer1: TTimer;
    XrayOn: TButton;
    XrayOff: TButton;
    DataSource1: TDataSource;
    Table1: TTable;
    Button2: TButton;
    Timer2: TTimer;
    GroupBox1: TGroupBox;
    CheckBox1: TCheckBox;
    CheckBox2: TCheckBox;
    CheckBox3: TCheckBox;
    CheckBox4: TCheckBox;
    CheckBox5: TCheckBox;
    CheckBox6: TCheckBox;
    Chart1: TChart;
    Series1: TFastLineSeries;
    Series2: TFastLineSeries;
    Series3: TFastLineSeries;
    Chart2: TChart;
    Series4: TFastLineSeries;
    Series5: TFastLineSeries;
    Button3: TButton;
    GroupBox2: TGroupBox;
    Label1: TLabel;
    Label2: TLabel;
    Label3: TLabel;
    Label4: TLabel;
    Label5: TLabel;
    Edit1: TEdit;
    Edit2: TEdit;
    Edit3: TEdit;
    Edit4: TEdit;
    Edit5: TEdit;
    Edit6: TEdit;
    Edit7: TEdit;
    Led1: TLed;
    Led2: TLed;
    Label6: TLabel;
    Edit8: TEdit;
    Label7: TLabel;
    Edit9: TEdit;
    Label8: TLabel;
    Edit10: TEdit;
    Label9: TLabel;
    Edit11: TEdit;
    Label10: TLabel;
    Label11: TLabel;
    Label12: TLabel;
    Label13: TLabel;
    Button4: TButton;
    Edit12: TEdit;
    Label14: TLabel;
    Button5: TButton;
    Table2: TTable;
    DataSource2: TDataSource;
  end;

```

## Xray Generation by Field Emission

```

Button6: TButton;
procedure FormActivate(Sender: TObject);
procedure Timer1Timer(Sender: TObject);
procedure Button1Click(Sender: TObject);
procedure XrayOnClick(Sender: TObject);
procedure XrayOffClick(Sender: TObject);
procedure Edit3Change(Sender: TObject);
procedure Timer2Timer(Sender: TObject);
procedure Button2Click(Sender: TObject);
procedure Button3Click(Sender: TObject);
procedure Button4Click(Sender: TObject);
procedure Edit9Change(Sender: TObject);
procedure Button5Click(Sender: TObject);
procedure Button6Click(Sender: TObject);
private
  { Private declarations }
public
  { Public declarations }
end;

//=====*)
// Default settings
//=====*)
const
  GateStart      : integer = 0;           // Start gate voltage
  GateStep       : integer = 1;          // Gate volate step (* 100V)
  GateMax        : integer = 60;         // Final gate voltage
  CaptStep       : integer = 100;        // Number of readings to average
  GateScale      : real = 85.8;          // Scale factor for Gate voltage
  AnodeScale     : real = 62.5;          // Scale factor for Anode voltage
  AnodeRes       : real = -1700;         // Anode current monitor res
  GateRes        : real = 4800;          // Gate current monitor res
  Startkv        : real = 20;            // Start anode kV           //30; //20;
  Stepkv         : real = 5;             // Anode voltage step //0; //5;
  Finalkv        : real = 55;            // Final anode voltage

var
  Form1: TForm1;
  Card : integer;
  CardNumber : Integer;
  ChannelNo  : integer;
  Value      : Double;
  Out_V      : array[0..1] of Double;
  n : integer;
  da_ch      : array[0..1] of Word;
  InputA     : Cardinal{Word};
  OutB_value : Cardinal;
  Dout       : boolean;
  log_file   : text;
  RunMacro   : boolean;
  Secctr     : integer;
  Rdgctr     : integer;
  Reading    : integer;
  KvList     : TList;
  KvArray    : array[0..100] of double;
  Capture    : boolean;
  CaptureNo  : integer;
  Capttime   : integer;
  GateTime   : integer;
  va : array[0..3] of Real;
  vt : array[0..100] of Real;
  vg : integer;
  testdone   : boolean = false;

  { Series1 : TFastLineSeries;}

implementation

{$R *.dfm}

//=====*)
// Exit program
//=====*)
procedure TForm1.Button1Click(Sender: TObject);
begin
  if table2.Active then Table2.Close;
  Timer1.Enabled := false;
  CloseFile(log_file);
  XrayOffClick(Sender);

```

## Chapter 12: Appendices

```
D2K_Release_Card(card);
Close;
end;

//=====
// Enable tank and turn on Xrays at nominal level
//=====
procedure TForm1.XrayOnClick(Sender: TObject);
begin
  D2K_DO_WriteLine (card,Channel_P1B,0,1);
  Edit3.Text := '50';
  Edit4.Text := '50';
end;

//=====
// Disable tank and turn off Xrays
//=====
procedure TForm1.XrayOffClick(Sender: TObject);
begin
  Capture := false;
  Edit3.Text := '0';
  Edit4.Text := '0';
  D2K_DO_WriteLine (card,Channel_P1B,0,0);
end;

//=====
// Initiate testing cycle as set in Table 1
//=====
procedure TForm1.Button2Click(Sender: TObject);
var
  n,m : real;
  count : integer;
begin
  Capture := false;
  Table1.Close;
  with Table1 do
  begin
    if not Active then
    begin
      TableName := 'Tankat1.db';
      Open;
    end;
    First;
    count := 0;
    while not Eof do
    begin
      n := FieldByName('Duration').AsFloat;
      m := FieldByName('Read').AsFloat;
      if m>0 then count := count+trunc((n/m));
      Next;
    end;
    First;
  end;
  RunMacro := true;
  Secctr := 0;
  Series1.Clear;
  Series2.Clear;
  Series3.Clear;
  Series4.Clear;
  Series5.Clear;
  Chart1.BottomAxis.Maximum := count;
  Chart2.BottomAxis.Maximum := count;
end;

//=====
// Initiate fast testing cycle as set in Table 2
//=====
procedure TForm1.Button3Click(Sender: TObject);
var
  n,m : real;
  count : integer;
begin
  Capture := false;
  Table1.Close;
  with Table1 do
  begin
    if not Active then
    begin
```

## Xray Generation by Field Emission

```

    TableName := 'Tankate2.db';
    Open;
end;
First;
count := 0;
while not Eof do
begin
    n := FieldByName('Duration').AsFloat;
    m := FieldByName('Read').AsFloat;
    if m>0 then count := count+trunc((n/m));
    Next;
end;
First;
end;
RunMacro := true;
Secctr := 0;
Series1.Clear;
Series2.Clear;
Series3.Clear;
Series4.Clear;
Series5.Clear;
Chart1.BottomAxis.Maximum := count;
Chart2.BottomAxis.Maximum := count;
end;

//=====
// Abort testing cycle as set in Table
//=====
procedure TForm1.Button4Click(Sender: TObject);
var
    count : integer;
begin
    count := 0;
    Capture := false;
    XrayOffClick(Sender);
    RunMacro := false;
    Table1.Close;
    Edit7.Text := 'Finished';
end;

//=====
// Initiate special CNT testing cycle
// Store data in Output data
//=====
procedure TForm1.Button5Click(Sender: TObject);
var
    count : integer;
    sx : shortstring;
begin
    for count := 0 to 3 do va[count] := 0;
    CaptureNo := 0;
    Capttime := CaptStep;
    Gatetime := GateStep;
    with Table2 do
    begin
        if not Active then
        begin
            TableName := 'Output.db';
            Open;
        end;
        while not eof do Delete;
        First;
        count := 0;
    end;
    Capture := true;
    D2K_DO_WriteLine (card,Channel_P1B,0,1);
    str(trunc((startkv*100/Anodescale)+0.5),sx);
    Edit3.Text := sx;
    vg := GateStart; //0;
    Edit4.Text := inttostr(vg); //'0';
end;

//=====
// Initiate special CNT seasoning cycle
// Store data in Log data
//=====
procedure TForm1.Button6Click(Sender: TObject);
var
    n : integer;

```

```

    sx : shortstring;
begin
    sx := DateTimetoStr(Now);
    writeln(log_file,sx);
    for n := 0 to 10000 do
    begin
        D2K_AI_VReadChannel(card, {channelNo}6, Value);
        str(Value*10:8:1,sx);
        Edit5.Text := sx;
        write(log_file,sx);
        D2K_AI_VReadChannel(card, {channelNo}7, Value);
        str(Value*10:8:1,sx);
        Edit12.Text := sx;
        writeln(log_file,sx);
    end;
    testdone := true;
end;

//=====
// Set anode and gate voltage manually
//=====
procedure TForm1.Edit3Change(Sender: TObject);
begin
    if Edit3.Text<>' ' then Out_V[0] := StrtoFloat(Edit3.Text)
    else Out_V[0] := 0;
    Out_V[0] := Out_V[0] / 10;
    if Edit4.Text<>' ' then Out_V[1] := StrtoFloat(Edit4.Text)
    else Out_V[1] := 0;
    Out_V[1] := Out_V[1] / 10;
    D2K_AO_Group_VUpdate (card, DA_Group_A, out_V[0]);
end;

//=====
// Set tank details in caption bar
//=====
procedure TForm1.Edit9Change(Sender: TObject);
begin
    Caption := 'Tank : '+Edit9.Text;
end;

//=====
// Initialise all hardware, etc
//=====
procedure TForm1.FormActivate(Sender: TObject);
begin
    Capture := false;
    Form1.Height := 768;
    Form1.Top := 0;
    Chart2.Top := 768-50-Chart2.Height;
    Chart1.Top := Chart2.Top-20-Chart1.Height;
    AssignFile(Log_file,'c:\log.dat');
    Rewrite(log_file);
    Dout := false;
    card := D2K_Register_Card(DAQ_2501, CardNumber);
    ChannelNo := 4;
    D2K_AI_CH_Config (card, channelNo, AD_B_10_V);
    ChannelNo := 5;
    D2K_AI_CH_Config (card, channelNo, AD_B_10_V);
    ChannelNo := 6;
    D2K_AI_CH_Config (card, channelNo, AD_B_10_V);
    ChannelNo := 7;
    D2K_AI_CH_Config (card, channelNo, AD_B_10_V);
    ChannelNo := 0;
    D2K_AI_CH_Config (card, channelNo, AD_B_10_V);
    ChannelNo := 1;
    D2K_AI_CH_Config (card, channelNo, AD_B_10_V);
    ChannelNo := 2;
    D2K_AI_CH_Config (card, channelNo, AD_B_10_V);
    { da_ch := 1;
    D2K_AO_CH_Config (card, da_ch, DAQ2K_DA_BiPolar, DAQ2K_DA_Int_REF, 10.0);
    D2K_AO_Group_Setup (card, DA_Group_A, 1, &da_ch);}
    D2K_AO_CH_Config (card, 0, DAQ2K_DA_UniPolar, DAQ2K_DA_Int_REF, 10.0);
    D2K_AO_CH_Config (card, 1, DAQ2K_DA_UniPolar, DAQ2K_DA_Int_REF, 10.0);
    da_ch[0] := 0;
    da_ch[1] := 1;
    D2K_AO_Group_Setup (card, DA_Group_A, 2, da_ch[0]);
//port configured
    D2K_DIO_PortConfig(card ,Channel_P1A, INPUT_PORT);

```

## Xray Generation by Field Emission

```

//port configured
  D2K_DIO_PortConfig(card, Channel_P1B, OUTPUT_PORT);
  XrayOffClick(Sender);
  Timer1.Enabled := true;
end;

//=====
// Timer measurement cycle
//=====
procedure TForm1.Timer1Timer(Sender: TObject);
var
  sx : shortstring;
  vl : array[0..3] of Real;
  di : array[0..5] of integer;
  j,k : integer;
  Nextkv : real;
begin
  if testdone then
  begin
    sx := DateTimetoStr(Now);
    writeln(log_file,sx);
    testdone := false;
  end;
  D2K_AI_VReadChannel(card, {channelNo}4, Value);
  str(Value*10:8:1,sx);
  vl[0] := Value*10;
  Edit1.Text := sx;
  D2K_AI_VReadChannel(card, {channelNo}5, Value);
  str(Value*10:8:1,sx);
  vl[1] := Value*10;
  Edit2.Text := sx;
  D2K_AI_VReadChannel(card, {channelNo}6, Value);
  str(Value*10:8:1,sx);
  vl[2] := Value*10;
  Edit5.Text := sx;
  D2K_AI_VReadChannel(card, {channelNo}7, Value);
  str(Value*10:8:1,sx);
  vl[3] := Value*10;
  Edit12.Text := sx;
  { if RunMacro then
  begin
    dec(rdgctr);
    if rdgctr<=0 then
    begin
      rdgctr := Reading;
      Writeln(log_file,vl[0]:8:1,vl[1]:8:1,vl[2]:8:1);
    end;
  end;}
  D2K_DI_ReadPort(card, Channel_P1A, InputA);
  Checkbox1.Checked := (InputA and (1 shl 0))=0;
  Checkbox2.Checked := (InputA and (1 shl 1))=0;
  Checkbox3.Checked := (InputA and (1 shl 2))=0;
  Checkbox4.Checked := (InputA and (1 shl 3))=0;
  Checkbox5.Checked := (InputA and (1 shl 4))<>0;
  Checkbox6.Checked := (InputA and (1 shl 5))=0;
  if Checkbox1.Checked then di[0] := 116 else di[0]:= 114;
  if Checkbox2.Checked then di[1] := 120 else di[1]:= 118;
  if Checkbox3.Checked then di[2] := 124 else di[2]:= 122;
  if Checkbox4.Checked then di[3] := 128 else di[3]:= 126;
  if Checkbox5.Checked then di[4] := 132 else di[4]:= 130;
  if Checkbox6.Checked then di[5] := 136 else di[5]:= 134;
  Led1.&On := Checkbox6.Checked;
  Led2.&On := not Checkbox6.Checked;

  if RunMacro then
  begin
    dec(rdgctr);
    if rdgctr<=0 then
    begin
      rdgctr := Reading;
      Writeln(log_file,vl[0]:8:1,vl[1]:8:1,vl[2]:8:1,di[0]:4,di[1]:4,di[2]:4,di
        [3]:4,di[4]:4,di[5]:4);
      Series1.Add(vl[0]);
      Series2.Add(vl[1]);
      Series3.Add(vl[2]*10);
      Series4.Add(di[4]-128);
      Series5.Add(di[5]-128);
    end;
  end;
end;

```

```

if Capture then
begin
  if vl[1]<vg+0.5 then
  begin
    for j := 0 to 3 do va[j] := va[j]+vl[j];
    dec(CaptureTime);
    Edit6.Text := inttostr(CaptureTime);
  end;
  if CaptureTime <= 0 then
  begin
    inc(CaptureNo);
    Table2.Append;
    Table2.FieldName('Reading').AsInteger := CaptureNo;
    Table2.FieldName('Time').AsDateTime := Now;
    Table2.FieldName('Date').AsDateTime := Now;
    Table2.FieldName('Result1').AsFloat := va[0]*AnodeScale/(100*Captstep);
    Table2.FieldName('Result2').AsFloat := va[1]*GateScale/Captstep;
    Table2.FieldName('Result3').AsFloat := va[2]*2*(100000/GateRes)/Captstep;
    Table2.FieldName('Result4').AsFloat := va[3]*2*(100000/AnodeRes)/Captstep;
    Table2.Post;
    for j := 0 to 3 do va[j] := 0;
    CaptureTime := CaptStep;
    dec(GateTime);
    if GateTime<=0 then
    begin
      sx := Edit4.Text;
      val(sx,vg,k);
      if GateStart=0 then inc(vg);
      if (vg>GateMax) or (GateStart<>0) then
      begin
        vg := GateStart; //0;
        sx := Edit3.Text;
        val(sx,Nextkv,k);
        Nextkv := Nextkv*Anodescale/100;
        Nextkv := Nextkv+Stepkv;
        str(trunc((Nextkv*100/Anodescale)+0.5),sx);
        Edit3.Text := sx;
        Edit4.Text := inttostr(GateStart); //'0';
        if Nextkv>Finalkv then
        begin
          Edit3.Text := '0';
          Capture := false;
        end;
      end;
      Edit4.Text := inttostr(vg);
      GateTime := GateStep;
    end;
  end;
end;
end;
end;

//=====
// Timer to read sequence data in <Tankate> database table
//=====
procedure TForm1.Timer2Timer(Sender: TObject);
var
  enable : integer;
begin
  if RunMacro then
  begin
    dec(secctr);
    Edit6.Text := InttoStr(secctr);
    if secctr<=0 then
    begin
      if Table1.Eof then
      begin
        RunMacro := false;
        Table1.Close;
        Edit7.Text := 'Finished';
      end
      else
      begin
        secctr := Table1.FieldName('Duration').AsInteger(+1);
        enable := Table1.FieldName('Enable').AsInteger;
        Edit7.Text := Table1.FieldName('Description').AsString;
        if enable=0 then D2K_DO_WriteLine (card,Channel_P1B,0,0)
          else D2K_DO_WriteLine (card,Channel_P1B,0,1);
        Edit3.Text := Table1.FieldName('Kv').AsString;
      end;
    end;
  end;
end;

```

## Xray Generation by Field Emission

```
    Edit4.Text := Table1.FieldByName('mA').AsString;
    Reading := Table1.FieldByName('Read').AsInteger;
    Reading := Reading*10;
    Table1.Next;
  end;
end;
end;
end;
//=====
// End of program
//=====
end.
```

## APPENDIX 4 – XGEN SOFTWARE

```

Motor control commands
//=====
// General slide command
//=====
// The motor is stepped on a threaded timer
// This allows the program to stay active during the stepping sequence
//=====
// Default motor step intervals
const
  stepspd   = 5;
  stepspd1  = 8;
  stepspd2  = 80;
var
  stepcount : integer;
  stepcnt   : integer;
  stepdirn  : integer;
  stept     : integer;
  steptt    : integer;
  stepptr   : integer;
  stepmotor : integer;
  steprun   : boolean = false;
  stepedge  : boolean;
  steparray : array[0..3,0..3] of integer;
  steps     : integer;
  array12   : integer = 1;           //selects whether slide or cathode

// Definition of the step sequence record
// {direction, time, count, motor}
type
  Stepcomm = record
    Cmess   : shortstring;
    Dirnum  : integer;
    Timenum : integer;
    Cntnum  : integer;
    Motnum  : integer;
  end;

// Sequence to drive the Cathode-Gap stepper motor
steparray1: array[0..4] of Stepcomm =
  (
    (Cmess : 'Homing'           ; Dirnum : 0; Timenum : 0; Cntnum : 3500; Motnum : 1),
    (Cmess : 'Moving on'       ; Dirnum : 0; Timenum : 20; Cntnum : 10; Motnum : 1),
    (Cmess : 'Moving off'      ; Dirnum : 1; Timenum : 20; Cntnum : 10; Motnum : 1),
    (Cmess : 'Move to position' ; Dirnum : 1; Timenum : 0; Cntnum : 400; Motnum : 1),
    (Cmess : 'Done'            ; Dirnum : 0; Timenum : 0; Cntnum : 0; Motnum : 1)
  );

// Sequence to drive the Cathode-Gap stepper motor
steparray2: array[0..3] of Stepcomm =
  (
    (Cmess : 'Homing'           ; Dirnum : 0; Timenum : 0; Cntnum : 2500; Motnum : 2),
    (Cmess : 'Moving off'       ; Dirnum : 1; Timenum : 10; Cntnum : 10; Motnum : 2),
    (Cmess : 'Move to position' ; Dirnum : 1; Timenum : 0; Cntnum : 2000; Motnum : 2),
    (Cmess : 'Done'            ; Dirnum : 0; Timenum : 0; Cntnum : 0; Motnum : 2)
  );

// Threaded timer routine
// Timer has resolution of 5ms and accuracy of 10ms
procedure TXGForm.CairnTimer2Timer(Sender: TObject);
begin
  if steprun then
  begin
    if (stepcount=0) and ((steptt=stept) or (steptt=0)) then
    begin
      if array12=1 then
      begin
        stepdirn := Steparray1[stepptr].Dirnum;
        stept     := Steparray1[stepptr].Timenum;
        stepcnt   := Steparray1[stepptr].Cntnum;
        stepmotor:= Steparray1[stepptr].Motnum;
        Editstate.Text := Steparray1[stepptr].Cmess;
        if (Editstate.Text='Move to position') then
          stepcnt := steps;
      end
    end
  end
end

```

## Xray Generation by Field Emission

```

else
begin
  stepdirn := Stepparray2[stepptr].Dirnum;
  stept := Stepparray2[stepptr].Timenum;
  stepcnt := Stepparray2[stepptr].Cntnum;
  stepmotor:= Stepparray2[stepptr].Motnum;
  Editstate.Text := Stepparray2[stepptr].Cmess;
  if (Editstate.Text='Move to position') then
    stepcnt := steps;
end;

stepcount:= stepcnt;           //reset step count
steptt := stept;              //reset step time
inc(stepptr);
if stepmotor=1 then
begin
  SioPuts(Port,'r13',3);      //motor enable
  SioPutc(Port,chr(13));
end
else
begin
  SioPuts(Port,'r10',3);      //motor enable
  SioPutc(Port,chr(13));
end;
sleep(10);
end;
writeln(logmotor,stepptr-1:5,stepdirn:5,steptt:5,stepcnt:5,stepcount:5,stepmotor:5);
if stepcnt=0 then
begin
  steprun := false;
  button29.Enabled := true;
  button30.Enabled := true;
  SioPuts(Port,'s13',3);      //motor disable
  SioPutc(Port,chr(13));
  sleep(10);
  SioPuts(Port,'s10',3);      //motor disable
  SioPutc(Port,chr(13));
  sleep(10);
end
else
begin
  if steptt>0 then dec(steptt)
  else
  begin
    steptt := stept;          //reset step time
    if stepdirn>0 then
    begin
      if steppedge then
      begin
        dec(stepcount);
        SioPuts(Port,'r11',3);  //motor back
        SioPutc(Port,chr(13));
      end
      else
      begin
        SioPuts(Port,'s11',3);  //motor back
        SioPutc(Port,chr(13));
      end;
    end;
  end
  else
  begin
    if steppedge then
    begin
      dec(stepcount);
      SioPuts(Port,'r12',3);    //motor forward
      SioPutc(Port,chr(13));
    end
    else
    begin
      SioPuts(Port,'s12',3);    //motor forward
      SioPutc(Port,chr(13));
    end;
  end;
  steppedge := not steppedge;
  if stepmotor=1 then
    EditRun1.Text := inttostr(stepcount)
  else
    EditRun1.Text := inttostr(stepcount);
end;
end;

```

```

    end;
  end;
end;

//=====
// Execute cathode movement
//=====
procedure TXGForm.Button29Click(Sender: TObject);
var
  n,m,k : integer;
begin
  array12 := 1;           //select cathode motor
  val(Editsteps1.Text,n,k);
  steps := n;
  if k=0 then
  begin
    button29.Enabled := false;   //disable buttons for duration
    button30.Enabled := false;
    stepptr := 0;
    stepcount := 0;
    stept := 0;
    steprun := true;
    Cairntimer2.Enabled := true;
  end;
end;

//=====
// Execute slide movement
//=====
procedure TXGForm.Button30Click(Sender: TObject);
var
  n,m,k : integer;
begin
  array12 := 2;           //select slide motor
  val(Editsteps2.Text,n,k);
  steps := n;
  if k=0 then
  begin
    button29.Enabled := false;   //disable buttons for duration
    button30.Enabled := false;
    stepptr := 0;
    stepcount := 0;
    stept := 0;
    steprun := true;
    Cairntimer2.Enabled := true;
  end;
end;

Turbo and pressure gauge commands
//=====
// Timer for polling pressure gauges
//=====
// The system sends alternate commands "PR1" and "PR2" to gauge
// Turbo pump may be enabled if :
// Pirani gives no errors
// Pirani pressure < 1e-2
// Turbo not over-ridden to off state
//=====
// Sequence controlled by readbk counter
// 0 = Read and parse full range gauge
// 1 = Send Pirani enquiry
// 2 = Read and parse Pirani gauge
// 3 = Send full range enquiry
//=====
procedure TXGForm.Timer6Timer(Sender: TObject);
var
  s,s1,s2,s3 : string;
  I, Code : Integer;
  CharCount : Integer;
  n,k,m : Integer;
  err : Integer;
  HVenable : boolean;
begin
  k := 0;
  i := 0;
  repeat
    inc(i);

```

## Xray Generation by Field Emission

```

Code := SioGetc(MPort);           // Read from gauge serial port
if Code < 0 then break;           // Exit if serial error
Inc(CharCount);
if code>32 then
  S := S + Chr(code);
until (code=CR) or (i>=40);

n := pos('E',s);                  // Test for exponent command
s3 := copy(s,n+1,length(s));

n := pos(',',s);                  // Test for delimiter ",",
s1 := copy(s,0,1);
s2 := copy(s,n+1,length(s));
val(s1,err,k);                    // Convert value of error status
case err of
  0 : s1 := 'OK';
  1 : s1 := 'UR';
  2 : s1 := 'OR';
  3 : s1 := 'ERR';
  4 : s1 := 'OFF';
  5 : s1 := 'NO';
  6 : s1 := 'ID';                 // Interpret error status
end;

if (readbk mod 4)=0 then
begin
  edit47.Text := s3;              // Display gauge reading
  edit51.Text := s2;
  edit53.Text := s1;
  inc(secctr);
  Edit48.Text := inttostr(secctr);
{$ifdef xgenlog}
  if secctr>=60 then
  begin
    writeln(logout,s2);
    secctr := 0;                 // Save data once per minute
  end;
{$endif}
  s := 'PR1';                     // Prepare next command
end;
if (readbk mod 4)=1 then
begin
  s := chr(05);                  // Send <ENQ> command to read
end;
if (readbk mod 4)=2 then
begin
  edit46.Text := s3;             // Display readings and status
  edit50.Text := s2;
  edit52.Text := s1;
  val(s3,m,k);                   // Fetch exponent into m to test
  if ((err>1) or (m<-2)) or turbo_off_override then
  begin
    Edit49.Text := 'Turbo off';   // Control turbo pump via output 9
    Edit49.Font.Color := clRed;
    sleep(50);
    SioPuts(Port,'r9',3);
    SioPutc(Port,chr(13));
    turbo_off_override := false;
  end;
  if {((err<=1) and (m<-2)) or} turbo_override then
  begin
    Edit49.Text := 'Turbo on';    // Control turbo pump via output 9
    Edit49.Font.Color := clBlue;
    sleep(50);
    SioPuts(Port,'s9',3);
    SioPutc(Port,chr(13));
    turbo_override := false;
  end;
  s := 'PR2';                     // Prepare next request (Pirani gauge)
end;
if (readbk mod 4)=3 then
begin
  s := chr(05);                  // Note "t" sometimes takes >100ms !
end;
inc(readbk);
SioRxClear(MPort);              // Send next request to gauge
{if length(s)=1 then} Sioputs(MPort,pchar(s),length(s));
if length(s)>1 then SioPutc(MPort,chr(13));
end;

```

```
Fan control commands
//=====
// Control for turning turbo cooling fan on/off
//=====
procedure TXGForm.Button27Click(Sender: TObject);
begin
  if Fan_control then
  begin
    Button27.Caption := '&Fan off';
    sleep(50);
    SioPuts(Port, 's1', 3);
    SioPutc(Port, chr(13));
  end
  else
  begin
    Button27.Caption := '&Fan on';
    sleep(50);
    SioPuts(Port, 'r1', 3);
    SioPutc(Port, chr(13));
  end;
  Fan_control := not Fan_control;
end;
```

## Xray Generation by Field Emission

## APPENDIX 5 – FIRMWARE FOR CNT GENERATOR

```

program hvconcnt;
//=====
// to do :
// Ctrip - fault on OT
//=====
// 0.00 First version                                05/11/05
// 0.01 Modify for production board                  11/12/05
//      Invert inhibit, An Vref
// 0.02 Improve readback accuracy - use one ref     18/12/05
// 3.00 First CNT version                            02/06/13
//=====
// to do - watchdog timer

{main procedure}
const
{Version}
  ver      : string[6] = 'V3.00';
{General}
  stt      : byte = 0;      //start of string
  cr       : byte = 13;
  lf       : byte = 10;
  esc      : byte = 27;
{Adc inputs}
  pkvdem   : byte = 0;
  pmadem   : byte = 1;
  pfilmon  : byte = 4;
  pvmonp   : byte = 5;
  pvmonn   : byte = 6;
  pimonn   : byte = 7;
  pstndby  : byte = 8;
  pfilmax  : byte = 9;
{Dac outputs}
  dhvout   : byte = 0;
  dfilout  : byte = 1;
  dvmon    : byte = 2;
  dimon    : byte = 3;
{Digital inputs - Port C}
  Enable   : byte = 0;
  OVCCA    : byte = 1;
  OVCA     : byte = 2;
  Ctrip    : byte = 3;
  Otemp    : byte = 4;
{LED, etc outputs - Port D}
  Test     : byte = 0;
  LedOC    : byte = 0;
  LedUC    : byte = 1;
  LedUCL   : byte = 2;
  LedUV    : byte = 3;
  LedUVL   : byte = 4;
  Clamp    : byte = 5;
  Fault    : byte = 6;
  Inhibit  : byte = 7;
{Timeouts}
  HVstep   : byte = 4;
  mastep   : byte = 8;
  matime   : word = 1000;
  UVTime   : word = 1500;
  UCTime   : word = 2500;
  OCTime   : word = 4000;
  EnaTime  : byte = 5;
var
  counter  : byte;
  m,n1    : byte;
  sx       : string[20];
  subctr   : byte;
  charin   : byte;
  termin   : boolean;
  inter    : boolean;
  temp,templ : word;
  hvenable: boolean;
  kvramp   : boolean;
  kvdone   : boolean;
  state    : byte;
  kvtarget: word;

```

## Xray Generation by Field Emission

```

matarget: word;
madone  : boolean;
maramp  : boolean;
madelay : word;
hvcont  : word;
hvmon   : word;
macont  : word;
mactual : integer;
filcont : word;
filadj  : integer;
filadj1 : integer;
UVDelay : word;
UCDelay : word;
OCDelay : word;
UClatch : boolean;
UVlatch : boolean;
OClatch : boolean;
ena1,ena2 : byte;
filtptr  : byte;
filt     : array[31] of integer;
{for serial interface}
  kvser   : word;

procedure interrupt;
begin
// Timer interrupt 2ms
  if testbit(INTCON, TMR0IF)=1 then
  begin
    inc(subctr);
    inter := true;
    TMR0L := 96;
    clearbit (INTCON, TMR0IF);
  end
  else
// Int2 input from encoder
  {
    if testbit (INTCON3, INT2IF)=1 then
    begin
      encint := true;
      clearbit (INTCON3, INT2IF);
    end
    else}
// Serial receive interrupt
  if testbit (PIR1,RCIF)=1 then
  begin
    charin := RCREG;
  end;
end;

procedure new_line;
begin
  USART_write(cr);
  USART_write(lf);
end;

procedure Usart_string(var s : string[25]);
var
  n : byte;
begin
  for n := stt to length(s)-1-stt do USART_Write(s[n]);
end;

procedure Usart_line(var s : string[40]);
var
  n : byte;
begin
  for n := stt to length(s)-1-stt do USART_Write(s[n]);
  new_line;
end;

// Write 12 bit word to DAC
procedure Dac_out(value:word; opno:byte);
var temp : byte;
    csno : byte;
begin
  if opno>1 then csno := 5 else csno := 4;
  clearbit(PORTB,csno);           //select chip
  temp := hi(value) and $0F;
  temp := temp or $70;           //$10 for rev 2 board, $30 for rev 1
  if opno and 1 = 1 then temp := temp or $80;

```

```

    SPI_Write(temp);
    temp := lo(value);
    SPI_Write(temp);
    setbit(PORTB,csno);
end;

procedure scan_inputs;
var
    n : byte;
    faultins : byte;
    temp2 : integer;
    temp3 : integer;
begin
    // Read demand inputs
    kvtarget := ADC_read(pkvdem);
    temp2 := kvtarget shr 5;
    kvtarget := kvtarget shl 2;           //scale to 4095
    kvtarget := kvtarget+temp2;
    if kvtarget>4095 then kvtarget := 4095;
    matarget := ADC_read(pmadem);
    matarget := matarget shl 2;           //scale to 4095

    // Test enable input
    // If no enable, clear outputs and targets
    if testbit(PORTC,Enable)=1 then
    begin
        inc(ena1);
        if ena1>=EnaTime then
        begin
            ena2 := 0;
            ena1 := EnaTime;
        end;
    end
    else
    begin
        inc(ena2);
        if ena2>=EnaTime then
        begin
            ena1 := 0;
            ena2 := EnaTime;
        end;
    end;
    if (ena1=EnaTime) then
    begin
        clearbit(PORTD,Inhibit); //was set in proto
        clearbit(PORTD,Clamp);
        clearbit(PORTD,fault);
        hvenable := false;
        kvtarget := 0;
        matarget := 0;
        hvcont := 0;
        macont := 0;
        madelay := 0;
        state := 0;
        temp3 := 0;
    end
    else
    begin
        setbit(PORTD,Inhibit); //was clear in proto
        if hvenable=false then //enable turned on clear latches
        begin
            kvramp := true;
            state := 1;
            UVlatch := false;
            UClatch := false;
            OClatch := false;
            setbit(PORTD,LedUVL);
            setbit(PORTD,LedUCL);
            setbit(PORTD,LedOC);
        end;
        hvenable := true;
    end;

    // This controls the Kv
    // On ramp-up after enable, set kvramp - state 2
    if kvtarget>hvcont then
    begin
        hvcont := hvcont+hvstep;
    end;
end;

```

## Xray Generation by Field Emission

```

    if hvcont>kvtarget then hvcont := kvtarget;
    if madelay<matime then inc(madelay);
end
else
begin
    hvcont := kvtarget;
    kvramp := false;
    if madelay<matime then inc(madelay);
    if (state=1) then state := 2;
    if (state=2) and (madelay=matime) then state:=3;
end;

// End of Kv ramp up
if hvenable and (kvramp=false) then
{   if state>=3 then
begin
    if kvdone = false then
    begin
        maramp := true;
        macont := 0;
        for n := 0 to 31 do filt[n] := 0;
    end;
    kvdone := true;
end
else
begin
    kvdone := false;
    madone := false;
    setbit(PORTD,LedUV);
    setbit(PORTD,LedUC);
    UVDelay := 0;
    UCDelay := 0;
    OCDelay := 0;
    UVlatch := false;
    UClatch := false;
    matarget := 0;
    macont := 0;
end;

if kvdone then
begin
    if matarget>macont then
    begin
        macont := macont+mastep;
        if macont>matarget then macont := matarget;
    end
    else
    begin
        macont := matarget;
        maramp := false;
        madone := true;
    end;
end;

if hvcont>4095 then hvcont := 4095;
dac_out(hvcont,dhvout);

//read and output mA monitor
temp := ADC_read(pvmonn);
temp2 := temp shr 5;
temp3 := temp shr 6;           //correct for loading
temp := temp+temp2+temp3;
mactual := temp shl 2;         //convert from 10 to 12 bits
if mactual<0 then mactual := 0;
temp := mactual;
if temp>4095 then temp := 4095;
dac_out(temp,dimon);

// Read and scale KV monitor and check undervoltage
// Modified for CNT generator
if kvdone then
begin
    temp := ADC_read(pvmonp);
    hvmon := temp; //+templ;
    temp2 := hvmon shr 5;
    temp3 := hvmon shr 7;       //correct for loading
    hvmon := hvmon+temp2+temp3;
    hvmon := hvmon shl 2;

```

```

hvmon := hvmon+3;
temp := hvmon;
if temp>4095 then temp := 4095;
dac_out(temp,dvmon);
templ := kvtarget;
templ := (templ*4) div 5;
if hvmon>templ then
begin
  setbit(PORTD,LedUV);
  UVdelay := 0;
end
else
begin
  clearbit(PORTD,LedUV);
  inc(UVdelay);
  if (UVdelay>UVtime) or (UVlatch=true) then
  begin
    UVdelay := UVtime;
    UVlatch := true;
  end;
  if UVlatch=true then clearbit(PORTD,LedUVL)
  else setbit(PORTD,LedUVL);
end;
end;

// Read and scale mA monitor and check under current
if madone then
begin
  templ := macont; //matarget;
  templ := (templ*4) div 5;
  if templ<512 then templ := 0;
  if mactual>templ then
  begin
    setbit(PORTD,LedUC);
    UCdelay := 0;
  end
  else
  begin
    clearbit(PORTD,LedUC);
    inc(UCdelay);
    if (UCdelay>Uctime) or (Uclatch=true) then
    begin
      UCdelay := Uctime;
      Uclatch := true;
    end;
  end;
  if Uclatch=true then clearbit(PORTD,LedUCL)
  else setbit(PORTD,LedUCL);
end;
end;

// Check fault conditions and clamp if necessary
if kvdone then
begin
  faultins := testbit(PORTC,OVCAn);
  n := testbit(PORTC,OVCca);
  if faultins>0 then faultins := n;
  if faultins>0 then
  begin
    setbit(PORTD,LedOC);
    OCdelay := 0;
  end
  else
  begin
    inc(OCdelay);
    if (OCdelay>Octime) or (Oclatch=true) then
    begin
      OCdelay := Octime;
      Oclatch := true;
    end;
  end;
  if Oclatch=true then clearbit(PORTD,LedOC)
  else setbit(PORTD,LedOC);
end;

// Check fault inputs and set fault output;
faultins := 0;
if testbit(PORTC,Otemp)=0 then inc(faultins);
if Oclatch=true then inc(faultins);
if Uclatch=true then inc(faultins);
if UVlatch=true then inc(faultins);

```

## Xray Generation by Field Emission

```

    if faultins>0 then setbit(PORTD,fault)
        else clearbit(PORTD,fault);

    faultins := 0;
    if UClatch=true then inc(faultins);
    if UVlatch=true then inc(faultins);
    if faultins>0 then setbit(PORTD,Clamp)
        else clearbit(PORTD,Clamp);
    end;
end
else
// This happens if Kvdone false
// Modified for CNT generator
begin
    if kvramp then
    begin
        temp := ADC_read(pvmonp);
        hvmon := temp; // for single anode supply
        temp2 := hvmon shr 5;
        temp3 := hvmon shr 7; //correct for loading x 1/25
        hvmon := hvmon+temp2+temp3;
        hvmon := hvmon shl 2;
        hvmon := hvmon+3;
        temp := hvmon;
        if temp>4095 then temp := 4095;
        dac_out(temp,dvmon);
    end
    else
    begin
        dac_out(0,dvmon);
    end;
end;
end;

// when kv ramped up, make filament value and limit
// according to Standby and Filmax preset pot values
if kvdone and (faultins=0) then
begin
    filadj := macont;
    filadj := filadj - mactual; //mod 4095
    inc(filtptr);
    if filtptr>7 then filtptr:=0;
    filt[filtptr] := filadj;
    for n := 0 to 7 do filadj1 := filadj1+filt[n];
    if filadj1>=0 then filadj := filadj1 shr 11
        else filadj := filadj1 shr 11;
    filadj1 := filadj1 - (filadj shl 11);
    filcont := filcont + filadj;
// New code for CNT
    filcont := macont;
end
else filcont := 0;

// limit filcont to min (standby) and max (filmax)
temp := ADC_read(pfilmax);
temp := temp shl 2;
if filcont>temp then filcont := temp;
temp := ADC_read(pstndby);
temp := temp shl 2;
// New code for CNT
temp := 0; // Do not set standby

if filcont<temp then filcont := temp;
if filcont>4095 then filcont := 4095;
dac_out(filcont,dfilout);

end;

```

## Chapter 12: Appendices

```

{Main routine}
//=====
// Initialise all hardware and registers
//=====
begin
  USART_init(9600);           // initialize USART (9600 baud rate, 1 stop bit, ...
  setbit (PIE1,RCIE);        //RX serial interrupt
  setbit (INTCON3, INT2IP);   //INT2 high priority
  setbit (INTCON3, INT2IE);   //INT2 enable
  TOCON := $C5;              // assign prescaler to TMRO
  TMR0L := 96;               // make up to 5ms
  INTCON := $A0+$40; //+$10; // enable TMRO interrupt, PIE, INTO

  ////////// select Vref and analog inputs, in order to use ADC_read //////////
  ADCON1 := $35;             // all porta pins as analog, VDD as Vref
  TRISA := $FF;             // all porta pins as inputs
  TRISB := $CF;
  TRISC := $FF;
  TRISD := $00;
  PORTD := $FF;
  clearbit(PORTD,clamp);
  //=====
  SPI_init;
  for n1 := 0 to 3 do dac_out(0,n1);
  kvser := 0;

  new_line;
  Usart_string('CDD HVcontrol card -- ');
  Usart_line(ver);
  setbit(PORTD,LedUCL);
  setbit(PORTD,LedUVL);
  setbit(PORTD,LedOC);
  charin := 0;
  termin := true;
  WDTCON := 1; {1}           //start watchdog

  while true do             // endless loop
  begin
    if inter then
    begin
      scan_inputs;
      inter := false;
    end;
    if subctr>=200 then      // one second timer
    begin
      subctr := 0;
      inc(counter);
      if counter>10 then counter := 0;
    end;

    if charin>0 then        // serial character received
    begin
      if charin>=32 then
      begin
        USART_Write(charin);
      end;
      charin := 0;
    end;
  // reset watch do timer
  asm
  CLRWDT
  end;
  end;

end.

```

## Xray Generation by Field Emission

## APPENDIX 6 – SOFTWARE FOR ENCODED APERTURE

```

{=====}
{ ENCODED APERTURE IMAGE CAPTURE PROGRAM          }
{  V0.1  Test program with motor interface        07/05/16  }
{=====}
// http://www.netlib.org/lapack/lapacke.html
// https://github.com/Reference-LAPACK/lapack/tree/master/LAPACKE
(*-----)
                                C Interface to LAPACK
-----

Introduction
-----

This library is a part of reference implementation for the C interface to
LAPACK project according to the specifications described at the forum for
the Intel(R) Math Kernel Library (Intel(R) MKL):
http://software.intel.com/en-us/forums/showthread.php?t=61234

This implementation provides a native C interface to LAPACK routines available
at www.netlib.org/lapack to facilitate usage of LAPACK functionality
for C programmers.
This implementation introduces:
- row-major and column-major matrix layout controlled by the first function
  parameter;
- an implementation with working arrays (middle-level interface) as well as
  without working arrays (high-level interface);
- input scalars passed by value;
- error code as a return value instead of the INFO parameter.

This implementation supports both the ILP64 and LP64 programming models,
and different complex type styles: structure, C99.

This implementation includes interfaces for the LAPACK-3.2.1 Driver and
Computational routines only.

-----

Product Directories
-----

The installation directory of this package has the following structure:

src                - C interface source files
utils              - C interface auxiliary files
include            - header files for C interface

-----

Installation
-----

The reference code for the C interface to LAPACK is built similarly to the
Basic Linear Algebra Subprograms (BLAS) and LAPACK. The build system produces
a static binary lapacke.a.

You need to provide a make.inc file in the top directory that defines the
compiler, compiler flags, names for binaries to be created/linked to. You may
choose the appropriate LP64/ILP64 model, convenient complex type style,
LAPACKE name pattern, and/or redefine system malloc/free in make.inc. Several
examples of make.inc are provided.

After setting up the make.inc, you can build C interface to LAPACK by typing

make lapacke
-----
*)

unit MotorInterface;

interface

uses
  Windows, Messages, SysUtils, Variants, Classes, Graphics, Controls, Forms,
  Dialogs, StdCtrls, CPort, ComObj, Grids, Dexela, png, Epix, dexu3,
  ExtCtrls, PNGImage;

type
  TMyByteArray = array of Byte;

type

```

## Xray Generation by Field Emission

```
TForm1 = class(TForm)
  GO: TButton;
  CYCLE: TButton;
  STOP: TButton;
  Position: TEdit;
  OnOffButton: TButton;
  PositionLabel: TLabel;
  ComPort1: TComPort;
  GetData: TButton;
  HOME: TButton;
  StringGrid1: TStringGrid;
  SEQUENCE: TButton;
  SpeedButton: TButton;
  SpeedLabel: TLabel;
  Speed: TEdit;
  RepeatLabel: TLabel;
  RepeatSeq: TEdit;
  GetData2: TButton;
  NextButton: TButton;
  NextEdit: TEdit;
  NextLabel: TLabel;
  NextDoneButton: TButton;
  CDDGrab: TButton;
  SaveCheckBox: TCheckBox;
  SaveButton: TButton;
  SaveEdit: TEdit;
  SaveNo: TButton;
  PictureSequence: TButton;
  Label1: TLabel;
  Label2: TLabel;
  Label3: TLabel;
  SequenceLong: TButton;
  StatusMotor: TMemo;
  StatusGrab: TMemo;
  StatusSequence: TMemo;
  GetTest: TButton;
  CollectDark: TButton;
  CollectFlood: TButton;
  LoadFlatField: TButton;
  RandomTest: TButton;
  RandomTestStart: TEdit;
  RandomTestFinish: TEdit;
  RandomTestNumber: TEdit;
  Label4: TLabel;
  Label5: TLabel;
  unitsedit: TEdit;
  unitsbutton: TButton;
  unitslabel: TLabel;
  DeconvolutionSequence: TButton;
  Label6: TLabel;
  Label7: TLabel;
  Label8: TLabel;
  Label9: TLabel;
  Label10: TLabel;
  Label11: TLabel;
  Label12: TLabel;
  SVDGet: TButton;
  Label13: TLabel;
  SVDSeq: TButton;
  Label14: TLabel;
  Label15: TLabel;
  SVDBlur: TEdit;
  procedure OnOffButtonClick(Sender: TObject);
  procedure check;
  procedure GOClick(Sender: TObject);
  procedure CYCLEClick(Sender: TObject);
  procedure STOPClick(Sender: TObject);
  procedure HOMEClick(Sender: TObject);
  procedure GetDataClick(Sender: TObject);
  procedure SEQUENCEClick(Sender: TObject);
  procedure SpeedButtonClick(Sender: TObject);
  procedure GetData2Click(Sender: TObject);
  procedure NextDoneButtonClick(Sender: TObject);
  procedure NextButtonClick(Sender: TObject);
  procedure CDDGrabClick(Sender: TObject);
  procedure get4;
  procedure SaveButtonClick(Sender: TObject);
  procedure SaveNoClick(Sender: TObject);
  procedure PictureSequenceClick(Sender: TObject);
```

```

    procedure SequenceLongClick(Sender: TObject);
    procedure GetTestClick(Sender: TObject);
    procedure CollectDarkClick(Sender: TObject);
    procedure CollectFloodClick(Sender: TObject);
    procedure LoadFlatFieldClick(Sender: TObject);
    procedure RandomTestClick(Sender: TObject);
    procedure RandomTestStartClick(Sender: TObject);
    procedure RandomTestFinishClick(Sender: TObject);
    procedure RandomTestNumberClick(Sender: TObject);
    procedure unitsbuttonClick(Sender: TObject);
    procedure DeconvolutionSequenceClick(Sender: TObject);
    procedure SVDGetClick(Sender: TObject);
    procedure SVDSeqClick(Sender: TObject);
private
    { Private declarations }
public
    { Public declarations }
    currentbuffer : integer;
    capturedbuffer : integer;
end;

var
    Form1: TForm1;
    M: integer;
    MyBytes: array[0..10] of TMyByteArray;
    S: Integer;
    T: Integer;
    MySnap: array[1..15] of Wordarray;
    LongSnap: array of LongWord;
    invATAAT : array of double;

    Blur : integer;           // might need to make this into an array
    SVD : array of double; // this might need to be an array of arrays. will load SVDs etc
into them

    {
    MySnap[1] - scrambled 16 bit picture
    MySnap[2] - unscrambled 16 bit picture
    MySnap[3] - storage of pictures
    .
    .
    MySnap[12]
    MySnap[13] - Dark
    MySnap[14] - Flood
    MySnap[15] - Combined picture
    }

const
    ROW_MAJOR = 101;
    COLUMN_MAJOR = 102;
    ATrans = 'N';
    NoTrans = 111;
    Trans = 112;
    Pic_Height = 1944;
    Pic_Width = 1536;
    Pic_Stride = Pic_Width * 2;

function LAPACKE_dgels (matrix_order : integer; trans : char; m : integer; n : integer;
    nrhs : integer; a : pdouble; lda : integer; b : pdouble;
    ldb : integer) : integer; stdcall; external 'liblapacke.dll';

function LAPACKE_dgetrf (matrix_order : integer; m : integer; n : integer; a : pdouble;
    lda : integer; ipiv : pinteger) : integer; stdcall;
external 'liblapacke.dll';

function LAPACKE_dgetri (matrix_order : integer; n : integer; a : pdouble; lda :
integer;
    ipiv : pinteger) : integer; stdcall; external 'liblapacke.dll';

function LAPACKE_dgesdd (matrix_order : integer; jobz : char; m : integer; n : integer;
    a : pdouble; lda : integer; s : pdouble; u : pdouble; ldu :
integer;
    vt : pdouble; ldvt : integer) : integer;
stdcall; external 'liblapacke.dll';

procedure cblas_dgemm (Order : integer; TransA : integer; TransB : integer; M :
integer;
    N : Integer; K : integer; alpha : double; A : pdouble;

```

## Xray Generation by Field Emission

```

lda : integer; B : pdouble; ldb : integer; beta : double;
C : pdouble; ldc : integer); stdcall; external 'libcbblas.dll';

implementation

{$R *.dfm}

{=====}
{ ON/OFF }
{=====}

procedure TForm1.OnOffButtonClick(Sender: TObject);
begin
  ComPort1.Port := 'COM11';
  if ComPort1.connected
  then
    begin
      ComPort1.Close;
      OnOffButton.Caption := 'SWITCH ON';
      StatusMotor.lines.add('ComPort closed');
      pxd_serialConfigure(1 shl BoardHandle, 0, 0, 8, 0, 1, 0, 0, 0); // these 3 lines
are from CDD_close but work on their own
      pxd_eventCapturedFieldClose(1 shl BoardHandle, capturedFieldSignalHandle);
      pxd_PIXCIClose();
      StatusGrab.Lines.Add('CDDClose');
      GO.Enabled := false;
      CYCLE.Enabled := false;
      STOP.Enabled := false;
      HOME.Enabled := false;
      SpeedButton.Enabled := false;
      SEQUENCE.Enabled := false;
      NextDoneButton.Enabled := false;
      NextButton.Enabled := false;
      PictureSequence.Enabled := false;
      DeconvolutionSequence.Enabled := false;
      SequenceLong.Enabled := false;
      CollectDark.Enabled := false;
      CollectFlood.Enabled := false;
      CDDGrab.Enabled := false;
      SaveButton.Enabled := false;
      SaveNo.Enabled := false;
      LoadFlatField.Enabled := false;
      unitsbutton.Enabled := false;
    end
  else
    begin
      ComPort1.Open;
      OnOffButton.Caption := 'SWITCH OFF';
      StatusMotor.lines.add('ComPort open');
      ComPort1.WriteString('A8000' + #13);
      StatusMotor.lines.add('Homing...');
      check;
      {ComPort1.WriteString('H' + #13);
      check;
      StatusMotor.lines.add('Fine Homing');
      sleep(500);}
      StatusMotor.lines.add('Ready');
      CDDInit;
      StatusGrab.Lines.Add('CDDInit');
      GO.Enabled := true;
      CYCLE.Enabled := true;
      HOME.Enabled := true;
      SpeedButton.Enabled := true;
      NextDoneButton.Enabled := false;
      NextButton.Enabled := false;
      SEQUENCE.Enabled := true;
      PictureSequence.Enabled := true;
      DeconvolutionSequence.Enabled := true;
      SequenceLong.Enabled := true;
      CollectDark.Enabled := true;
      if not fileexists('c:\cddsoft\dex\sensor1512.fmt') or
(Epix.CDDInit('c:\cddsoft\dex\sensor1512.fmt', 115200) < 0) then
        begin
          showmessage('Unable to initialize camera link sensor');
          Application.Terminate;
          exit;
        end;
      StatusGrab.Lines.Add('Turn Xrays OFF and Collect Dark');
      CDDGrab.Enabled := true;
    end
  end
end

```

## Chapter 12: Appendices

```

        SaveButton.Enabled := true;
        SaveNo.Enabled := true;
        LoadFlatField.Enabled := true;
        unitsbutton.Enabled := true;
    end;
end;

{=====}
{ GETTING DATA FROM EXCEL }
{=====}

procedure TForm1.GetDataClick(Sender: TObject);
const
    xlCellTypeLastCell = $0000000B;
var
    i, j, x, y: Integer;
    Excel: OleVariant;
begin
    if not fileexists(GetCurrentDir + '\Positions.xls') then
    begin
        showmessage('Positions.xls is not in the same folder as the program');
        Application.Terminate;
        exit;
    end;
    StatusMotor.Lines.Add('Importing data from Excel...');
    Excel := CreateOleObject('Excel.Application');
    Excel.Visible := False;
    Excel.Workbooks.Open(GetCurrentDir + '\Positions.xls');

    Excel.Cells.SpecialCells(xlCellTypeLastCell, EmptyParam).Activate; // Get the value of
the last row
    x := Excel.ActiveCell.Row; // Get the value of the last column
    y := Excel.ActiveCell.Column;

    StringGrid1.RowCount := x; // Set Stringgrid's row & col dimensions.
    StringGrid1.ColCount := y;

    for i := 1 to (x + 1) do // rows (first one is '1')
        for j := 1 to (y + 1) do // columns (first one is '1')
            StringGrid1.Cells[(j-1), (i-1)] := Excel.ActiveSheet.Cells[i,j];
        Excel.Workbooks.Close;
        SEQUENCE.Enabled := true;
        PictureSequence.Enabled := true;
        DeconvolutionSequence.Enabled := true;
        SequenceLong.Enabled := true;
        StatusMotor.Lines.Add('Data imported from Excel');
    end;

{=====}
{ GETTING DATA FROM MANUAL INPUT }
{=====}

procedure TForm1.GetData2Click(Sender: TObject);
var
    I: Integer;
begin
    GO.Enabled := false;
    CYCLE.Enabled := false;
    STOP.Enabled := false;
    HOME.Enabled := false;
    SpeedButton.Enabled := false;
    unitsbutton.Enabled := false;
    SEQUENCE.Enabled := false;
    PictureSequence.Enabled := false;
    DeconvolutionSequence.Enabled := false;
    SequenceLong.Enabled := false;
    GetData.Enabled := false;
    GetData2.Enabled := false;
    NextDoneButton.Enabled := true;
    NextButton.Enabled := true;
    M := 0;
    for I := 0 to StringGrid1.RowCount do
        StringGrid1.Cells[0,I] := '';
    StringGrid1.RowCount := 0;
    StringGrid1.ColCount := 1;
end;

procedure TForm1.NextButtonClick(Sender: TObject);

```

## Xray Generation by Field Emission

```
begin
  StringGrid1.RowCount := stringgrid1.RowCount + 1;
  StringGrid1.Cells[0,M] := NextEdit.Text;
  inc(M);
  NextEdit.Text := '';
end;

procedure TForm1.NextDoneButtonClick(Sender: TObject);
begin
  if Comport1.connected then
  begin
    GO.Enabled := true;
    CYCLE.Enabled := true;
    HOME.Enabled := true;
    SpeedButton.Enabled := true;
    unitsbutton.Enabled := true;
    SEQUENCE.Enabled := true;
    PictureSequence.Enabled := true;
    DeconvolutionSequence.Enabled := true;
    SequenceLong.Enabled := true;
  end;
  GetData2.Enabled := true;
  NextDoneButton.Enabled := false;
  NextButton.Enabled := false;
  StringGrid1.RowCount := stringgrid1.RowCount - 1;
end;

procedure TForm1.RandomTestClick(Sender: TObject);
var
  K: integer;

begin
  StringGrid1.RowCount := strtoint(RandomTestNumber.Text);
  for K := 0 to StringGrid1.RowCount - 1 do
    StringGrid1.Cells[0, K] := inttostr(strtoint(RandomTestStart.Text) +
    random(strtoint(RandomTestFinish.Text) - strtoint(RandomTestStart.Text))) +
    StatusSequence.Lines.Add('Custom Random Test');
  end;

procedure TForm1.RandomTestFinishClick(Sender: TObject);
begin
  RandomTestFinish.Text := '';
end;

procedure TForm1.RandomTestNumberClick(Sender: TObject);
begin
  RandomTestNumber.Text := '';
end;

procedure TForm1.RandomTestStartClick(Sender: TObject);
begin
  RandomTestStart.Text := '';
end;

procedure TForm1.GetTestClick(Sender: TObject);
var
  K: integer;

begin
  if T <> 2 then
  if T <> 1 then
  if T <> 0 then
  T := 0;

  case T of
    0:
      begin
        inc(T);
        StringGrid1.RowCount := 101;
        for K := 2550 to 2650 do
          StringGrid1.Cells[0,K - 2550] := inttostr(K);
          StatusSequence.Lines.Add('Test 101 2550 - 2650');
        end;
      1:
        begin
          inc(T);
          StringGrid1.RowCount := 11;
          for K := 2560 to 2570 do
            StringGrid1.Cells[0,K - 2560] := inttostr(K);
```

```

        StatusSequence.Lines.Add('Test 11 2560 - 2570');
    end;
2:
begin
    T := 0;
    StringGrid1.RowCount := 51;
    for K := 0 to 50 do
        StringGrid1.Cells[0, K] := inttostr(1575 + random(1850));
        StatusSequence.Lines.Add('Test 51 RANDOM 1575 - 3425');
    end;
end;
end;

{=====}
{ MOTOR INTERFACE COMMANDS }
{=====}

procedure TForm1.check; // waits until motor is in position
var
instr: string;

begin
    instr := '';
    while instr <> '*' do
        begin
            ComPort1.ReadStr(instr, length('*'));
        end;
    end;

procedure TForm1.SpeedButtonClick(Sender: TObject);
begin
    ComPort1.WriteStr('M' + Speed.Text + #13);
    StatusMotor.lines.add('Movement speed is now ' + speed.text);
end;

procedure TForm1.GOClick(Sender: TObject);
begin
    ComPort1.WriteStr('A' + Position.text + #13);
    StatusMotor.Lines.add('Moving to ' + Position.text);
    check;
    StatusMotor.lines.add('Arrived at ' + Position.text);
end;

procedure TForm1.CYCLEClick(Sender: TObject);
begin
    ComPort1.WriteStr('C' + #13);
    STOP.Enabled := true;
    CYCLE.Enabled := false;
    StatusMotor.lines.add('Cycling...');
end;

procedure TForm1.STOPClick(Sender: TObject);
begin
    ComPort1.WriteStr('S' + #13);
    STOP.Enabled := false;
    CYCLE.Enabled := true;
    StatusMotor.lines.add('Stopping cycling');
end;

procedure TForm1.unitsbuttonClick(Sender: TObject);
begin
    // if (strtoint(UnitsEdit.text) < 75) and (strtoint(UnitsEdit.text) > 10)
    // then
    // begin
        ComPort1.WriteStr('U' + UnitsEdit.Text + #13);
        StatusMotor.lines.add('Units are now ' + UnitsEdit.Text);
    // end
    // else
        // StatusMotor.Lines.Add('Wrong units / units too high')
    end;

procedure TForm1.HOMEClick(Sender: TObject);
begin
    ComPort1.WriteStr('H' + #13);
    StatusMotor.lines.add('Homing...');
    check;
    StatusMotor.lines.add('Fine Homing');
    sleep(500); // allow time to creep of the sensor
end;

```

## Xray Generation by Field Emission

```

    StatusMotor.lines.add('Ready');
end;

procedure TForm1.SEQUENCEClick(Sender: TObject);
var
    SEQ, S, Z: integer;
    instr: string;
begin
    instr := '';
    Z := strtoint(RepeatSeq.text);
    for S := 1 to Z do
        begin
            StatusMotor.lines.add('Sequence ' + inttostr(S));
            for SEQ := 0 to (StringGrid1.RowCount - 1) do // set SEQ to max no of rows
                begin
                    ComPort1.WriteStr('A' + StringGrid1.cells[0,SEQ] + #13);
                    StatusMotor.lines.add('Moving to ' + inttostr(SEQ + 1));
                    check;
                    StatusMotor.lines.add('Arrived at ' + inttostr(SEQ + 1));
                end;
            end;
            StatusMotor.lines.add('Done');
        end;
end;

{=====}
{ SEQUENCES WITH TAKING IMAGES }
{=====}

procedure TForm1.SVDGetClick(Sender: TObject);
var
    // file reading variables
    PSFtxt : TextFile;
    code : char;

    // deconvolution variables
    AT, VE : array of double;
    K, I : Integer;
    PSF : array of byte;

    // svd stuff
    Ajobz : char;
    SS, U, VT, Asuperb : array of double;
    E : array of double;

    // dgemm stuff
    Aalpha, Abeta : double;

    // picture dimensions
    H, Q, F : cardinal;
begin
    // prepare constants
    F := strtoint(SVDBlur.Text);
    H := Pic_Height div F;

    // load a PSF
    AssignFile(PSFtxt, 'PSF.txt');
    FileMode := fmOpenRead;
    Reset(PSFtxt);
    SetLength(PSF, 1944);
    Blur := 0;
    while not Eof(PSFtxt) do
        begin
            Read(PSFtxt, code);
            PSF[Blur] := strtoint(code);
            inc(Blur);
        end;
    SetLength(PSF, Blur);
    CloseFile(PSFtxt);
    Q := H + 1 - Blur;

    // load PSF into stringgrid1
    StringGrid1.rowcount := 0;
    for K := 0 to Blur - 1 do
        if PSF[K] = 1 then
            begin
                StringGrid1.rowcount := StringGrid1.rowcount + 1;
            end;
    end;
end;

```

## Chapter 12: Appendices

```

        StringGrid1.cells[0, StringGrid1.rowcount - 2] := inttostr(2000 - K * F); //
adjust to starting position
    end;
StringGrid1.rowcount := StringGrid1.rowcount - 1;

// get a circulant PSF (in column_major)
SetLength(AT, H * Q); // * H
for I := 0 to (Q - 1) do
    for K := 0 to (H - 1) do
        if (K <= Blur - 1) then // and (I * H + K + I <= I * H + H - 1)
            AT[I * H + K + I] := PSF[K];
SetLength(PSF, 0);

// get SVD of AT
Ajobz := 'A';
SetLength(SS, Q);
SetLength(U, H * H);
SetLength(VT, Q * Q); // H * H
SetLength(ASuperb, Q - 2);
LAPACKE_dgesdd (COLUMN_MAJOR, Ajobz, H, Q, addr(AT[0]), H, addr(SS[0]), addr(U[0]), H,
addr(VT[0]), Q);
SetLength (ASuperb, 0);
SetLength (AT, 0);

// create E-1, in column_major order
SetLength(E, H * Q);
for K := 0 to Q - 1 do
    E[K * H + K] := 1 / SS[K];
SetLength (SS, 0);

// now use dgemm twice
Aalpha := 1.0;
Abeta := 1.0;
SetLength(VE, Q * H);
SetLength(SVD, Q * H);
cblas_dgemm (COLUMN_MAJOR, Trans, Trans, Q, H, Q, Aalpha, addr(VT[0]), Q, addr(E[0]),
H, Abeta, addr(VE[0]), Q);
cblas_dgemm (COLUMN_MAJOR, NoTrans, Trans, Q, H, H, Aalpha, addr(VE[0]), Q,
addr(U[0]), H, Abeta, addr(SVD[0]), Q);
SetLength (U, 0);
SetLength (VT, 0);
SetLength (VE, 0);
SetLength (E, 0);

end;

procedure TForm1.SVDSeqClick(Sender: TObject);
var
    // deconvolution variables
    B, BFull, XD : array of double;
    X : wordarray;
    K, I, C : Integer;

    // dgemm stuff
    Aalpha, Abeta : double;

    // picture dimensions
    H, F, Q : cardinal;

    // picture sequence variables
    SEQ, N : integer;
    instr : string;
    y, xs, xx : integer;

begin
    // prepare all variables
    F := strtoint(SVDBlur.Text);
    H := Pic_Height div F;
    Q := H + 1 - Blur;
    instr := '';
    N := 0;
    SetLength(dump[1], Pic_Height * Pic_Width); // scrambled 14 bit pics
    SetLength(MySnap[1], Pic_Height * Pic_Width); // scrambled 16 bit pics
    SetLength(MySnap[2], Pic_Height * Pic_Width); // unscrambled, corrected 16 bit pics
    SetLength(LongSnap, Pic_Height * Pic_Width); // added picture

    // for many pictures/samples, loop would start here
    for K := 0 to Pic_Height * Pic_Width - 1 do

```

## Xray Generation by Field Emission

```

begin
  LongSnap[K] := 0;
end;

StatusSequence.Lines.Add('Started Sequence Grab');
for SEQ := 0 to (StringGrid1.RowCount - 1) do
// get positions from stringgrid
  begin
    ComPort1.WriteStr('A' + StringGrid1.cells[0,SEQ] + #13);
// move
    check;
// wait until in position
    Get4;
// take 4 pics and add
    for y := 0 to Pic_Height - 1 do
// unscramble
      for xs := 0 to 5 do
        for xx := 0 to 255 do
          MySnap[2][y*Pic_Stride div 2 + xs*256 + xx] := (MySnap[1][y*Pic_Stride div 2
+ xs + xx*6]);
        for K := 0 to Pic_Height*Pic_Width - 1 do
// flat field correction
          begin
            if MySnap[2][K] - MySnap[13][K] < 0 then
              begin
                MySnap[2][K] := 0;
              end
            else
              begin
                dec(MySnap[2][K], MySnap[13][K]);
              end;
            MySnap[2][K] := MySnap[2][K] * MySnap[14][Pic_Height*Pic_Width - 1] div
MySnap[14][K];
          end;
          for K := 0 to Pic_Height * Pic_Width - 1 do
// add pictures
            inc(LongSnap[K], MySnap[2][K]);
            inc(N);
            Savepng16tofile(('C:\Remotedebug\Test' + inttostr(N) + '.png'), Pic_Width,
Pic_Height, Pic_Stride, MySnap[2]); // save pics to png
          end;
          StatusSequence.Lines.Add('All pictures taken');
          SetLength(dump[1], 0);
// set unused stuff to 0
          SetLength(MySnap[1], 0);
          for K := 0 to Pic_Height * Pic_Width - 1 do
// save added picture
            MySnap[2][K] := LongSnap[K] div StringGrid1.RowCount;
            Savepng16tofile(('C:\Remotedebug\SVDadded.png'), Pic_Width, Pic_Height, Pic_Stride,
MySnap[2]);
            SetLength(MySnap[2], 0);

if F <> 1 then
  begin
    // rotate LongSnap into BFull
    SetLength(BFull, Pic_Height * Pic_Width);
    for C := 0 to Pic_Width - 1 do
      for K := 0 to Pic_Height - 1 do
        BFull[C * Pic_Height + K] := LongSnap[C + Pic_Width * K];
    SetLength(LongSnap, 0); // reset B
    SetLength(B, H * Pic_Width);
    for K := 0 to H * Pic_Width - 1 do
      B[K] := 0;
    // shrink
    SetLength(B, H * Pic_Height);
    for C := 0 to Pic_Width - 1 do
      for K := 0 to H - 1 do
        for I := 0 to F - 1 do
          B[C * H + K] := B[C * H + K] + (BFull[C * Pic_Height + K * F + I] / F);
    SetLength(BFull, 0);
  end
else
  begin
    // rotate LongSnap into B
    SetLength(B, Pic_Height * Pic_Width);
    for C := 0 to Pic_Width - 1 do
      for K := 0 to Pic_Height - 1 do
        B[C * Pic_Height + K] := LongSnap[C + Pic_Width * K];
    SetLength(LongSnap, 0);
  end
end
end

```

```

end;

// reconstruct B using SVD, save into XD, then round + rotate to X and finally save to
.png
Aalpha := 1.0;
Abeta  := 1.0;
SetLength(XD, Q * Pic_Width);
cblas_dgemm (COLUMN_MAJOR, NoTrans, NoTrans, Q, Pic_Width, H, Aalpha, addr(SVD[0]), Q,
addr(B[0]), H, Abeta, addr(XD[0]), Q);

// rotate back, get output image
if F <> 1 then
begin
SetLength(X, Q * Pic_Width);
for C := 0 to Pic_Width - 1 do
for K := 0 to (Pic_Height div F) - 1 do
X[C + Pic_Width * K] := Round(XD[C * Q + K]);
Savepng16tofile((GetCurrentDir + '\' + SVDBlur.Text + 'SVDImage0.png'), Pic_Width,
Q, Pic_Stride, X);
{ // expand
for C := 0 to Pic_Width - 1 do
for K := 0 to Pic_Height - 1 do
for I := 0 to F - 1 do
BFull[C * Pic_Height + K * F + I] := B[C * H + K];
setlength(B, 0);}
end
else
begin
SetLength(X, Q * Pic_Width);
for C := 0 to Pic_Width - 1 do
for K := 0 to Q - 1 do
X[C + Pic_Width * K] := Round(XD[C * Q + K]);
Savepng16tofile((GetCurrentDir + '\' + 'SVDImage.png'), Pic_Width, Q, Pic_Stride, X);
end;
SetLength(X, 0);
SetLength(B, 0);
SetLength(XD, 0);
StatusSequence.Lines.Add('Sequence Completed');
end;

procedure TForm1.DeconvolutionSequenceClick(Sender: TObject);
var
// deconvolution variables
AT, B : array of double;
X : wordarray;
K, I, C : Integer;
PSF : array of byte;
Blur : integer;

// picture sequence variables
SEQ, S, N, Z : integer;
instr : string;
y, xs, xx : integer;

begin

// get a PSF
SetLength(PSF, 52);
PSF[0] := 1;
PSF[2] := 1;
PSF[7] := 1;
PSF[8] := 1;
PSF[9] := 1;
PSF[15] := 1;
PSF[17] := 1;
PSF[22] := 1;
PSF[23] := 1;
PSF[26] := 1;
PSF[27] := 1;
PSF[28] := 1;
PSF[29] := 1;
PSF[31] := 1;
PSF[32] := 1;
PSF[33] := 1;
PSF[35] := 1;
PSF[37] := 1;
PSF[38] := 1;

```

## Xray Generation by Field Emission

```

PSF[39] := 1;
PSF[42] := 1;
PSF[45] := 1;
PSF[46] := 1;
PSF[49] := 1;
PSF[50] := 1;
PSF[51] := 1;

// load PSF into stringgrid1
StringGrid1.rowcount := 0;
for K := 0 to 51 do
  if PSF[K] = 1 then
    begin
      StringGrid1.rowcount := StringGrid1.rowcount + 1;
      StringGrid1.cells[0, StringGrid1.rowcount - 2] := inttostr(2000 - K); // adjust to
starting position
    end;
  StringGrid1.rowcount := StringGrid1.rowcount - 1;

// prepare all variables
Blur := 1 + strtoint(StringGrid1.cells[0, 0]) - strtoint(StringGrid1.cells[0,
StringGrid1.rowcount - 1]);
instr := '';
N := 0;
Z := strtoint(RepeatSeq.text); // faster than doing strtoint every pass
SetLength(dump[1], Pic_Height*Pic_Width); // scrambled 14 bit pics
SetLength(MySnap[1], Pic_Height*Pic_Width); // scrambled 16 bit pics
SetLength(MySnap[2], Pic_Height*Pic_Width); // unscrambled, corrected 16 bit pics
SetLength(LongSnap, (Pic_Height + Blur - 1)*Pic_Width); // added picture

for K := 0 to (Pic_Height + Blur - 1)*Pic_Width - 1 do
  begin
    LongSnap[K] := 0;
  end;
StatusSequence.Lines.Add('Started Sequence Grab');
for S := 1 to Z do
// repeat a number of times
  begin
    for SEQ := 0 to (StringGrid1.RowCount - 1) do
// get positions from stringgrid
      begin
        ComPort1.WriteStr('A' + StringGrid1.cells[0,SEQ] + #13);
// move
        check;
// wait until in position
        Get4;
// take 4 pics and add
        for y := 0 to Pic_Height - 1 do
// unscramble
          for xs := 0 to 5 do
            for xx := 0 to 255 do
              MySnap[2][y*Pic_Stride div 2 + xs*256 + xx] := (MySnap[1][y*Pic_Stride div 2 +
xs + xx*6]);
            for K := 0 to Pic_Height*Pic_Width - 1 do
// flat field correction
              begin
                if MySnap[2][K] - MySnap[13][K] < 0 then
                  begin
                    MySnap[2][K] := 0;
                  end
                else
                  begin
                    dec(MySnap[2][K], MySnap[13][K]);
                  end;
                MySnap[2][K] := MySnap[2][K] * MySnap[14][Pic_Height*Pic_Width - 1] div
MySnap[14][K];
                // MySnap[2][K] := MySnap[2][K] * 65535 div MySnap[14][K];
              end;
            for K := 0 to Pic_Height * Pic_Width - 1 do
// add pictures
              inc(LongSnap[K], MySnap[2][K]);
              inc(N);
              Savepng16tofile(('C:\Remotedebug\Test' + inttostr(N) + '.png'), Pic_Width,
Pic_Height, Pic_Stride, MySnap[2]); // save pics to png
            end;
          end;
        StatusSequence.Lines.Add('All pictures taken');
        SetLength(dump[1], 0);
// set unused stuff to 0

```

```

SetLength(MySnap[1], 0);
SetLength(MySnap[2], (Pic_Height + Blur - 1) * Pic_Width);
for K := 0 to (Pic_Height + Blur - 1) * Pic_Width - 1 do
// save added picture
  MySnap[2][K] := LongSnap[K] div StringGrid1.RowCount;
  Savepng16tofile(('C:\Remotedebug\LAadded.png'), Pic_Width, Pic_Height + Blur - 1,
Pic_Stride, MySnap[2]);
  SetLength(MySnap[2], 0);

// rotate longsnap into B
SetLength(B, (Pic_Height + Blur - 1) * Pic_Width);
for C := 0 to Pic_Width - 1 do
  for K := 0 to (Pic_Height + Blur - 1) - 1 do
    B[C * (Pic_Height + Blur - 1) + K] := LongSnap[C + Pic_Width * K];
SetLength(longsnap, 0);

// get a circulant PSF (transpose of A)
SetLength(AT, Pic_Height * (Pic_Height + Blur - 1));
for I := 0 to Pic_Height - 1 do
  for K := 0 to (Pic_Height + Blur - 1) - 1 do
    if K <= Blur - 1 then
      AT[I * (Pic_Height + Blur - 1) + K + I] := PSF[K];
SetLength(PSF, 0);

StatusSequence.Lines.Add('LAPacke start');
LAPACKE_dgels (COLUMN_MAJOR, ATrans, (Pic_Height + Blur - 1), Pic_Height, Pic_Width,
addr(AT[0]), (Pic_Height + Blur - 1), addr(B[0]), (Pic_Height + Blur - 1));
StatusSequence.Lines.Add('LAPacke done');
SetLength(AT, 0);

// check final pic
SetLength(X, (Pic_Height + Blur - 1) * Pic_Width);
for C := 0 to Pic_Width - 1 do
  for K := 0 to Pic_Height - 1 do
    begin
      if B[C * (Pic_Height + Blur - 1) + K] > 65535 then
        B[C * (Pic_Height + Blur - 1) + K] := 65535;
      if B[C * (Pic_Height + Blur - 1) + K] < 0 then
        B[C * (Pic_Height + Blur - 1) + K] := 0;
      X[C + Pic_Width * K] := ABS(Round(B[C * (Pic_Height + Blur - 1) + K]));
    end;
Savepng16tofile((GetCurrentDir + '\LApic.png'), Pic_Width, Pic_Height, Pic_Stride, X);
SetLength(X, 0);
SetLength(B, 0);
SetLength(X, 0);
StatusSequence.Lines.Add('LA done');

end;

procedure TForm1.PictureSequenceClick(Sender: TObject);
var
  SEQ, S, N, K, Z, O: integer;
  instr: string;
  y, xs, x : integer;
  PixelAdded, Offset: array of integer;
  LongerSnap: array of int64;

begin
  instr := '';
// prepare all variables
  N := 0;
  Z := strtoint(RepeatSeq.text); // faster than doing strtoint every pass
  O := strtoint(StringGrid1.Cells[0,0]); // reference position
  SetLength(dump[1], Pic_Height*Pic_Width); // scrambled 14 bit pics
  SetLength(MySnap[1], Pic_Height*Pic_Width); // scrambled 16 bit pics
  SetLength(MySnap[2], Pic_Height*Pic_Width); // unscrambled, corrected 16 bit pics
  SetLength(LongSnap, Pic_Height*Pic_Width); // sum of all pics
  SetLength(LongerSnap, Pic_Height*Pic_Width); // sum of longsnavs
  SetLength(PixelAdded, Pic_Height*Pic_Width); // counts how many pics were added
  together in each pixel
  SetLength(Offset, StringGrid1.RowCount); // remembers offset for each picture
  {for K := 0 to StringGrid1.RowCount - 1 do
    offset[K] := strtoint(StringGrid1.Cells[0,K]) - O;}
// calculate offsets
  for K := 0 to Pic_Height*Pic_Width - 1 do
    begin
      LongerSnap[K] := 0;
      LongerSnap[K] := 0;

```

## Xray Generation by Field Emission

```

    PixelAdded[K] := 0;
  end;
  StatusSequence.Lines.Add('Started Sequence Grab');
  for S := 1 to Z do
  // repeat a number of times
  begin
    for SEQ := 0 to (StringGrid1.RowCount - 1) do
  // get positions from stringgrid
    begin
      ComPort1.WriteStr('A' + StringGrid1.Cells[0,SEQ] + #13);
  // move
      check;
  // wait until in position
      Get4;
  // take 4 pics and add
      for y := 0 to Pic_Height - 1 do
  // unscramble
        for xs := 0 to 5 do
          for x := 0 to 255 do
            MySnap[2][y*Pic_Stride div 2 + xs*256 + x] := (MySnap[1][y*Pic_Stride div 2 +
xs + x*6]);
          for K := 0 to Pic_Height*Pic_Width - 1 do
  // flat field correction
            begin
              dec(MySnap[2][K], MySnap[13][K]);
              MySnap[2][K] := MySnap[2][K] * MySnap[14][Pic_Height*Pic_Width - 1] div
MySnap[14][K];
            end;
            offset[SEQ] := strtoint(StringGrid1.Cells[0,SEQ]) - 0; // change to 2100 or sth
            for K := 0 to Pic_Height*Pic_Width - 1 do
              begin
  // add
                inc(LongSnap[K], MySnap[2][K]);
                // inc(PixelAdded[K]);
              end;
              inc(N);
              Savepng16tofile(('C:\Remotedebug\Test' + inttostr(N) + '.png'), Pic_Width,
Pic_Height, Pic_Stride, MySnap[2]); // save pics to png
            end;
          end;

          for K := 0 to Pic_Height*Pic_Width - 1 do
  // get combined pic without offset
            MySnap[2][K] := LongSnap[K] div StringGrid1.RowCount;
            Savepng16tofile(('C:\Remotedebug\FinalPic0.png'), Pic_Width, Pic_Height, Pic_Stride,
MySnap[2]); // save combined pic w/o offset

          for S := 0 to StringGrid1.RowCount - 1 do
  // add LongSnap to LongerSnap with offset many times
            for K := 0 to Pic_Height*Pic_Width - 1 do
              if (K-Pic_Width*offset[S] >= 0) and (K-Pic_Width*offset[S] <= Pic_Width*Pic_Height
- 1) then
                begin
                  inc(LongerSnap[K], LongSnap[K-Pic_Width*offset[S]]);
                  inc(PixelAdded[K], StringGrid1.RowCount);
                end;
              end;

            for K := 0 to Pic_Height*Pic_Width - 1 do
  // average
              MySnap[2][K] := LongerSnap[K] div (PixelAdded[K]);

              Savepng16tofile(('C:\Remotedebug\FinalPic1.png'), Pic_Width, Pic_Height, Pic_Stride,
MySnap[2]); // save combined pic
              StatusSequence.Lines.Add('Finished Sequence Grab');
              SetLength(dump[1], 0);
  // set unused stuff to 0
              SetLength(MySnap[1], 0);
              SetLength(MySnap[2], 0);
              SetLength(LongSnap, 0);
              SetLength(PixelAdded, 0);
            end;

  procedure TForm1.SequenceLongClick(Sender: TObject);
  var
    SEQ, S, N, K, Z, O, offset: integer;
    instr: string;
    y, xs, x: integer;
    PixelAdded: array of integer;

```

```

begin
  instr := '';
  // prepare all variables
  N := 0;
  Z := strtoint(RepeatSeq.text); // faster than doing strtoint every pass
  O := strtoint(StringGrid1.Cells[0,0]); // reference position
  SetLength(dump[1], Pic_Height*Pic_Width); // scrambled 14 bit pics
  SetLength(MySnap[1], Pic_Height*Pic_Width); // scrambled 16 bit pics
  SetLength(MySnap[2], Pic_Height*Pic_Width); // unscrambled, corrected 16 bit pics
  SetLength(LongSnap, Pic_Height*Pic_Width); // sum of all pics
  SetLength(PixelAdded, Pic_Height*Pic_Width); // counts how many pics were added
  together in each pixel
  for K := 0 to Pic_Height*Pic_Width - 1 do
    begin
      LongSnap[K] := 0;
      PixelAdded[K] := 0;
    end;
  StatusSequence.Lines.Add('Started Sequence Grab');
  for S := 1 to Z do
  // repeat a number of times
    begin
      for SEQ := 0 to (StringGrid1.RowCount - 1) do
      // get positions from stringgrid
        begin
          ComPort1.WriteStr('A' + StringGrid1.cells[0,SEQ] + #13);
        // move
          check;
        // wait until in position
          Get4;
        // take 4 pics and add
          for y := 0 to Pic_Height - 1 do
        // unscramble
          for xs := 0 to 5 do
            for x := 0 to 255 do
              MySnap[2][y*Pic_Stride div 2 + xs*256 + x] := (MySnap[1][y*Pic_Stride div 2 +
xs + x*6]);
            for K := 0 to Pic_Height*Pic_Width - 1 do
        // flat field correction
          begin
            dec(MySnap[2][K], MySnap[13][K]);
            MySnap[2][K] := MySnap[2][K] * MySnap[14][Pic_Height*Pic_Width - 1] div
MySnap[14][K];
          end;
          offset := strtoint(StringGrid1.Cells[0,SEQ]) - O;
        // calculate offset
          for K := 0 to Pic_Height*Pic_Width - 1 do
        // add
          if (K-Pic_Width*offset >= 0) and (K-Pic_Width*offset <= Pic_Width*Pic_Height -
1) then
            begin
              inc(LongSnap[K], MySnap[2][K-Pic_Width*offset]);
              inc(PixelAdded[K]);
            end;
            inc(N);
            Savepng16tofile(('C:\Remotedebug\Test' + inttostr(N) + '.png'), Pic_Width,
Pic_Height, Pic_Stride, MySnap[2]); // save pics to png
          end;
        // average
          for K := 0 to Pic_Height*Pic_Width - 1 do
            MySnap[2][K] := LongSnap[K] div PixelAdded[K];
            Savepng16tofile(('C:\Remotedebug\FinalPic2.png'), Pic_Width, Pic_Height, Pic_Stride,
MySnap[2]); // save combined pic
          StatusSequence.Lines.Add('Finished Sequence Grab');
          SetLength(dump[1], 0);
        // set unused stuff to 0
          SetLength(MySnap[1], 0);
          SetLength(MySnap[2], 0);
          SetLength(LongSnap, 0);
          SetLength(PixelAdded, 0);
        end;

  {=====}
  { CDDGRAB INTERFACE }
  {=====}

procedure TForm1.CDDGrabClick(Sender: TObject);
var

```

## Xray Generation by Field Emission

```

K: integer;
y, xs, x : integer;

begin
  SetLength(dump[1], Pic_Height*Pic_Width);
  SetLength(MySnap[1], Pic_Height*Pic_Width);
  SetLength(MySnap[2], Pic_Height*Pic_Width);
  // SetLength(MyBytes[0], Pic_Height*Pic_Width);

  StatusGrab.Lines.Add('Grabbing picture...');
  Get4; // take 4 pictures, add them, save into MySnap[1]
  StatusGrab.Lines.Add('unscrambling...');
  // height := pxd_imageYdim; //
  // width := pxd_imageXdim div 2;

  // Bytes Unscrambler
  {for y := 0 to Pic_Height - 1 do
    for xs := 0 to 5 do
      for x := 0 to 255 do
        MyBytes[0][y*Pic_Stride + xs*256 + x] := (MySnap[1][y*Pic_Stride div 2 + xs +
x*6]) div 256;
        StatusGrab.Lines.Add('unscrambled into MyBytes[0]');}

  // Bit Swapper
  {for k:= 0 to Pic_Width * Pic_Height - 1 do
    MySnap[1][K] := ((MySnap[1][K] shr 8) and $ff) or ((MySnap[1][K] and $ff) shl 8);
    StatusGrab.Lines.Add('Bits swapped');}

  for y := 0 to Pic_Height - 1 do
    for xs := 0 to 5 do
      for x := 0 to 255 do
        MySnap[2][y*Pic_Stride div 2 + xs*256 + x] := (MySnap[1][y*Pic_Stride div 2 + xs +
x*6]);
        StatusGrab.Lines.Add('unscrambled into MySnap[2]');

  // correction
  StatusGrab.Lines.Add('Correcting...');
  for K := 0 to Pic_Height*Pic_Width - 1 do
// flat field correction
  begin
    if MySnap[2][K] - MySnap[13][K] < 0 then
      begin
        MySnap[2][K] := 0;
      end
    else
      begin
        dec(MySnap[2][K], MySnap[13][K]);
      end;
    MySnap[2][K] := MySnap[2][K] * MySnap[14][Pic_Height*Pic_Width - 1] div
MySnap[14][K];
  end;
  StatusGrab.Lines.Add('Corrected');

  // Bytes Unscrambler
  {for K := 0 to Pic_Height*Pic_Width do
    MyBytes[0][K] := MySnap[2][K] div 256;
    StatusGrab.Lines.Add('unscrambled into MyBytes[0]');}

  if SaveCheckBox.Checked = true then
  begin
    if S = 10 then
      begin
        StatusGrab.Lines.Add('Overwriting');
        S := 1;
      end
    else
      inc(S);
    SetLength(MySnap[S+2], Pic_Height*Pic_Width);
    SetLength(MyBytes[S], Pic_Height*Pic_Stride);
    StatusGrab.Lines.Add('Saving to ' + inttostr(S));
    {for K := 0 to Pic_Height*Pic_Stride do
      MyBytes[S][K] := MyBytes[0][K];} // save Bytes
    for K := 0 to Pic_Height*Pic_Width do
      MySnap[S+2][K] := MySnap[2][K]; // save Snaps; since MySnap[1] and [2] are already
used, saving starts from 3
    StatusGrab.Lines.Add('Saved to ' + inttostr(S));
  end;
  SetLength(dump[1], 0);
  SetLength(MySnap[1], 0);

```

```

end;

procedure TForm1.Get4; // takes and adds 4 pictures together, saves them in to MySnap[1]
var
  J, K: Integer;
begin
  for K := 0 to Pic_Height*Pic_Width - 1 do // reset MySnap[1] and [2]
    begin
      MySnap[1][K] := 0;
      MySnap[2][K] := 0;
    end;
  for J := 0 to 3 do
    begin
      for K := 0 to Pic_Height*Pic_Width - 1 do // reset dump
        dump[1][K] := 0;
        currentbuffer := 1;
        SetTriggerMode(dexela.CC1);
        CDD_grab(false, false);
        for K := 0 to Pic_Height*Pic_Width do
          begin
            inc(MySnap[1][K], dump[1][K]);
          end;
        end;
    end;
end;

procedure TForm1.CollectDarkClick(Sender: TObject); // xray off, save into MySnap[13]
var
  y, x, xs: Integer;
begin
  ComPort1.WriteStr('A8000' + #13);
  StatusGrab.Lines.add('Moving the tray out of the way');
  StatusMotor.Lines.add('Moving to 8000');
  check;
  StatusMotor.Lines.add('Arrived at 8000');
  SetLength(MySnap[13], Pic_Height*Pic_Width);
  SetLength(dump[1], Pic_Height*Pic_Width);
  SetLength(MySnap[1], Pic_Height*Pic_Width);
  SetLength(MySnap[2], Pic_Height*Pic_Width);
  StatusGrab.Lines.Add('Grabbing picture...');
  Get4; // take 4 pictures, add them, save into MySnap[1]
  StatusGrab.Lines.Add('unscrambling...');
  for y := 0 to Pic_Height - 1 do
    for xs := 0 to 5 do
      for x := 0 to 255 do
        MySnap[13][y*Pic_Stride div 2 + xs*256 + x] := (MySnap[1][y*Pic_Stride div 2 + xs
+ x*6]);
      savepng16tofile(('C:\Remotedebug\Dark.png'), Pic_Width, Pic_Height, Pic_Stride,
MySnap[13]);
      StatusGrab.Lines.Add('Collected dark');
      StatusGrab.Lines.Add('Turn Xrays ON and Collect Flood');
      CollectFlood.Enabled := true;
    end;
end;

procedure TForm1.CollectFloodClick(Sender: TObject); // xray on, save into MySnap[13]
var
  y, x, xs: Integer;
  K: Integer;
  mm: int64;
begin
  mm := 0;
  ComPort1.WriteStr('A8000' + #13);
  StatusGrab.Lines.add('Moving the tray out of the way');
  StatusMotor.Lines.add('Moving to 8000');
  check;
  StatusMotor.Lines.add('Arrived at 8000');
  SetLength(MySnap[14], Pic_Height*Pic_Width);
  SetLength(dump[1], Pic_Height*Pic_Width);
  SetLength(MySnap[1], Pic_Height*Pic_Width);
  SetLength(MySnap[2], Pic_Height*Pic_Width);
  StatusGrab.Lines.Add('Grabbing picture...');
  Get4; // take 4 pictures, add them, save into MySnap[1]
  StatusGrab.Lines.Add('unscrambling...');
  for y := 0 to Pic_Height - 1 do
    for xs := 0 to 5 do
      for x := 0 to 255 do

```

## Xray Generation by Field Emission

```
MySnap[14][y*Pic_Stride div 2 + xs*256 + x] := (MySnap[1][y*Pic_Stride div 2 + xs
+ x*6]);
for K := 0 to Pic_Height*Pic_Width - 1 do
begin
  if MySnap[14][K] - MySnap[13][K] <= 0 then
  begin
    MySnap[14][K] := 1;
    inc(mm);
  end
  else
  begin
    dec(MySnap[14][K], MySnap[13][K]);
    inc(mm, MySnap[14][K] - MySnap[13][K]);
  end;
end;
MySnap[14][Pic_Height*Pic_Width - 1] := mm div Pic_Height*Pic_Width;

savepng16tofile('C:\Remotedebug\Flood.png', Pic_Width, Pic_Height, Pic_Stride,
MySnap[14]);
StatusGrab.Lines.Add('Collected flood');
end;

procedure TForm1.LoadFlatFieldClick(Sender: TObject);
var
  width, height, stride: Cardinal;
begin
  if not fileexists(GetCurrentDir + '\Dark.png') then
  begin
    showmessage('Dark.png is not in the same folder as the program');
    Application.Terminate;
    exit;
  end;
  if not fileexists(GetCurrentDir + '\Flood.png') then
  begin
    showmessage('Flood.png is not in the same folder as the program');
    Application.Terminate;
    exit;
  end;
  height := Pic_Height;
  width := Pic_Width;
  stride := 2*width;
  readpng16fromfile(GetCurrentDir + '\Dark.png', width, height, stride, MySnap[13]);
  readpng16fromfile(GetCurrentDir + '\Flood.png', width, height, stride, MySnap[14]);
  StatusGrab.Lines.Add('Flat Field Correction parameters obtained')
end;

{=====}
{ SAVING PICTURES TO .png FILES
{=====}

procedure TForm1.SaveButtonClick(Sender: TObject);
begin
  savepng16tofile('C:\Remotedebug\CurrentTest.png', Pic_Width, Pic_Height, Pic_Stride,
MySnap[2]);
  StatusGrab.Lines.Add('Saved Current Picture');
end;

procedure TForm1.SaveNoClick(Sender: TObject);
begin
  savepng16tofile('C:\Remotedebug\MySnap' + SaveEdit.text + '.png', Pic_Width,
Pic_Height, Pic_Stride, MySnap[strtoint(SaveEdit.text)]);
  StatusGrab.Lines.Add('Saved Picture ' + SaveEdit.text);
end;

end.
```

## APPENDIX 7 – MOTOR CALIBRATION

Underlying data from the Motor Calibration studies (chapter 6)

Cathode Gap

Measurement

Number of Steps on GUI	Meas_1	Meas_2	Meas_3	Meas_4	Meas_5	Measured $\langle \rangle$	sd
100	12.0	11.5	12.0	12.0	11.0	11.70	0.45
200	24.5	24.0	25.0	26.5	27.0	25.40	1.29
400	53.0	52.5	55.0	57.0	55.0	54.50	1.80
600	82.0	83.0	84.0	85.0	83.5	83.50	1.12
800	111.0	112.5	112.0	113.0	113.0	112.30	0.84
900	125.0	127.0	125.5	125.0	125.0	125.50	0.87
1000	137.5	138.0	138.0	138.0	138.0	137.90	0.22
1300	180.5	180.0	184.5	182.5	180.0	181.50	1.97
1600	226.0	226.0	224.0	226.0	225.0	225.40	0.89
2000	280.0	278.0	280.0	278.5	277.0	278.70	1.30
2500	350.5	350.0	353.5	351.5	350.0	351.10	1.47

Anode-Cathode Slide

Measurement

Number of Steps on GUI	Meas_1	Meas_2	Meas_3	Meas_4	Meas_5	Measured $\langle \rangle$	sd
500	9.0	10.0	8.5	7.5	7.5	8.5	1.1
1000	45.0	46.5	45.0	46.5	46.5	45.9	0.8
1500	86.0	86.0	85.5	88.5	86.5	86.5	1.2
2000	125.5	125.5	126.0	127.0	125.5	125.9	0.7
2500	162.5	164.0	163.0	165.5	164.5	163.9	1.2
3000	202.0	207.0	203.0	207.5	205.5	205.0	2.4
3500	243.0	247.0	244.0	245.0	244.0	244.6	1.5
4000	282.0	287.5	281.0	284.0	283.5	283.6	2.5
5000	361.0	360.0	361.5	364.0	364.5	362.2	2.0
6000	440.5	440.0	441.5	445.0	443.0	442.0	2.0
500	9.0	10.0	8.5	7.5	7.5	8.5	1.1